MATHEMATICAL AND COMPUTATIONAL MODELING OF FLEXOELECTRICITY AT MESOSCOPIC AND ATOMISTIC SCALES

David Codony

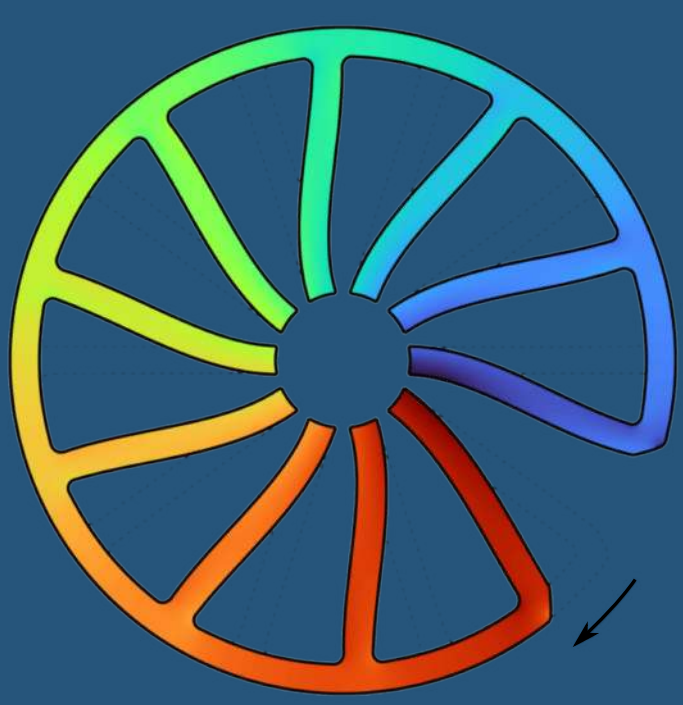

Doctoral Thesis
Barcelona, January 2021

MATHEMATICAL AND COMPUTATIONAL MODELING OF FLEXOELECTRICITY AT MESOSCOPIC AND ATOMISTIC SCALES

David Codony

Doctoral Thesis
Advisor: Irene Arias
Barcelona, January 2021

School of Mathematics and Statistics
Doctoral Degree in Applied Mathematics
Universitat Politècnica de Catalunya

UNIVERSITAT POLITÈCNICA DE CATALUNYA
BARCELONATECH
Facultat de Matemàtiques i Estadística

Doctoral Degree in Applied Mathematics
School of Mathematics and Statistics
Universitat Politècnica de Catalunya

Mathematical and computational modeling of flexoelectricity at mesoscopic and atomistic scales

by

David Codony

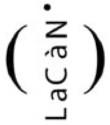

LaCàN: Laboratory of Mathematical and Computational Modeling

Advisor: Irene Arias
Barcelona, January 19, 2021

“The only impossible journey
is the one you never begin.”
–Anthony J. Robbins

Abstract

Mathematical and computational modeling of flexoelectricity at mesoscopic and atomistic scales

David Codony

This PhD thesis focuses on the development of mathematical and computational models for flexoelectricity, a relatively new electromechanical coupling that is present in any dielectric at the micron and sub-micron scales. The work is framed in the context of both continuum and quantum mechanics, and explores the gap between these two disciplines.

On the one hand, the focus is put on the mathematical modeling of the flexoelectric effect by means of continuum (electro-) mechanics, and the development of computational techniques required to numerically solve the associated boundary value problems. The novel computational infrastructure developed in this work is able to predict the performance of engineered devices for electromechanical transduction at sub-micron scales, where flexoelectricity is always present, without any particular restrictions in geometry, material choice, boundary conditions or nonlinearity. The numerical examples within this document show that flexoelectricity can be harnessed in multiple different ways towards the development of breakthrough applications in nanotechnology.

On the other hand, the flexoelectric effect is also studied at an atomistic level by means of quantum mechanics. This work proposes a novel methodology to quantify the flexoelectric properties of dielectric materials, by means of connecting ab-initio atomistic simulations with the proposed models at a coarser, continuum scales. The developed approach sheds some light on a controversial topic within the density functional theory community, where large disagreements among different theoretical derivations are typically found. The ab-initio computations serve not only to assess the material parameters within the continuum models, but also to validate their inherent assumptions regarding the relevant physics at the nanoscale.

Keywords: Flexoelectricity, Continuum mechanics, Quantum mechanics, Mathematical modeling, Computational modeling.

Acknowledgments

It has been a privilege to join the research group of my supervisor, Prof. Irene Arias, to study a very interesting and challenging topic. I express my sincerest gratitude to her for sharing her knowledge and supporting me throughout my research, while allowing me some freedom to work and learn on my own. She also instructed me in a honest, collaborative and science-oriented research, which I truly appreciate.

I extend my gratitude to Prof. Phanish Suryanarayana, who supported me during my research stay in Georgia Tech, and introduced me in a topic that was far from my background. I appreciate the time and efforts he invested in me and in making our collaboration fruitful.

I also want to acknowledge many other professors and researchers who have truly been a source of knowledge, help, motivation and inspiration for me. The first one in this list is Prof. Sonia Fernández-Méndez, who has been the largest source of knowledge and a key support for me since the beginning of my research, and allowed me to participate in other projects such as teaching or mentoring other students. I want to honestly acknowledge the contributions of Dr. Onofre Marco to my work and his personal support, which have been essential to my success. I am thankful to Prof. Marino Arroyo who has been a well of wisdom and inspiration, and also to Dr. Alejandro Torres-Sánchez and Esther Sala-Lardies for their help in specific topics during my research. I am happy to acknowledge the help and support received from other researchers in the FLEXOCOMP group, specially Jordi Barceló-Mercader, Dr. Prakhar Gupta and Alice Mocci who have been close collaborators to my projects and played a relevant role in their success. Also, I thank Abhiraj Sharma, Qimen Xu and Shashikant Kumar for the help provided during my research stay in Georgia Tech. Lastly, I acknowledge the continuous support provided by the staff in LaCàN and Georgia Tech.

On the personal side, I extend my gratitude to the aforementioned people, as well as to my colleagues and friends at LaCàN, CIMNE, Georgia Tech, Atlanta and Barcelona. A special mention is reserved to my family and to my partner for their unfailing and unconditional support. I will find the time for expressing my sincere and personal acknowledgement to each of them.

I gratefully acknowledge the financial support of the European Research Council (Starting Grant 679451 to Prof. Irene Arias).

Contents

List of Figures

List of Tables

Chapter 1

Introduction

1.1 Motivation

Electroactive materials are able to transform mechanical energy into electrical energy (and viceversa), hence their ubiquity in modern technologies (cf. Fig. 1.1). One of the main applications is to generate electrical power from mechanical sources (energy harvesting), such as vibrations associated with operating machinery, movements of the human body, ocean waves, wind, and others (Dagdeviren *et al.*, 2016). Another usage consists on converting a mechanical input into an electrical output just for sensing and measuring devices. Conversely, the application of electric fields to electroactive materials can yield well-controlled mechanical forces for actuation in robotics, biomedical devices, motors and personal electronics among others.

The underlying physics that drive electromechanical transduction can be very different in nature, and vary depending on the considered material. One of the most well-known and exploited electromechanical coupling is *piezoelectricity*, by which the mechanical strains $\boldsymbol{\varepsilon}$ and the electric polarization $\boldsymbol{p}$ are linearly coupled:

$$p_l = d_{lij}\varepsilon_{ij}, \tag{1.1}$$

where $\mathbf{d}$ is the tensor of piezoelectricity. This is the case of piezoelectric ceramics, which are polarized upon deformation, and conversely deform when an electrical field is applied. Piezoelectricity can be intuitively understood by the ionic crystal model under compression or tension (cf. Fig. 1.2a), in which the electric dipole moment increases or decreases due to a shift between the centers of gravity of the negative and the positive ions. Piezoelectricity allows reversibility, in the sense that reversal of the input (e.g. compression instead of tension) yields an opposite output (e.g. increasing or decreasing polarization field). However, it is restricted to crystalline dielectrics with a non-centrosymmetric structure. Otherwise, the dipole moment is not affected by the mechanical input (i.e. the piezoelectricity tensor vanishes).

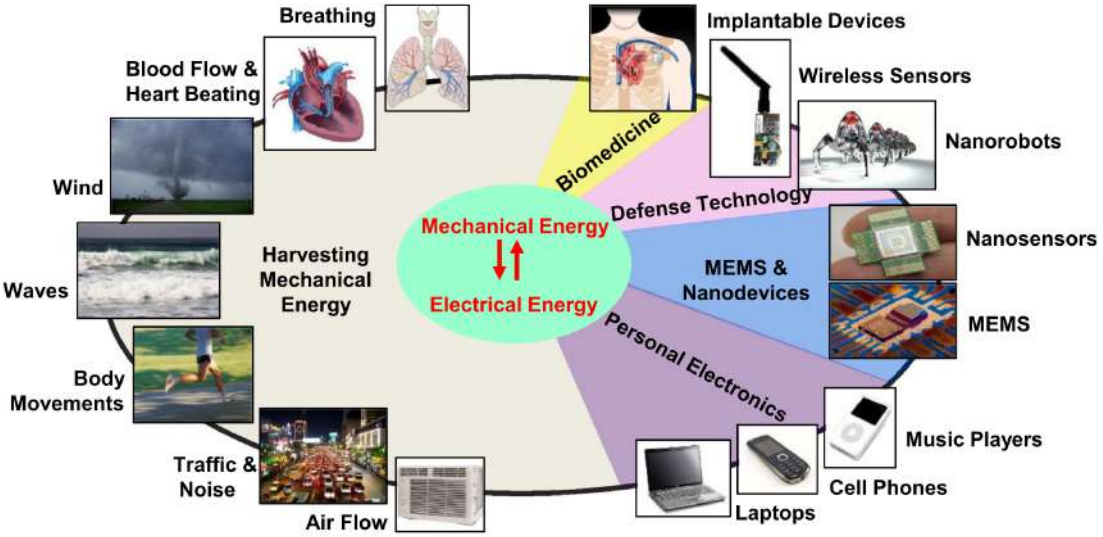

Figure 1.1: Applications of electromechanical transduction. Possible sources of energy harvesting (left) and its usage for sensing and actuation (right). Figure adapted from Dagdeviren *et al.* (2016).

Soft materials such as piezoelectric polymers or dielectric elastomers exhibit a different mechanism named *electrostriction* or Maxwell-stress effect. The application of an electric field through a compliant dielectric induces an electrostatic stress in it, as a result from the Coulombic attraction between the charges of opposite sign located on both sides of the material (cf. Fig. 1.2b). It can be mathematically written as

$$\sigma_{ij} = m_{klij} e_k e_l, \tag{1.2}$$

where the stresses $\boldsymbol{\sigma}$ are coupled to the square of the electric field $\boldsymbol{e}$ through the electrostriction tensor $\mathbf{m}$. In contrast to piezoelectricity, electrostriction is present in all dielectrics (referred to as universality), albeit it is only relevant in soft materials. However, it presents two noticeable drawbacks. On the one hand, it is a one-way coupling only: electric field (or polarization) is not generated by the application of strain. Hence, they can only be used as actuators. On the other hand, it does not allow reversibility: regardless of the sign of the applied electric field, the material will always deform in the same direction (either compression or expansion).

Some dielectrics exhibit as well other physical couplings, such as pyroelectricity (temperature-dependent polarization) or ferroelectricity (reversible spontaneous polarization), to name a few. All this variety of electromechanical couplings has been largely studied, is quite well understood and is suitable to describe the behavior of dielectrics at the macro- and mesoscale. However, at smaller (micro- and nano-) scales, additional effects become relevant and must be taken into account as well. One of these less studied electromechanical couplings constitutes the focus of the present manuscript: *flexoelectricity*.

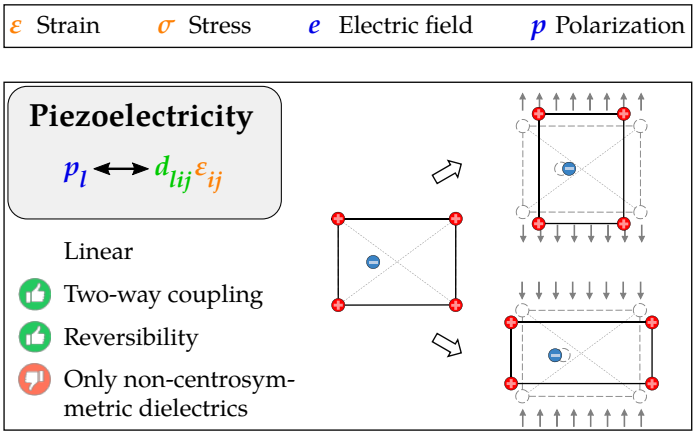

(a) Piezoelectricity

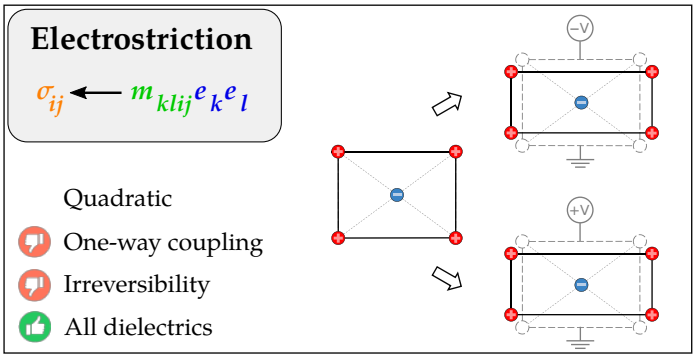

(b) Electrostriction

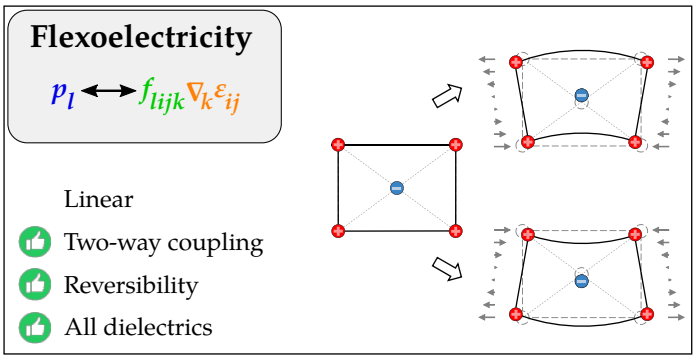

(c) Flexoelectricity

Figure 1.2: 2D sketches of different physics for electromechanical transduction in a crystalline dielectric.

The flexoelectric effects consists on the coupling between electric polarization and strain gradients. The (direct) flexoelectric effect is understood as the material polarization due to inhomogeneous deformation (e.g. bending or twisting) and is mathematically expressed as

$$p_l = f_{lijk}\frac{\partial \varepsilon_{ij}}{\partial x_k}, \tag{1.3}$$

where $\boldsymbol{f}$ is the flexocoupling tensor. In hard materials, it can be intuitively understood as well by the ionic crystal model under bending (cf. Fig. 1.2c), in which a non-zero net dipole moment arises, even in centrosymmetric materials. Therefore, it is present in all dielectrics, regardless of their crystalline structure. Similarly to piezoelectricity, it is a two-way coupling, and hence it is also possible inducing a bending deformation by applying an external electric field. Moreover, thanks to its linearity it is reversible in sign. Figure 1.3 shows the linearity of the direct flexoelectric effect measured in different dielectrics.

There also exists a thermodynamically conjugate converse flexoelectric effect that consists on the generation of stress $\boldsymbol{\sigma}$ due to the application of an inhomogeneous electric field $\boldsymbol{e}$, i.e.

$$\sigma_{ij} = f_{lijk}\frac{\partial e_l}{\partial x_k}. \tag{1.4}$$

The term "flexoelectricity" may refer to the direct flexoelectric effect only, or to both the direct and converse flexoelectric effects, depending on the context.

Due to their convenient properties (that is, universality, reversibility and being a two-way coupling) as compared to piezoelectricity or electrostriction, flexoelectricity seems to be a promising mechanism to be exploited in modern technologies. However, it has only gained attention very recently (cf. Fig. 1.4). The reason behind this is that the flexoelectric material constants are typically very small, and therefore sufficiently large strain gradients are required in order to trigger a sizable flexoelectric effect. Since strain-gradients scale inversely to spatial dimension, they are typically small at the meso- and macroscale, but considerably large in the micro- and nanoscale. Therefore, flexoelectricity is by nature a size dependent effect, relevant only at the microscale and nanoscale. It is not surprising that the rise of scientific and industrial interest in flexoelectricity coincides in time with the investment and developments in various nanotechnologies, such as nanomedicine, nanobiotechnology and nanoremediation, or the discovery of atomically-thin materials (2D monolayers) such as graphene, featuring unprecedented and exciting mechanical and optical properties with multiple potential applications.

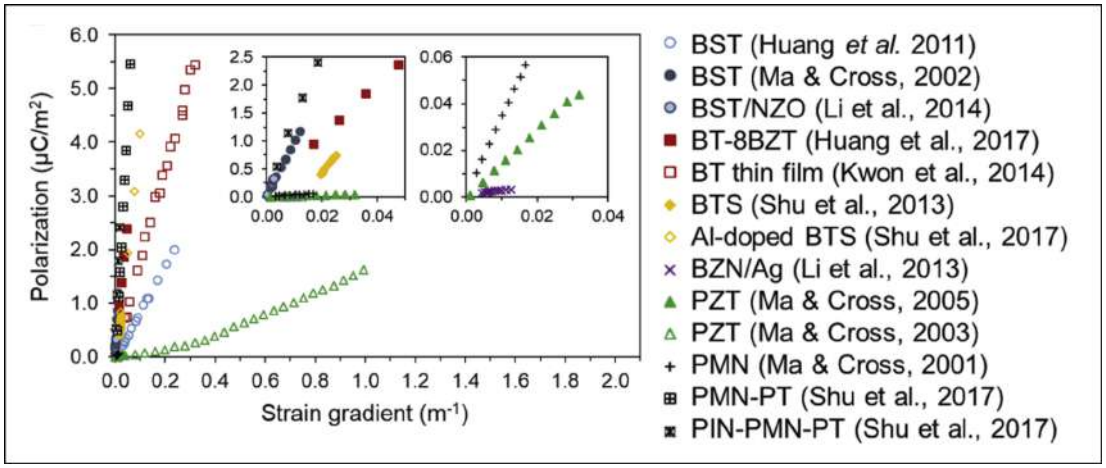

Figure 1.3: Linearity of flexoelectric polarization with respect to strain gradient. Figure adapted from Wang *et al.* (2019).

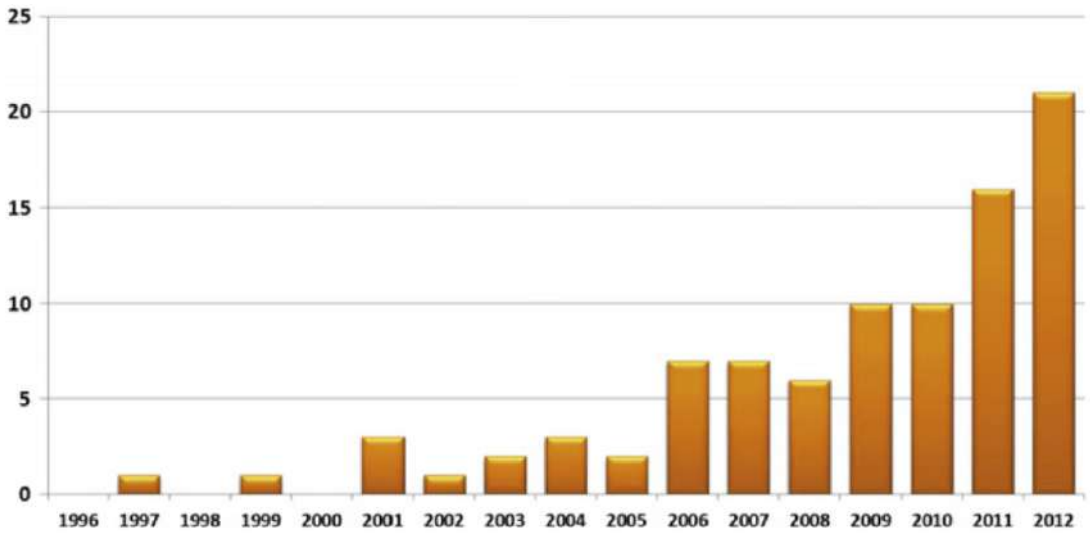

Figure 1.4: The number of publications on flexoelectricity in solids per year. Figure adapted from Yudin and Tagantsev (2013).

1.2 State of the art of the flexoelectric effect

The state of the art of the flexoelectric effect is briefly summarized in Fig. 1.5. The most characteristic (and challenging) feature is perhaps its underlying multiscale nature in the majority of the areas, from its observation, understanding, modeling and quantification until the computationally-based functional design of electromechanical devices for specific technological applications. In what follows, we summarize the most relevant aspects of the flexoelectric effect.

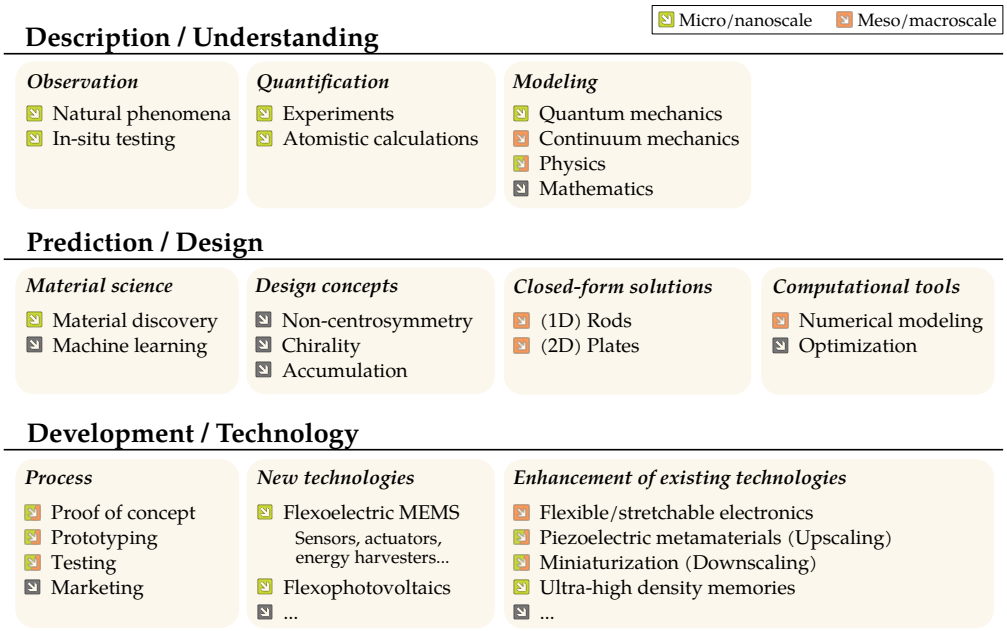

Figure 1.5: State of the art of flexoelectricity, and its underlying multiscale nature.

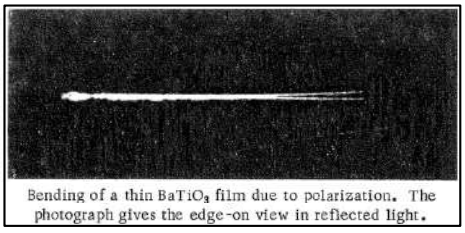
Bending of a thin $BaTiO_3$ film due to polarization. The photograph gives the edge-on view in reflected light.

(a) A clamped, closed-circuited 2.5 µm-thin $BaTiO_3$ film under an external transversal electric field generated by a potential difference of 20 V, undergoes bending deformation with a curvature of 0.15mm^{-1}.

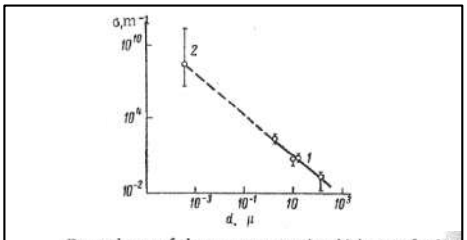
Dependence of the curvature on the thickness of a film: 1) experimental points; 2) extrapolation to a value of d corresponding to a hypothetical "monomolecular" film.

(b) The induced curvature κ depends on the thickness of the film T as $\kappa \propto T^{-2}$.

Figure 1.6: First experiment demonstrating flexoelectricity. Figure adapted from Bursian and Zaikovskii (1968).

1.2.1 Observation

The flexoelectric effect was experimentally observed for the first time in 1968 by Bursian and Zaikovskii (1968), after the theoretical predictions by Mashkevich and Tolpygo (1957). In this experiment (see Fig. 1.6), various single-crystal thin films of barium titanate ($BaTiO_3$) of thicknesses in the range of 0.1 – 10μm were subjected to transversal electric field (actuation mode). The bending was found to be always in the direction of the positive electrode, i.e. it was a reversible effect. Moreover, the bending of the film also produced a charge on its surfaces (sensing mode), confirming the two-way nature of the coupling.

Since then, flexoelectricity has been observed in multiple materials: biomaterials such as cellular membranes (Ahmadpoor and Sharma, 2015, Petrov, 2002, Todorov *et al.*, 1991) and viruses (Kalinin *et al.*, 2006), soft materials such as liquid crystals (Harden *et al.*, 2006, Meyer, 1969, Petrov, 1975, Prost and Marcerou, 1977, Trabi *et al.*, 2008) or polymers (Baskaran *et al.*, 2011a, 2012, 2011b, Breger *et al.*, 1976, Deng *et al.*, 2014a, Marvan and Havránek, 1998, Zhang *et al.*, 2016b, Zhou *et al.*, 2017), hard ceramics (Cross, 2006, Ma and Cross, 2002, 2001a,b), and even in atomically-thin nanomaterials such as graphene (Kalinin and Meunier, 2008) or carbon nanotubes (Dumitrică *et al.*, 2002).

In order to illustrate the ubiquity of flexoelectricity in nature, the following examples are of particular interest. A biological material in which flexoelectricity plays a role is the stomatopods dactyl club. Stomatopods, such as the peacock mantis shrimp (see Fig. 1.7), are marine crustaceans that use damage-tolerant hammerlike claws for defense and to attack their prey. The claws undergo repeated high-velocity and high-force impacts (Weaver *et al.*, 2012). The mechanical structure of the claw of the Peacock Mantis shrimp is formed by different regions with highly anisotropic Young modulus distribution, generating large stress-gradients that trigger the flexoelectric effect, resulting in a voltage of 1-2 V across the thickness of the impact surface. As pointed out by Vásquez Sancho (2018), flexoelectricity is known to be able to increase a material's toughness (Abdollahi *et al.*, 2015b), which is the most characteristic feature of this crustacean's club.

Another impressive implication of flexoelectricity in biology is found in the mammalian hearing mechanism (cf. Fig. 1.8). Hair cells are the primary sensory receptors in the auditory system that transform the mechanical vibrations of sound into sensible electrical action potential and, although the corresponding mechanism is still not fully understood, one possible explanation is the stereocilia in inner hair cells being flexoelectric (Ahmadpoor and Sharma, 2015, Krichen and Sharma, 2016, Oghalai *et al.*, 2000, Peng *et al.*, 2011).

Finally, it is worth mentioning another exciting implication in biology, found in human bones self-healing (cf. Fig. 1.9). As reported by Vasquez-Sancho *et al.* (2018), micro-cracks in bones generate very large strain gradients, inducing an electric field in the vicinity of the affected area due to the flexoelectric nature of the bone mineral hydroxyapatite. This crack-generated electrical stimulus is large enough to drive the activity of osteoblasts towards damaged regions, thus initiating the crack-healing process.

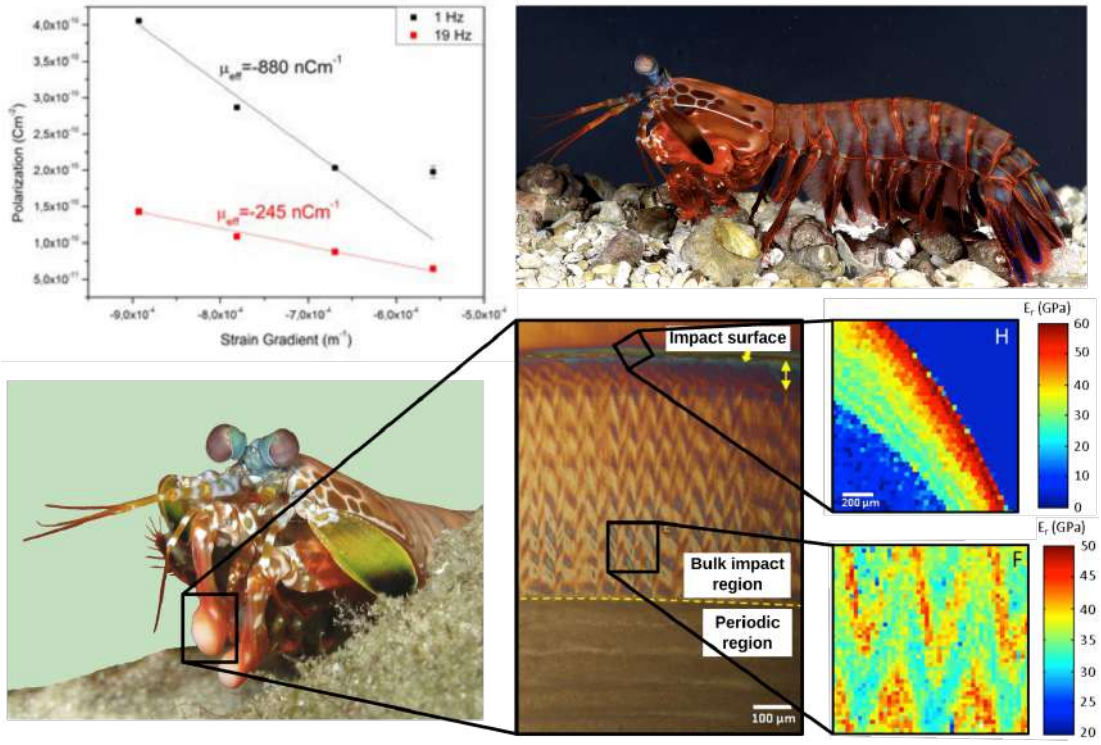

Figure 1.7: Flexoelectric effect in the peacock mantis shrimp dactyl club. The insets show the multi-regional nature of the stomatopod dactyl club, revealing a gradient in mineralization, increasing towards the club surface. The outer impact region is dense and highly mineralized, and the inner periodic region is more organic. The insets show the highly anisotropic Young modulus of each region. Such anisotropy induces a stress gradient at each impact that generates a voltage of 1-2 V across the thickness of the impact surface thanks to the flexoelectric effect. Figures adapted from Vásquez Sancho (2018), Weaver *et al.* (2012), Wikimedia Commons (2010, 2020), Yaraghi *et al.* (2016).

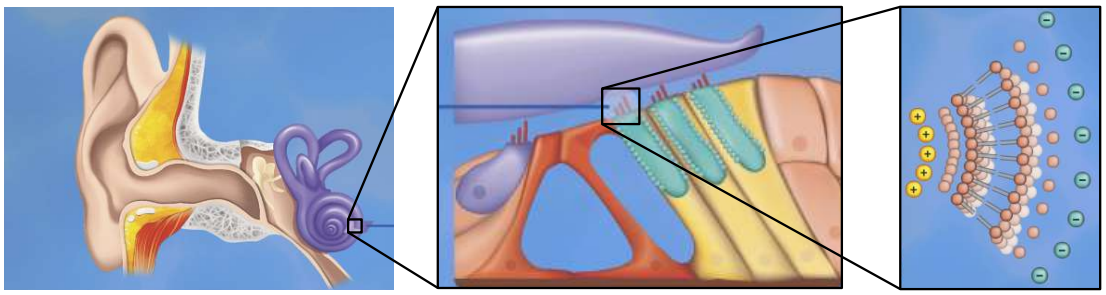

Figure 1.8: Flexoelectric effect in mammalian hearing mechanism. Hair bundles consist of several stereocilia that are connected by thin fibers organized in rows of decreasing height. Bending of the hair bundle toward the tallest (shortest) row make the cellular inner environment more electrically positive (negative). During these processes, a voltage difference emerges across the thickness of the stereocilia membrane due to the flexoelectric response of the cellular membrane. Caption and Figure adapted from Krichen and Sharma (2016).

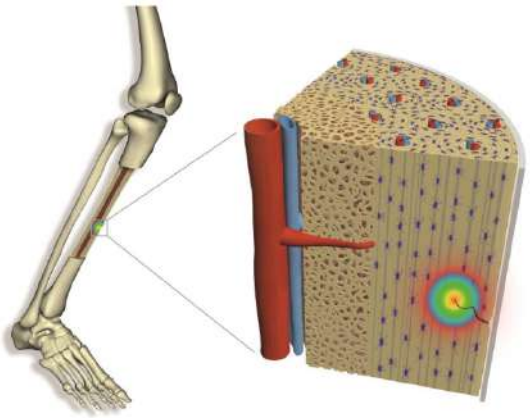

Figure 1.9: Flexoelectric effect in human bones. Strain gradients can be large around small defects such as micro-cracks in bone mineral, so gradient-induced electricity (flexoelectricity) is also expected to be large around such defects. Caption and Figure adapted from Vasquez-Sancho *et al.* (2018).

1.2.2 Quantification

The experimental quantification of the flexoelectric tensor is very challenging, due to (*i*) the high resolution equipment required to capture such small values, (*ii*) the difficulty in experiments in isolating the flexoelectric effect from other physics, and (*iii*) the high number of independent components of the flexoelectric tensor. In general, the flexoelectricity tensor has 54 independent components (Le Quang and He, 2011, Shu *et al.*, 2011), although they are reduced

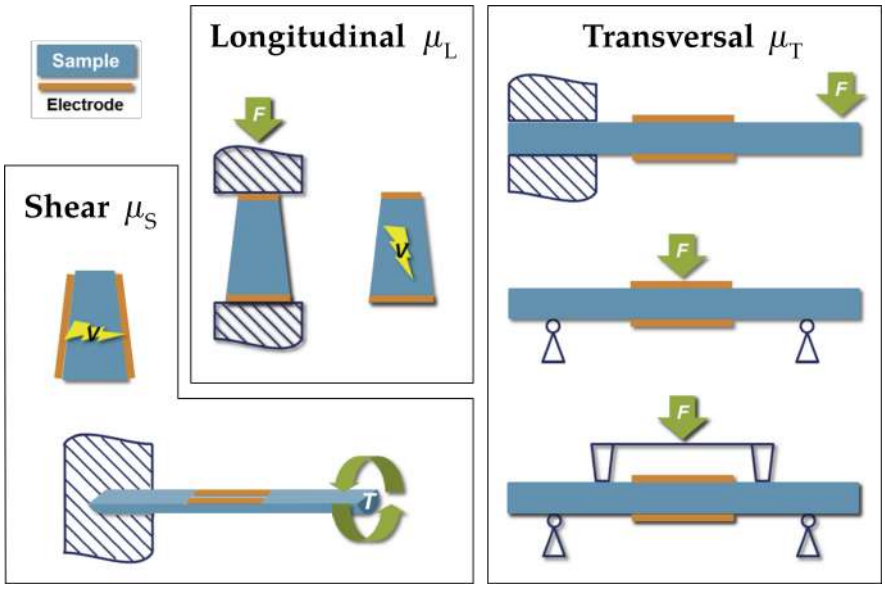

Figure 1.10: Schematics of flexoelectric experimental setups for the direct measurements of flexoelectric constants. Figure adapted from Wang *et al.* (2019).

to only 3 coefficients for materials possessing cubic symmetry (such as perovskite oxides in paraelectric phase), i.e. the longitudinal (μ_L), transversal (μ_T) and shear (μ_S) coefficients. Many experimental methods have been developed for each coefficient, as summarized in Fig. 1.10.

The longitudinal coefficient can be assessed by the truncated pyramid compression (Cross, 2006, Hana, 2007, Marvan and Havránek, 1998), where the different sizes of the bases induce a longitudinal strain gradient $\nabla_z \varepsilon_{zz}$ that yields a vertical electric field e_z. Another method based on converse flexoelectricity consists on applying a graded electric field $\nabla_z e_z$ across the truncated pyramid and measuring the resulting vertical strain ε_{zz} via high-resolution optical approaches (Fu *et al.*, 2006, Hana *et al.*, 2006).

The experimental setups for assessing the transversal coefficient rely on beam bending, where the transversal variation of the axial strain $\nabla_z \varepsilon_{xx}$ generates a transversal electric field e_z. Various setups have been used to induce bending, such as the cantilever loading (Huang *et al.*, 2017, 2011, Kwon *et al.*, 2014, Li *et al.*, 2014, 2013, Ma and Cross, 2002, 2005, 2006, 2001a, Shu *et al.*, 2017, 2016, 2013), and the three- or four-point bending (Ma and Cross, 2003, Narvaez and Catalan, 2014, Narvaez *et al.*, 2015, Zubko *et al.*, 2007).

For the shear coefficient, there is no well-established procedure based on the direct flexoelectric effect to date. This is due to the difficulty in generating a sustained shear strain gradient generating a non-vanishing net polarization. There do exist approaches based on the converse effect, by electrically loading a truncated pyramid across the lateral sides (Shu *et al.*, 2014), which yields an electric field gradient-induced deformation. Another approach based on the direct flexoelectric effect consists on applying a torque load upon a half cylindrical specimen (Zhang *et al.*, 2017), yielding a strain-gradient-induced electric field. However, the measured coefficient does not correspond to the shear flexoelectric coefficient μ_S of cubic crystals. As pointed out by Mocci *et al.* (2020), an axial variation of the cross section size (i.e. the radius varying along the axial direction) would be required in order to generate the proper electric field to characterize μ_S.

Other than experiments, the flexoelectric coefficient can be assessed by theoretical computations (even in materials that have been predicted to be stable, but not yet synthesized). A rough estimate of the flexocoupling coefficient was first provided by Kogan (1964) using a simple phenomenological model:

$$f \approx \frac{1}{4\pi\epsilon_0}\frac{q}{a}, \tag{1.5}$$

where q is the electronic charge, a is an interatomic spacing of a few angstroms and ϵ_0 is the vacuum permittivity. Since then, there have been a number of attempts to properly quantify the flexoelectric response in solids by means of first-principles calculations. There are mainly two approaches: (*i*) the indirect approach, which relies on the first-principles theory of flexoelectricity (Dreyer *et al.*, 2018, Hong and Vanderbilt, 2013, Resta, 2010, Stengel, 2013, 2014) based on density functional perturbation theory (DFPT) (Baroni *et al.*, 2001, Gonze and Lee, 1997), and (*ii*) the direct approach, where the induced polarization of a bent material is

computed at different curvatures by means of ab-initio atomistic computations (Dumitrică *et al.*, 2002, Kalinin and Meunier, 2008, Shi *et al.*, 2018), such as density functional theory (DFT) (Hohenberg and Kohn, 1964, Kohn and Sham, 1965), and the flexoelectric coefficient is assessed as the change rate of curvature-induced polarization. A more comprehensive review of the topic is reported in Section 4.1. However, we point out here that such computations are in general difficult. For the direct approach, the commercial implementations typically assume periodic boundary conditions, which are not fulfilled in bending states unless supercells are considered, leading to very expensive computations. Moreover, the results are sensitive to the choice and size of the supercell, and most of the times implicitly assume different boundary conditions as those enforced in experiments (Wang *et al.*, 2019). One the contrary, indirect approaches involve intricate derivations that require the decomposition of the tensor into lattice-mediated, frozen-ion and mixed contributions (Wang *et al.*, 2019).

In any case, there is a well-known order-of-magnitude discrepancy between the theoretically estimated and the experimentally measured flexoelectric coefficients. Specifically, experimental measurement of the flexoelectric coefficient in the paraelectric phase of many perovskite oxides reaches up to several tens of μC/m, whereas theoretical estimations suggest the intrinsic flexoelectricity should not exceed several nC/m (Wang *et al.*, 2019). This discrepancy can be due to many reasons, but from the experimental side, many sources of error can arise. For instance, experiments based on the application of electric field intrinsically trigger the electrostrictive effect along with the flexoelectric one, so both responses must be properly separated. Other physics can be present, such as the pseudo Jahn-Teller effect (Bersuker, 2013) or surface effects (Narvaez *et al.*, 2015, Yurkov and Tagantsev, 2016). Another source of error is due to the oversimplification of strain gradient distribution, specially in the setups relying in the truncated pyramid geometry (Abdollahi *et al.*, 2015a, 2014). Apart from comparing to experiments, disagreement in the orders of magnitude and even the sign of flexoelectric tensors also exist among different theoretical calculations, which may be attributed to different electric boundary conditions considered, different force-patterns or the inclusion of surface effects (Wang *et al.*, 2019).

1.2.3 Theoretical and computational modeling

The research on flexoelectricity is rapidly increasing, and so is the development of theoretical and computational models for it. They are necessary due to many reasons. On the one hand, theoretical models are useful in order to conceptualize the flexoelectric effect and fully understand it. On the other hand, the experiments to characterize the flexoelectric coefficients inevitably depend on an underlying model whose parameters are to be fit with experimental data. More importantly, the development of proof-of-concept technologies based on the flexoelectric effect requires computational (including also optimization) tools in order to predict and maximize the performance of a certain device, and demonstrate its feasibility.

There exist a wide range of theoretical and computational models of flexoelectricity, detailed in the *State of the art* Section of the different Chapters in this manuscript, i.e. Sections 2.1 and

3.1 respectively. Here we just point out the associated difficulties and challenges present in such modeling.

The main difficulties are related with the multiscale, multiphysics nature of flexoelectricity. While many approaches attempt to model flexoelectricity from a phenomenological or continuum point of view, the multiple underlying physics present at the atomic scale make it difficult to state general models taking all of them into account. A complete model must treat with many physics that are intrinsically coupled at sub-micron scales, such as surface effects, magnetism, thermodynamics, dislocations and defects, etc. In that case, the model becomes intractable since it depends on a plethora of material parameters that cannot be individually assessed. Otherwise, many assumptions must be done in order to neglect some of them, which decreases the validity of the model.

Another difficulty in mathematical and computational models arise from the non-locality of the flexoelectric effect, i.e., strain or polarization gradients. By virtue of that, flexoelectricity in a solid dielectric is governed by a system of (at least) fourth-order partial differential equations. Therefore, analytical solutions are restricted to very simple 1D or 2D geometries. Multidimensional modeling of flexoelectricity necessitates from numerical approximations, but the fourth-order nature of the equations requires $C1$ continuity of the approximation of the state variables, precluding the use of many standard techniques such as the finite element method. To this end, many alternative numerical strategies are present in the literature, but typically present some limitations or inefficiencies.

In short, the theoretical and computational modeling of flexoelectricity are very challenging, and require intensive research.

1.2.4 Technological applications

The presence of flexoelectricity in technology is nowadays still limited, given that it has gained attention very recently only, with many open questions remaining in order to fully understand the underlying transduction mechanisms. Moreover, manufacturing sub-micron scale devices involves advanced machinery and is typically expensive. However, there exist a wide range of potential technological applications where flexoelectricity may yield a breakthrough.

A generalized emerging trend in technology is the *miniaturization* of existing devices towards smaller scales. Since flexoelectricity plays a role in any dielectric at sub-micron scales, it must be taken into account even in non-flexoelectricity-based devices. Otherwise, the interplay of flexoelectricity with other physics, such as piezoelectricity, may lead to a tremendous throughput drop or even to a dysfunctionality of the device. A numerical analysis of such phenomena in flexural bimorph configurations is provided in Abdollahi and Arias (2015), showing that the designs of sub-micron scale piezoelectric bimorph transducers must be flexoelectric-aware, since they exhibit dramatically different behavior than that at larger scales, where the flexoelectric effect is not relevant (see Fig. 1.11).

Conversely, flexoelectricity can be harnessed to enhance the apparent piezoelectric behavior. One of the most exciting applications of flexoelectricity at the mesoscale is in implantable

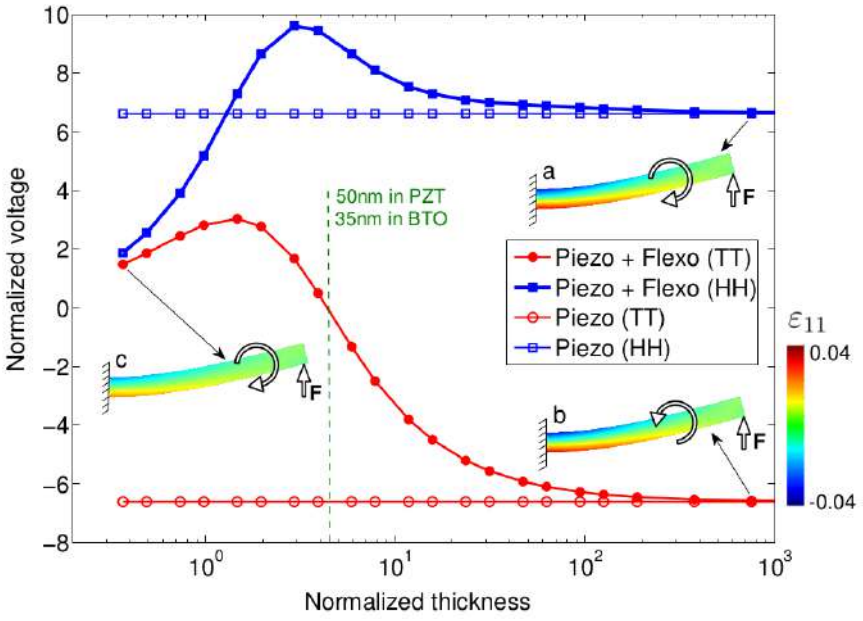

(a) Sensor mode

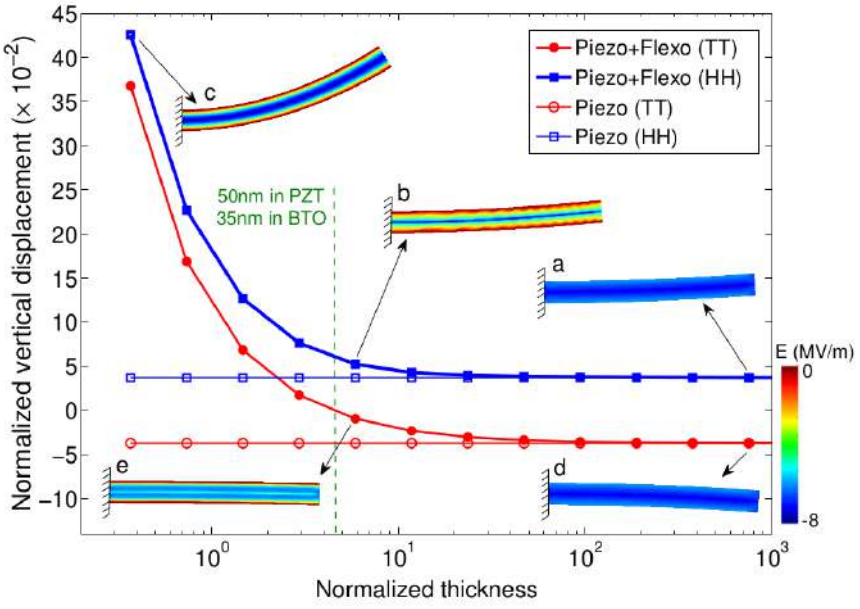

(b) Actuator mode

Figure 1.11: Constructive and destructive interplay between piezoelectricity and flexoelectricity in flexural series bimorph devices. The miniaturization of the devices to sub-micron scales yields dramatically different responses than those at larger scales. Figure adapted from Abdollahi and Arias (2015).

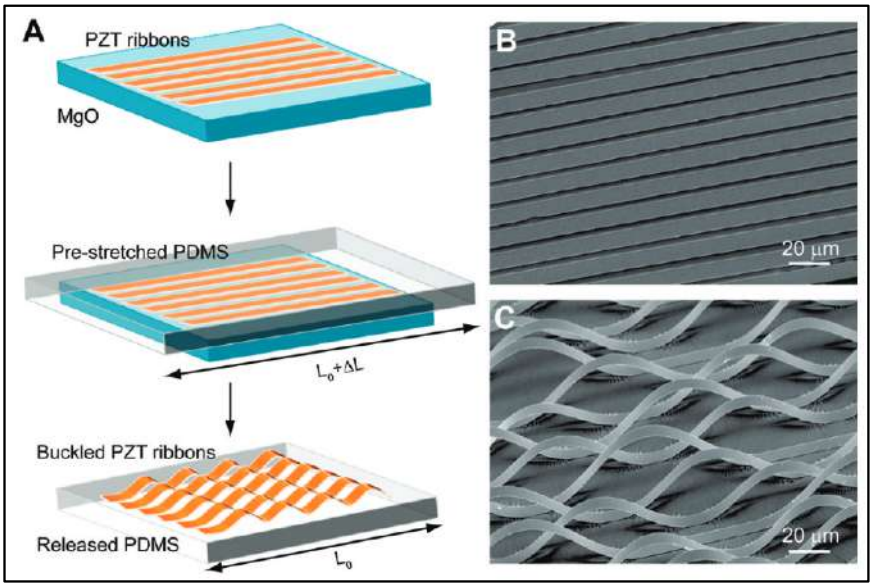

Figure 1.12: Manufacture of wavy piezoelectric nanoribbons on silicone rubber substrate for application in flexible energy conversion. Figure adapted from Qi *et al.* (2011).

or wearable energy harvesting systems. Such devices are typically attached onto soft, biocompatible substrates that require conforming to irregularly curved surfaces, and must be able to undergo flexing and stretching modes without failure. The work in Qi *et al.* (2011) presents a novel strategy to do so, based on the generation of wavy lead zirconate titanate (PZT) piezoelectric ribbons of nanoscopic thickness onto a soft poly(dimethyl-siloxane) (PDMS) substrate. The buckled shape of the ribbons is obtained by releasing a pre-strained substrate with attached nanoribbons on it (see Fig. 1.12). The structure easily accommodates large compressive and tensile strains without fracture by simply changing the wave amplitudes. Furthermore, the buckled shape is beneficial not only to increase the fracture strength, but also to increase the electromechanical transduction. By measuring the apparent piezoelectric response on buckled and flat regions of the nanoribbons, it was found that buckled regions present a substantial 70% increase of response as compared to flat regions, mainly attributed to the flexoelectric effect. The maximum curvature of the nanoribbons was found to be of 30 mm^{-1}, which is several orders of magnitude larger than those achieved by standard four-point bending tests, thus yielding a large flexoelectric response. Thanks to the positive interplay between piezoelectricity and flexoelectricity at the nanoscopic level, the highest piezoelectric response on a stretchable medium was reported to date. We refer to Chen *et al.* (2010), Dong *et al.* (2020), Feng *et al.* (2011), Han *et al.* (2016), Park *et al.* (2010), Su *et al.* (2018) for other relevant studies or experiments regarding flexoelectricity in wrinkled or buckled deformation modes with application to flexible electronics.

Another application of flexoelectricity that has recently gained a lot of interest is to create apparently piezoelectric materials without using piezoelectric constituents (Chu *et al.*, 2009,

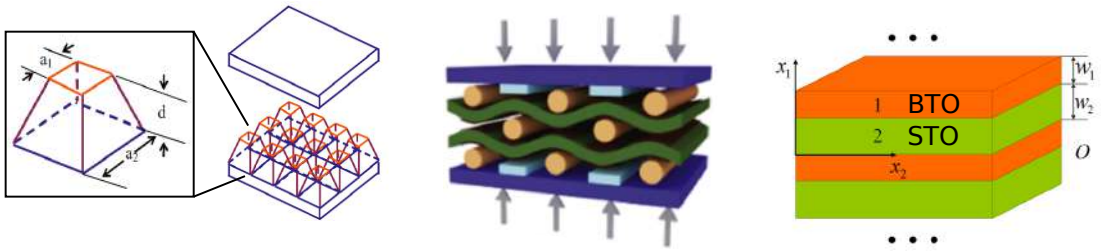

(a) Truncated micro-pyramids under compression.

(b) Flexure-mode composite.

(c) Multimaterial stacks.

Figure 1.13: Material architectures yielding an effective piezoelectric response. Figures adapted from Chu *et al.* (2009), Liu *et al.* (2016a), Zhu *et al.* (2006).

Fousek *et al.*, 1999, Fu *et al.*, 2007, Sharma *et al.*, 2010, 2007, Zhang *et al.*, 2016c, Zhou *et al.*, 2015, Zhu *et al.*, 2006). Apart from piezoelectric ceramics being typically very brittle, two main reasons behind this interest are mentioned next. On the one hand, the dielectric materials with larger piezoelectric response are typically lead-oxide-based, containing more than 60% lead in weight, which has recently raised an increasing concern due to its toxicity (Hong *et al.*, 2016, Rödel *et al.*, 2009, Zhou *et al.*, 2015). To date, other alternative dielectrics have been explored, but they have either lower temperature stability or lower piezoelectric response, reducing its performance. On the other hand, conventional piezoelectric ceramics lose their piezoelectric properties near the Curie temperature (Zhang *et al.*, 2016c), which limits their application at higher temperatures. One approach to resolving these issues consists on designing piezoelectric composites or metamaterials, in which the apparent piezoelectric response originates from their non-centrosymmetric geometrical microstructure, even in centrosymmetric crystalline structures that do not feature piezoelectricity. Under a uniform compression, the internal geometrical features of the microstructure will generate strain gradients, triggering the flexoelectric effect. The overall symmetry of the nanostructure must be properly designed such that the net average of the polarization due to the presence of strain gradients is non-zero (Sharma *et al.*, 2007), yielding an apparent piezoelectric behavior at coarser scales, thus *upscaling* the flexoelectric effect. A wide range of material architectures have been proposed (cf. Fig. 1.13), including multimaterial stacks (Liu *et al.*, 2016a), geometrically polarized cavities in the material (Sharma *et al.*, 2007) and the juxtaposition on a plane of polar elements, such as truncated micro-pyramids working under compression (Cross, 2006, Fousek *et al.*, 1999, Fu *et al.*, 2007, Zhu *et al.*, 2006) or the flexure-mode composites (Chu *et al.*, 2009, Wan *et al.*, 2017).

At a nanoscopic level, one of the most exciting applications of flexoelectricity is in nanogenerators harnessing energy from mechanical vibrations (Jiang *et al.*, 2013, Majdoub *et al.*, 2008). Energy harvesting from dynamical systems for applications in self-powered miniature sensors and electronic devices has emerged as an intensely researched topic (Ahmadpoor and Sharma, 2015). As an example, Deng *et al.* (2014a) developed a theoretical continuum model for flexoelectric nanoscale energy harvesting based on a microscale cantilever resonator (see

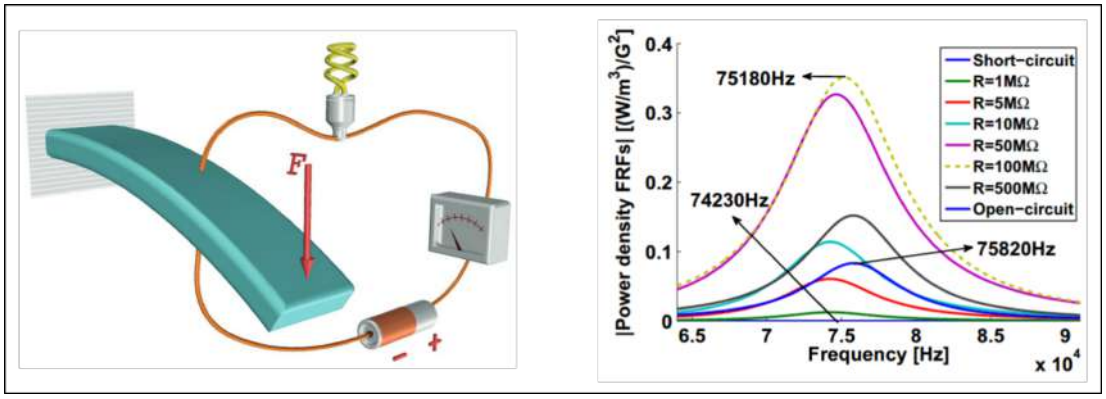

Figure 1.14: Schematic of a centrosymmetric flexoelectric energy harvester under base excitation. The cantilever beam undergoes bending vibrations, generating an alternating potential difference across the electrodes thanks to the flexoelectric effect. The power density varies as a function of the resistance load and the vibrating frequency. Figure adapted from Ahmadpoor and Sharma (2015), Deng *et al.* (2014a).

Fig. 1.14), working under applied mechanical base excitation. The output power density and conversion efficiency increase significantly when the beam thickness reduces from micro to nanoscale, and hence flexoelectricity-based sub-micron energy harvesting can be a viable alternative to piezoelectrics, specially at high temperatures where flexoelectricity, unlike piezoelectricity, persists well beyond the Curie temperature point (Deng *et al.*, 2014a). However, till now, electromechanical energy converting efficiency of manufactured flexoelectric energy harvesters reaches only to 6.6% (Liang *et al.*, 2017, Shu *et al.*, 2019).

Another interesting application in the realm of nano-/micro-electromechanical systems (NEMS/MEMS) is that of sensors and actuators. Bhaskar *et al.* (2016) manufactured a silicon-compatible thin-film cantilever actuator with a single flexoelectrically-active layer of $SrTiO_3$, as depicted in Fig. 1.15. The obtained performance (curvature divided by electric field) reaches 3.33 MV^{-1}, comparable to that of state-of-the-art piezoelectric bimorph cantilevers. Hence, flexoelectricity is proven to be a viable route to lead-free MEMS/NEMS systems.

Finally, another attractive application of flexoelectricity is the domain tailoring and polarization switching, which could be used for the development of ultra-high storage density memory applications (Lu *et al.*, 2012, Park *et al.*, 2018). Ferroelectric materials are characterized by a permanent electric dipole that can be reversed through the application of an external electric field. However, the stress gradient generated by the tip of an atomic force microscope can also switch the polarization in the nanoscale volume of a ferroelectric film thanks to the flexoelectric effect, without the need of applying an external electric field (see Fig. 1.16). The resolutions achieved by mechanical polarization switching are much higher than those obtained by the traditional electrical polarization switching, and hence the storage capacity of such materials can be dramatically increased. Thus, flexoelectricity may enable a

new generation of ultra-high storage density memory applications in which memory bits are written mechanically and read electrically.

To conclude this Section, we point out that flexoelectricity can be linked to many other important physical behaviors, and hence many other applications are envisioned in the near future. Some examples are (*i*) photoflexoelectricity (Shu *et al.*, 2020, Yang *et al.*, 2018), a very recently discovered physical effect combining photovoltaic energy conversion and flexoelectricity, or (*ii*) the flexocaloric effect (Chen *et al.*, 2018, Liu *et al.*, 2016b, Patel *et al.*, 2017), coupling strain gradients with thermal currents.

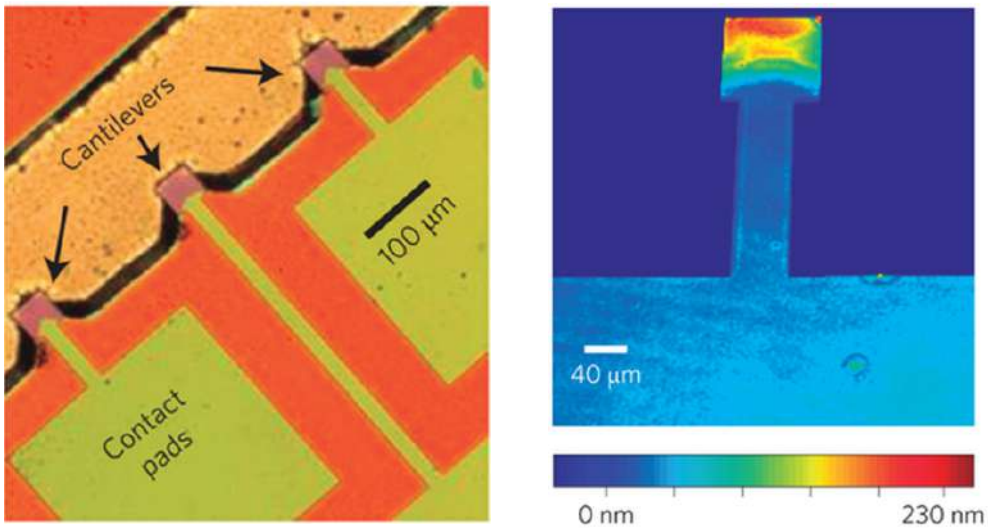

Figure 1.15: Optical image of a flexoelectric nano-actuator made of an array of $SrTiO_3$ nanocantilevers. The colour scale corresponds to the out-of-plane displacement. Figure adapted from Bhaskar *et al.* (2016).

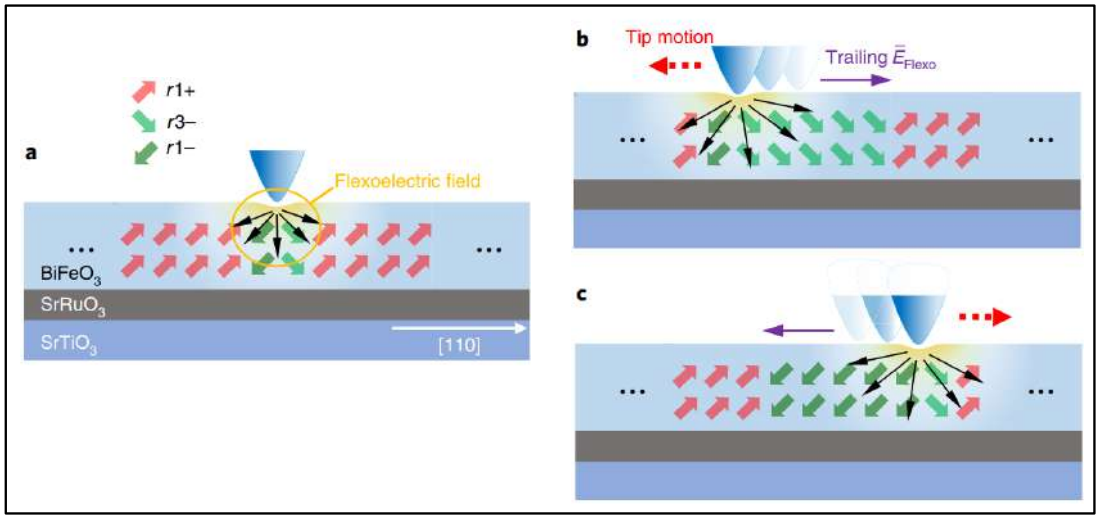

Figure 1.16: Schematic of mechanical polarization switching due to the trailing flexoelectric field generated by the scanning probe microscope tip motion thanks to the flexoelectric effect. Figure adapted from Park *et al.* (2018).

1.3 Goals and objectives

The main objective of this thesis is twofold. On the one hand, it aims to extend the current state of the art of the flexoelectric effect, with a particular focus on the mathematical modeling and the computational techniques required to solve boundary value problems of practical engineering interest with potential applications in technology. Specifically, the computational framework must be able to reliably and efficiently predict the electromechanical behavior of engineered devices at sub-micron scales, where flexoelectricity is always present, without any particular restrictions in geometry, material choice, boundary conditions or nonlinearity. The ultimate goal is to provide a tool that can pave the way for the development of functional technological devices for electromechanical transduction at the microscopic and nanoscopic scales.

On the other hand, such a modeling involves material parameters that are still under debate, with large disagreement between theoretical derivations and experimental computations. Even the actual physics involved in electromechanical transduction at the atomic and molecular level are not completely clear. The second goal of the thesis is to shed light on this matter by connecting ab-initio atomistic simulations with the proposed models at a coarser, continuum scale, bridging the gap between these two approaches. On the one hand, atomistic computations can validate continuum models and check that they capture the relevant inherent physics. On the other hand, the material parameters in the continuum models can be directly assessed by ab-initio computations, complementing the experimental characterization.

The specific objectives of this thesis are listed as follows:

- Explore and understand the variety of continuum models for flexoelectricity at infinitesimal deformations, rigorously establishing the connections between them and clarifying the interpretation of high-order boundary conditions.
- Extend such continuum models to the regime of finite deformations, including other relevant physics that are not present in linearized models.
- Develop an efficient computational infrastructure for flexoelectricity, capable of solving boundary value problems in arbitrary geometries and different boundary conditions. The tool must be able to predict the electromechanical performance of flexoelectricity-based devices with potential application in technology.
- Understand and handle the numerical difficulties arising from a fourth-order PDE system.
- Propose functional sub-micron electromechanical devices based on flexoelectricity, and assess their performance with the proposed computational tool.
- Link the continuum modeling with atomistic simulations to characterize the flexoelectric tensor of materials of interest from first principles.
- Validate the continuum model assumptions by means of ab-initio simulations.

1.4 Outline

The manuscript is organized as follows. Chapter 2 explores, formulates and discusses the variety of macroscopic models describing the flexoelectric effect at the continuum level. In plain words, describes the equations that define flexoelectricity, and the associated boundary value problems. Section 3 details the numerical approach that is considered to solve the boundary value problems, and illustrates it with a variety of setups and applications with technological and engineering interest. Section 4 relies in the models in Section 2 for deriving a proper methodology to quantify the flexoelectric tensor by means of atomistic simulations, based on density functional theory. The transversal coefficient of several monolayers is assessed following this approach. Finally, Section 5 summarizes and concludes the manuscript.

1.5 Research stay at Georgia Tech

The author of this manuscript has participated in a five-month-long research stay at the Georgia Institute of Technology (Georgia Tech) in Atlanta, GA (USA), from March 1st until July 31st 2019. The purpose of this visit was to start a fruitful academic collaboration between the FLEXOCOMP group in Universitat Politècnica de Catalunya, lead by Prof. Irene Arias, and the MP&M group in Georgia Tech, lead by Prof. Phanish Suryanarayana, on the study of atomistic and continuum bridging of electroactive materials, with particular focus on the flexoelectric effect.

Prof. Arias' group is focused on building a conceptual and computational infrastructure in the frame of continuum mechanics to understand and model flexoelectricity, and use it to assist its experimental observation and to enable the rational simulation-based design of flexoelectricity-based technologies. The group has remarkable expertise on finite element calculations, continuum mechanics and electroactive materials.

Prof. Suryanarayana's group is interested in developing mathematical and computational tools in the frame of first principle calculations, that allow for the accurate and efficient characterization of materials at different length scales. The group has remarkable expertise on ab-initio calculations, density functional theory and atomistic-continuum bridging techniques.

The collaboration between the two groups can be very fruitful, since both are interested in studying the same physical phenomenon from two different but complementary perspectives.

In this case, the goal of the visit was to establish the connection between atomistic and continuum scales, towards the validation of the continuum models used in Barcelona, the quantification of the flexoelectric tensor of materials of interest and the understanding of the structure-property relation with regards to flexoelectricity. By running simulations on the in-house code of Prof. Suryanarayana's group, based on non-standard ab-initio techniques, the electronic structure of flexoelectric materials under non-periodic loading conditions such as bending or twisting can be determined. Then, it remains exploring how to properly extract the flexoelectric material parameters for continuum models that best fit the atomistic data.

This research collaboration is related to Chapter 4 of this manuscript. So far, two papers have been produced, i.e. Codony *et al.* (2020a) and Kumar *et al.* (2020), and are briefly explained in the publications list in Section 1.6. The collaboration is still on-going, with many ideas in mind to investigate, as reported in Section 4.3.

1.6 List of publications

This manuscript gathers most of the published and unpublished (to this date) original research done by the author during his PhD. The following lists organize the original contributions of this manuscript's author depending on the relation with the thesis.

1.6.1 Publications derived from this thesis

1.6.1.1 Scientific journal articles published or under review

***D. Codony**, O. Marco, S. Fernández-Méndez, and I. Arias. An Immersed Boundary Hierarchical B-spline method for flexoelectricity.* Comput. Meth. Appl. Mech. Eng. ***354**, 750 (2019).*

> This paper develops a computational framework with unfitted meshes to solve linear piezoelectricity and flexoelectricity electromechanical boundary value problems at infinitesimal strains. It corresponds to the Nitsche's direct flexoelectricity formulation in Section 2.2.2.1.b and the immersed boundary numerical method in 3.2.3.

***D. Codony**, P. Gupta, O. Marco, and I. Arias. Modeling flexoelectricity in soft dielectrics at finite deformation.* J. Mech. Phys. Sol. ***146**, 104182 (2020b).*

> This paper develops the equilibrium equations describing the flexoelectric effect in soft dielectrics under large deformations, described in this document in Section 2.2.4.1.a. The numerical implementation is based on the body-fitted approach described in Section 3.2.2, and the numerical algorithm to solve the nonlinear system of equations and corresponding numerical examples are reported in Section 3.2.6 of this document. A theory of geometrically nonlinear extensible flexoelectric slender rods under open and closed circuit conditions is further developed, providing closed form analytical solutions for cantilever bending and buckling under mechanical and electrical actuation, with very good agreement with the numerical implementation.

***D. Codony**, I. Arias, and P. Suryanarayana. Transversal flexoelectric coefficient for nanostructures at finite deformations from first principles.* arXiv preprint *arXiv: 2010.017 47. Under review (2020a).*

> In this paper, a reformulation of the flexoelectric tensor from ab-initio simulations is proposed, overcoming an ill-definition typically present in other first principle works. The approach is particularized to assess the transversal flexoelectric coefficient of different

> atomic monolayers, such as graphene and its Group-IV analogues, from symmetry-adapted DFT calculations. It is the first publication arising from the collaboration with the MP&M group in Georgia Tech 1.5, and is the basis of Section 4.2 of this manuscript.

1.6.1.2 Scientific journal articles in preparation

The following works are original contributions of the manuscript's author that are under preparation.

***D. Codony**, S. Fernández-Méndez, S., and I. Arias,* Nitsche's method for finite deformation flexoelectricity, *In preparation (2021a).*

> This work is a combination of the computational framework for unfitted meshes and high-order continuity of the approximation space in Codony *et al.* (2019) with the formulation of the flexoelectric effect in soft dielectrics under large deformations in Codony *et al.* (2020b). Section 3.2.7 of this manuscript briefly comments on this idea. The resulting tool allows the computation of arbitrarily shaped compliant flexoelectric materials with multiple potential applications, as illustrated in the example in Section 3.2.7.1.

***D. Codony**, and I. Arias,* Residual-based weak form stabilization for flexoelectricity, *In preparation (2021b).*

> As reported in Section 3.3.1, the numerical solution to the Lifshitz-invariant flexoelectricity problem may feature boundary layers in the electric field, leading to spurious oscillations which completely spoil the quality of the results. This work resorts to the Galerkin least-squares (GLS) method to stabilize the problem by increasing the effective mechanical and electrical length scales in a self-consistent manner, providing control on the second derivatives of the state variables.

***D. Codony**, and I. Arias,* Lifshitz-invariant flexoelectricity, *In preparation (2021a).*

> This paper formulates the Lifshitz-invariant flexoelectricity model, accounting for both the direct and converse flexoelectric effects. The boundary terms are detailed and compared to the standard direct flexoelectricity models, yielding two boundary value problems with very different properties. Both models are compared by means of numerical computations in several flexoelectricity benchmarks. The paper originates from the preliminary work reported in Sections 2.2.2.2 and 2.2.2.3 of this manuscript.

***D. Codony**, and I. Arias,* Switchable flexoelectric device by buckling, *In preparation (2021c).*

> This work is an extension of the numerical example in 3.2.7.1 to other flexoelectric devices working under buckling conditions. Sensitivity and optimization analyses are

> performed in order to maximize the net electromechanical transduction of the devices.

***D. Codony**, A. Mocci, O. Marco, and I. Arias,* Wheel-shaped and helical torsional flexoelectric devices, *In preparation (2021b).*

> This work is an extension of the numerical example in 3.2.5.2 where a torsional actuation induces bending of the internal components of the device, generating an electric field thanks to the flexoelectric effect. By accounting for three-dimensional devices working under the same idea, a much larger net electric voltage is accumulated, leading to an effective upscaling of the flexoelectric effect towards larger scales.

1.6.2 Other related publications

The manuscript's author has participated in the following works that are closely related to this thesis.

*S. Kumar, **D. Codony**, I. Arias, and P. Suryanarayana. Flexoelectricity in atomic monolayers from first principles.* Nanoscale *(2020).*

> This work extends the methodology developed in Codony *et al.* (2020a) to other fifty atomic monolayers, such as Group III and IV monochalcogenides, Group V monolayers, Group V chalcogenides and transition metal di- and trichalcogenides. A simplified model for the flexoelectric effect is proposed, depending on the monolayer thickness, the elastic modulus and the atomic polarizability. It is the second publication arising from the collaboration with the MP&M group in Georgia Tech 1.5, and is related with Section 4.3 of this manuscript.

*J. Ventura, **D. Codony**, and S. Fernández-Méndez. A C0 interior penalty finite element method for flexoelectricity.* arXiv preprint *arXiv: 2008.12391. Under review (2020).*

> This work proposes a C0 Interior Penalty Method (C0-IPM) for the computational modelling of flexoelectricity, allowing standard high-order C0 finite element approximations. It involves second derivatives in the interior of the elements, plus integrals on the mesh faces in order to weakly enforce C1 continuity of the approximation space across elements. It is the result of the Master's thesis of Jordi Ventura (Ventura Siches, 2020), who was co-advised by Prof. Sonia Fernández-Méndez and this manuscript's author.

*J. Barceló-Mercader, **D. Codony**, O. Marco, S. Fernández-Méndez, and I. Arias,* Nitsche's method for interfaces in flexoelectricity and application to periodic structures. *To be submitted (2021b).*

> A general framework for the numerical computation of flexoelectric devices composed by multiple materials is presented in this work. The method relies on the weak enforcement of high-order interface conditions using Nitsche's method. The approach is also suitable for simulating periodic materials formed by a repeating unit cell. The numerical simulations illustrate the usefulness of the proposed approach towards the design of functional electromechanic multi-material devices and metamaterials, harnessing the flexoelectric effect. It is implemented within the computational framework iHB-FEM described in Section 3.2.1.

J. Barceló-Mercader, ***D. Codony****, and I. Arias,* Generalized periodicity conditions for the computational modeling of flexoelectric metamaterials. *To be submitted (2021a).*

> This work develops generalized periodic conditions in order to characterize the behavior of architected periodically-arranged materials by reducing the numerical computation to a single unit cell. In doing so, the bulk response of the architected material is very efficiently computed without the need of considering a sufficiently large sample. The implementation is a module of the computational framework iHB-FEM described in Section 3.2.1.

A. Mocci, J. Barceló-Mercader, ***D. Codony****, and I. Arias,* Geometrically polarized architected dielectrics with effective piezoelectricity. *To be submitted (2021).*

> This paper uses the computational machinery developed in Barceló-Mercader *et al.* (2021a) in order to characterize the effective piezoelectric coefficient of non-piezoelectric metamaterials working under compression. Different bending-dominated lattices, geometrical orientations, constituents thickness and flexoelectric materials are considered in order to assess the throughput sensitivity. The proposed flexoelectricity-based metamaterials have a comparable performance to currently-used piezoelectrics.

1.6.3 Patents

I. Arias, A. Abdollahi, A. Mocci, and ***D. Codony****, Lattice structure with piezoelectric behavior, a force or movement sensor and an actuator containing said lattice structure.* European patent office. *In process (2020).*

> This patent contains several functional flexoelectricity-based devices that have been rationalized and developed at the FLEXOCOMP group, including sensors, actuators and metamaterials.

1.6.4 Conference proceedings

During the PhD thesis, the research done has been presented in a number of international conferences. The presentations delivered by the PhD candidate are listed below.

- ***D. Codony**, O. Marco, S. Fernández-Méndez, and I. Arias.* Numerical solution of strain-gradient elasticity based on an immersed boundary B-spline framework. *16th European Mechanics of Materials Conference (EMMC16). Nantes, FR (2018).*

- ***D. Codony**, O. Marco, S. Fernández-Méndez, and I. Arias.* Numerical solution of the flexoelectric coupling based on an immersed boundary B-spline framework. *10th European Solid Mechanics Conference (ESMC2018). Bologna, IT (2018).*

- ***D. Codony**, O. Marco, S. Fernández-Méndez, and I. Arias.* Immersed boundary hierarchical B-spline method for the numerical simulation of nano-scale electromechanical transduction. *13th World Congress in Computational Mechanics (ECCM2018). New York City, NY, USA (2018)*

- ***D. Codony**, O. Marco, S. Fernández-Méndez, and I. Arias.* An immersed boundary hierarchical B-spline-based computational approach for nano-scale electromechanics. *55th Technical Meeting of the Society of Engineering Science (SES2018). Leganés, SP (2018).*

- ***D. Codony**, O. Marco, J. Barceló-Mercader, S. Fernández-Méndez, and I. Arias.* Unfitted B-spline-based computational approach for non-local continuum mechanics. Application to hard and soft flexoelectric materials and composites. *56th Technical Meeting of the Society of Engineering Science (SES2019). St Louis, MO, USA (2019).*

Chapter 2

Continuum modeling of flexoelectricity

2.1 State of the art

Phenomenological models for flexoelectricity in crystalline dielectrics were first proposed by Kogan (1964) after the early studies by Mashkevich and Tolpygo (1957) and Tolpygo (1963). The first comprehensive theoretical works by Tagantsev (1986, 1991) clarified the distinction between piezoelectricity and flexoelectricity. In the mechanics community, Mindlin (1968) formalized the converse flexoelectric effect in elastic dielectrics. A complete unified continuum framework, including strain gradient elasticity, both direct and converse flexoelectric couplings, and the polarization inertia effect was proposed later by Sahin and Dost (1988). More recently, a simplified framework for isotropic dielectrics was proposed by Maranganti *et al.* (2006).

Nowadays, there exist a plethora of different continuum flexoelectricity theories. Some of them reformulate the models by variants of gradient elasticity theory (Askes and Aifantis, 2011, Mindlin and Eshel, 1968), such as the couple-stress theory (Hadjesfandiari, 2013, Mindlin and Tiersten, 1962, Poya *et al.*, 2019), and rotation-gradient theory (Anqing *et al.*, 2015, Li *et al.*, 2015). Other authors consider the couplings with further physics, such as the flexoelectric effect in ferroelectrics (Catalan *et al.*, 2004, Eliseev *et al.*, 2009), the coupling with magnetic fields (Eliseev *et al.*, 2011, Liu, 2014) or photovoltaics (Shu *et al.*, 2020, Yang *et al.*, 2018), and the contributions of surface effects (Shen and Hu, 2010). General variational principles for flexoelectric materials can be found in Hu and Shen (2010), Liu (2014), Shen and Hu (2010). The reader is referred to Krichen and Sharma (2016), Nguyen *et al.* (2013), Wang *et al.* (2019), Yudin and Tagantsev (2013), Zubko *et al.* (2013) for comprehensive reviews of flexoelectricity in solids. Another focus of recent research is the modelling of flexoelectricity for soft materials (e.g. polymers and elastomers), which requires a finite deformation framework (Liu, 2014, McBride *et al.*, 2020, Poya *et al.*, 2019, Thai *et al.*, 2018, Yvonnet and Liu, 2017).

All the aforementioned theories of flexoelectricity can be classified depending on the

following considerations:

- The choice of variables describing the flexoelectric effect. For the mechanics, either the displacement gradient or its symmetrized form (i.e. strain) can be used, which give rise to type-I or type-II flexoelectricity, respectively. For the dielectrics, the most usual variable is the electric polarization. However, there exist many theories taking the electric field or the electric displacement instead.
- The flexoelectric coupling considered, either the direct one, the converse, both, or the Lifshitz-invariant form. Section 2.1.1 further elaborates on this topic.
- The dielectric media surrounding the flexoelectric solid being included in the modeling or not.

In the next Sections we describe the different type-II flexoelectricity models neglecting the surrounding media. Section 2.1.2 does so taking the polarization as primal electric variable, whereas in Section 2.1.3 the electric field is considered instead. Finally, in Section 2.1.4 the recent advances on flexoelectricity for highly deformable materials are further discussed.

2.1.1 Direct and converse flexoelectric effects

Following the work by Maranganti *et al.* (2006), Yudin and Tagantsev (2013), the most general (type-II) quadratic expression for the internal energy density describing the bulk static flexoelectric effect in centrosymmetric dielectrics can be written in terms of the strain tensor $\boldsymbol{\varepsilon} = \frac{1}{2}\left(\nabla \boldsymbol{u} + (\nabla \boldsymbol{u})^{\mathrm{T}}\right)$, the electric polarization field $\boldsymbol{P}$ and their corresponding spatial gradients in the following form:

$$\begin{aligned}\psi^{(0)}(\boldsymbol{\varepsilon}, \nabla\boldsymbol{\varepsilon}, \boldsymbol{P}, \nabla\boldsymbol{P}) = \frac{1}{2}c_{ijkl}\varepsilon_{ij}\varepsilon_{kl} + \frac{1}{2}a_{kl}P_kP_l + \frac{1}{2}h_{ijklmn}\varepsilon_{ij,k}\varepsilon_{lm,n} + \frac{1}{2}b_{ijkl}P_{i,k}P_{j,l} \\ - f^{(1)}_{lijk}\varepsilon_{ij,k}P_l - f^{(2)}_{lijk}\varepsilon_{ij}P_{l,k},\end{aligned} \tag{2.1}$$

where

- $\boldsymbol{c}$ is the usual fourth-order elasticity tensor,
- $\boldsymbol{a}$ is the usual second-order reciprocal dielectric susceptibility tensor,
- $\boldsymbol{h}$ is the sixth-order strain gradient elasticity tensor, representing the purely non-local elastic effects,
- $\boldsymbol{b}$ is the fourth-order polarization gradient tensor, representing the purely non-local effects of polarization,
- $\boldsymbol{f}^{(1)}$ is the direct flexocoupling tensor,
- $\boldsymbol{f}^{(2)}$ is the polarization gradient-strain coupling tensor introduced by Mindlin in his theory of polarization gradient (Mindlin, 1968). In a more modern context, it is also known as the converse flexocoupling tensor.

The two latter terms in Eq. (2.1) can be rewritten as follows:

$$f^{(1)}_{lijk}\varepsilon_{ij,k}P_l + f^{(2)}_{lijk}\varepsilon_{ij}P_{l,k} = \frac{1}{2}f_{lijk}\left(\varepsilon_{ij,k}P_l - \varepsilon_{ij}P_{l,k}\right) + \frac{1}{2}\left(f^{(1)}_{lijk} + f^{(2)}_{lijk}\right)\frac{\partial\left(\varepsilon_{ij}P_l\right)}{\partial x_k}, \tag{2.2}$$

with the (effective) flexocoupling tensor

$$f_{lijk} = f^{(1)}_{lijk} - f^{(2)}_{lijk}. \tag{2.3}$$

The first term in the right hand side of Eq. (2.2) is known as the Lifshitz invariant (Landau and Lifshitz, 2013, Lifshitz and Landau, 1984, Sharma *et al.*, 2010), and represents both the direct and converse flexoelectric effects as discussed later on. The second term in Eq. (2.2) is a null-Lagrangian (Evans, 2010), in the sense that its bulk integral can be written as a surface integral by means of the divergence theorem as

$$\int_\Omega \frac{1}{2}\left(f^{(1)}_{lijk} + f^{(2)}_{lijk}\right)\frac{\partial\left(\varepsilon_{ij}P_l\right)}{\partial x_k}\,\mathrm{d}\Omega = \int_\Gamma \frac{1}{2}\left(f^{(1)}_{lijk} + f^{(2)}_{lijk}\right)\varepsilon_{ij}P_l n_k\,\mathrm{d}\Gamma, \tag{2.4}$$

and hence it does not affect the Euler-Lagrange equations. For this reason, it has often been omitted in the literature (Sharma *et al.*, 2010, Yudin and Tagantsev, 2013), yielding an alternative internal energy density to Eq. (2.1) as

$$\begin{aligned}\psi^{(\mathrm{Lif})}(\boldsymbol{\varepsilon}, \nabla\boldsymbol{\varepsilon}, \boldsymbol{P}, \nabla\boldsymbol{P}) = {} & \frac{1}{2}c_{ijkl}\varepsilon_{ij}\varepsilon_{kl} + \frac{1}{2}a_{kl}P_kP_l + \frac{1}{2}h_{ijklmn}\varepsilon_{ij,k}\varepsilon_{lm,n} + \frac{1}{2}b_{ijkl}P_{i,j}P_{k,l} \\ & - \frac{1}{2}f_{lijk}\left(\varepsilon_{ij,k}P_l - \varepsilon_{ij}P_{l,k}\right).\end{aligned} \tag{2.5}$$

Although formulations differing in null Lagrangians result in the same Euler-Lagrange equations, they differ in the definition of the Neumann boundary conditions. See Ghiba *et al.* (2017) for an in-depth discussion in the context of strain-gradient elasticity models. Null Lagrangians are thus viewed as modeling choices. This issue is addressed in Section 2.2.2.3 which highlights the importance of this modeling choice.

The bulk constitutive electromechanical equations for the physical stress $\boldsymbol{\sigma}$ and physical electric field $\boldsymbol{E}$ are

$$E_l = \frac{\partial\psi}{\partial P_l} - \frac{\partial}{\partial x_k}\left(\frac{\partial\psi}{\partial P_{l,k}}\right) = a_{kl}P_k - b_{ijlk}P_{i,jk} - f_{lijk}\varepsilon_{ij,k}, \tag{2.6a}$$

$$\sigma_{ij} = \frac{\partial\psi}{\partial\varepsilon_{ij}} - \frac{\partial}{\partial x_k}\left(\frac{\partial\psi}{\partial\varepsilon_{ij,k}}\right) = c_{ijkl}\varepsilon_{kl} - h_{ijklmn}\varepsilon_{lm,nk} + f_{lijk}P_{l,k}, \tag{2.6b}$$

with ψ representing either $\psi^{(0)}$ or $\psi^{(\mathrm{Lif})}$.

The two constitutive equations for mechanics and dielectrics in Eq. (2.6) are coupled due to the *direct* and *converse* flexoelectric effects. On the one hand, the direct flexoelectric effect in Eq. (2.6a) induces an electric field (or polarization) proportional to the strain gradient, whereas

the converse effect in Eq. (2.6b) consists on a contribution to the mechanical stress (or strain) proportional to the gradient of polarization. Note that both flexoelectric effects are governed by the same flexocoupling tensor $\boldsymbol{f}$.

The direct and converse flexoelectricity terms in Eq. (2.5) differ by a null Lagrangian. Hence, an alternative expression for the internal energy density that is often used to model flexoelectricity is given by

$$\psi^{(\mathrm{Dir})}(\boldsymbol{\varepsilon}, \nabla\boldsymbol{\varepsilon}, \boldsymbol{P}) = \frac{1}{2} c_{ijkl}\varepsilon_{ij}\varepsilon_{kl} + \frac{1}{2} a_{kl}P_kP_l + \frac{1}{2} h_{ijklmn}\varepsilon_{ij,k}\varepsilon_{lm,n} - f_{lijk}\varepsilon_{ij,k}P_l, \tag{2.7}$$

where the gradient polarization term has also been neglected for simplicity ($\boldsymbol{b} = \boldsymbol{0}$).

We name $\psi^{(\mathrm{Dir})}$ the *direct* flexoelectric energy density. However, one should keep in mind that this energy density also features *both* direct and converse flexoelectric effects. This is apparent by evaluating the resulting constitutive equations:

$$E_l = a_{kl}P_k - f_{lijk}\varepsilon_{ij,k}, \tag{2.8a}$$

$$\sigma_{ij} = c_{ijkl}\varepsilon_{kl} - h_{ijklmn}\varepsilon_{lm,nk} + f_{lijk}P_{l,k}, \tag{2.8b}$$

where the flexoelectric coupling appears in the expressions of the electric field *and* the stress. The direct flexoelectric energy density $\psi^{(\mathrm{Dir})}$ is convenient (and hence popular) since the dependence on the polarization gradient vanishes. This facilitates the derivations of closed-form analytical solutions for simple flexoelectric devices, e.g. Euler-Bernoulli beams (Baroudi *et al.*, 2018, Deng *et al.*, 2014a, Liang *et al.*, 2014, Yan and Jiang, 2013, Yan, 2017) and Timoshenko beams (Zhang *et al.*, 2016a), and also facilitates the implementation of numerical solution methods, typically based on the finite element (or related) methods.

2.1.2 Polarization-based models: Free energy minimization

Let us present the flexoelectricity models that take the polarization as the primal electrical unknown. This is the most natural choice, since it yields a variational formulation in terms of the physical free energy such that, upon *minimization* over the admissible states, Euler-Lagrange equations and boundary conditions follow as necessary conditions (Liu, 2014).

Following Maranganti *et al.* (2006) or Liu (2014), such physical free energy takes the form

$$\Pi[\boldsymbol{u}, \boldsymbol{P}] = \int_\Omega \left(\psi^{\mathrm{Int}}(\boldsymbol{u}, \boldsymbol{P}) + \frac{1}{2}\epsilon_0 \|\boldsymbol{E}\|^2 \right) \mathrm{d}\Omega - W^{\mathrm{ext}}, \tag{2.9}$$

where Ω represents the flexoelectric material, ψ^{Int} is the internal energy density of the flexoelectric material (either $\psi^{(0)}$ in (2.1), the direct form $\psi^{(\mathrm{Dir})}$ in (2.7) or the Lifshitz-invariant form $\psi^{(\mathrm{Lif})}$ in (2.5)), $\frac{1}{2}\epsilon_0\|\boldsymbol{E}\|^2$ is the electrostatic energy density, with ϵ_0 being the vacuum permittivity, and W^{ext} is the external work.

The corresponding variational principle is stated as a constrained minimization problem of

the form

$$(\boldsymbol{u}^*, \boldsymbol{P}^*) = \arg\min_{\boldsymbol{u}} \min_{\boldsymbol{P}} \Pi[\boldsymbol{u}, \boldsymbol{P}], \tag{2.10a}$$

s.t.

$$\nabla \times \boldsymbol{E} = 0, \tag{2.10b}$$

$$\nabla \cdot \boldsymbol{D} = 0, \tag{2.10c}$$

where Eq. (2.10b) and (2.10c) are the stationary Maxwell's equations in matter (i.e. the Maxwell-Faraday's and Gauss's laws).

Such minimization leads to the following Euler-Lagrange equations (Liu, 2014, Maranganti *et al.*, 2006):

$$\nabla \cdot \boldsymbol{\sigma} = \boldsymbol{0} \ \text{ in } \Omega, \qquad \text{where} \qquad \boldsymbol{\sigma} = \frac{\partial \psi^{\text{Int}}}{\partial \boldsymbol{\varepsilon}} - \nabla \cdot \frac{\partial \psi^{\text{Int}}}{\partial \nabla \boldsymbol{\varepsilon}}, \tag{2.11a}$$

$$\nabla \cdot (\epsilon_0 \boldsymbol{E} + \boldsymbol{P}) = 0 \ \text{ in } \Omega, \qquad \text{where} \qquad \boldsymbol{E} = \frac{\partial \psi^{\text{Int}}}{\partial \boldsymbol{P}} - \nabla \cdot \frac{\partial \psi^{\text{Int}}}{\partial \nabla \boldsymbol{P}}, \tag{2.11b}$$

$$\text{s.t.} \quad \nabla \times \boldsymbol{E} = \boldsymbol{0} \ \text{ in } \Omega. \tag{2.11c}$$

Note that Eq. (2.11a) and Eq. (2.11b) describe a coupled elliptic problem, whereas Eq. (2.11c) is an additional constraint that requires the irrotationality of the electric field $\boldsymbol{E}$. This condition is inconvenient to find solutions for $\boldsymbol{u}$ and $\boldsymbol{P}$, either analytical closed forms or numerical approximations (Liu, 2014). Hence, many authors prefer electric field-based models instead of polarization-based ones, since the electric field can be then irrotational by construction.

2.1.3 Electric field-based models: Enthalpy optimization

We present now flexoelectricity models that take the electric field as the primal electrical unknown, instead of the electric polarization. Note that the Maxwell-Faraday's law ($\nabla \times \boldsymbol{E} = \boldsymbol{0}$) implies the existence of an electric potential ϕ such that

$$\boldsymbol{E} = -\nabla \phi. \tag{2.12}$$

Hence, by considering ϕ as the actual electrical unknown, Maxwell-Faraday's law is automatically fulfilled, without the need of including it as a constraint.

Following Abdollahi *et al.* (2014), Deng *et al.* (2014a), Zhuang *et al.* (2020), the variational formulation is written in terms of the free *enthalpy* (also called electrical Gibbs free energy)

$$\Pi[\boldsymbol{u}, \boldsymbol{E}] = \int_\Omega \overline{\psi}(\boldsymbol{u}, \boldsymbol{E}) \, \mathrm{d}\Omega - W^{\text{ext}}, \tag{2.13}$$

where $\overline{\psi}$ is the electrical *enthalpy* density. The corresponding variational principle is

$$(\boldsymbol{u}^*, \phi^*) = \arg \min_{\boldsymbol{u}} \max_{\phi} \Pi[\boldsymbol{u}, -\nabla\phi], \tag{2.14}$$

which is now an *unconstrained* optimization problem. The solution of this problem yields the following Euler-Lagrange equations (Zhuang *et al.*, 2020):

$$\nabla \cdot \boldsymbol{\sigma} = \boldsymbol{0} \ \text{ in } \Omega, \qquad \text{where} \qquad \boldsymbol{\sigma} = \frac{\partial \overline{\psi}}{\partial \boldsymbol{\varepsilon}} - \nabla \cdot \frac{\partial \overline{\psi}}{\partial \nabla \boldsymbol{\varepsilon}}, \tag{2.15a}$$

$$\nabla \cdot \boldsymbol{D} = 0 \ \text{ in } \Omega, \qquad \text{where} \qquad \boldsymbol{D} = \frac{\partial \overline{\psi}}{\partial \boldsymbol{E}} - \nabla \cdot \frac{\partial \overline{\psi}}{\partial \nabla \boldsymbol{E}}, \tag{2.15b}$$

which describe a coupled elliptic problem with no additional constraints.

Analogously to Section 2.1.1, several flexoelectric enthalpy forms can be defined. The ones which are worth mentioning for later reference are the Direct $\left(\overline{\psi}^{(\mathrm{Dir})}\right)$ and Lifshitz-invariant $\left(\overline{\psi}^{(\mathrm{Lif})}\right)$ flexoelectricity forms of the enthalpy, namely

$$\overline{\psi}^{(\mathrm{Dir})}(\boldsymbol{\varepsilon}, \nabla\boldsymbol{\varepsilon}, \boldsymbol{E}) = \frac{1}{2} c_{ijkl}\varepsilon_{ij}\varepsilon_{kl} - \frac{1}{2}\kappa_{ij}E_iE_j + \frac{1}{2}h_{ijklmn}\varepsilon_{ij,k}\varepsilon_{lm,n} - \mu^{(1)}_{lijk}E_l\varepsilon_{ij,k}, \tag{2.16}$$

and

$$\begin{aligned}\overline{\psi}^{(\mathrm{Lif})}(\boldsymbol{\varepsilon}, \nabla\boldsymbol{\varepsilon}, \boldsymbol{E}, \nabla\boldsymbol{E}) = {} & \frac{1}{2} c_{ijkl}\varepsilon_{ij}\varepsilon_{kl} - \frac{1}{2}\kappa_{ij}E_iE_j - \frac{1}{2}M_{ijkl}E_{i,k}E_{j,l} \\ & + \frac{1}{2}h_{ijklmn}\varepsilon_{ij,k}\varepsilon_{lm,n} - \frac{1}{2}\mu_{lijk}\left(E_l\varepsilon_{ij,k} - E_{l,k}\varepsilon_{ij}\right),\end{aligned} \tag{2.17}$$

where $\boldsymbol{\kappa}$ is the dielectricity tensor, $\boldsymbol{M}$ is the gradient dielectricity tensor, and $\boldsymbol{\mu}$ is the flexoelectric tensor.

2.1.4 Models at finite deformation

In recent years, several reasons justify an increasing interest in flexoelectricity in polymeric materials. On the one hand, a large flexoelectric response is expected. Experiments hint that the flexoelectric coefficients of polymers are at least the same order of magnitude as those of hard crystalline materials (Baskaran *et al.*, 2011a, 2012, Chu and Salem, 2012), but being much more deformable, much larger flexoelectric polarization is possible. On the other hand, electromechanical actuation of polymers by flexoelectricity overcomes the current limitations of traditional actuation based on the Maxwell stress effect, which are: *(i)* one-way coupling, i.e. mechanical deformation does not produce an electric field, *(ii)* very large electric fields are required (which may lead to dielectric breakdown), and *(iii)* reversal of electric field does not reverse the direction of the deformation (Krichen and Sharma, 2016, O'Halloran *et al.*, 2008, Pelrine *et al.*, 1998, Rosset and Shea, 2016). The versatility of the flexoelectric actuation as compared to Maxwell stress-based actuation fosters the rational design of a new generation

of efficient electromechanical elastomeric devices, such as sensors, actuators and energy harvesters, based on the flexoelectric effect (Huang *et al.*, 2018, Jiang *et al.*, 2013, Wang *et al.*, 2019).

The mechanism of flexoelectricity in (soft) polymers is more complicated than in hard crystalline materials or other soft materials such as liquid crystals or cellular membranes. In the former, the flexoelectric effect can be intuitively understood by the ionic crystal model under bending, in which a non-zero net dipole moment arises due to a shift between the centers of gravity of the negative and the positive ions. In the latter, flexoelectricity results from the reorientation of irregularly shaped polarized molecules under strain gradients (Nguyen *et al.*, 2013). However, in the case of polymers, both glassy and crystalline components contribute to flexoelectricity (Baskaran *et al.*, 2011a, 2012). We refer to Krichen and Sharma (2016), Nguyen *et al.* (2013), Wang *et al.* (2019), Yudin and Tagantsev (2013), Zubko *et al.* (2013) for excellent and comprehensive reviews of flexoelectricity in solids.

The literature about continuum theories of flexoelectric polymers or elastomers undergoing large deformations is still scarce (Liu, 2014, McBride *et al.*, 2020, Nguyen *et al.*, 2019, Poya *et al.*, 2019, Thai *et al.*, 2018, Yvonnet and Liu, 2017, Zhuang *et al.*, 2019). Some of these works model flexoelectricity as a linear coupling between strain gradients and the electric displacement (Poya *et al.*, 2019) or the electric field (McBride *et al.*, 2020, Nguyen *et al.*, 2019, Zhuang *et al.*, 2019) instead of the electric polarization, which is the most natural choice according to experiments and first-principle calculations (Hong and Vanderbilt, 2013, Ma and Cross, 2002, 2001a, Resta, 2010, Zubko *et al.*, 2007). Furthermore, works modeling flexoelectricity as a coupling between strain gradients and electric polarization consider a coupling tensor of mixed material-spatial character (Liu, 2014, Thai *et al.*, 2018, Yvonnet and Liu, 2017), leading in general to a lack of objectivity.

2.2 Main contributions

In view of the current state of the art, several points are addressed and investigated here in terms of modeling of flexoelectricity within the framework of continuum (electro-)mechanics. In particular, a topic that is studied is the relation between the energy and enthalpy forms of the flexoelectric coupling, which remains unclear. This analysis is performed for both the direct (Section 2.2.1.1) and Lifshitz-invariant (Section 2.2.1.2) flexoelectricity forms in an infinitesimal deformation framework, and the particularity of considering the gradient polarization term is also studied in Section 2.2.1.3. The same analysis is performed on a finite deformation framework for the direct flexoelectricity model in Section 2.2.3. We propose a formulation with a fully material flexoelectric coupling between strain gradient and electric polarization, in contrast to previous works in the literature, which yields an objective enthalpy functional by construction.

Based on the enthalpy forms of the direct and Lifshitz-invariant flexoelectricity models, the associated variational principles and boundary value problems are derived in Sections 2.2.2

and 2.2.4 for infinitesimal and finite strains, respectively. Each boundary value problem is formulated considering strong and weak imposition of essential boundary conditions, in order to be suitable formulations for the numerical solution in conforming and non-conforming spatial discretizations, respectively.

The last topic, addressed in Section 2.2.2.3, is a comparison between the direct and Lifshitz-invariant flexoelectricity boundary value problems in benchmark setups such as cantilever bending and actuation, where very different responses are detected, and very interesting insights are obtained.

2.2.1 Legendre transform: the connection between the two families of flexoelectricity functionals

The variational models based on energy functional minimization, with an internal energy density of the form $\psi(\boldsymbol{u}, \boldsymbol{P})$ (cf. Section 2.1.2), and the ones based on enthalpy functional optimization, with an enthalpy density of the form $\overline{\psi}(\boldsymbol{u}, \boldsymbol{E})$ (cf. Section 2.1.3), are related by means of a partial Legendre transform. That is: given one form, the other one is uniquely determined, and can be directly obtained by a partial Legendre transform. Both formulations are then equivalent.

However, in the literature of flexoelectric modeling, there is some lack explaining this relation and detailing in which sense they are equivalent. In this Section we derive the form of the enthalpy density $\overline{\psi}$ given an expression for the energy density ψ, revealing the assumptions that must be made and the relations between the material parameters of each form.

A dielectric body in equilibrium necessarily satisfies mechanical balance laws of linear and angular momentum and Maxwell equations. In the absence of a magnetic field, they are expressed as

$$\nabla\cdot\boldsymbol{\sigma} + \boldsymbol{b} = \boldsymbol{0} \quad \text{in } \Omega, \tag{2.18a}$$

$$\boldsymbol{\sigma} = \boldsymbol{\sigma}^T \quad \text{in } \Omega, \tag{2.18b}$$

$$\nabla \times \boldsymbol{E} = \boldsymbol{0} \quad \text{in } \Omega, \tag{2.18c}$$

$$\nabla\cdot\boldsymbol{D} - q = 0 \quad \text{in } \Omega; \tag{2.18d}$$

where $\boldsymbol{\sigma}$ is the physical stress, $\boldsymbol{E}$ is the the electric field, $\boldsymbol{D}$ is the electric displacement, and $\boldsymbol{b}$ and q are the body force and electric charge per unit volume. Equation (2.18c) implies the existence of an electric potential ϕ such that $\boldsymbol{E} = -\nabla\phi$.

The total energy density is given by $\psi(\boldsymbol{u}, \boldsymbol{P}, \boldsymbol{E}) = \psi^{\text{Int}}(\boldsymbol{u}, \boldsymbol{P}) + \frac{1}{2}\epsilon_0 \boldsymbol{E}\cdot\boldsymbol{E}$, where ψ^{Int} is the internal energy density of the material and the second term refers to the electrostatic energy density, with ϵ_0 being the electric permittivity of vacuum. The differentiation of the total energy density with respect to the electric field $\boldsymbol{E}$ yields the classical constitutive law for

$\boldsymbol{D} := \partial_{\boldsymbol{E}}(\psi)$ for a dielectric material:

$$\boldsymbol{D}(\boldsymbol{P}, \boldsymbol{E}) = \epsilon_0 \boldsymbol{E} + \boldsymbol{P}, \tag{2.19}$$

where $\boldsymbol{P} := \partial_{\boldsymbol{E}}\left(\psi^{\text{Int}}\right)$ is the electric polarization.

2.2.1.1 Direct flexoelectricity

Let us consider in this Section the *direct* flexoelectricity internal energy density, i.e. $\psi^{\text{Int}} \equiv \psi^{(\text{Dir})}$ as described in Eq. (2.7). In order to find the equivalent internal enthalpy density $\overline{\psi}^{\text{Int}}$, we resort to a partial Legendre transform and define the following internal dual potential (or internal *enthalpy*)

$$\begin{aligned}\overline{\psi}^{\text{Int}}(\boldsymbol{u}, \boldsymbol{E}) &= \min_{\boldsymbol{P}} \left(\psi^{\text{Int}}(\boldsymbol{u}, \boldsymbol{P}) - \boldsymbol{P} \cdot \boldsymbol{E}\right) \\ &= \min_{\boldsymbol{P}} \left(\frac{1}{2} c_{ijkl}\varepsilon_{ij}\varepsilon_{kl} + \frac{1}{2} a_{ml} P_m P_l + \frac{1}{2} h_{ijklmn}\varepsilon_{ij,k}\varepsilon_{lm,n} - f^{(1)}_{lijk}\varepsilon_{ij,k} P_l - P_l E_l\right).\end{aligned} \tag{2.20}$$

The stationarity condition of the minimization results in

$$E_l = \frac{\partial \psi^{\text{Int}}}{\partial P_l} = a_{ml} P_m - f^{(1)}_{lijk}\varepsilon_{ij,k}, \tag{2.21}$$

which can be inverted to

$$P_m = a^{-1}_{lm}\left(E_l + f^{(1)}_{lijk}\varepsilon_{ij,k}\right) = a^{-1}_{lm}\left(E_l + E^{\text{Flexo}}_l\right), \tag{2.22}$$

where $E^{\text{Flexo}}_l = f^{(1)}_{lijk}\varepsilon_{ij,k}$ is the so-called flexoelectric field. By inserting Eq. (2.22) into (2.20), and exploiting the intrinsic symmetry of $\boldsymbol{a}$, the internal enthalpy density is obtained as

$$\begin{aligned}\overline{\psi}^{\text{Int}}(\boldsymbol{u}, \phi) = &\frac{1}{2} c_{ijkl}\varepsilon_{ij}\varepsilon_{kl} - \frac{1}{2} a^{-1}_{ij} E_i E_j + \frac{1}{2} h_{ijklmn}\varepsilon_{ij,k}\varepsilon_{lm,n} \\ &- \frac{1}{2} a^{-1}_{ab} f^{(1)}_{aijk} f^{(1)}_{blmn}\varepsilon_{ij,k}\varepsilon_{lm,n} - a^{-1}_{lm} f^{(1)}_{mijk} E_l \varepsilon_{ij,k}.\end{aligned} \tag{2.23}$$

The total enthalpy density is obtained by substracting the electrostatic energy density to the internal enthalpy (Dorfmann and Ogden, 2014, 2017, Liu, 2014). Further, for convenience, let us define the dielectricity ($\boldsymbol{\kappa}$), the (direct) flexoelectricity ($\boldsymbol{\mu}^{(1)}$) and effective strain gradient elasticity ($\overline{\boldsymbol{h}}$) tensors as follows:

$$\kappa_{ij} = a^{-1}_{ij} + \epsilon_0 \delta_{ij}, \tag{2.24a}$$

$$\mu^{(1)}_{lijk} = a^{-1}_{lm} f^{(1)}_{mijk}, \tag{2.24b}$$

$$\overline{h}_{ijklmn} = h_{ijklmn} - a^{-1}_{ab} f^{(1)}_{aijk} f^{(1)}_{blmn}. \tag{2.24c}$$

Then, the total enthalpy density for the direct flexoelectricity model reads

$$\begin{aligned}\overline{\psi}^{(\mathrm{Dir})}(\boldsymbol{u},\phi) &= \overline{\psi}^{\mathrm{Int}}(\boldsymbol{u},\phi) - \frac{1}{2}\epsilon_0 E_i E_i \\ &= \frac{1}{2}c_{ijkl}\varepsilon_{ij}\varepsilon_{kl} - \frac{1}{2}\kappa_{ij}E_iE_j + \frac{1}{2}\overline{h}_{ijklmn}\varepsilon_{ij,k}\varepsilon_{lm,n} - \mu^{(1)}_{lijk}E_l\varepsilon_{ij,k},\end{aligned} \tag{2.25}$$

which closely resembles the expression for the total enthalpy density in Eq. (2.16). Eq. (2.24) reveals the relation between the energy-density tensors $\{\boldsymbol{a}, \boldsymbol{f}^{(1)}, \boldsymbol{h}\}$ and their enthalpy-density counterparts $\{\boldsymbol{\kappa}, \boldsymbol{\mu}^{(1)}, \overline{\boldsymbol{h}}\}$. Further, by assuming the standard expression for isotropic reciprocal dielectric susceptibility tensors $\boldsymbol{a} = (\chi_e\epsilon_0)^{-1}\mathbf{I} = (\epsilon - \epsilon_0)^{-1}\mathbf{I}$, Eq. (2.24) simplifies to

$$\kappa_{ij} = \epsilon\delta_{ij}, \tag{2.26a}$$

$$\mu^{(1)}_{lijk} = \chi_e\epsilon_0 f^{(1)}_{lijk}, \tag{2.26b}$$

$$\overline{h}_{ijklmn} = h_{ijklmn} - \chi_e\epsilon_0 f^{(1)}_{aijk}f^{(1)}_{almn} = h_{ijklmn} - \frac{\mu^{(1)}_{aijk}\mu^{(1)}_{almn}}{\chi_e\epsilon_0}, \tag{2.26c}$$

which yields the standard definition of $\boldsymbol{\kappa}$ for isotropic dielectrics, as a function of its electric permittivity ϵ, and reveals a well-known feature of flexoelectricity: its linear growth with the dielectric susceptibility χ_e, cf. Fig. 2.1. This is the reason why materials with high dielectric constant (e.g. ferroelectric perovskites) typically feature also large flexoelectric constants (Nguyen *et al.*, 2013, Zhuang *et al.*, 2020, Zubko *et al.*, 2013). Eq. (2.26c) is also noticeable, since it shows that the (effective) strain gradient elasticity tensor is modified due to the flexoelectric coupling.

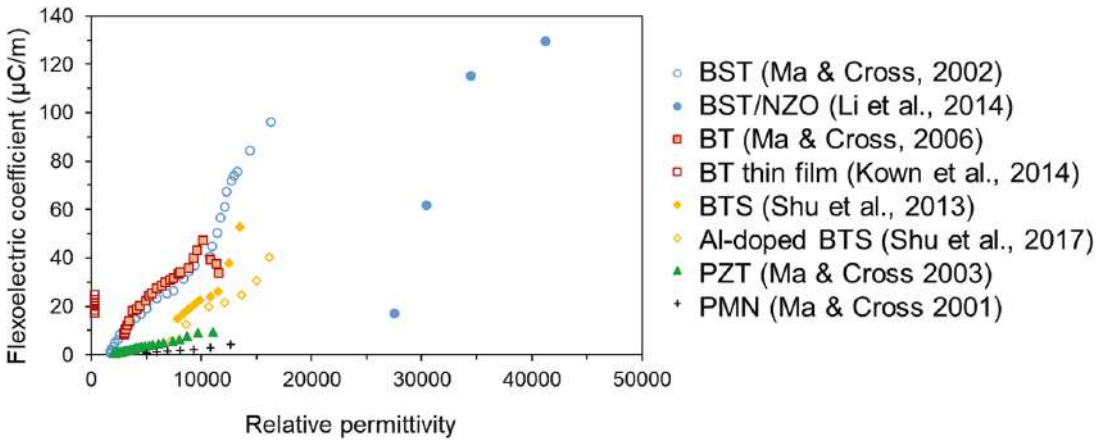

Figure 2.1: Linear trend of the scaling of the flexoelectric coefficient with respect to relative permittivity $\epsilon_r = \chi_e + 1$. Adapted from Wang *et al.* (2019).

2.2.1.2 Lifshitz-invariant flexoelectricity (without gradient polarization)

The derivation of the enthalpy density corresponding to the Lifshitz-invariant flexoelectric internal energy density in Eq. (2.5) is analogous to the derivation of the direct flexoelectricity case in Section 2.2.1.1, *provided that gradient polarization is neglected.* This assumption is sometimes taken in the literature, cf. the formulation in Zubko *et al.* (2013) for 1D. The case including gradient polarization is explored later in Section 2.2.1.3.

Let us consider an internal energy density of the following form

$$\psi^{(\mathrm{Int})}(\boldsymbol{\varepsilon}, \nabla\boldsymbol{\varepsilon}, \boldsymbol{P}, \nabla\boldsymbol{P}) = \frac{1}{2}c_{ijkl}\varepsilon_{ij}\varepsilon_{kl} + \frac{1}{2}a_{kl}P_kP_l + \frac{1}{2}h_{ijklmn}\varepsilon_{ij,k}\varepsilon_{lm,n} - \frac{1}{2}f_{lijk}\left(\varepsilon_{ij,k}P_l - \varepsilon_{ij}P_{l,k}\right), \tag{2.27}$$

where gradient polarization term $\boldsymbol{b}$ is neglected from Eq. (2.5). Then, the stationary condition of the following minimization,

$$\begin{aligned}\overline{\psi}^{\mathrm{Int}}(\boldsymbol{u}, \boldsymbol{E}) &= \min_{\boldsymbol{P}}\left(\psi^{\mathrm{Int}}(\boldsymbol{u}, \boldsymbol{P}) - \boldsymbol{P}\cdot\boldsymbol{E}\right)\\ &= \min_{\boldsymbol{P}}\Big(\frac{1}{2}c_{ijkl}\varepsilon_{ij}\varepsilon_{kl} + \frac{1}{2}a_{kl}P_kP_l + \frac{1}{2}h_{ijklmn}\varepsilon_{ij,k}\varepsilon_{lm,n}\\ &\qquad - \frac{1}{2}f_{lijk}\left(\varepsilon_{ij,k}P_l - \varepsilon_{ij}P_{l,k}\right) - P_lE_l\Big),\end{aligned} \tag{2.28}$$

results in

$$E_l = \frac{\partial\psi^{\mathrm{Int}}}{\partial P_l} - \frac{\partial}{\partial x_k}\left(\frac{\partial\psi^{\mathrm{Int}}}{\partial P_{l,k}}\right) = a_{ml}P_m - f_{lijk}\varepsilon_{ij,k}, \tag{2.29}$$

which closely resembles Eq. (2.21), the only difference being $\boldsymbol{f}$ instead of $\boldsymbol{f}^{(1)}$. Hence, the inverse relation

$$P_m = a^{-1}_{lm}\left(E_l + f_{lijk}\varepsilon_{ij,k}\right) \tag{2.30}$$

is inserted into (2.28), and after substracting the electrostatic energy density, the following total enthalpy density is obtained:

$$\begin{aligned}\overline{\psi}^{(\mathrm{Lif}_0)}(\boldsymbol{u}, \phi) &= \overline{\psi}^{\mathrm{Int}}(\boldsymbol{u}, \phi) - \frac{1}{2}\epsilon_0E_iE_i\\ &= \frac{1}{2}c_{ijkl}\varepsilon_{ij}\varepsilon_{kl} - \frac{1}{2}\kappa_{ij}E_iE_j + \frac{1}{2}h_{ijklmn}\varepsilon_{ij,k}\varepsilon_{lm,n} + \frac{1}{2}a^{-1}_{ab}f^{(1)}_{aijk}f^{(1)}_{blmn}\varepsilon_{ij,kn}\varepsilon_{lm}\\ &\quad - \frac{1}{2}\mu_{lijk}\left(E_l\varepsilon_{ij,k} - E_{l,k}\varepsilon_{ij}\right),\end{aligned} \tag{2.31}$$

where the definitions in Eq. (2.24a) and (2.24b) have been analogously considered, here for the full (not the direct) flexocoupling and flexoelectric tensors.

The last step consists on rewriting the fourth term in Eq. (2.31) as

$$\frac{1}{2}a^{-1}_{ab}f^{(1)}_{aijk}f^{(1)}_{blmn}\varepsilon_{ij,kn}\varepsilon_{lm} = -\frac{1}{2}a^{-1}_{ab}f^{(1)}_{aijk}f^{(1)}_{blmn}\varepsilon_{ij,k}\varepsilon_{lm,n} + \frac{\partial\left(\frac{1}{2}a^{-1}_{ab}f^{(1)}_{aijk}f^{(1)}_{blmn}\varepsilon_{ij,k}\varepsilon_{lm}\right)}{\partial x_n} \tag{2.32}$$

where the last term is neglected from the bulk enthalpy density since it is attributed to the surface by means of the divergence theorem, as done in Section 2.1.1 to obtain the Lifshitz-invariant internal energy density. With this consideration, the final version of the total enthalpy density for the Lifshitz-invariant form of flexoelectricity is obtained as

$$\begin{aligned}\overline{\psi}^{(\mathrm{Lif}_0)}(\boldsymbol{u},\boldsymbol{E}) &= \overline{\psi}^{\mathrm{Int}}(\boldsymbol{u},\boldsymbol{E}) - \frac{1}{2}\epsilon_0 E_i E_i \\ &= \frac{1}{2}c_{ijkl}\varepsilon_{ij}\varepsilon_{kl} - \frac{1}{2}\kappa_{ij}E_iE_j + \frac{1}{2}\overline{h}_{ijklmn}\varepsilon_{ij,k}\varepsilon_{lm,n} - \frac{1}{2}\mu_{lijk}\left(E_l\varepsilon_{ij,k} - E_{l,k}\varepsilon_{ij}\right),\end{aligned} \tag{2.33}$$

which has the well-known form of the total enthalpy density in Lifshitz-invariant flexoelectricity present in Eq. (2.17). The same effective strain gradient elasticity tensor from Eq. (2.24c) is retrieved here. In fact, the direct and Lifshitz-invariant total enthalpy densities in Eq. (2.25) and Eq. (2.33) are related with each other by means of an integration by parts of the flexoelectricity term, exactly in the same way as done in Section 2.1.1 for the energy densities.

2.2.1.3 Lifshitz-invariant flexoelectricity (with gradient polarization)

In this Section, the enthalpy density corresponding to the Lifshitz-invariant flexoelectric internal energy density in Eq. (2.5), *including gradient polarization*, is derived via a partial Legendre transform. The procedure is analogous to the previous Sections, but slightly modified in order to properly treat the high-order electric terms coming from gradient polarization. In this case, the typical flexoelectric energy and enthalpy forms are *not* equivalent, as shown next.

Let us begin with the total energy density in Eq. (2.5), that is,

$$\begin{aligned}\psi^{\mathrm{Int}} \equiv \psi^{(\mathrm{Lif})}(\boldsymbol{\varepsilon},\nabla\boldsymbol{\varepsilon},\boldsymbol{P},\nabla\boldsymbol{P}) &= \frac{1}{2}c_{ijkl}\varepsilon_{ij}\varepsilon_{kl} + \frac{1}{2}a_{kl}P_kP_l + \frac{1}{2}h_{ijklmn}\varepsilon_{ij,k}\varepsilon_{lm,n} + \frac{1}{2}b_{ijkl}P_{i,j}P_{k,l} \\ &\quad - \frac{1}{2}f_{lijk}\left(\varepsilon_{ij,k}P_l - \varepsilon_{ij}P_{l,k}\right),\end{aligned} \tag{2.34}$$

this time including the gradient polarization term modeled by the material tensor $\boldsymbol{b}$. In order to simplify the derivations next, let's assume that $\boldsymbol{a} = (\chi_e\epsilon_0)^{-1}\mathbf{I}$ is isotropic and that $\boldsymbol{b}$ takes the simplified form of $b_{ijkl} = \ell^2_{\mathrm{elec}}a_{ik}\delta_{jl} = \ell^2_{\mathrm{elec}}(\chi_e\epsilon_0)^{-1}\delta_{ik}\delta_{jl}$, with a length scale parameter ℓ_{elec}.

The stationary condition of the Legendre transform minimization reads

$$\begin{aligned}\overline{\psi}^{\mathrm{Int}}(\boldsymbol{u},\boldsymbol{E}) &= \min_{\boldsymbol{P}}\left(\psi^{\mathrm{Int}}(\boldsymbol{u},\boldsymbol{P})-\boldsymbol{P}\cdot\boldsymbol{E}\right)\\ &= \min_{\boldsymbol{P}}\Big(\frac{1}{2}c_{ijkl}\varepsilon_{ij}\varepsilon_{kl}+\frac{1}{2}(\chi_e\epsilon_0)^{-1}P_lP_l+\frac{1}{2}h_{ijklmn}\varepsilon_{ij,k}\varepsilon_{lm,n}+\frac{1}{2}(\chi_e\epsilon_0)^{-1}\ell_{\mathrm{elec}}^2P_{l,k}P_{l,k}\\ &\qquad -\frac{1}{2}f_{lijk}\left(\varepsilon_{ij,k}P_l-\varepsilon_{ij}P_{l,k}\right)-P_lE_l\Big),\end{aligned}\tag{2.35}$$

which results in

$$E_l=\frac{\partial\psi^{\mathrm{Int}}}{\partial P_l}-\frac{\partial}{\partial x_k}\left(\frac{\partial\psi^{\mathrm{Int}}}{\partial P_{l,k}}\right)=\widehat{E}_l-\tilde{E}_{lk,k},\tag{2.36}$$

with

$$\widehat{E}_l=\frac{\partial\psi^{\mathrm{Int}}}{\partial P_l}=(\chi_e\epsilon_0)^{-1}P_l-\frac{1}{2}f_{lijk}\varepsilon_{ij,k},\tag{2.37a}$$

$$\tilde{E}_{lk}=\frac{\partial\psi^{\mathrm{Int}}}{\partial P_{l,k}}=\ell_{\mathrm{elec}}^2(\chi_e\epsilon_0)^{-1}P_{l,k}+\frac{1}{2}f_{lijk}\varepsilon_{ij}.\tag{2.37b}$$

Since it is difficult to invert the expression $\boldsymbol{E}(\boldsymbol{P},\nabla\boldsymbol{P})$ in Eq. (2.36) to get $\boldsymbol{P}(\boldsymbol{E},\nabla\boldsymbol{E})$, let us just invert the expression $\widehat{\boldsymbol{E}}(\boldsymbol{P})$ in Eq. (2.37a) to get $\boldsymbol{P}(\widehat{\boldsymbol{E}})$ as

$$P_l(\widehat{\boldsymbol{E}})=\chi_e\epsilon_0\left(\widehat{E}_l+\frac{1}{2}f_{lijk}\varepsilon_{ij,k}\right),\tag{2.38}$$

hence

$$P_{l,k}(\widehat{\boldsymbol{E}})=\chi_e\epsilon_0\left(\widehat{E}_{l,k}+\frac{1}{2}f_{labc}\varepsilon_{ab,ck}\right)\tag{2.39}$$

and Eq. (2.37b) turns out

$$\tilde{E}_{lk}(\widehat{\boldsymbol{E}})=\ell_{\mathrm{elec}}^2\left(\widehat{E}_{l,k}+\frac{1}{2}f_{labc}\varepsilon_{ab,ck}\right)+\frac{1}{2}f_{lijk}\varepsilon_{ij}.\tag{2.40}$$

Thus, by Eq. (2.36),

$$\begin{aligned}E_l(\widehat{\boldsymbol{E}}) &= \widehat{E}_l-\tilde{E}_{lk,k},\\ &= \widehat{E}_l-\ell_{\mathrm{elec}}^2\left(\widehat{E}_{l,kk}+\frac{1}{2}f_{labc}\varepsilon_{ab,ckk}\right)-\frac{1}{2}f_{lijk}\varepsilon_{ij,k}\\ &= \breve{E}_l-\ell_{\mathrm{elec}}^2\nabla^2\left(\breve{E}_l+f_{lijk}\varepsilon_{ij,k}\right)\\ &= E_l(\breve{\boldsymbol{E}})\end{aligned}\tag{2.41}$$

where $\breve{E}_l := \widehat{E}_l-\frac{1}{2}f_{lijk}\varepsilon_{ij,k}$ is defined for convenience. Note that with this definiton, the

polarization in Eq. (2.38) is rewritten as

$$P_l(\breve{\boldsymbol{E}}) = \chi_e \epsilon_0 \left(\breve{E}_l + f_{lijk} \varepsilon_{ij,k} \right), \tag{2.42}$$

which is analogous to the expression for polarization in Eq. (2.30) in the case where $\boldsymbol{b}$ was neglected, where $\boldsymbol{E}$ is replaced by $\breve{\boldsymbol{E}}$. In fact, note that $\breve{\boldsymbol{E}} \longrightarrow \boldsymbol{E}$ in the limit of $\ell_{\text{elec}} \longrightarrow 0$, so in view of Eq. (2.41) and (2.42), $\boldsymbol{E}$ can be interpreted in this context as the sum of a local contribution from $\breve{\boldsymbol{E}}$ (local electric field) and a nonlocal contribution from $\boldsymbol{P}(\breve{\boldsymbol{E}})$:

$$E_l(\breve{\boldsymbol{E}}) = \breve{E}_l - (\chi_e \epsilon_0)^{-1} \ell_{\text{elec}}^2 \nabla^2 P_l(\breve{\boldsymbol{E}}), \tag{2.43}$$

being ∇^2 the vector Laplacian operator.

By means of Eq. (2.42) and (2.43), substracting the electrostatic energy density from Eq. (2.35) and doing the appropriate integration by parts, the following total enthalpy density is obtained as a function of $\breve{\boldsymbol{E}}$ as

$$\begin{aligned} \overline{\psi}^{(\text{Lif})}(\boldsymbol{u}, \breve{\boldsymbol{E}}) &= \overline{\psi}^{\text{Int}}(\boldsymbol{u}, \boldsymbol{E}(\breve{\boldsymbol{E}})) - \frac{1}{2} \epsilon_0 E_l(\breve{\boldsymbol{E}}) E_l(\breve{\boldsymbol{E}}) \\ &= \overline{\psi}^{(\text{Lif}_0)}(\boldsymbol{u}, \breve{\boldsymbol{E}}) - \frac{1}{2} M_{ijkl} \breve{E}_{i,k} \breve{E}_{j,l} + \mathcal{O}(\nabla\nabla\boldsymbol{\varepsilon}, \nabla\nabla\breve{\boldsymbol{E}}), \end{aligned} \tag{2.44}$$

where $\overline{\psi}^{(\text{Lif}_0)}$ is defined in Eq. (2.33), higher order terms $\mathcal{O}$ are neglected, and

$$M_{ijkl} = (\epsilon + \epsilon_0) \delta_{ik} \delta_{jl} \ell_{\text{elec}}^2 = b_{ijkl} \left(\epsilon^2 - \epsilon_0^2 \right) \tag{2.45}$$

is the gradient dielectricity tensor.

Hence, Eq. (2.44) resembles the expression for the total enthalpy density in Eq. (2.17), including the gradient dielectricity term. However, a fundamental difference is that the expression obtained here is written in terms of $\breve{\boldsymbol{E}}$, i.e. the local electric field, instead of the full expression $\boldsymbol{E}$ of the electric field. This fact implies rewriting the Maxwell–Faraday equation in Eq. (2.18c) in terms of $\breve{\boldsymbol{E}}$ as

$$\nabla \times E_l = \nabla \times \left(\breve{E}_l - \ell_{\text{elec}}^2 \nabla^2 \left(\breve{E}_l + f_{lijk} \varepsilon_{ij,k} \right) \right) = \boldsymbol{0} \tag{2.46}$$

or

$$\left(1 - \ell_{\text{elec}}^2 \nabla^2 \right) \left(\nabla \times \breve{\boldsymbol{E}} \right) = \ell_{\text{elec}}^2 \nabla^2 \left(\nabla \times \boldsymbol{E}^{\text{Flexo}} \right) \neq \boldsymbol{0}. \tag{2.47}$$

In other, words, the local field $\breve{\boldsymbol{E}}$ is *not* irrotational, even if the flexoelectric coupling is vanished. Hence, it cannot be expressed as (minus) the gradient of a (local) electric potential, as usually assumed in Eq. (2.1.3). Therefore, the energy density- and the enthalpy density-based Lifshitz-invariant flexoelectric models are *not* equivalent, unless the polarization gradient (and gradient dielectricity) terms are neglected.

However, which model is more representative of the actual physics is an open question, far beyond the scope of this study. When it comes to numerical modeling, the enthalpy-based approach is preferable since *(i)* the electrostatics are already taken into account, without the need of handling two different variables for the electric and polarization fields, and *(ii)* the electric potential can be considered directly as state variable instead of the electric field, so there is no need of including the Maxwell-Faraday equation as an additional constraint to the variational principle.

2.2.2 Variational models at infinitesimal deformation

In this Section, we consider different flexoelectric *enthalpy* density models and derive their corresponding variational models and associated boundary value problems, that will be numerically solved as explained in Chapter 3.

Let Ω be a physical domain in $\mathbb{R}^3$. The domain boundary, $\partial\Omega$, can be conformed by several smooth portions as $\partial\Omega = \bigcup_f \partial\Omega_f$ (Fig. 2.2a). At each point $\boldsymbol{x} \in \partial\Omega_f$ we define $\boldsymbol{n}^f$ as the outward unit *normal vector*. The boundary of the f-th portion of $\partial\Omega$ is denoted as $\partial\partial\Omega_f$, which is a closed curve. At each point $\boldsymbol{x} \in \partial\partial\Omega_f$ we define $\boldsymbol{m}^f$ as the unit *co-normal vector* pointing outwards of $\partial\Omega_f$, which is orthogonal to the normal vector $\boldsymbol{n}^f$ and to the tangent vector of the curve $\partial\partial\Omega_f$, $\boldsymbol{s}^f$ (see Fig. 2.2b and 2.2c). The orientation of $\boldsymbol{s}^f$ is arbitrary and not relevant in the derivations next.

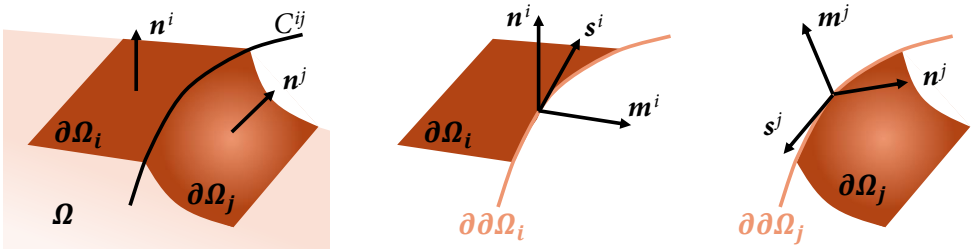

(a) (b) (c)

Figure 2.2: Sketch of the geometry of $\Omega \in \mathbb{R}^3$. (a) Detail of $\partial\Omega$ subdivided in smooth portions $\partial\Omega_i$ and $\partial\Omega_j$, with their corresponding normal vectors $\boldsymbol{n}^i$ and $\boldsymbol{n}^j$, (b) detail of $\partial\Omega_i$, with the triplet $\{\boldsymbol{m}^i, \boldsymbol{s}^i, \boldsymbol{n}^i\}$ defined on $\partial\partial\Omega_i$, and (c) detail of $\partial\Omega_j$, with the triplet $\{\boldsymbol{m}^j, \boldsymbol{s}^j, \boldsymbol{n}^j\}$ defined on $\partial\partial\Omega_j$. Figure adapted from Codony *et al.* (2019).

Following Eq. (2.13), the generic form of the enthalpy functional $\Pi[\boldsymbol{u}, \phi]$ of a flexoelectric material is written as

$$\Pi[\boldsymbol{u}, \phi] = \int_\Omega \left(\overline{\psi}(\boldsymbol{u}, \phi) + \mathcal{W}^\Omega(\boldsymbol{u}, \phi) \right) \mathrm{d}\Omega + \int_{\partial\Omega} \mathcal{W}^{\partial\Omega}(\boldsymbol{u}, \phi)\, \mathrm{d}\Gamma + \int_C \mathcal{W}^C(\boldsymbol{u}, \phi)\, \mathrm{d}s \tag{2.48}$$

where $\overline{\psi}$ is the internal bulk enthalpy density in Ω and $\mathcal{W}^\Omega$, $\mathcal{W}^{\partial\Omega}$ and $\mathcal{W}^C$ represent the external work density per unit volume, area and length, respectively. The corresponding

variational principle corresponds to an unconstrained optimization of the form

$$(\boldsymbol{u}^*, \phi^*) = \arg\min_{\boldsymbol{u}} \max_{\phi} \Pi[\boldsymbol{u}, \phi]. \tag{2.49}$$

Different boundary value problems arise depending on the flexoelectric form that is chosen to describe $\overline{\psi}$. We show next the derivations for the *direct* and *Lifshitz-invariant* flexoelectric forms.

2.2.2.1 Direct flexoelectricity form

According to Eq. (2.16), the direct flexoelectricity enthalpy density is stated as

$$\overline{\psi}^{(\mathrm{Dir})}(\boldsymbol{\varepsilon}, \nabla\boldsymbol{\varepsilon}, \boldsymbol{E}) := \frac{1}{2}\varepsilon_{ij}c_{ijkl}\varepsilon_{kl} + \frac{1}{2}\varepsilon_{ij,k}h_{ijklmn}\varepsilon_{lm,n} - \frac{1}{2}E_l\kappa_{lm}E_m - E_l\mu_{lijk}\varepsilon_{ij,k}, \tag{2.50}$$

and the admissible external sources of work are

$$\mathcal{W}^{\Omega}(\boldsymbol{u}, \phi) := -\overline{b}_i u_i + \overline{q}\phi, \tag{2.51a}$$

$$\mathcal{W}^{\partial\Omega}(\boldsymbol{u}, \phi) := -t_i u_i - r_i \partial^n u_i + w\phi, \tag{2.51b}$$

$$\mathcal{W}^{C}(\boldsymbol{u}, \phi) := -j_i u_i, \tag{2.51c}$$

where $\overline{\boldsymbol{b}}$ is the external body force per unit volume, $\overline{q}$ is the external free electric charge per unit volume, $\boldsymbol{t}$ and $\boldsymbol{j}$ are the forces per unit area (i.e. traction) and length, w is the surface charge density (i.e. electric charge per unit area) and $\boldsymbol{r}$ is the double traction (i.e. moment per unit area).

The boundary of the domain $\partial\Omega$ is split into several disjoint *Dirichlet* and *Neumann* boundaries as

$$\partial\Omega = \partial\Omega_u \cup \partial\Omega_t = \partial\Omega_v \cup \partial\Omega_r = \partial\Omega_\phi \cup \partial\Omega_w, \tag{2.52}$$

where $\partial\Omega_u$, $\partial\Omega_v$ and $\partial\Omega_\phi$ are the Dirichlet boundaries corresponding to prescribed values for the displacement, its normal derivative and the electric potential, and $\partial\Omega_t$, $\partial\Omega_r$ and $\partial\Omega_w$ the Neumann boundaries corresponding to prescribed values of their enthalpy conjugates, i.e. the traction, the double traction and the surface charge density. The edges C of $\partial\Omega$ are also split into $C = C_u \cup C_j$ corresponding to the Dirichlet and Neumann edge partitions, respectively, where either the displacement field or the forces per unit length are prescribed. Here, C_u is corresponds to the curves within the classical Dirichlet boundary, namely $C_u = C \cap \overline{\partial\Omega_u}$, and $C_v = C \setminus C_u$.

The corresponding boundary and edge conditions are mathematically written as

$$\boldsymbol{u} - \overline{\boldsymbol{u}} = \boldsymbol{0} \quad \text{on } \partial\Omega_u, \qquad \boldsymbol{t}(\boldsymbol{u},\phi) - \overline{\boldsymbol{t}} = \boldsymbol{0} \quad \text{on } \partial\Omega_t; \tag{2.53a}$$

$$\partial^n(\boldsymbol{u}) - \overline{v} = 0 \quad \text{on } \partial\Omega_v, \qquad r(\boldsymbol{u},\phi) - \overline{r} = 0 \quad \text{on } \partial\Omega_r; \tag{2.53b}$$

$$\phi - \overline{\phi} = 0 \quad \text{on } \partial\Omega_\phi, \qquad w(\boldsymbol{u},\phi) - \overline{w} = 0 \quad \text{on } \partial\Omega_w; \tag{2.53c}$$

$$\boldsymbol{u} - \overline{\boldsymbol{u}} = \boldsymbol{0} \quad \text{on } C_u, \qquad \boldsymbol{j}(\boldsymbol{u},\phi) - \overline{\boldsymbol{j}} = \boldsymbol{0} \quad \text{on } C_j; \tag{2.53d}$$

where $\overline{\boldsymbol{u}}$, $\overline{v}$ and $\overline{\phi}$ are the prescribed displacement, normal derivative of the displacement and electric potential at the Dirichlet boundaries, and $\overline{\boldsymbol{t}}$, $\overline{r}$, $\overline{w}$ and $\overline{\boldsymbol{j}}$ are the traction, double traction, surface charge and the line force fields prescribed on the Neumann boundaries. The expressions $\boldsymbol{t}(\boldsymbol{u},\phi)$, $r(\boldsymbol{u},\phi)$, $w(\boldsymbol{u},\phi)$ and $\boldsymbol{j}(\boldsymbol{u},\phi)$ will be derived later as a result of the variational principle in Eq. (2.56).

Many authors in the literature of computational flexoelectricity neglect the edge conditions in Eq. (2.53d) (Abdollahi *et al.*, 2015a, 2014, Aravas, 2011, Mao and Purohit, 2014). In the cases where essential boundary conditions are enforced strongly, as in conforming FE or meshless discretizations, this fact has no practical relevance since the strong imposition on $\partial\Omega_u$ automatically implies the strong imposition on the adjacent edges in C_u as well. However, it is important to underline that in frameworks where boundary conditions are enforced weakly, dismissing edge conditions is equivalent to considering homogeneous Neumann edge conditions, which is wrong on C_u (Dirichlet edges). Edge conditions are kept here to ensure self-consistency and a well-defined boundary value problem.

2.2.2.1.a Standard framework: Strong boundary conditions

The standard approach in computational mechanics to take into account Dirichlet boundary conditions consists on assuming that the functional space of the state variables already fulfills Dirichlet boundary conditions. Therefore, it is not required to include Dirichlet boundary conditions explicitly into the weak form.

By means of Eq. (2.50)-(2.53), the enthalpy functional in Eq. (2.48) is written as

$$\Pi_{\mathrm{D}}^{(\mathrm{Dir})}[\boldsymbol{u},\phi] = \Pi^{\Omega}[\boldsymbol{u},\phi] + \Pi^{\mathrm{Neumann}}[\boldsymbol{u},\phi], \tag{2.54}$$

where

$$\Pi^{\Omega}[\boldsymbol{u},\phi] = \int_\Omega \left(\overline{\psi}^{(\mathrm{Dir})}(\boldsymbol{\varepsilon}(\boldsymbol{u}), \nabla\boldsymbol{\varepsilon}(\boldsymbol{u}), \boldsymbol{E}(\phi)) - \overline{b}_i u_i + \overline{q}\phi \right) \mathrm{d}\Omega, \tag{2.55a}$$

$$\Pi^{\mathrm{Neumann}}[\boldsymbol{u},\phi] = \int_{\partial\Omega_t} -\overline{t}_i u_i \,\mathrm{d}\Gamma + \int_{\partial\Omega_r} -\overline{r}_i \partial^n u_i \,\mathrm{d}\Gamma + \int_{\partial\Omega_w} \overline{w}\phi \,\mathrm{d}\Gamma + \int_{C_j} -\overline{j}_i u_i \,\mathrm{d}s. \tag{2.55b}$$

The equilibrium states $(\boldsymbol{u}^*, \phi^*)$ of the body correspond to the saddle points in the enthalpy

potential fulfilling the following variational principle:

$$(\boldsymbol{u}^*, \phi^*) = \arg \min_{\boldsymbol{u} \in \mathcal{U}_\mathrm{D}} \max_{\phi \in \mathcal{P}_\mathrm{D}} \Pi_\mathrm{D}^{(\mathrm{Dir})}[\boldsymbol{u}, \phi], \tag{2.56}$$

with the functional spaces $\mathcal{U}_\mathrm{D}$ and $\mathcal{P}_\mathrm{D}$ having sufficient regularity and fulfilling the Dirichlet boundary conditions in Eq. (2.53), that is:

$$\mathcal{U}_\mathrm{D} := \{\boldsymbol{u} \in [H^2(\Omega)]^3 \mid \boldsymbol{u} - \overline{\boldsymbol{u}} = \boldsymbol{0} \text{ on } \partial\Omega_u \text{ and on } C_u, \text{ and } \partial^n \boldsymbol{u} - \overline{\boldsymbol{v}} = \boldsymbol{0} \text{ on } \partial\Omega_v\}, \tag{2.57a}$$

$$\mathcal{P}_\mathrm{D} := \{\phi \in H^1(\Omega) \mid \phi - \overline{\phi} = 0 \text{ on } \partial\Omega_\phi\}. \tag{2.57b}$$

The weak form of the problem is found by enforcing $\delta\Pi_\mathrm{D}^{(\mathrm{Dir})} = 0$ for all admissible variations $\delta\boldsymbol{u} \in \mathcal{U}_0$ and $\delta\phi \in \mathcal{P}_0$, with

$$\mathcal{U}_0 := \{\delta\boldsymbol{u} \in [H^2(\Omega)]^3 \mid \delta\boldsymbol{u} = \boldsymbol{0} \text{ on } \partial\Omega_u \text{ and on } C_u, \text{ and } \partial^n \delta\boldsymbol{u} = \boldsymbol{0} \text{ on } \partial\Omega_v\}, \tag{2.58a}$$

$$\mathcal{P}_0 := \{\delta\phi \in H^1(\Omega) \mid \delta\phi = 0 \text{ on } \partial\Omega_\phi\}. \tag{2.58b}$$

The weak form reads: *Find* $(\boldsymbol{u}, \phi) \in \mathcal{U}_D \otimes \mathcal{P}_D$ *such that,* $\forall(\delta\boldsymbol{u}, \delta\phi) \in \mathcal{U}_0 \otimes \mathcal{P}_0$,

$$\begin{aligned}
\delta\Pi_\mathrm{D}^{(\mathrm{Dir})} &\equiv \delta_{\boldsymbol{u}}\Pi_\mathrm{D}^{(\mathrm{Dir})} + \delta_\phi\Pi_\mathrm{D}^{(\mathrm{Dir})} \\
&\equiv \int_\Omega \left(\widehat{\sigma}_{ij}\delta\varepsilon_{ij} + \tilde{\sigma}_{ijk}\delta\varepsilon_{ij,k} - \widehat{D}_l\delta E_l - \overline{b}_i\delta u_i + \overline{q}\delta\phi \right) \mathrm{d}\Omega \\
&\quad + \int_{\partial\Omega_t} -\overline{t}_i\delta u_i \,\mathrm{d}\Gamma + \int_{\partial\Omega_r} -\overline{r}_i\partial^n\delta u_i \,\mathrm{d}\Gamma + \int_{\partial\Omega_w} \overline{w}\delta\phi \,\mathrm{d}\Gamma + \int_{C_j} -\overline{j}_i\delta u_i \,\mathrm{d}s \\
&= 0,
\end{aligned} \tag{2.59}$$

where we use the notation $\delta\boldsymbol{\varepsilon} := \boldsymbol{\varepsilon}(\delta\boldsymbol{u})$, $\delta\nabla\boldsymbol{\varepsilon} := \nabla\boldsymbol{\varepsilon}(\delta\boldsymbol{u})$ and $\delta\boldsymbol{E} := \boldsymbol{E}(\delta\phi)$.
The Cauchy stress $\hat{\boldsymbol{\sigma}}(\boldsymbol{\varepsilon}, \nabla\boldsymbol{\varepsilon}, \boldsymbol{E})$, the double stress $\tilde{\boldsymbol{\sigma}}(\boldsymbol{\varepsilon}, \nabla\boldsymbol{\varepsilon}, \boldsymbol{E})$ and the electric displacement $\hat{\boldsymbol{D}}(\boldsymbol{\varepsilon}, \nabla\boldsymbol{\varepsilon}, \boldsymbol{E})$ in Eq. (2.59) are the conjugate quantities to the strain $\boldsymbol{\varepsilon}$, the strain gradient $\nabla\boldsymbol{\varepsilon}$ and the electric field $\boldsymbol{E}$, respectively, as follows:

$$\widehat{\sigma}_{ij}(\boldsymbol{\varepsilon}, \nabla\boldsymbol{\varepsilon}, \boldsymbol{E}) := \frac{\partial\overline{\psi}^{(\mathrm{Dir})}(\boldsymbol{\varepsilon}, \nabla\boldsymbol{\varepsilon}, \boldsymbol{E})}{\partial\varepsilon_{ij}} = c_{ijkl}\varepsilon_{kl}, \tag{2.60a}$$

$$\tilde{\sigma}_{ijk}(\boldsymbol{\varepsilon}, \nabla\boldsymbol{\varepsilon}, \boldsymbol{E}) := \frac{\partial\overline{\psi}^{(\mathrm{Dir})}(\boldsymbol{\varepsilon}, \nabla\boldsymbol{\varepsilon}, \boldsymbol{E})}{\partial\varepsilon_{ij,k}} = h_{ijklmn}\varepsilon_{lm,n} - \mu_{lijk}E_l, \tag{2.60b}$$

$$\widehat{D}_l(\boldsymbol{\varepsilon}, \nabla\boldsymbol{\varepsilon}, \boldsymbol{E}) := -\frac{\partial\overline{\psi}^{(\mathrm{Dir})}(\boldsymbol{\varepsilon}, \nabla\boldsymbol{\varepsilon}, \boldsymbol{E})}{\partial E_l} = \kappa_{lm}E_m + \mu_{lijk}\varepsilon_{ij,k}. \tag{2.60c}$$

The Euler-Lagrange equations associated with the weak form in Eq. (2.59) and the expressions $\boldsymbol{t}(\boldsymbol{u}, \phi)$, $\boldsymbol{r}(\boldsymbol{u}, \phi)$, $w(\boldsymbol{u}, \phi)$ and $\boldsymbol{j}(\boldsymbol{u}, \phi)$ from the Neumann boundary conditions in Eq. (2.53) are found by integrating Eq. (2.59) by parts twice and making use of the divergence and surface

divergence theorems (Codony *et al.*, 2019). The resulting Euler-Lagrange equations are

$$\begin{cases} \left(\widehat{\sigma}_{ij} - \tilde{\sigma}_{ijk,k}\right)_{,j} + \overline{b}_i = 0 & \text{in } \Omega, \\ \widehat{D}_{l,l} - \overline{q} = 0 & \text{in } \Omega, \end{cases} \tag{2.61}$$

which can be interpreted as a two-way coupling between a fourth-order elliptic PDE for the mechanics and a second-order elliptic PDE for the electrostatics. In view of Eq. (2.61), the definition of the physical stress $\boldsymbol{\sigma}$ arises naturally as

$$\sigma_{ij}(\boldsymbol{u}, \phi) := \widehat{\sigma}_{ij}(\boldsymbol{u}, \phi) - \tilde{\sigma}_{ijk,k}(\boldsymbol{u}, \phi) = c_{ijkl}\varepsilon_{kl} - h_{ijklmn}\varepsilon_{lm,nk} + \mu_{lijk}E_{l,k}. \tag{2.62}$$

The expressions $\boldsymbol{t}(\boldsymbol{u}, \phi)$, $\boldsymbol{r}(\boldsymbol{u}, \phi)$, $w(\boldsymbol{u}, \phi)$ and $\boldsymbol{j}(\boldsymbol{u}, \phi)$ from the Neumann boundary conditions in Eq. (2.53) are

$$t_i(\boldsymbol{u}, \phi) = \left(\widehat{\sigma}_{ij} - \tilde{\sigma}_{ijk,k} - \nabla^S_k \tilde{\sigma}_{ikj}\right) n_j + \tilde{\sigma}_{ijk}\tilde{N}_{jk} \quad \text{on } \partial\Omega, \tag{2.63a}$$

$$r_i(\boldsymbol{u}, \phi) = \tilde{\sigma}_{ijk} n_j n_k \quad \text{on } \partial\Omega, \tag{2.63b}$$

$$w(\boldsymbol{u}, \phi) = -\widehat{D}_l n_l \quad \text{on } \partial\Omega, \tag{2.63c}$$

$$j_i(\boldsymbol{u}, \phi) = \left[\!\left[\tilde{\sigma}_{ijk} m_j n_k\right]\!\right] \quad \text{on } C, \tag{2.63d}$$

where $\nabla^S \cdot$ is the surface divergence operator, $\tilde{\mathbf{N}}$ is the second-order geometry operator (a measure of the curvature of $\partial\Omega$) and $[\![\ ]\!]$ is the jump operator defined on C (we refer to Codony *et al.* (2019) for further details).

Remark 2.1 (*Second order boundary conditions in a FE framework).* In practice, in a FE context, the functional spaces in Eq. (2.57) and (2.58) are approximated by means of a set of linear combinations of basis and test functions. However, $\mathcal{U}_{\mathrm{D}}$ and $\mathcal{U}_0$ are in general difficult to approximate since they require fulfilling second order Dirichlet conditions for the displacement field (i.e. prescribing its normal derivative). The typical approach to overcome this difficulty is considering $\partial\Omega_v = \emptyset$, which implies that only second order *Neumann* boundary conditions are allowed, i.e. $\partial\Omega = \partial\Omega_r$ (Abdollahi *et al.*, 2014, Deng *et al.*, 2017, Ghasemi *et al.*, 2017, Mao *et al.*, 2016, Zhuang *et al.*, 2019). This choice is further justified by the unclear physical interpretation of second order Dirichlet boundary conditions (McBride *et al.*, 2020).

2.2.2.1.b Nitsche's method: Weak boundary conditions

In Section 2.2.2.1.a the functional spaces of the state variables are chosen such that Dirichlet boundary conditions are automatically fulfilled. An alternative to enforce essential boundary conditions without constraining the functional spaces consists on incorporating them into the enthalpy functional, in a way that equilibrium states $(\boldsymbol{u}^*, \phi^*)$ satisfying the corresponding variational principle necessarily fulfill the Dirichlet boundary conditions. We propose here the Nitsche's method (Nitsche, 1971) due to its simple form and convenient numerical properties (i.e. self-consistency, symmetry, optimal error convergence rates and preservation of the

number of degrees of freedom (Fernández-Méndez and Huerta, 2004)) as compared to other alternatives such as the Lagrange multipliers or the penalty methods.

Following Nitsche's approach, the enthalpy functional $\Pi_{\mathrm{D}}^{(\mathrm{Dir})}$ in Eq. (2.54) is modified as

$$\Pi^{(\mathrm{Dir})}[\boldsymbol{u},\phi] = \Pi_{\mathrm{D}}^{(\mathrm{Dir})}[\boldsymbol{u},\phi] + \Pi^{\mathrm{Nitsche}}[\boldsymbol{u},\phi], \tag{2.64}$$

where $\Pi^{\mathrm{Nitsche}}[\boldsymbol{u},\phi]$ acts on the Dirichlet boundaries incorporating essential boundary conditions in Eq. (2.53) weakly as follows:

$$\begin{aligned}\Pi^{\mathrm{Nitsche}}[\boldsymbol{u},\phi] = &\int_{\partial\Omega_u}\left(\frac{1}{2}\beta_u\left(u_i-\overline{u}_i\right)^2-\left(u_i-\overline{u}_i\right)t_i(\boldsymbol{u},\phi)\right)\,\mathrm{d}\Gamma\\ &+\int_{\partial\Omega_v}\left(\frac{1}{2}\beta_v\left(\partial^n u_i-\overline{v}_i\right)^2-\left(\partial^n u_i-\overline{v}_i\right)r_i(\boldsymbol{u},\phi)\right)\,\mathrm{d}\Gamma\\ &+\int_{\partial\Omega_\phi}\left(-\frac{1}{2}\beta_\phi\left(\phi-\overline{\phi}\right)^2+\left(\phi-\overline{\phi}\right)w(\boldsymbol{u},\phi)\right)\,\mathrm{d}\Gamma\\ &+\int_{C_u}\left(\frac{1}{2}\beta_{C_u}\left(u_i-\overline{u}_i\right)^2-\left(u_i-\overline{u}_i\right)j_i(\boldsymbol{u},\phi)\right)\,\mathrm{ds},\end{aligned} \tag{2.65}$$

with the numerical parameters $\beta_u,\beta_v,\beta_\phi,\beta_{C_u}\in\mathbb{R}^+$. The expressions $\boldsymbol{t}(\boldsymbol{u},\phi)$, $\boldsymbol{r}(\boldsymbol{u},\phi)$, $w(\boldsymbol{u},\phi)$ and $\boldsymbol{j}(\boldsymbol{u},\phi)$ are now conjugate to the Dirichlet boundary conditions. The (positive or negative) penalty terms inserted in each boundary integral are quadratic in the Dirichlet boundary conditions, and its only purpose is to ensure equilibrium states $(\boldsymbol{u}^*,\phi^*)$ being, respectively, actual minima and maxima of the energy functional with respect to $\boldsymbol{u}$ and ϕ (Codony *et al.*, 2019).

The variational principle associated to $\Pi^{(\mathrm{Dir})}$ for the equilibrium states $(\boldsymbol{u}^*,\phi^*)$ is

$$(\boldsymbol{u}^*,\phi^*) = \arg\min_{\boldsymbol{u}\in\mathcal{U}}\max_{\phi\in\mathcal{P}}\Pi^{(\mathrm{Dir})}[\boldsymbol{u},\phi], \tag{2.66}$$

where $\mathcal{P} := H^1(\Omega)$, and $\mathcal{U}$ is the space of functions belonging to $\left[H^2(\Omega)\right]^3$ with L^2-integrable third derivatives on the boundary $\partial\Omega_u$, to account for the integrals involving $\boldsymbol{t}(\boldsymbol{u},\phi)$ in Eq. (2.63a). The variational principle in Eq. (2.66) leads to the same Euler-Lagrange equations in Eq. (2.61) and definitions of $\boldsymbol{t}(\boldsymbol{u},\phi)$, $\boldsymbol{r}(\boldsymbol{u},\phi)$, $w(\boldsymbol{u},\phi)$ and $\boldsymbol{j}(\boldsymbol{u},\phi)$ in Eq. (2.63) as the constrained variational principle in Eq. (2.56) (Codony *et al.*, 2019). However, the weak form arising from $\delta\Pi^{(\mathrm{Dir})}=0$ incorporates Dirichlet boundary conditions weakly, and hence the unconstrained functional spaces for the state variables and their corresponding admissible variations coincide, i.e. $\boldsymbol{u},\delta\boldsymbol{u}\in\mathcal{U}$ and $\phi,\delta\phi\in\mathcal{P}$.

The weak form reads: *Find* $(\boldsymbol{u}, \phi) \in \mathcal{U} \otimes \mathcal{P}$ *such that,* $\forall (\delta\boldsymbol{u}, \delta\phi) \in \mathcal{U} \otimes \mathcal{P}$,

$$
\begin{aligned}
\delta\Pi^{(\mathrm{Dir})} &\equiv \delta_{\boldsymbol{u}}\Pi^{(\mathrm{Dir})} + \delta_{\phi}\Pi^{(\mathrm{Dir})} \\
&\equiv \int_{\Omega} \left(\widehat{\sigma}_{ij}\delta\varepsilon_{ij} + \tilde{\sigma}_{ijk}\delta\varepsilon_{ij,k} - \widehat{D}_l\delta E_l - \overline{b}_i\delta u_i + \overline{q}\delta\phi \right) \mathrm{d}\Omega \\
&\quad + \int_{\partial\Omega_t} -\overline{t}_i\delta u_i \,\mathrm{d}\Gamma + \int_{\partial\Omega_u} \Big((u_i - \overline{u}_i)\left(\beta_u\delta u_i - \delta t_i\right) - t_i\delta u_i \Big) \,\mathrm{d}\Gamma \\
&\quad + \int_{\partial\Omega_r} -\overline{r}_i\partial^n\delta u_i \,\mathrm{d}\Gamma + \int_{\partial\Omega_v} \Big((\partial^n u_i - \overline{v}_i)\left(\beta_v\partial^n\delta u_i - \delta r_i\right) - r_i\partial^n\delta u_i \Big) \,\mathrm{d}\Gamma \\
&\quad + \int_{\partial\Omega_w} \overline{w}\delta\phi \,\mathrm{d}\Gamma + \int_{\partial\Omega_\phi} \Big(-\left(\phi - \overline{\phi}\right)\left(\beta_\phi\delta\phi - \delta w\right) + w\delta\phi \Big) \,\mathrm{d}\Gamma \\
&\quad + \int_{C_j} -\overline{j}_i\delta u_i \,\mathrm{d}s + \int_{C_u} \Big((u_i - \overline{u}_i)\left(\beta_u\delta u_i - \delta j_i\right) - j_i\delta u_i \Big) \\
&= 0,
\end{aligned}
\tag{2.67}
$$

with $\delta\boldsymbol{t} := \boldsymbol{t}(\delta\boldsymbol{u}, \delta\phi)$, $\delta\boldsymbol{r} := \boldsymbol{r}(\delta\boldsymbol{u}, \delta\phi)$, $\delta w := w(\delta\boldsymbol{u}, \delta\phi)$ and $\delta\boldsymbol{j} := \boldsymbol{j}(\delta\boldsymbol{u}, \delta\phi)$.

Remark 2.2 (*Value of the penalty parameters in the discrete case).* Note that Eq. (2.67) is self-consistent for any value of the penalty parameters $\beta_u, \beta_v, \beta_{C_u}, \beta_\phi$. However, in the discrete space of numerical approximation of the state variables, they must be large enough to ensure stability, i.e. maintain the min-max nature of the variational principle in Eq. (2.66). Arbitrarily large values are not suitable since the conditioning of the linear system is deteriorated. The analytical derivation of lower bounds of the penalty parameters can be found in Codony *et al.* (2019) for the discrete case, but moderate values of the penalty parameters are typically enough to ensure convergence and enforce boundary conditions properly (Codony *et al.*, 2019, Fernández-Méndez and Huerta, 2004, Schillinger *et al.*, 2016). Thus, the explicit computation of stability lower bounds can be avoided by writing the penalty parameters in terms of a *dimensionless* parameter $\zeta \in \mathbb{R}^+$ as follows:

$$
\beta_u = \frac{Y}{h}\zeta, \quad \beta_v = \frac{\left(\ell_{\mathrm{mech}}^2 + \ell_\mu^2\right) Y}{h}\zeta, \quad \beta_{C_u} = \frac{\left(\ell_{\mathrm{mech}}^2 + \ell_\mu^2\right) Y}{h^2}\zeta, \quad \beta_\phi = \frac{\epsilon}{h}\zeta,
\tag{2.68}
$$

where h denotes the characteristic length of the discretization (typically, the mesh size), Y is the Young modulus, ϵ is the electric permittivity, ℓ_{mech} is the mechanical length scale, $\ell_\mu \sim \mu/\sqrt{Y\epsilon}$ is the flexoelectric length scale and μ is the flexoelectric tensor (see Appendix A for further details on material parameters). In the computations in this manuscript, the constant value $\zeta = 100$ is large enough to provide stable results, regardless of the (unfitted) discretization of Ω, as further commented in Chapter 3.

2.2.2.2 Lifshitz-invariant flexoelectricity form

According to Eq. (2.17), the Lifshitz-invariant flexoelectric enthalpy density is stated as

$$\begin{aligned}\overline{\psi}^{(\mathrm{Lif})}(\boldsymbol{\varepsilon}, \nabla\boldsymbol{\varepsilon}, \boldsymbol{E}, \nabla\boldsymbol{E}) \coloneqq & \frac{1}{2}\varepsilon_{ij}c_{ijkl}\varepsilon_{kl} + \frac{1}{2}\varepsilon_{ij,k}h_{ijklmn}\varepsilon_{lm,n} - \frac{1}{2}E_l\kappa_{lm}E_m \\ & - \frac{1}{2}E_{i,j}M_{ijkl}E_{k,l} - \frac{1}{2}\mu_{lijk}\left(E_l\varepsilon_{ij,k} - E_{l,k}\varepsilon_{ij}\right). \end{aligned} \tag{2.69}$$

The admissible external sources of work are the ones corresponding to the direct flexoelectricity form in Eq. (2.51), plus the high order dielectric quantities $\wp$ (electric charge density per unit length) and $\mathfrak{r}$ (double charge density, i.e. charge moment per unit area), analogous to $\boldsymbol{j}$ and $\boldsymbol{r}$ from mechanics:

$$\mathcal{W}^{\Omega}(\boldsymbol{u}, \phi) \coloneqq -\overline{b}_i u_i + \overline{q}\phi, \tag{2.70a}$$

$$\mathcal{W}^{\partial\Omega}(\boldsymbol{u}, \phi) \coloneqq -t_i u_i - r_i\partial^n u_i + w\phi + \mathfrak{r}\partial^n\phi, \tag{2.70b}$$

$$\mathcal{W}^{C}(\boldsymbol{u}, \phi) \coloneqq -j_i u_i + \wp\phi. \tag{2.70c}$$

Accordingly, the boundary of the domain $\partial\Omega$ is split into several disjoint Dirichlet and Neumann boundaries as

$$\partial\Omega = \partial\Omega_u \cup \partial\Omega_t = \partial\Omega_v \cup \partial\Omega_r = \partial\Omega_\phi \cup \partial\Omega_w = \partial\Omega_\varphi \cup \partial\Omega_{\mathfrak{r}}, \tag{2.71}$$

where the high-order nature of the dielectrics leads to the definition of the Dirichlet $\partial\Omega_\varphi$ and Neumann $\partial\Omega_{\mathfrak{r}}$ boundaries corresponding to prescribed values for the normal derivative of the electric potential and its conjugate, i.e. the double charge density $\mathfrak{r}$. The edges C of $\partial\Omega$ are also split into

$$C = C_u \cup C_j = C_\phi \cup C_\wp, \tag{2.72}$$

corresponding to the Dirichlet and Neumann edge partitions, respectively, where either the electric potential ϕ or the electric charge density per unit length $\wp$ are prescribed.

The corresponding boundary and edge conditions are mathematically written as

$$\boldsymbol{u} - \overline{\boldsymbol{u}} = \boldsymbol{0} \quad \text{on } \partial\Omega_u, \qquad \boldsymbol{t}(\boldsymbol{u}, \phi) - \overline{\boldsymbol{t}} = \boldsymbol{0} \quad \text{on } \partial\Omega_t; \tag{2.73a}$$

$$\boldsymbol{u} - \overline{\boldsymbol{u}} = \boldsymbol{0} \quad \text{on } C_u, \qquad \boldsymbol{j}(\boldsymbol{u}, \phi) - \overline{\boldsymbol{j}} = \boldsymbol{0} \quad \text{on } C_j; \tag{2.73b}$$

$$\partial^n(\boldsymbol{u}) - \overline{\boldsymbol{v}} = \boldsymbol{0} \quad \text{on } \partial\Omega_v, \qquad \boldsymbol{r}(\boldsymbol{u}, \phi) - \overline{\boldsymbol{r}} = \boldsymbol{0} \quad \text{on } \partial\Omega_r; \tag{2.73c}$$

$$\phi - \overline{\phi} = 0 \quad \text{on } \partial\Omega_\phi, \qquad w(\boldsymbol{u}, \phi) - \overline{w} = 0 \quad \text{on } \partial\Omega_w; \tag{2.73d}$$

$$\phi - \overline{\phi} = 0 \quad \text{on } C_\phi, \qquad \wp(\boldsymbol{u}, \phi) - \overline{\wp} = 0 \quad \text{on } C_\wp; \tag{2.73e}$$

$$\partial^n(\phi) - \overline{\varphi} = \boldsymbol{0} \quad \text{on } \partial\Omega_\varphi, \qquad \mathfrak{r}(\boldsymbol{u}, \phi) - \overline{\mathfrak{r}} = \boldsymbol{0} \quad \text{on } \partial\Omega_{\mathfrak{r}}; \tag{2.73f}$$

where $\overline{\varphi}$, $\overline{\wp}$ and $\overline{\mathfrak{r}}$ are the prescribed values of φ, $\wp$ and $\mathfrak{r}$ on the corresponding boundaries.

Analogously to the direct flexoelectricity form, the Neumann expressions $\boldsymbol{t}(\boldsymbol{u},\phi)$, $\boldsymbol{j}(\boldsymbol{u},\phi)$, $\boldsymbol{r}(\boldsymbol{u},\phi)$, $w(\boldsymbol{u},\phi)$, $\wp(\boldsymbol{u},\phi)$ and $\mathfrak{r}(\boldsymbol{u},\phi)$ will be derived later as a result of the variational principle in Eq. (2.76).

2.2.2.2.a Standard framework

By means of Eq. (2.69)-(2.73), the enthalpy functional in Eq. (2.48) is written as

$$\Pi_{\mathrm{D}}^{(\mathrm{Lif})}[\boldsymbol{u},\phi] = \Pi^{\Omega}[\boldsymbol{u},\phi] + \Pi^{\mathrm{Neumann}}[\boldsymbol{u},\phi], \tag{2.74}$$

where

$$\Pi^{\Omega}[\boldsymbol{u},\phi] = \int_{\Omega} \left(\overline{\psi}^{(\mathrm{Lif})}(\boldsymbol{\varepsilon}(\boldsymbol{u}), \nabla\boldsymbol{\varepsilon}(\boldsymbol{u}), \boldsymbol{E}(\phi), \nabla\boldsymbol{E}(\phi)) - \overline{b}_i u_i + \overline{q}\phi \right) \mathrm{d}\Omega, \tag{2.75a}$$

$$\begin{aligned}\Pi^{\mathrm{Neumann}}[\boldsymbol{u},\phi] = &\int_{\partial\Omega_t} -\overline{t}_i u_i \,\mathrm{d}\Gamma + \int_{\partial\Omega_r} -\overline{r}_i \partial^n u_i \,\mathrm{d}\Gamma + \int_{C_j} -\overline{j}_i u_i \,\mathrm{ds} \\ &+ \int_{\partial\Omega_w} \overline{w}\phi \,\mathrm{d}\Gamma + \int_{\partial\Omega_{\mathfrak{r}}} \overline{\mathfrak{r}}\partial^n\phi \,\mathrm{d}\Gamma + \int_{C_\wp} \overline{\wp}\phi \,\mathrm{ds}.\end{aligned} \tag{2.75b}$$

The equilibrium states $(\boldsymbol{u}^*,\phi^*)$ of the body correspond to the saddle points in the enthalpy potential fulfilling the following variational principle:

$$(\boldsymbol{u}^*,\phi^*) = \arg \min_{\boldsymbol{u}\in\mathcal{U}_{\mathrm{D}}} \max_{\phi\in\mathcal{P}_{\mathrm{D}}} \Pi_{\mathrm{D}}^{(\mathrm{Lif})}[\boldsymbol{u},\phi], \tag{2.76}$$

with the functional spaces $\mathcal{U}_{\mathrm{D}}$ and $\mathcal{P}_{\mathrm{D}}$ having sufficient regularity and fulfilling Dirichlet boundary conditions in Eq. (2.73), that is:

$$\mathcal{U}_{\mathrm{D}} := \{\boldsymbol{u} \in [H^2(\Omega)]^3 \mid \boldsymbol{u} - \overline{\boldsymbol{u}} = \boldsymbol{0} \text{ on } \partial\Omega_u \text{ and on } C_u, \text{ and } \partial^n\boldsymbol{u} - \overline{\boldsymbol{v}} = \boldsymbol{0} \text{ on } \partial\Omega_v\}, \tag{2.77a}$$

$$\mathcal{P}_{\mathrm{D}} := \{\phi \in H^2(\Omega) \mid \phi - \overline{\phi} = 0 \text{ on } \partial\Omega_\phi \text{ and on } C_\phi, \text{ and } \partial^n\phi - \overline{\varphi} = \boldsymbol{0} \text{ on } \partial\Omega_\varphi\}. \tag{2.77b}$$

The weak form of the problem is found by enforcing $\delta\Pi_{\mathrm{D}}^{(\mathrm{Lif})} = 0$ for all admissible variations $\delta\boldsymbol{u} \in \mathcal{U}_0$ and $\delta\phi \in \mathcal{P}_0$, with

$$\mathcal{U}_0 := \{\delta\boldsymbol{u} \in [H^2(\Omega)]^3 \mid \delta\boldsymbol{u} = \boldsymbol{0} \text{ on } \partial\Omega_u \text{ and on } C_u, \text{ and } \partial^n\delta\boldsymbol{u} = \boldsymbol{0} \text{ on } \partial\Omega_v\}, \tag{2.78a}$$

$$\mathcal{P}_0 := \{\delta\phi \in H^2(\Omega) \mid \delta\phi = 0 \text{ on } \partial\Omega_\phi \text{ and on } C_\phi, \text{ and } \partial^n\delta\phi = \boldsymbol{0} \text{ on } \partial\Omega_\varphi\}. \tag{2.78b}$$

The weak form reads: *Find* $(\boldsymbol{u},\phi)\in\mathcal{U}_D\otimes\mathcal{P}_D$ *such that,* $\forall(\delta\boldsymbol{u},\delta\phi)\in\mathcal{U}_0\otimes\mathcal{P}_0$,

$$\begin{aligned}\delta\Pi_{\mathrm{D}}^{(\mathrm{Lif})} &\equiv \delta_{\boldsymbol{u}}\Pi_{\mathrm{D}}^{(\mathrm{Lif})}+\delta_{\phi}\Pi_{\mathrm{D}}^{(\mathrm{Lif})}\\ &\equiv \int_{\Omega}\left(\widehat{\sigma}_{ij}\delta\varepsilon_{ij}+\widetilde{\sigma}_{ijk}\delta\varepsilon_{ij,k}-\widehat{D}_{l}\delta E_{l}-\widetilde{D}_{lm}\delta E_{l,m}-\overline{b}_{i}\delta u_{i}+\overline{q}\delta\phi\right)\mathrm{d}\Omega\\ &\quad+\int_{\partial\Omega_t}-\overline{t}_{i}\delta u_{i}\,\mathrm{d}\Gamma+\int_{\partial\Omega_r}-\overline{r}_{i}\partial^{n}\delta u_{i}\,\mathrm{d}\Gamma+\int_{C_j}-\overline{j}_{i}\delta u_{i}\,\mathrm{d}s\\ &\quad+\int_{\partial\Omega_w}\overline{w}\delta\phi\,\mathrm{d}\Gamma+\int_{\partial\Omega_{\mathfrak{r}}}\overline{\mathfrak{r}}\partial^{n}\delta\phi\,\mathrm{d}\Gamma+\int_{C_{\wp}}\overline{\wp}\delta\phi\,\mathrm{d}s\\ &=0,\end{aligned}\tag{2.79}$$

with $\delta\nabla\boldsymbol{E}:=\nabla\boldsymbol{E}(\delta\phi)$.
The Cauchy stress $\widehat{\boldsymbol{\sigma}}(\boldsymbol{\varepsilon},\nabla\boldsymbol{\varepsilon},\boldsymbol{E},\nabla\boldsymbol{E})$, the double stress $\widetilde{\boldsymbol{\sigma}}(\boldsymbol{\varepsilon},\nabla\boldsymbol{\varepsilon},\boldsymbol{E},\nabla\boldsymbol{E})$, the electric displacement $\widehat{\boldsymbol{D}}(\boldsymbol{\varepsilon},\nabla\boldsymbol{\varepsilon},\boldsymbol{E},\nabla\boldsymbol{E})$ and the double electric displacement $\widetilde{\boldsymbol{D}}(\boldsymbol{\varepsilon},\nabla\boldsymbol{\varepsilon},\boldsymbol{E},\nabla\boldsymbol{E})$ in Eq. (2.79) are the conjugate quantities to the strain $\boldsymbol{\varepsilon}$, the strain gradient $\nabla\boldsymbol{\varepsilon}$, the electric field $\boldsymbol{E}$ and the electric field gradient $\nabla\boldsymbol{E}$, respectively, as follows:

$$\widehat{\sigma}_{ij}(\boldsymbol{\varepsilon},\nabla\boldsymbol{\varepsilon},\boldsymbol{E},\nabla\boldsymbol{E}):=\frac{\partial\overline{\psi}^{(\mathrm{Lif})}(\boldsymbol{\varepsilon},\nabla\boldsymbol{\varepsilon},\boldsymbol{E},\nabla\boldsymbol{E})}{\partial\varepsilon_{ij}}=c_{ijkl}\varepsilon_{kl}+\frac{1}{2}\mu_{lijk}E_{l,k},\tag{2.80a}$$

$$\widetilde{\sigma}_{ijk}(\boldsymbol{\varepsilon},\nabla\boldsymbol{\varepsilon},\boldsymbol{E},\nabla\boldsymbol{E}):=\frac{\partial\overline{\psi}^{(\mathrm{Lif})}(\boldsymbol{\varepsilon},\nabla\boldsymbol{\varepsilon},\boldsymbol{E},\nabla\boldsymbol{E})}{\partial\varepsilon_{ij,k}}=h_{ijklmn}\varepsilon_{lm,n}-\frac{1}{2}\mu_{lijk}E_{l},\tag{2.80b}$$

$$\widehat{D}_{l}(\boldsymbol{\varepsilon},\nabla\boldsymbol{\varepsilon},\boldsymbol{E},\nabla\boldsymbol{E}):=-\frac{\partial\overline{\psi}^{(\mathrm{Lif})}(\boldsymbol{\varepsilon},\nabla\boldsymbol{\varepsilon},\boldsymbol{E},\nabla\boldsymbol{E})}{\partial E_{l}}=\kappa_{lm}E_{m}+\frac{1}{2}\mu_{lijk}\varepsilon_{ij,k},\tag{2.80c}$$

$$\widetilde{D}_{lk}(\boldsymbol{\varepsilon},\nabla\boldsymbol{\varepsilon},\boldsymbol{E},\nabla\boldsymbol{E}):=-\frac{\partial\overline{\psi}^{(\mathrm{Lif})}(\boldsymbol{\varepsilon},\nabla\boldsymbol{\varepsilon},\boldsymbol{E},\nabla\boldsymbol{E})}{\partial E_{l,k}}=M_{ijlk}E_{i,j}-\frac{1}{2}\mu_{lijk}\varepsilon_{ij}.\tag{2.80d}$$

The Euler-Lagrange equations associated with the weak form in Eq. (2.79) and the expressions $\boldsymbol{t}(\boldsymbol{u},\phi)$, $\boldsymbol{j}(\boldsymbol{u},\phi)$, $\boldsymbol{r}(\boldsymbol{u},\phi)$, $w(\boldsymbol{u},\phi)$, $\wp(\boldsymbol{u},\phi)$ and $\mathfrak{r}(\boldsymbol{u},\phi)$ from the Neumann boundary conditions in Eq. (2.73) are found by integrating Eq. (2.79) by parts twice and making use of the divergence and surface divergence theorems, analogously to the direct flexoelectricity form, but now for both mechanics and dielectrics. The resulting Euler-Lagrange equations are

$$\begin{cases}\left(\widehat{\sigma}_{ij}-\widetilde{\sigma}_{ijk,k}\right)_{,j}+\overline{b}_{i}=0 & \text{in }\Omega,\\ \left(\widehat{D}_{l}-\widetilde{D}_{lk,k}\right)_{,l}-\overline{q}=0 & \text{in }\Omega,\end{cases}\tag{2.81}$$

which can be interpreted as a two-way coupling between two fourth-order elliptic PDEs arising from mechanics and electrostatics.

The expressions $\boldsymbol{t}(\boldsymbol{u},\phi)$, $\boldsymbol{j}(\boldsymbol{u},\phi)$, $\boldsymbol{r}(\boldsymbol{u},\phi)$, $w(\boldsymbol{u},\phi)$, $\wp(\boldsymbol{u},\phi)$ and $\mathfrak{r}(\boldsymbol{u},\phi)$ from the Neumann

boundary conditions in Eq. (2.73) are

$$t_i(\boldsymbol{u},\phi) = \left(\widehat{\sigma}_{ij} - \tilde{\sigma}_{ijk,k} - \nabla_k^S \tilde{\sigma}_{ikj}\right) n_j + \tilde{\sigma}_{ijk}\tilde{N}_{jk} \quad \text{on } \partial\Omega, \tag{2.82a}$$

$$j_i(\boldsymbol{u},\phi) = \left[\!\left[\tilde{\sigma}_{ijk} m_j n_k\right]\!\right] \quad \text{on } C, \tag{2.82b}$$

$$r_i(\boldsymbol{u},\phi) = \tilde{\sigma}_{ijk} n_j n_k \quad \text{on } \partial\Omega, \tag{2.82c}$$

$$w(\boldsymbol{u},\phi) = -\left(\widehat{D}_l - \widetilde{D}_{lk,k} - \nabla_k^S \widetilde{D}_{kl}\right) n_l - \widetilde{D}_{jk}\tilde{N}_{jk} \quad \text{on } \partial\Omega, \tag{2.82d}$$

$$\wp(\boldsymbol{u},\phi) = -\left[\!\left[\widetilde{D}_{jk} m_j n_k\right]\!\right] \quad \text{on } C, \tag{2.82e}$$

$$\mathfrak{r}(\boldsymbol{u},\phi) = -\widetilde{D}_{jk} n_j n_k \quad \text{on } \partial\Omega. \tag{2.82f}$$

Note that the Lifshitz flexoelectricity strong form in Eq. (2.81) reduces to the direct flexoelectricity strong form in Eq. (2.61) by vanishing the gradient dielectricity material tensor $\mathbf{M}$. However, the boundary terms in Eq. (2.82) and Eq. (2.63) remain different, since the expressions for $\hat{\boldsymbol{\sigma}}$, $\tilde{\boldsymbol{\sigma}}$, $\hat{\boldsymbol{D}}$ and $\tilde{\boldsymbol{D}}$ in Eq. (2.80) and (2.60) differ.

Remark 2.3 (*Second order boundary conditions in a FE framework).* Analogously to Remark 2.1, due to the unclear physical interpretation of second order dielectric Dirichlet boundary conditions, it makes sense to consider only second order *Neumann* boundary conditions, i.e. $\partial\Omega_\varphi = \emptyset$, hence $\partial\Omega = \partial\Omega_\mathfrak{r}$. This choice also facilitates the construction of the functional spaces for the test and shape functions. Moreover, typically second order *homogeneous* Neumann boundary conditions are considered, which further reduces the corresponding implementation.

2.2.2.2.b Nitsche's method

The enthalpy functional $\Pi_{\mathrm{D}}^{(\mathrm{Lif})}$ in Eq. (2.74) is modified as

$$\Pi^{(\mathrm{Lif})}[\boldsymbol{u},\phi] = \Pi_{\mathrm{D}}^{(\mathrm{Lif})}[\boldsymbol{u},\phi] + \Pi^{\mathrm{Nitsche}}[\boldsymbol{u},\phi], \tag{2.83}$$

where $\Pi^{\text{Nitsche}}[\boldsymbol{u}, \phi]$ acts on the Dirichlet boundaries incorporating essential boundary conditions in Eq. (2.73) weakly, analogously to Eq. (2.65):

$$\begin{aligned}
\Pi^{\text{Nitsche}}[\boldsymbol{u}, \phi] = & \int_{\partial\Omega_u} \left(\frac{1}{2}\beta_u \Big(u_i - \overline{u}_i \Big)^2 - \Big(u_i - \overline{u}_i \Big) t_i(\boldsymbol{u}, \phi) \right) \mathrm{d}\Gamma \\
& + \int_{\partial\Omega_v} \left(\frac{1}{2}\beta_v \Big(\partial^n u_i - \overline{v}_i \Big)^2 - \Big(\partial^n u_i - \overline{v}_i \Big) r_i(\boldsymbol{u}, \phi) \right) \mathrm{d}\Gamma \\
& + \int_{C_u} \left(\frac{1}{2}\beta_{C_u} \Big(u_i - \overline{u}_i \Big)^2 - \Big(u_i - \overline{u}_i \Big) j_i(\boldsymbol{u}, \phi) \right) \mathrm{ds} \\
& + \int_{\partial\Omega_\phi} \left(-\frac{1}{2}\beta_\phi \Big(\phi - \overline{\phi} \Big)^2 + \Big(\phi - \overline{\phi} \Big) w(\boldsymbol{u}, \phi) \right) \mathrm{d}\Gamma \\
& + \int_{\partial\Omega_\varphi} \left(-\frac{1}{2}\beta_\varphi \Big(\partial^n \phi - \overline{\varphi} \Big)^2 + \Big(\partial^n \phi - \overline{\varphi} \Big) \mathfrak{r}(\boldsymbol{u}, \phi) \right) \mathrm{d}\Gamma \\
& + \int_{C_u} \left(-\frac{1}{2}\beta_{C_\phi} \Big(\phi - \overline{\phi} \Big)^2 + \Big(\phi - \overline{\phi} \Big) \wp(\boldsymbol{u}, \phi) \right) \mathrm{ds},
\end{aligned} \tag{2.84}$$

with the numerical parameters $\beta_u, \beta_v, \beta_{C_u}, \beta_\phi, \beta_\varphi, \beta_{C_\phi} \in \mathbb{R}^+$.

The variational principle associated to $\Pi^{(\text{Lif})}$ for the equilibrium states $(\boldsymbol{u}^*, \phi^*)$ is

$$(\boldsymbol{u}^*, \phi^*) = \arg \min_{\boldsymbol{u} \in \mathcal{U}} \max_{\phi \in \mathcal{P}} \Pi^{(\text{Lif})}[\boldsymbol{u}, \phi], \tag{2.85}$$

where $\mathcal{P}$ and $\mathcal{U}$ are the spaces of functions belonging to $\left[H^2(\Omega)\right]^q$ with L^2-integrable third derivatives on the boundary $\partial\Omega_u$ and $\partial\Omega_\phi$ respectively, where q represents the number of dimensions of the state variables, i.e. $q = 1$ in the case of $\mathcal{P}$, and $q = 3$ for $\mathcal{U}$. The variational principle in Eq. (2.85) leads to the same Euler-Lagrange equations in Eq. (2.81) and definitions of Neumann terms in Eq. (2.82) as the constrained variational principle in Eq. (2.76).

Finally, the Nitsche's weak form of the Lifshitz flexoelectric boundary value problem reads:

Find $(\boldsymbol{u}, \phi) \in \mathcal{U} \otimes \mathcal{P}$ *such that,* $\forall (\delta\boldsymbol{u}, \delta\phi) \in \mathcal{U} \otimes \mathcal{P}$,

$$
\begin{aligned}
\delta\Pi^{(\mathrm{Lif})} &\equiv \delta_{\boldsymbol{u}}\Pi^{(\mathrm{Lif})} + \delta_{\phi}\Pi^{(\mathrm{Lif})} \\
&\equiv \int_{\Omega} \left(\widehat{\sigma}_{ij}\delta\varepsilon_{ij} + \widetilde{\sigma}_{ijk}\delta\varepsilon_{ij,k} - \widehat{D}_{l}\delta E_{l} - \widetilde{D}_{lm}\delta E_{l,m} - \overline{b}_{i}\delta u_{i} + \overline{q}\delta\phi \right) \mathrm{d}\Omega \\
&\quad + \int_{\partial\Omega_t} -\overline{t}_{i}\delta u_{i}\,\mathrm{d}\Gamma + \int_{\partial\Omega_u} \Big((u_i - \overline{u}_i)\left(\beta_u \delta u_i - \delta t_i\right) - t_i \delta u_i \Big)\,\mathrm{d}\Gamma \\
&\quad + \int_{\partial\Omega_r} -\overline{r}_{i}\partial^{n}\delta u_{i}\,\mathrm{d}\Gamma + \int_{\partial\Omega_v} \Big((\partial^n u_i - \overline{v}_i)\left(\beta_v \partial^n \delta u_i - \delta r_i\right) - r_i \partial^n \delta u_i \Big)\,\mathrm{d}\Gamma \\
&\quad + \int_{C_j} -\overline{j}_{i}\delta u_{i}\,\mathrm{d}s + \int_{C_u} \Big((u_i - \overline{u}_i)\left(\beta_{C_u} \delta u_i - \delta j_i\right) - j_i \delta u_i \Big) \\
&\quad + \int_{\partial\Omega_w} \overline{w}\delta\phi\,\mathrm{d}\Gamma + \int_{\partial\Omega_\phi} \Big(-\left(\phi - \overline{\phi}\right)\left(\beta_\phi \delta\phi - \delta w\right) + w\delta\phi \Big)\,\mathrm{d}\Gamma \\
&\quad + \int_{\partial\Omega_{\mathfrak{r}}} \overline{\mathfrak{r}}\partial^{n}\delta\phi\,\mathrm{d}\Gamma + \int_{\partial\Omega_\varphi} \Big(-(\partial^n\phi - \overline{\varphi})\left(\beta_\varphi \partial^n\delta\phi - \delta\mathfrak{r}\right) + \mathfrak{r}\partial^n\delta\phi \Big)\,\mathrm{d}\Gamma \\
&\quad + \int_{C_{\wp}} \overline{\wp}\delta\phi\,\mathrm{d}s + \int_{C_\phi} \Big(-\left(\phi - \overline{\phi}\right)\left(\beta_{C_\phi}\delta\phi - \delta\wp\right) + \wp\delta\phi \Big) \\
&= 0,
\end{aligned}
\tag{2.86}
$$

with $\delta\mathfrak{r} := \mathfrak{r}(\delta\boldsymbol{u}, \delta\phi)$ and $\delta\wp := \wp(\delta\boldsymbol{u}, \delta\phi)$.

Remark 2.4 (*Value of the penalty parameters in the discrete case).* Analogously to Remark 2.2, the penalty parameters $\beta_\varphi, \beta_{C_\phi}$ introduced in this Section can be written in terms of the dimensionless parameter $\zeta \in \mathbb{R}^+$ as

$$
\beta_\varphi = \frac{\left(\ell_{\mathrm{elec}}^2 + \ell_\mu^2\right)\epsilon}{h}\zeta, \quad \beta_{C_\phi} = \frac{\left(\ell_{\mathrm{elec}}^2 + \ell_\mu^2\right)\epsilon}{h^2}\zeta,
\tag{2.87}
$$

where ℓ_{elec} is the dielectric length scale, cf. Appendix A.

In the case of flexoelectricity, as in other related high-order problems, the lack of physical understanding of the boundary conditions hinders the choice of appropriate physically-based null-Lagrangians, and other criteria such as conveniece or simplicity are used. In Section 2.2.2.3, the boundary value problems resulting from these two formulations are compared. This insight will be used to rationally derive appropriate null Lagrangians for flexoelectricity.

2.2.2.3 Comparison of both models

As pointed out in Section 2.1.1, the Lifshitz-invariant and direct flexoelectricity boundary value problems are not equivalent, even though their associated Euler-Lagrange equations coincide since the definition of boundary terms (e.g. tractions and surface charges) differ, cf. Eq. (2.82) and Eq. (2.63). Consequently, when solving specific boundary value problems, a traction-free or charge-free-surface boundary conditions have different meaning in each formulation and

thus the resulting physical and mathematical problems are different. The relation between the resulting boundary value problems and its implications on the modeled physics has not been addressed yet.

Here, the direct and Lifshitz-invariant flexoelectricity models are compared in different (2D plane strain) standard benchmarks, namely *(i)* the cantilever beam bending and *(ii)* the cantilever beam actuation. The problems are numerically solved by means of the immersed boundary B-spline method, detailed in Chapter 3. Some of the results corresponding to the Direct flexoelectricity form were already presented in Codony *et al.* (2019), whereas the Lifshitz-invariant flexoelectricity results are yet to be published. To the best author's knowledge, Lifshitz-invariant flexoelectricity benchmarks had never been reported before within the computational flexoelectricity community.

In both experiments we consider a cantilever of length $L = 8\mu m$ and thickness $H = 0.4\mu m$. The material properties are simple enough to isolate the transversal flexoelectric effect, i.e. a Young modulus $Y = 100$ GPa, electric permittivity $\epsilon = 11$ nC/Vm and transversal flexoelectric coefficient $\mu_T = 1$ μC/m. The other material parameters are set to 0. For a complete description of material tensors, we refer to Appendix A.1. In each case, free surfaces are assumed to be free of tractions and surface charges, with the definition of tractions and surface charges resulting in each model.

2.2.2.3.a Cantilever bending

Cantilever bending is the most well-known benchmark for flexoelectricity, widely used by experimentalists to capture the transversal flexoelectric effect (Baskaran *et al.*, 2012, Chu and Salem, 2012, Ma and Cross, 2002, 2005, 2006). It has been also studied numerically (Abdollahi *et al.*, 2014, Codony *et al.*, 2019, Zhuang *et al.*, 2020) and analytically (Majdoub *et al.*, 2009, 2008).

In this experiment the left tip is clamped and a vertical force $F = -1\mu N/\mu m$ is applied on the top right corner. The right tip is electrically grounded and the other boundaries are free, which corresponds to open-circuit electrical boundary conditions (Fig. 2.3a). The transversal flexoelectric effect is triggered due to the mechanically-induced gradient of axial strains along each beam cross section.

The results are shown in Fig. 2.3. Indeed, Direct and Lifshitz-invariant flexoelectric formulations lead to different electromechanical responses. Two main differences are pointed out next. Firstly, the mechanical results are quite similar. The axial strains vary linearly along the cross sections of the bent beam in both cases (Fig. 2.3c), as expected. However, the flexoelectricity-induced stiffening of the beam (Codony *et al.*, 2020b) is different in each case. Comparing the maximum deflection of the Direct-flexoelectric beam (0.30 μm) and the Lifshitz-invariant-flexoelectric beam (0.24 μm) with respect to a standard elastic one (0.32 μm), it becomes apparent that the effective stiffness is increased around 7% in the former and a 33% in the latter.

Nevertheless, the most interesting difference arises in the electrical response, as shown in

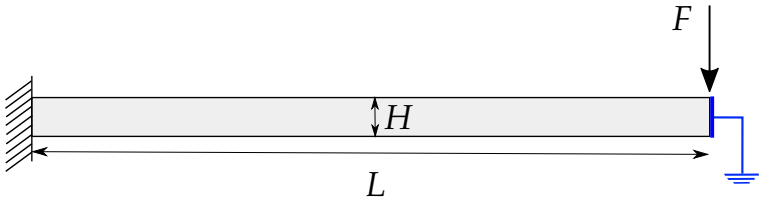

(a) Geometry and boundary conditions.

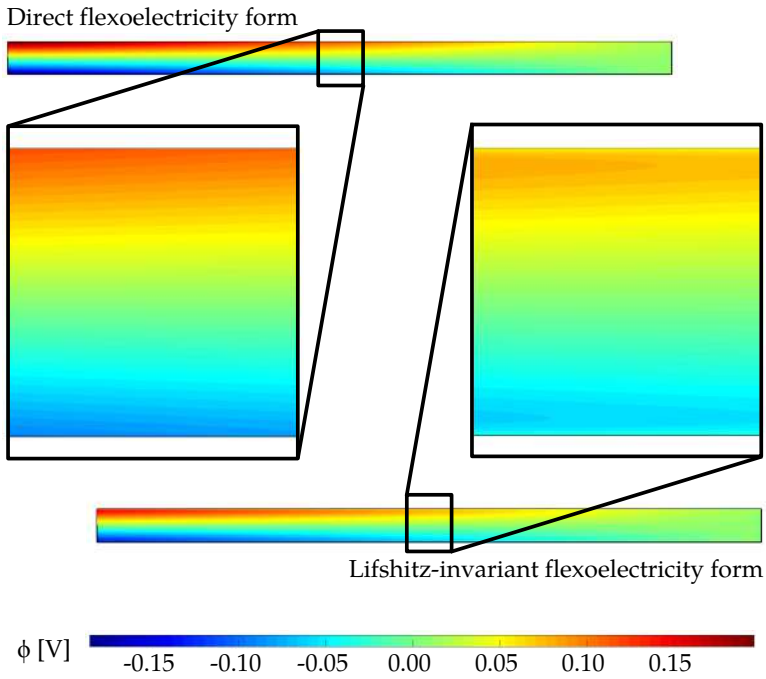

(b) Electric potential distribution within the beams.

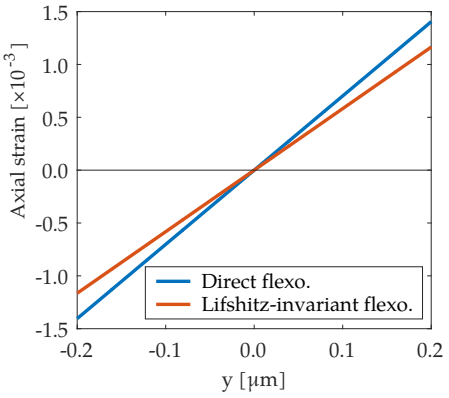

(c) Axial strains at the cross section $x = L/2$.

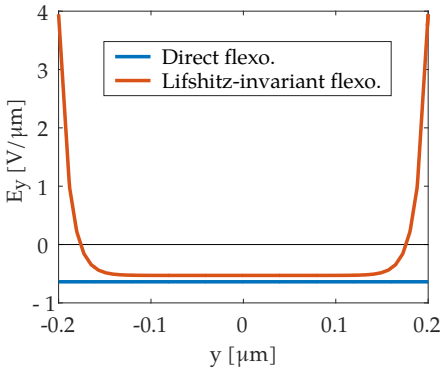

(d) Transversal electric fields at the cross section $x = L/2$.

Figure 2.3: Comparison of Direct and Lifshitz-invariant flexoelectricity forms (I): Cantilever bending

Figs. 2.3b and 2.3d. While the Direct flexoelectricity form presents an electric potential varying linearly along a cross section of the beam, the Lifshitz-invariant form features *boundary layers* with opposite sign than that of the bulk. This phenomenon is highlighted in Fig. 2.3d, which depicts the transversal electric fields along the middle cross section. This finding is interesting and is briefly addressed in Section 2.3.3.

Remark 2.5 (*Numerical stabilization).* As discussed later on in Section 3.3.1, the appearance of a boundary layer may lead to mesh-dependent spurious oscillations in the numerical solutions. Hence, some stabilization technique is required in that case. The simulations presented in this Section are properly stabilized according to the approach described in Section 3.3.1.

2.2.2.3.b Cantilever actuator

In this experiment we explore the transversal flexoelectric effect triggered by electrical actuation. This device was first used by Bursian and Zaikovskii (1968) to experimentally demonstrate for the first time the flexoelectric effect, which had been predicted theoretically by Mashkevich and Tolpygo (1957). Computational studies are also present in Abdollahi *et al.* (2014), Zhuang *et al.* (2020).

Here, an electric field across the beam thickness is enforced by attaching an electrode on the top boundary at prescribed voltage $V = 5\,\mathrm{V}$, while the bottom boundary is grounded, which corresponds to closed-circuit electrical boundary conditions (Fig. 2.4a). Mechanically, the left tip is clamped, and no force is applied. Due to the transversal flexoelectric effect, the electric field will yield an axial strain gradient along the thickness of the beam, inducing a constant curvature.

The results are shown in Fig. 2.4, and are quite similar to the ones reported in the cantilever bending case. The two differences between the Direct and Lifshitz-invariant flexoelectricity models are also present here. The latter presents more stiffening, in view of the maximum deflections obtained: $0.30\,\mu\mathrm{m}$ for the Direct case and only $0.12\,\mu\mathrm{m}$ for the Lifshitz-invariant one. Boundary layers in the electric field distribution are also obtained here for the Lifshitz-invariant form (Fig. 2.4d). However, in this case the bulk electric field is much larger than the boundary layer effect, and hence the electric potential distributions are much more alike (Fig. 2.4b).

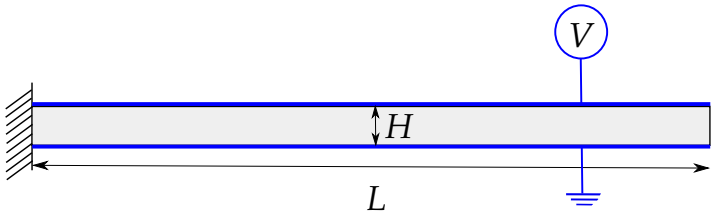

(a) Geometry and boundary conditions.

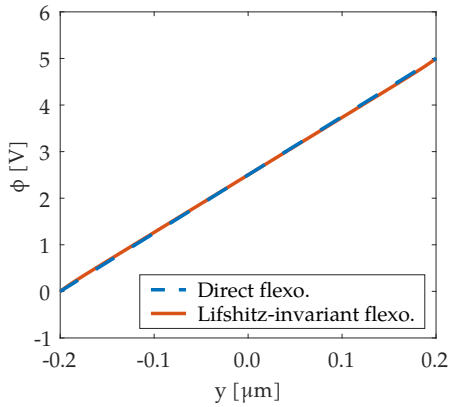

(b) Electric potential at the cross section $x = L/2$.

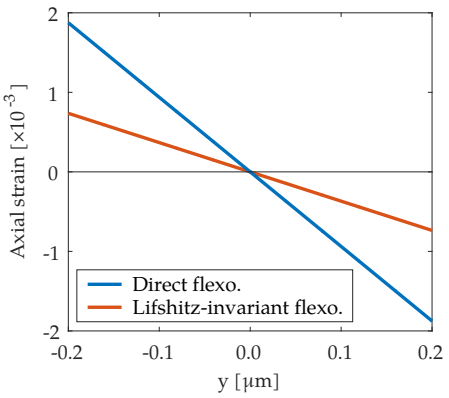

(c) Axial strains at the cross section $x = L/2$.

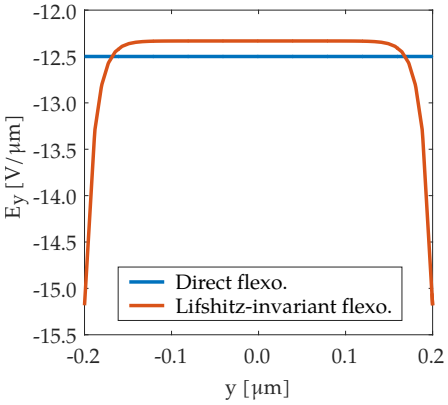

(d) Transversal electric fields at the cross section $x = L/2$.

Figure 2.4: Comparison of Direct and Lifshitz-invariant flexoelectricity forms (II): Cantilever actuator

2.2.3 Legendre transform in a finite deformation framework: Direct flexoelectric energy density

The derivation of the Legendre transform in a finite deformation framework is analogous to the case of infinitesimal deformation in Section 2.2.1. However, it involves certain subtleties and generalizations that are not trivial at all, and hence it is worth revisiting the process. We do so in this Section for the direct flexoelectricity model, and leave the case of Lifshitz-invariant flexoelectricity model as future work, cf. Section 2.3.1.

Consider a deformable dielectric body described by Ω_0 in the reference (or undeformed) configuration, and by Ω in the current (or deformed) configuration. The deformation map $\boldsymbol{\chi} : \Omega_0 \longrightarrow \Omega$ maps every material point $\boldsymbol{X} \in \Omega_0$ to the spatial point $\boldsymbol{x} = \boldsymbol{\chi}(\boldsymbol{X}) \in \Omega$. Whenever index notations are used, uppercase and lowercase indexes refer to quantities in the reference and the current configurations, respectively. The deformation gradient $\mathbf{F}$, the Jacobian determinant J, and the right and left Cauchy-Green deformation tensors $\mathbf{C}, \mathbf{B}$ are defined as

$$F_{iI}(\boldsymbol{X}) := \frac{\partial \chi_i(\boldsymbol{X})}{\partial X_I}, \qquad J := \det(\mathbf{F}), \qquad C_{IJ} := F_{kI}F_{kJ}, \qquad B_{ij} := F_{iK}F_{jK}. \tag{2.88}$$

Standard strain measures in the reference and the current configurations are the Green-Lagrangian $\mathfrak{E}$ and the Almansi-Eulerian $\mathfrak{e}$ strain tensors given by

$$\mathfrak{E}_{IJ} := \frac{1}{2}\left(C_{IJ} - \delta_{IJ}\right), \qquad \mathfrak{e}_{ij} := \frac{1}{2}\left(\delta_{ij} - B^{-1}_{ij}\right) = \mathfrak{E}_{IJ}F^{-1}_{Ii}F^{-1}_{Jj}. \tag{2.89}$$

The gradient of the deformation gradient $\tilde{\mathbf{F}}$, the gradient of the Cauchy-Green deformation tensor $\widetilde{\mathbf{C}}$ and the Green-Lagrangian strain gradient $\widetilde{\mathfrak{E}}$ as

$$\tilde{F}_{iJK} := \frac{\partial F_{iJ}}{\partial X_K} = \frac{\partial^2 x_i}{\partial X_J \partial X_K}, \tag{2.90a}$$

$$\widetilde{C}_{IJK} := \frac{\partial C_{IJ}}{\partial X_K} = 2 \operatorname*{symm}_{IJ}\left(\tilde{F}_{kIK}F_{kJ}\right), \tag{2.90b}$$

$$\widetilde{\mathfrak{E}}_{IJK} := \frac{\partial \mathfrak{E}_{IJ}}{\partial X_K} = \frac{1}{2}\widetilde{C}_{IJK}; \tag{2.90c}$$

where $\operatorname{symm}_{IJ}\left(A_{IJ}\right) := \left(A_{IJ} + A_{JI}\right)/2$. Note that the relation $\widetilde{\mathfrak{E}}(\,\tilde{\mathbf{F}}\,)$ in Eq. (2.90c) is inverted as

$$\tilde{F}_{iJK} = \left(\widetilde{\mathfrak{E}}_{IJK} + \widetilde{\mathfrak{E}}_{KIJ} - \widetilde{\mathfrak{E}}_{KJI}\right)F^{-1}_{Ii}, \tag{2.91}$$

analogously to the relation between second derivative of displacement and strain gradients in the limit of infinitesimal deformation, cf. Schiaffino *et al.* (2019).

This body in equilibrium necessarily satisfies mechanical balance laws of linear and angular momentum, and Maxwell equations. In the absence of a magnetic field, they can be expressed

in an Eulerian frame as

$$\nabla\cdot\boldsymbol{\sigma} + \boldsymbol{b} = \boldsymbol{0} \qquad \text{in } \Omega, \tag{2.92a}$$
$$\boldsymbol{\sigma} = \boldsymbol{\sigma}^T \qquad \text{in } \Omega, \tag{2.92b}$$
$$\nabla \times \boldsymbol{e} = \boldsymbol{0} \qquad \text{in } \Omega, \tag{2.92c}$$
$$\nabla\cdot\boldsymbol{d} - q = 0 \qquad \text{in } \Omega; \tag{2.92d}$$

where $\boldsymbol{\sigma}$ is the physical stress, $\boldsymbol{e}$ is the the electric field, $\boldsymbol{d}$ is the electric displacement, and $\boldsymbol{b}$ and q are the body force and electric charge per unit volume. Equation (2.92c) implies the existence of an electric potential ϕ such that $\boldsymbol{e} = -\nabla\phi$. The linear constitutive law for $\boldsymbol{d}$ for a dielectric material is

$$\boldsymbol{d}(\boldsymbol{p}, \boldsymbol{e}) = \epsilon_0 \boldsymbol{e} + \boldsymbol{p} \qquad \text{or, equivalently,} \qquad \boldsymbol{d}(\boldsymbol{p}, \phi) = -\epsilon_0 \nabla\phi + \boldsymbol{p}, \tag{2.93}$$

where $\boldsymbol{p}$ is the electric polarization, which is work-conjugate to $\boldsymbol{e}$, and ϵ_0 is the electric permittivity of vacuum.

To formulate the problem in a material frame, the Lagrangian second Piola-Kirchhoff physical stress tensor $\mathbf{S}$ is defined from the work-conjugacy relation $\sigma_{ij}\mathfrak{e}_{ij} = \frac{1}{J} S_{IJ}\mathfrak{E}_{IJ}$, where $\sigma_{ij}\mathfrak{e}_{ij}$ is a mechanical work density per unit physical volume and $S_{IJ}\mathfrak{E}_{IJ}$ a mechanical work density per unit reference volume, leading to

$$S_{IJ} = J F^{-1}_{Ii} F^{-1}_{Jj} \sigma_{ij}. \tag{2.94}$$

To follow an analogous procedure with the electric displacement (Dorfmann and Ogden, 2005, 2014, 2017, Lax and Nelson, 1976, Steinmann and Vu, 2017, Vu *et al.*, 2007), we first identify the nominal or material electric field. The electric potential can be expressed in the material frame as $\Phi(\boldsymbol{X}) = \phi(\chi(\boldsymbol{X}))$, and the nominal electric field $\boldsymbol{E} = -\nabla_0\Phi$ defined as the negative of its material gradient. By the chain rule, we thus find that

$$E_I = -\frac{\partial\Phi}{\partial X_I} = -\frac{\partial\phi}{\partial x_i}\frac{\partial x_i}{\partial X_I} = e_i F_{iI}. \tag{2.95}$$

Then, from the work-conjugacy relation $d_i e_i = \frac{1}{J} D_I E_I$, we identify the nominal electric displacement as

$$D_I = J F^{-1}_{Ii} d_i. \tag{2.96}$$

Since electric displacement and polarization are physically equivalent quantities, we analogously find

$$P_I = J F^{-1}_{Ii} p_i. \tag{2.97}$$

Using Eq. (2.88) and (2.94)-(2.97), the balance equations in Eq. (2.92a)-(2.92d) and the constitutive law for dielectrics in Eq. (2.93) are written in material form as

$$\left(F_{iI}S_{IJ}\right)_{,J} + B_i = 0_i \qquad \text{in } \Omega, \tag{2.98a}$$

$$S_{IJ} = S_{JI} \qquad \text{in } \Omega, \tag{2.98b}$$

$$E_L + \Phi_{,L} = 0 \qquad \text{in } \Omega, \tag{2.98c}$$

$$D_K = \epsilon_0 J C^{-1}_{KL} E_L + P_K \qquad \text{in } \Omega, \tag{2.98d}$$

$$D_{K,K} - Q = 0 \qquad \text{in } \Omega, \tag{2.98e}$$

with $\boldsymbol{B} = J\boldsymbol{b}$ and $Q = Jq$.

Now, the Lagrangian internal energy density per unit reference volume of the flexoelectric solid is defined as (Codony *et al.*, 2020b)

$$\Psi^{\text{Int}}(\mathfrak{E}, \widetilde{\mathfrak{E}}, \boldsymbol{P}) = \Psi^{\text{Mech}}(\mathfrak{E}, \widetilde{\mathfrak{E}}) + \Psi^{\text{Diele}}(\mathfrak{E}, \boldsymbol{P}) + \Psi^{\text{Flexo}}(\boldsymbol{P}, \widetilde{\mathfrak{E}}). \tag{2.99}$$

We allow Ψ^{Mech} to depend on Lagrangian strain and strain gradient as required for stability (Liu, 2014). The isotropic dielectric energy per unit reference volume follows by transforming the spatial expression per unit physical volume $\psi^{\text{Diele}}(\boldsymbol{p}) = \dfrac{1}{2(\epsilon - \epsilon_0)} p_i p_i$ (Liu, 2014) by recalling Eq. (2.97), resulting in

$$\Psi^{\text{Diele}}(\mathfrak{E}, \boldsymbol{P}) = \frac{1}{2J(\epsilon - \epsilon_0)} P_I C_{IJ} P_J, \tag{2.100}$$

where ϵ denotes the electric permittivity of the material. The flexoelectric coupling linking polarization and strain gradient is encoded by Ψ^{Flexo}, which for simplicity we assume to be independent on strain.

The spatial expression of the electrostatic energy density $\psi^{\text{Elec}}(\boldsymbol{e}) = \frac{1}{2}\epsilon_0 e_i e_i$ (Liu, 2014) can also be expressed in the material frame by recalling Eq. (2.95), resulting in the energy density per unit reference volume

$$\Psi^{\text{Elec}}(\mathfrak{E}, \boldsymbol{E}) = \frac{J\epsilon_0}{2} E_I C^{-1}_{IJ} E_J. \tag{2.101}$$

To formulate a unified potential self-consistently accounting for the material electromechanics and for electrostatics, $\Psi^{\text{Int}}(\mathfrak{E}, \widetilde{\mathfrak{E}}, \boldsymbol{P})$ and $\Psi^{\text{Elec}}(\mathfrak{E}, \boldsymbol{E})$ must be expressed in terms of the same variables. To accomplish this, we resort to a partial Legendre transform and define the following internal dual potential

$$\bar{\Psi}^{\text{Int}}(\mathfrak{E}, \widetilde{\mathfrak{E}}, \boldsymbol{E}) = \min_{\boldsymbol{P}} \left(\Psi^{\text{Int}}(\mathfrak{E}, \widetilde{\mathfrak{E}}, \boldsymbol{P}) - \boldsymbol{P} \cdot \boldsymbol{E}\right). \tag{2.102}$$

The stationarity condition of the minimization results in

$$\boldsymbol{E}(\mathfrak{E}, \widetilde{\mathfrak{E}}, \boldsymbol{P}) = \frac{\partial \Psi^{\text{Int}}}{\partial \boldsymbol{P}}. \tag{2.103}$$

In principle, this expression can be inverted to find $\boldsymbol{P}(\boldsymbol{E}, \mathfrak{E}, \widetilde{\mathfrak{E}})$, which plugged into $\Psi^{\text{Int}}(\mathfrak{E}, \widetilde{\mathfrak{E}}, \boldsymbol{P}) - \boldsymbol{P} \cdot \boldsymbol{E}$ results in the dual potential $\bar{\Psi}^{\text{Int}}(\mathfrak{E}, \widetilde{\mathfrak{E}}, \boldsymbol{E})$.

If we postulate the following *direct* flexoelectric coupling

$$\Psi^{\text{Flexo}}(\boldsymbol{P}, \widetilde{\mathfrak{E}}) = -P_L f_{LIJK} \widetilde{\mathfrak{E}}_{IJK}, \tag{2.104}$$

where f_{LIJK} is a purely Lagrangian tensor as further discussed in Remark 2.6, this inversion can be made explicit yielding

$$E_L = \frac{1}{J(\epsilon - \epsilon_0)} C_{LM} P_M - f_{LIJK} \widetilde{\mathfrak{E}}_{IJK}, \tag{2.105}$$

$$P_M = J(\epsilon - \epsilon_0) C^{-1}_{ML} \left(E_L + f_{LIJK} \widetilde{\mathfrak{E}}_{IJK} \right) = J(\epsilon - \epsilon_0) C^{-1}_{ML} \left(E_L + E^{\text{Flexo}}_L \right), \tag{2.106}$$

where we have defined $E^{\text{Flexo}}_L = f_{LIJK} \widetilde{\mathfrak{E}}_{IJK}$ for convenience.

Replacing Eq. (2.106) in Eq. (2.102) and rearranging terms, we find

$$\begin{aligned} \bar{\Psi}^{\text{Int}}(\mathfrak{E}, \widetilde{\mathfrak{E}}, \boldsymbol{E}) = \Psi^{\text{Mech}}(\mathfrak{E}, \widetilde{\mathfrak{E}}) &- \frac{J}{2}(\epsilon - \epsilon_0) E^{\text{Flexo}}_I C^{-1}_{IJ} E^{\text{Flexo}}_J \\ &- \frac{J}{2}(\epsilon - \epsilon_0) E_I C^{-1}_{IJ} E_J - J(\epsilon - \epsilon_0) E_I C^{-1}_{IJ} E^{\text{Flexo}}_J. \end{aligned} \tag{2.107}$$

Now, the total electromechanical enthalpy accounting for electrostatics $\bar{\Psi}^{\text{Enth}} = \bar{\Psi}^{\text{Int}} - \Psi^{\text{Elec}}$ (Dorfmann and Ogden, 2014, 2017, Liu, 2014) can be written from Eq. (2.107) and (2.101) as

$$\bar{\Psi}^{\text{Enth}}(\mathfrak{E}, \widetilde{\mathfrak{E}}, \boldsymbol{E}) = \bar{\Psi}^{\text{Mech}}(\mathfrak{E}, \widetilde{\mathfrak{E}}) + \bar{\Psi}^{\text{Diele}}(\mathfrak{E}, \boldsymbol{E}) + \bar{\Psi}^{\text{Flexo}}(\mathfrak{E}, \widetilde{\mathfrak{E}}, \boldsymbol{E}), \tag{2.108}$$

with

$$\bar{\Psi}^{\text{Mech}}(\mathfrak{E}, \widetilde{\mathfrak{E}}) = \Psi^{\text{Mech}}(\mathfrak{E}, \widetilde{\mathfrak{E}}) - \frac{J}{2}(\epsilon - \epsilon_0) E^{\text{Flexo}}_M C^{-1}_{ML} E^{\text{Flexo}}_L, \tag{2.109}$$

$$\bar{\Psi}^{\text{Diele}}(\mathfrak{E}, \boldsymbol{E}) = -\frac{1}{2} E_M \left(J C^{-1}_{ML} \epsilon \right) E_L, \tag{2.110}$$

$$\bar{\Psi}^{\text{Flexo}}(\mathfrak{E}, \widetilde{\mathfrak{E}}, \boldsymbol{E}) = -E_M \left(J C^{-1}_{ML} \mu_{LIJK} \right) \widetilde{\mathfrak{E}}_{IJK}; \tag{2.111}$$

where $\boldsymbol{\mu} = (\epsilon - \epsilon_0)\boldsymbol{f}$ is the flexoelectricity tensor (Wang *et al.*, 2019, Zubko *et al.*, 2013), described in Eq. (A.8). The *effective* mechanical energy density of the system (Wang *et al.*, 2019) in Eq. (2.109) can be written as

$$\bar{\Psi}^{\text{Mech}}(\mathfrak{E}, \widetilde{\mathfrak{E}}) = \Psi^{\text{Elast}}(\mathfrak{E}) + \Psi^{\text{StrGr}}(\mathfrak{E}, \widetilde{\mathfrak{E}}) - \frac{1}{2} \widetilde{\mathfrak{E}}_{IJK} \left(\frac{\mu_{AIJK} J C^{-1}_{AB} \mu_{BLMN}}{\epsilon - \epsilon_0} \right) \widetilde{\mathfrak{E}}_{LMN}, \tag{2.112}$$

where the two first terms coming from Ψ^{Mech} correspond to a classical hyperelastic potential (e.g. Saint-Venant-Kirchhoff, cf. Eq. (A.9), or Neo-Hookean, cf. Eq. (A.10), constitutive models) and a strain gradient elasticity potential respectively. The third term, i.e. the flexoelectricity-induced mechanical energy, has the same structure as the strain gradient elasticity potential. For convenience, we thus define

$$\bar{\Psi}^{\text{Mech}}(\mathfrak{E}, \widetilde{\mathfrak{E}}) = \Psi^{\text{Elast}}(\mathfrak{E}) + \frac{1}{2}\widetilde{\mathfrak{E}}_{IJK}\bar{h}_{IJKLMN}\widetilde{\mathfrak{E}}_{LMN}, \tag{2.113}$$

where $\bar{\mathbf{h}}(\mathfrak{E}, \widetilde{\mathfrak{E}})$ is the *effective* strain gradient elasticity tensor. In this work, for simplicity, it is taken as constant, i.e. $\bar{\mathbf{h}}(\mathfrak{E}, \widetilde{\mathfrak{E}}) = \mathbf{h}$ as described in Eq. (A.2). This choice corresponds to the extension of the Saint-Venant-Kirchhoff elasticity model to strain gradient elasticity.

Finally, the electromechanical enthalpy density corresponding to a dielectric material with the direct flexoelectric coupling is

$$\bar{\Psi}^{\text{Enth}}(\mathfrak{E}, \widetilde{\mathfrak{E}}, \boldsymbol{E}) = \Psi^{\text{Elast}}(\mathfrak{E}) + \frac{1}{2}\widetilde{\mathfrak{E}}_{IJK}\bar{h}_{IJKLMN}\widetilde{\mathfrak{E}}_{LMN} - \frac{1}{2}E_M\bar{\kappa}_{ML}E_L - E_M\bar{\mu}_{MIJK}\widetilde{\mathfrak{E}}_{IJK}, \tag{2.114}$$

where

$$\bar{\kappa}_{ML}(\mathfrak{E}) := JC^{-1}_{ML}\epsilon, \tag{2.115}$$

$$\bar{\mu}_{MIJK}(\mathfrak{E}) := JC^{-1}_{ML}\mu_{LIJK} \tag{2.116}$$

are the *effective* dielectricity and flexoelectricity tensors respectively, which explicitly depend on the Green-Lagrangian strain $\mathfrak{E}$.

Remark 2.6 (*Objectivity of the proposed flexoelectric coupling).* In the present formulation, μ_{LIJK} is a purely Lagrangian tensor, and hence it is meaningful to view it as a material constant with the same material symmetries and intrinsic symmetry ($\mu_{LIJK} = \mu_{LJIK}$) as the infinitesimal strain flexoelectric tensor (Krichen and Sharma, 2016, Majdoub *et al.*, 2008, Zubko *et al.*, 2013). We note, however, that in previous literature a distinct notion of polarization per unit undeformed volume is introduced as $\boldsymbol{p}^{\mathbf{r}} = J\boldsymbol{p}$, i.e. a volume-normalized spatial polarization related to our material or nominal polarization by $p^{\text{r}}{}_i = F_{iI}P_I$ (Dorfmann and Ogden, 2014, 2017, Liu, 2014). The polarization $\boldsymbol{p}^{\mathbf{r}}$ is not work-conjugate to the Lagrangian electric field $\boldsymbol{E}$, and it can be problematic when used to formulate flexoelectric couplings, as in Deng *et al.* (2014b,c), Liu (2014), Thai *et al.* (2018), Yvonnet and Liu (2017), which consider the following coupling:

$$\Psi^{\text{Flexo}}(\tilde{\mathbf{F}}, \boldsymbol{p}^{\mathbf{r}}) = -p^{\text{r}}{}_l\mathcal{F}_{liJK}\tilde{F}_{iJK}. \tag{2.117}$$

The tensor $\mathcal{F}$ is a mixed spatial-material flexoelectric tensor, which unlike the infinitesimal flexoelectric tensor is intrinsically symmetric with respect to its last two indices ($\mathcal{F}_{liJK} = \mathcal{F}_{liKJ}$). By comparing Eq. (2.117) and (2.104), using Eq. (2.90c) and (2.91), the relation $p^{\text{r}}{}_i = F_{iI}P_I$ and

the chain rule, we find the relation between $\boldsymbol{f}$ and $\mathscr{F}$ as

$$\mathscr{F}_{liJK} = -\frac{\partial^2 \Psi^{\text{Flexo}}}{\partial p^{\text{r}}{}_l \partial \widetilde{F}_{iJK}} = \underset{JK}{\text{symm}} \left(f_{LIJK} \right) F_{iI} F^{-1}_{Ll}, \tag{2.118a}$$

$$f_{LIJK} = -\frac{\partial^2 \Psi^{\text{Flexo}}}{\partial P_L \partial \widetilde{\mathfrak{E}}_{IJK}} = \left(\mathscr{F}_{liJK} F^{-1}_{Ii} + \mathscr{F}_{ljIK} F^{-1}_{Jj} - \mathscr{F}_{lkIJ} F^{-1}_{Kk} \right) F_{lL}. \tag{2.118b}$$

In the limit of infinitesimal deformation, $\mathscr{F}$ and $\boldsymbol{f}$ correspond to the so-called type-I ($\boldsymbol{f}^{\text{I}}$) and type-II ($\boldsymbol{f}^{\text{II}}$) flexocoupling tensors, respectively, and choosing one or the other is just a matter of convenience, cf. Schiaffino *et al.* (2019). However this equivalence does not hold anymore in a finite deformation framework, since $\boldsymbol{f}$ is purely Lagrangian whereas $\mathscr{F}$ is not. Equation (2.118b) clearly shows that taking $\mathscr{F}$ as a material constant, as done in Yvonnet and Liu (2017) and Thai *et al.* (2018), directly implies a very particular dependence of the Lagrangian flexoelectric tensor $\boldsymbol{f}$ on deformation, breaking the invariance of the enthalpy density with respect to a superimposed rigid body motion (Codony *et al.*, 2020b), and hence yielding a non-objective potential, which is a basic requirement of hyperelastic (and related) finite deformation models. The purely Lagrangian approach described in this work overcomes this difficulty, since it is objective by construction.

Remark 2.7 (*Link to the linear theory of flexoelectricity).* In the limit of infinitesimal deformation, and keeping terms up to second order, the enthalpy density in Eq. (2.114) reduces to the one present in the linear theory of flexoelectricity, cf. Eq. (2.50), since

$$J \longrightarrow 1 + \nabla \cdot \boldsymbol{u} \approx 1, \tag{2.119a}$$

$$\mathbf{C}^{-1} \longrightarrow \mathbf{I} - 2\boldsymbol{\varepsilon} \approx \mathbf{I}, \tag{2.119b}$$

$$\mathfrak{E} \longrightarrow \boldsymbol{\varepsilon}, \tag{2.119c}$$

$$\bar{\kappa}(\mathfrak{E}) \longrightarrow \epsilon \mathbf{I} = \boldsymbol{\kappa}, \tag{2.119d}$$

$$\bar{\boldsymbol{\mu}}(\mathfrak{E}) \longrightarrow \boldsymbol{\mu}. \tag{2.119e}$$

Remark 2.8 (*Characterization of the flexoelectric tensor).* The expression of the polarization in spatial frame is found by inserting (2.97) into Eq. (2.106), yielding

$$p_l = \left((\epsilon - \epsilon_0) E_L + \mu_{LIJK} \widetilde{\mathfrak{E}}_{IJK} \right) F^{-1}_{Ll}. \tag{2.120}$$

Hence, we infer

$$\mu_{LIJK} = \left. \frac{\partial \left(p_l F_{lL} \right)}{\partial \widetilde{\mathfrak{E}}_{IJK}} \right|_{\boldsymbol{E}}. \tag{2.121}$$

Equation (2.121) describes a way to characterize the flexoelectricity tensor from measurements of the spatial polarization and the Green-Lagrangian strain gradients in a finite deformation framework, either experimentally or by means of ab-initio methods based on quantum mechan-

ics. The latter approach is used in Section 4.2.1 to characterize the transversal flexoelectricity coefficient of nanostructures under bending by means of the cyclic density functional theory.

2.2.4 Variational models at finite deformation

The generic material form of the enthalpy functional $\Pi[\boldsymbol{\chi}, \Phi]$ governing the physics of a flexoelectric body is written as

$$\Pi[\boldsymbol{\chi}, \Phi] = \int_{\Omega_0} \left(\bar{\Psi}^{\text{Enth}}(\boldsymbol{\chi}, \Phi) + \mathcal{W}^{\Omega_0}(\boldsymbol{\chi}, \Phi) \right) \mathrm{d}\Omega_0 + \int_{\partial\Omega_0} \mathcal{W}^{\partial\Omega_0}(\boldsymbol{\chi}, \Phi)\, \mathrm{d}\Gamma_0 + \int_{C_0} \mathcal{W}^{C_0}(\boldsymbol{\chi}, \Phi)\, \mathrm{d}s_0 \quad (2.122)$$

where $\bar{\Psi}^{\text{Enth}}$ is the internal bulk enthalpy density per unit reference volume Ω_0, and $\mathcal{W}^{\Omega_0}$, $\mathcal{W}^{\partial\Omega_0}$ and $\mathcal{W}^{C_0}$ represent the external work density per unit reference volume, area and length, respectively. Different boundary value problems arise depending on the flexoelectric form that is chosen to describe $\bar{\Psi}^{\text{Enth}}$. We show next the *direct* flexoelectric form, and leave the *Lifshitz-invariant* flexoelectric form as future work (see Section 2.3.1).

2.2.4.1 Direct flexoelectricity form

As derived in the previous Section (see Eq. (2.114)), the internal energy enthalpy corresponding to a dielectric material with the direct flexoelectric coupling is

$$\bar{\Psi}^{\text{Enth}}(\mathfrak{E}, \widetilde{\mathfrak{E}}, \boldsymbol{E}) = \Psi^{\text{Elast}}(\mathfrak{E}) + \frac{1}{2}\widetilde{\mathfrak{E}}_{IJK} h_{IJKLMN} \widetilde{\mathfrak{E}}_{LMN} - \frac{1}{2} E_M \bar{\kappa}_{ML} E_L - E_M \bar{\mu}_{MIJK} \widetilde{\mathfrak{E}}_{IJK}, \quad (2.123)$$

and the admissible external sources of work are

$$\mathcal{W}^{\Omega_0}(\boldsymbol{\chi}, \Phi) := -\overline{B}_i \chi_i + \overline{Q}\Phi, \quad (2.124a)$$

$$\mathcal{W}^{\partial\Omega_0}(\boldsymbol{\chi}, \Phi) := -T_i \chi_i - R_i \partial_0^N \chi_i + W\Phi, \quad (2.124b)$$

$$\mathcal{W}^{C_0}(\boldsymbol{\chi}, \Phi) := -J_i \chi_i; \quad (2.124c)$$

where $\overline{\boldsymbol{B}}$ is the prescribed external body force per unit reference volume, $\overline{Q}$ is the external free electric charge per unit reference volume, $\boldsymbol{T}$ and $\boldsymbol{J}$ are the forces per unit reference area and length, W is the surface charge density (i.e. electric charge per unit area) and $\boldsymbol{R}$ is the double traction (i.e. moment per unit reference area). Note that $\boldsymbol{T}$, $\boldsymbol{J}$, $\boldsymbol{R}$ and $\overline{\boldsymbol{B}}$ are written in spatial frame coordinates (indicated by the lowercase subscripts), but normalized with respect to volume, area and length in the material frame.

The boundary of the reference body, $\partial\Omega_0$, is split in several disjoint Dirichlet and Neumann sets as follows:

$$\partial\Omega_0 = \partial\Omega_0^{\chi} \cup \partial\Omega_0^{T} = \partial\Omega_0^{V} \cup \partial\Omega_0^{R} = \partial\Omega_0^{\Phi} \cup \partial\Omega_0^{W}. \quad (2.125)$$

On the Dirichlet boundaries $\partial\Omega_0^{\chi}$, $\partial\Omega_0^{V}$ and $\partial\Omega_0^{\Phi}$, the deformation map $\boldsymbol{\chi}$, normal derivatives

of the deformation map $\partial_0^N \boldsymbol{\chi}$, and electric potential Φ are prescribed, respectively. On the Neumann boundaries $\partial\Omega_0^T$, $\partial\Omega_0^R$ and $\partial\Omega_0^W$, their respective work conjugate quantities are prescribed, i.e. the surface traction, the surface double traction and the surface charge density. The edges of the boundary of the reference body C_0 are also split in Dirichlet in Neumann sets as

$$C_0 = C_0^\chi \cup C_0^J, \tag{2.126}$$

depending on whether the deformation map or edge forces are prescribed. For simplicity, the prescribed Neumann boundary terms and source terns are treated as dead loads, i.e. they do not depend on $\boldsymbol{\chi}$ or Φ.

The corresponding boundary and edge conditions are mathematically written as

$$\boldsymbol{\chi} - \overline{\boldsymbol{\chi}} = \mathbf{0} \quad \text{on } \partial\Omega_0^\chi, \qquad \boldsymbol{T}(\boldsymbol{\chi}, \Phi) - \overline{\boldsymbol{T}} = \mathbf{0} \quad \text{on } \partial\Omega_0^T; \tag{2.127a}$$

$$\partial_0^N \boldsymbol{\chi} - \overline{\boldsymbol{V}} = \mathbf{0} \quad \text{on } \partial\Omega_0^V, \qquad \boldsymbol{R}(\boldsymbol{\chi}, \Phi) - \overline{\boldsymbol{R}} = \mathbf{0} \quad \text{on } \partial\Omega_0^R; \tag{2.127b}$$

$$\Phi - \overline{\Phi} = 0 \quad \text{on } \partial\Omega_0^\Phi, \qquad W(\boldsymbol{\chi}, \Phi) - \overline{W} = 0 \quad \text{on } \partial\Omega_0^W; \tag{2.127c}$$

$$\boldsymbol{\chi} - \overline{\boldsymbol{\chi}} = \mathbf{0} \quad \text{on } C_0^\chi, \qquad \boldsymbol{J}(\boldsymbol{\chi}, \Phi) - \overline{\boldsymbol{J}} = \mathbf{0} \quad \text{on } C_0^J; \tag{2.127d}$$

where $\overline{\boldsymbol{\chi}}$, $\overline{\boldsymbol{V}}$ and $\overline{\Phi}$ are the prescribed deformation map, normal derivative of the deformation map and electric potential at the Dirichlet boundaries, and $\overline{\boldsymbol{T}}$, $\overline{\boldsymbol{R}}$, $\overline{W}$ and $\overline{\boldsymbol{J}}$ are the traction, double traction, surface charge and the line force fields prescribed on the Neumann boundaries. The expressions $\boldsymbol{T}(\boldsymbol{\chi}, \Phi)$, $\boldsymbol{R}(\boldsymbol{\chi}, \Phi)$, $W(\boldsymbol{\chi}, \Phi)$ and $\boldsymbol{J}(\boldsymbol{\chi}, \Phi)$ will be derived later as a result of the variational principle in Eq. (2.132).

Remark 2.9 (*Deformation map or displacement field as the mechanical state variable).* The linear theory of flexoelectricity (cf. Section 2.2.2) is written in terms of the displacement field $\boldsymbol{u}$, whereas in the framework of finite deformations, the deformation map $\boldsymbol{\chi}$ is used. In fact, the theory of flexoelectricity at finite deformations developed in the present Section can also be written in terms of the displacement field $\boldsymbol{u}$ by writing the deformation map $\boldsymbol{\chi}$ as a function of $\boldsymbol{u}$ as follows:

$$\boldsymbol{\chi}(\boldsymbol{u}) = \mathbf{I} \cdot \boldsymbol{X} + \boldsymbol{u}. \tag{2.128}$$

The deformation gradient is rewritten accordingly as

$$F_{iI}(\boldsymbol{u}) = \delta_{iI} + \frac{\partial u_i(\boldsymbol{X})}{\partial X_I}, \tag{2.129}$$

and so on for the rest of the kinematic tensors of the theory, as well as the boundary conditions. Note that the variations $\delta\boldsymbol{\chi} = \delta\boldsymbol{u}$, and hence writing the weak form in terms of $\boldsymbol{u}$ is trivial. In this work, however, $\boldsymbol{\chi}$ is kept as the primary state variable to emphasize the conceptual difference of the meaning of $\boldsymbol{u}$ in the two theories, and to emphasize the existence of the two

frames $\boldsymbol{\chi}$ and $\boldsymbol{X}$.

2.2.4.1.a Standard framework

Assuming that the functional spaces of the state variables fulfill Dirichlet boundary conditions, inserting Eq. (2.123)-(2.127) into Eq. (2.122) leads to

$$\Pi_{\mathrm{D}}^{(\mathrm{Dir})}[\boldsymbol{\chi}, \Phi] = \Pi^{\Omega_0}[\boldsymbol{\chi}, \Phi] + \Pi^{\mathrm{Neumann}}[\boldsymbol{\chi}, \Phi], \tag{2.130}$$

where

$$\Pi^{\Omega_0}[\boldsymbol{\chi}, \Phi] = \int_{\Omega_0} \left(\bar{\Psi}^{\mathrm{Enth}}(\mathfrak{E}(\boldsymbol{\chi}), \widetilde{\mathfrak{E}}(\boldsymbol{\chi}), \boldsymbol{E}(\Phi)) - \overline{B}_i \chi_i + \overline{Q}\Phi \right) \mathrm{d}\Omega_0, \tag{2.131a}$$

$$\begin{aligned} \Pi^{\mathrm{Neumann}}[\boldsymbol{\chi}, \Phi] = & \int_{\partial\Omega_0^T} -\overline{T}_i \chi_i \, \mathrm{d}\Gamma_0 \\ & + \int_{\partial\Omega_0^R} -\overline{R}_i \partial_0^N \chi_i \, \mathrm{d}\Gamma_0 + \int_{\partial\Omega_0^W} \overline{W}\Phi \, \mathrm{d}\Gamma_0 + \int_{C_0^J} -\overline{J}_i \chi_i \, \mathrm{d}s_0. \end{aligned} \tag{2.131b}$$

The equilibrium states $(\boldsymbol{\chi}^*, \Phi^*)$ of the body correspond to the saddle points in the enthalpy potential fulfilling the following variational principle:

$$(\boldsymbol{\chi}^*, \Phi^*) = \arg \min_{\boldsymbol{\chi} \in \mathcal{X}_{\mathrm{D}}} \max_{\Phi \in \mathcal{P}_{\mathrm{D}}} \Pi_{\mathrm{D}}^{(\mathrm{Dir})}[\boldsymbol{\chi}, \Phi], \tag{2.132}$$

with the functional spaces $\mathcal{X}_{\mathrm{D}}$ and $\mathcal{P}_{\mathrm{D}}$ having sufficient regularity and fulfilling Dirichlet boundary conditions (2.127):

$$\begin{aligned} \mathcal{X}_{\mathrm{D}} := \{ & \boldsymbol{\chi} \in [H^2(\Omega_0)]^3 \mid \boldsymbol{\chi} - \overline{\boldsymbol{\chi}} = \boldsymbol{0} \text{ on } \partial\Omega_0^{\chi} \text{ and on } C_0^{\chi}, \text{ and} \\ & \partial_0^N \boldsymbol{\chi} - \overline{\boldsymbol{V}} = \boldsymbol{0} \text{ on } \partial\Omega_0^V \}, \end{aligned} \tag{2.133a}$$

$$\mathcal{P}_{\mathrm{D}} := \{ \Phi \in H^1(\Omega_0) \mid \Phi - \overline{\Phi} = 0 \text{ on } \partial\Omega_0^{\Phi} \}. \tag{2.133b}$$

The weak form of the problem is found by enforcing $\delta\Pi_{\mathrm{D}}^{(\mathrm{Dir})} = 0$ for all admissible variations $\delta\boldsymbol{\chi} \in \mathcal{X}_0$ and $\delta\Phi \in \mathcal{P}_0$, with

$$\mathcal{X}_0 := \{ \delta\boldsymbol{\chi} \in [H^2(\Omega_0)]^3 \mid \delta\boldsymbol{\chi} = \boldsymbol{0} \text{ on } \partial\Omega_0^{\chi} \text{ and on } C_0^{\chi}, \text{ and } \partial_0^N \delta\boldsymbol{\chi} = \boldsymbol{0} \text{ on } \partial\Omega_0^V \}, \tag{2.134a}$$

$$\mathcal{P}_0 := \{ \delta\Phi \in H^1(\Omega_0) \mid \delta\Phi = 0 \text{ on } \partial\Omega_{\Phi} \}. \tag{2.134b}$$

The weak form reads: *Find* $(\boldsymbol{\chi}, \Phi) \in \mathcal{X}_D \otimes \mathcal{P}_D$ *such that,* $\forall (\delta\boldsymbol{\chi}, \delta\Phi) \in \mathcal{X}_0 \otimes \mathcal{P}_0$,

$$\begin{aligned}\delta\Pi_{\mathrm{D}}^{(\mathrm{Dir})} &= \delta_{\boldsymbol{\chi}}\Pi_{\mathrm{D}}^{(\mathrm{Dir})} + \delta_{\Phi}\Pi_{\mathrm{D}}^{(\mathrm{Dir})} \\ &= \int_{\Omega_0} \left(\hat{S}_{IJ}\delta\mathfrak{E}_{IJ} + \tilde{S}_{IJK}\delta\widetilde{\mathfrak{E}}_{IJK} - \hat{D}_L\delta E_L - \overline{B}_i\delta\chi_i + \overline{Q}\delta\Phi \right) \mathrm{d}\Omega_0 \\ &\quad - \int_{\partial\Omega_0^T} \overline{T}_i\delta\chi_i \,\mathrm{d}\Gamma_0 - \int_{\partial\Omega_0^R} \overline{R}_i\partial_0^N\delta\chi_i \,\mathrm{d}\Gamma_0 - \int_{C_0^J} \overline{J}_i\delta\chi_i \,\mathrm{d}s_0 + \int_{\partial\Omega_0^W} \overline{W}\delta\Phi \,\mathrm{d}\Gamma_0, \\ &= 0; \end{aligned} \tag{2.135}$$

where

$$\delta E_L := -\frac{\partial(\delta\Phi)}{\partial X_L}, \tag{2.136a}$$

$$\delta F_{iI} := \frac{\partial(\delta\chi_i)}{\partial X_I}, \tag{2.136b}$$

$$\delta\tilde{F}_{iIJ} := \frac{\partial^2(\delta\chi_i)}{\partial X_I \partial X_J}, \tag{2.136c}$$

$$\delta\mathfrak{E}_{IJ} := \frac{1}{2}\delta C_{IJ} = \underset{IJ}{\mathrm{symm}} \left(\delta F_{kI} F_{kJ} \right), \tag{2.136d}$$

$$\delta\widetilde{\mathfrak{E}}_{IJK} := \frac{1}{2}\delta\widetilde{C}_{IJK} = \underset{IJ}{\mathrm{symm}} \left(\delta F_{kI}\tilde{F}_{kJK} + F_{kI}\delta\tilde{F}_{kJK} \right). \tag{2.136e}$$

We have introduced the local second Piola-Kirchhoff stress $\hat{\mathbf{S}}$, the second Piola-Kirchhoff double stress $\tilde{\mathbf{S}}$ and the local electric displacement $\hat{\boldsymbol{D}}$ defined as follows:

$$\hat{S}_{IJ}(\boldsymbol{\chi}, \Phi) = \frac{\partial\bar{\Psi}^{\mathrm{Enth}}}{\partial\mathfrak{E}_{IJ}} = 2\frac{\partial\Psi^{\mathrm{Elast}}(\mathbf{C})}{\partial C_{IJ}} + J\mathscr{C}_{MLIJ}E_M \left(\frac{1}{2}\epsilon E_L + \mu_{LABK}\widetilde{\mathfrak{E}}_{ABK} \right), \tag{2.137}$$

$$\tilde{S}_{IJK}(\boldsymbol{\chi}, \Phi) = \frac{\partial\bar{\Psi}^{\mathrm{Enth}}}{\partial\widetilde{\mathfrak{E}}_{IJK}} = h_{IJKLMN}\widetilde{\mathfrak{E}}_{LMN} - JC_{LM}^{-1}E_M\mu_{LIJK}, \tag{2.138}$$

$$\hat{D}_L(\boldsymbol{\chi}, \Phi) = -\frac{\partial\bar{\Psi}^{\mathrm{Enth}}}{\partial E_L} = JC_{KL}^{-1}\left(\epsilon E_K + \mu_{KIJM}\widetilde{\mathfrak{E}}_{IJM} \right), \tag{2.139}$$

with

$$\mathscr{C}_{ABCD} = \frac{2}{J}\frac{\partial\left(-JC_{AB}^{-1}\right)}{\partial C_{CD}} = \left(C_{AC}^{-1}C_{BD}^{-1} + C_{BC}^{-1}C_{AD}^{-1} - C_{AB}^{-1}C_{CD}^{-1} \right). \tag{2.140}$$

Analogously to the linear theory of flexoelectricity (see Section 2.2.2.1.a), Eq. (2.135) can be integrated by parts and, by invoking the divergence and surface divergence theorems, the strong form in Eq. (2.98) is recovered along with the following definitions of the physical second Piola-Kirchhoff stress $\mathbf{S}$, the nominal electric displacement $\boldsymbol{D}$, the surface traction $\mathbf{T}$, the

double traction $\mathbf{R}$, the surface charge density W and the edge forces $\mathbf{J}$ (Codony *et al.*, 2020b):

$$\begin{aligned}
S_{IJ}(\boldsymbol{\chi},\Phi) &:= \hat{S}_{IJ}(\boldsymbol{\chi},\Phi) - \tilde{S}_{IJK,K}(\boldsymbol{\chi},\Phi) \\
&= 2\frac{\partial \Psi^{\text{Elast}}(\mathbf{C})}{\partial C_{IJ}} - \bar{h}_{IJKLMN}\widetilde{\mathfrak{E}}_{LMN,K} + \frac{J}{2}\mathscr{C}_{MLIJ}E_M\epsilon E_L + JC^{-1}_{LM}E_{M,K}\mu_{LIJK}, \quad (2.141a)\\
D_L(\boldsymbol{\chi},\Phi) &:= \widehat{D}_L(\boldsymbol{\chi},\Phi) \\
&= JC^{-1}_{KL}\left(\epsilon E_K + \mu_{KIJM}\widetilde{\mathfrak{E}}_{IJM}\right), \quad (2.141b)\\
T_i(\boldsymbol{\chi},\Phi) &:= F_{iI}\left[\left(S_{IJ} - \tilde{S}_{IKJ,N}P_{NK}\right)N_J + \tilde{S}_{IJK}\tilde{N}_{JK}\right] - \tilde{F}_{iIN}P_{NK}\tilde{S}_{IKJ}N_J, \quad (2.141c)\\
R_i(\boldsymbol{\chi},\Phi) &:= F_{iI}\tilde{S}_{IJK}N_JN_K, \quad (2.141d)\\
W(\boldsymbol{\chi},\Phi) &:= -D_LN_L, \quad (2.141e)\\
J_i(\boldsymbol{\chi},\Phi) &:= \left[\left[F_{iI}\tilde{S}_{IJK}M_JN_K\right]\right]; \quad (2.141f)
\end{aligned}$$

where $\boldsymbol{N}$, $\boldsymbol{M}$, $\mathbf{P}$ and $\tilde{\mathbf{N}}$ are the analogues of the normal vector, conormal vector, surface projection operator and second-order geometry tensor, as defined in Section 2.2.2, computed in the reference frame Ω_0.

Upon inspection, the second Piola-Kirchhoff stress tensor $\mathbf{S}$ in Eq. (2.141a) is composed by four terms. The first two terms correspond to the classical and high-order mechanical stresses, respectively. The third one corresponds to the total second Piola-Maxwell stress tensor $\mathbf{S}^{\text{Maxwell}}$. This becomes evident by expanding it as

$$S^{\text{Maxwell}}{}_{IJ} := \frac{J}{2}\mathscr{C}_{MLIJ}E_M\epsilon E_L = JF^{-1}_{Ii}F^{-1}_{Jj}\epsilon\left[\left(E_MF^{-1}_{Mi}\right)\left(E_LF^{-1}_{Lj}\right) - \frac{1}{2}\left(E_MF^{-1}_{Ma}\right)\left(E_LF^{-1}_{La}\right)\delta_{ij}\right], \quad (2.142)$$

and obtanining its spatial counterpart by using Eq. (2.94) and (2.95) as

$$\boldsymbol{\sigma}^{\text{Maxwell}} := \epsilon\left(\boldsymbol{e}\otimes\boldsymbol{e} - \frac{1}{2}|\boldsymbol{e}|^2\mathbf{I}\right). \quad (2.143)$$

The last term corresponds to the total flexoelectricity-induced stress, and is analogous to the term appearing in the linear theory of flexoelectricity, cf. Eq. (2.62), with an *effective* flexoelectricity tensor (cf. Eq. (2.116)) depending on the deformation state.

The nominal electric displacement in Eq. (2.141b), in turn, is also analogous to the electric displacement in the linear theory of flexoelectricity, cf. Eq. (2.60c), with *effective* dielectricity (cf. Eq. (2.115)) and flexoelectricity tensors.

This model is illustrated and analyzed in Section 3.2.6 resorting to numerical computation of a cantilever rod, which constitutes the simplest functional flexoelectric device. The successful electromechanical modeling of flexoelectric devices at large deformations, including novel physics such as electrostriction (based on the Maxwell stress effect) and novel electromechanical mechanisms (such as mechanically and electrically-induced buckling) enables the rational design of soft flexoelectric devices harnessing the intrinsic nonlinearities of the physics, which are not present in former linear flexoelectricity models.

2.2.4.1.b Nitsche's method

Following Nitsche's approach, and analogously to Section 2.2.2.1.b, the enthalpy functional $\Pi_{\mathrm{D}}^{(\mathrm{Dir})}$ in Eq. (2.130) is modified as

$$\Pi^{(\mathrm{Dir})}[\boldsymbol{\chi}, \Phi] = \Pi_{\mathrm{D}}^{(\mathrm{Dir})}[\boldsymbol{\chi}, \Phi] + \Pi^{\mathrm{Nitsche}}[\boldsymbol{\chi}, \Phi], \tag{2.144}$$

where $\Pi^{\mathrm{Nitsche}}[\boldsymbol{\chi}, \Phi]$ acts on the Dirichlet boundaries incorporating essential boundary conditions in Eq. (2.127) weakly as follows:

$$\begin{aligned}
\Pi^{\mathrm{Nitsche}}[\boldsymbol{\chi}, \Phi] = & \int_{\partial\Omega_0^\chi} \left(\frac{1}{2}\beta_\chi \left(\chi_i - \overline{\chi}_i\right)^2 - \left(\chi_i - \overline{\chi}_i\right) T_i(\boldsymbol{\chi}, \Phi) \right) \mathrm{d}\Gamma_0 \\
& + \int_{\partial\Omega_0^V} \left(\frac{1}{2}\beta_V \left(\partial_0^N \chi_i - \overline{V}_i\right)^2 - \left(\partial_0^N \chi_i - \overline{V}_i\right) R_i(\boldsymbol{\chi}, \Phi) \right) \mathrm{d}\Gamma_0 \\
& + \int_{\partial\Omega_0^\Phi} \left(-\frac{1}{2}\beta_\Phi \left(\Phi - \overline{\Phi}\right)^2 + \left(\Phi - \overline{\Phi}\right) W(\boldsymbol{\chi}, \Phi) \right) \mathrm{d}\Gamma_0 \\
& + \int_{C_0^\chi} \left(\frac{1}{2}\beta_{C_\chi} \left(\chi_i - \overline{\chi}_i\right)^2 - \left(\chi_i - \overline{\chi}_i\right) J_i(\boldsymbol{\chi}, \Phi) \right) \mathrm{d}s_0,
\end{aligned} \tag{2.145}$$

with the numerical parameters $\beta_\chi, \beta_V, \beta_\Phi, \beta_{C_\chi} \in \mathbb{R}^+$.

The variational principle associated to $\Pi^{(\mathrm{Dir})}$ for the equilibrium states $(\boldsymbol{\chi}^*, \Phi^*)$ is

$$(\boldsymbol{\chi}^*, \Phi^*) = \arg \min_{\boldsymbol{\chi} \in \mathcal{X}} \max_{\Phi \in \mathcal{P}} \Pi^{(\mathrm{Dir})}[\boldsymbol{\chi}, \Phi], \tag{2.146}$$

where $\mathcal{P} := H^1(\Omega_0)$, and $\mathcal{X}$ is the space of functions belonging to $\left[H^2(\Omega_0)\right]^3$ with L^2-integrable third derivatives on the boundary $\partial\Omega_0^\chi$.

The weak form reads: *Find* $(\boldsymbol{\chi}, \Phi) \in \mathcal{X} \otimes \mathcal{P}$ *such that,* $\forall (\delta\boldsymbol{\chi}, \delta\Phi) \in \mathcal{X} \otimes \mathcal{P}$,

$$\begin{aligned}
\delta\Pi^{(\mathrm{Dir})} &= \delta_{\boldsymbol{u}}\Pi^{(\mathrm{Dir})} + \delta_\phi \Pi^{(\mathrm{Dir})} \\
&= \int_{\Omega_0} \left(\hat{S}_{IJ}\delta\mathfrak{E}_{IJ} + \tilde{S}_{IJK}\delta\widetilde{\mathfrak{E}}_{IJK} - \hat{D}_L \delta E_L - \overline{B}_i \delta\chi_i + \overline{Q}\delta\Phi \right) \mathrm{d}\Omega_0 \\
&\quad + \int_{\partial\Omega_0^T} -\overline{T}_i \delta\chi_i \,\mathrm{d}\Gamma_0 + \int_{\partial\Omega_0^\chi} \left(\left(\chi_i - \overline{\chi}_i\right) \left(\beta_\chi \delta\chi_i - \delta T_i\right) - T_i \delta\chi_i \right) \mathrm{d}\Gamma_0 \\
&\quad + \int_{\partial\Omega_0^R} -\overline{R}_i \partial_0^N \delta\chi_i \,\mathrm{d}\Gamma_0 + \int_{\partial\Omega_V} \left(\left(\partial_0^N \chi_i - \overline{V}_i\right) \left(\beta_V \partial_0^N \delta\chi_i - \delta R_i\right) - R_i \partial_0^N \delta\chi_i \right) \mathrm{d}\Gamma_0 \\
&\quad + \int_{\partial\Omega_0^W} \overline{W}\delta\Phi \,\mathrm{d}\Gamma_0 + \int_{\partial\Omega_0^\Phi} \left(-\left(\Phi - \overline{\Phi}\right) \left(\beta_\Phi \delta\Phi - \delta W\right) + W\delta\Phi \right) \mathrm{d}\Gamma_0 \\
&\quad + \int_{C_0^J} -\overline{J}_i \delta\chi_i \,\mathrm{d}s_0 + \int_{C_0^\chi} \left(\left(\chi_i - \overline{\chi}_i\right) \left(\beta_{C_\chi} \delta\chi_i - \delta J_i\right) - J_i \delta\chi_i \right) \mathrm{d}s_0 \\
&= 0;
\end{aligned} \tag{2.147}$$

with

$$\begin{aligned}
\delta \boldsymbol{T}(\boldsymbol{\chi}, \phi; \delta\boldsymbol{\chi}, \delta\Phi) &:= \delta F_{iI} \left[\left(S_{IJ} - \tilde{S}_{IKJ,N} P_{NK} \right) N_J + \tilde{S}_{IJK} \tilde{N}_{JK} \right] \\
&\quad + F_{iI} \left[\left(\delta S_{IJ} - \delta\tilde{S}_{IKJ,N} P_{NK} \right) N_J + \delta\tilde{S}_{IJK} \tilde{N}_{JK} \right] \\
&\quad - \left(\delta\tilde{F}_{iIN} \tilde{S}_{IKJ} + \tilde{F}_{iIN} \delta\tilde{S}_{IKJ} \right) P_{NK} N_J, && \text{(2.148a)} \\
\delta \boldsymbol{R}(\boldsymbol{\chi}, \phi; \delta\boldsymbol{\chi}, \delta\Phi) &:= \left(\delta F_{iI} \tilde{S}_{IJK} + F_{iI} \delta\tilde{S}_{IJK} \right) N_J N_K, && \text{(2.148b)} \\
\delta W(\boldsymbol{\chi}, \phi; \delta\boldsymbol{\chi}, \delta\Phi) &:= - \delta D_L N_L, && \text{(2.148c)} \\
\delta \boldsymbol{J}(\boldsymbol{\chi}, \phi; \delta\boldsymbol{\chi}, \delta\Phi) &:= \left[\left[\left(\delta F_{iI} \tilde{S}_{IJK} + F_{iI} \delta\tilde{S}_{IJK} \right) M_J N_K \right] \right]. && \text{(2.148d)}
\end{aligned}$$

The expressions for $\delta \mathrm{S}(\boldsymbol{\chi}, \phi; \delta\boldsymbol{\chi}, \delta\Phi)$, $\delta\tilde{\mathrm{S}}(\boldsymbol{\chi}, \phi; \delta\boldsymbol{\chi}, \delta\Phi)$, $\delta\nabla\tilde{\mathrm{S}}(\boldsymbol{\chi}, \phi; \delta\boldsymbol{\chi}, \delta\Phi)$ and $\delta\boldsymbol{D}(\boldsymbol{\chi}, \phi; \delta\boldsymbol{\chi}, \delta\Phi)$ are quite lengthy, and can be found in Appendix B.

2.3 On-going and future work

2.3.1 Legendre transform and variational model for Lifshitz-invariant flexoelectricity at finite deformation

The Legendre transform at finite deformations presented in Section 2.2.3 for the direct flexoelectric model can also be derived for the Lifshitz-invariant model, as done in Section 2.2.1.3 for infinitesimal deformations. The only relevant difference with respect to the infinitesimal deformation framework is the appearance of additional terms in the enthalpy density arising from the integration by parts of certain terms depending on the deformation state.

However, we did not investigated this line of research (yet) since, prior to modeling finite deformations, the features and properties of the Lifshitz-invariant model (e.g. the appearance of a boundary layer) should be completely understood at infinitesimal deformations, as well as the appropriate numerical stabilization that is required (see Section 3.3.1) in order to properly solve the boundary value problem.

2.3.2 Consideration of a dielectric surrounding media

In this work we only considered boundary value problems involving the flexoelectric material being object of study. However, the media (typically air) surrounding it is also dielectric (although not polarizable), and hence the electric potential is not confined to the material but extends towards the surroundings. Rather than considering homogeneous electric Neumann boundary conditions on the free surfaces, it may be more realistic to directly model the surrounding medium as a dielectric, interacting with the solid by means of electrical interface conditions, and prescribing Dirichlet or Robin boundary conditions far enough from the sample, cf. Fig. 2.5. This issue becomes more relevant when considering soft materials with relatively low dielectric constant (Thai *et al.*, 2018, Yvonnet and Liu, 2017).

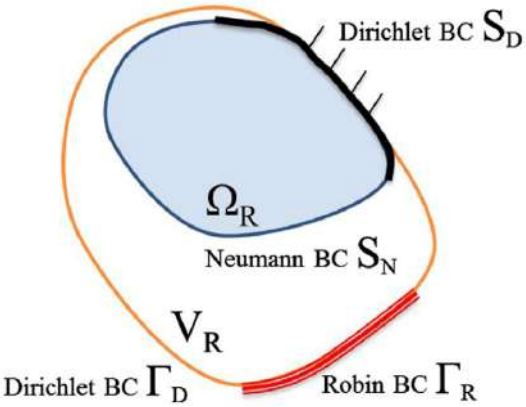

Mechanical and electrical boundary conditions are imposed on the reference configuration: the deformation $\chi = \chi_0$ on S_D and a traction of $\tilde{\mathbf{t}}^e$ is applied on S_N; the electric potential on Γ_D is prescribed as $\xi = \xi_b$ and a Robin boundary condition is applied on Γ_R. Here, S_D and S_N are a subdivision of $\partial\Omega_R$ while Γ_D and Γ_R are a subdivision of ∂V_R.

Figure 2.5: Sketch of a flexoelectric material Ω_R embedded in a dielectric media V_R. Adapted from Liu (2014).

2.3.3 Surface effects

In the context of flexoelectricity, boundary layers are usually attributed to surface piezoelectricity (Liang *et al.*, 2014, Shen and Hu, 2010, Yan, 2017, Zhuang *et al.*, 2019, Zubko *et al.*, 2013), which is seen as a different electromechanical coupling between strains and polarization developed at the boundary of the samples, coexisting with the bulk flexoelectric effect (see Fig. 2.6). It is usually modeled by a zero-thickness layer at the boundaries, which leads to a surface energy density contribution on top of the bulk energy density.

In the computational experiments reported in Section 2.2.2.3, however, boundary layers are obtained from the Lifshitz-invariant form of flexoelectricity (cf. Fig. 2.3d), which is associated to a purely bulk energy density. This finding suggests that there might exist a link between surface piezoelectricity and bulk flexoelectricity explained, at least in part, by the Lifshitz-invariant form of flexoelectricity. Moreover, note that the surface piezoelectricity and bulk flexoelectricity tensors have the same units, further supporting this idea.

The exploration of surface effects and their relation to existing bulk flexoelectricity models is a matter of author's very recent and future research. The MSc. thesis of M. Dingle (Dingle Palmer, 2020), co-supervised by the author of this manuscript, takes the first steps in this direction.

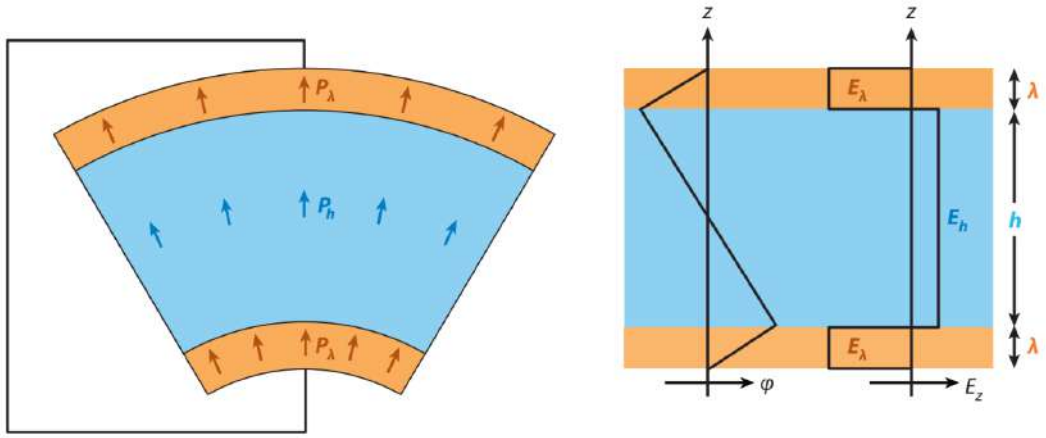

Surface piezoelectricity. Upon bending, as shown on the left, the tensile/compressive strains in the top/bottom surface layers give rise to a polarization P_λ in the piezoelectric surface layers of thickness λ. Because the normal component of the electric displacement must remain constant, this surface polarization gives rise to electric fields E_b and thus to a polarization P_b within the nonpiezoelectric bulk. The measured average polarization of the whole structure therefore depends not only on the dielectric properties of the piezoelectric surface layers but also on those of the bulk. The potential φ and field E profiles along the sample thickness are shown on the right.

Figure 2.6: Surface piezoelectricity model. Adapted from Zubko *et al.* (2013).

2.3.4 Photoflexoelectricity

Photoflexoelectricity (Yang *et al.*, 2018) is a very recent physical effect by which photovoltaic energy conversion and flexoelectricity are combined. Traditional solar cells are based on the photovoltaic effect, by which built-in semiconducting junctions induce an electrical current in the presence of light (photons), and is usually manifested only in noncentrosymmetric (piezoelectric or ferroelectric) semiconductors. However, it has been recently shown (Yang *et al.*, 2018) that any semiconductor (including the centrosymmetric ones, which do not feature semiconducting junctions) under applied strain-gradients feature also a bulk photovoltaic effect, thanks to the electromechanical interaction induced by flexoelectricity. This finding may extend nowadays solar cell technologies by boosting the solar energy conversion efficiency from a wide pool of established semiconductors.

Conversely, it has also been shown (Shu *et al.*, 2020) that the effective flexoelectric coefficients of semiconductors under a source of light are orders of magnitude higher than in the dark, and much larger than those of traditional dielectric insulators, cf. Fig. 2.7.

This interesting phenomenon has been scarcely modeled and numerically solved, and is of the interest of future research of this manuscript's author.

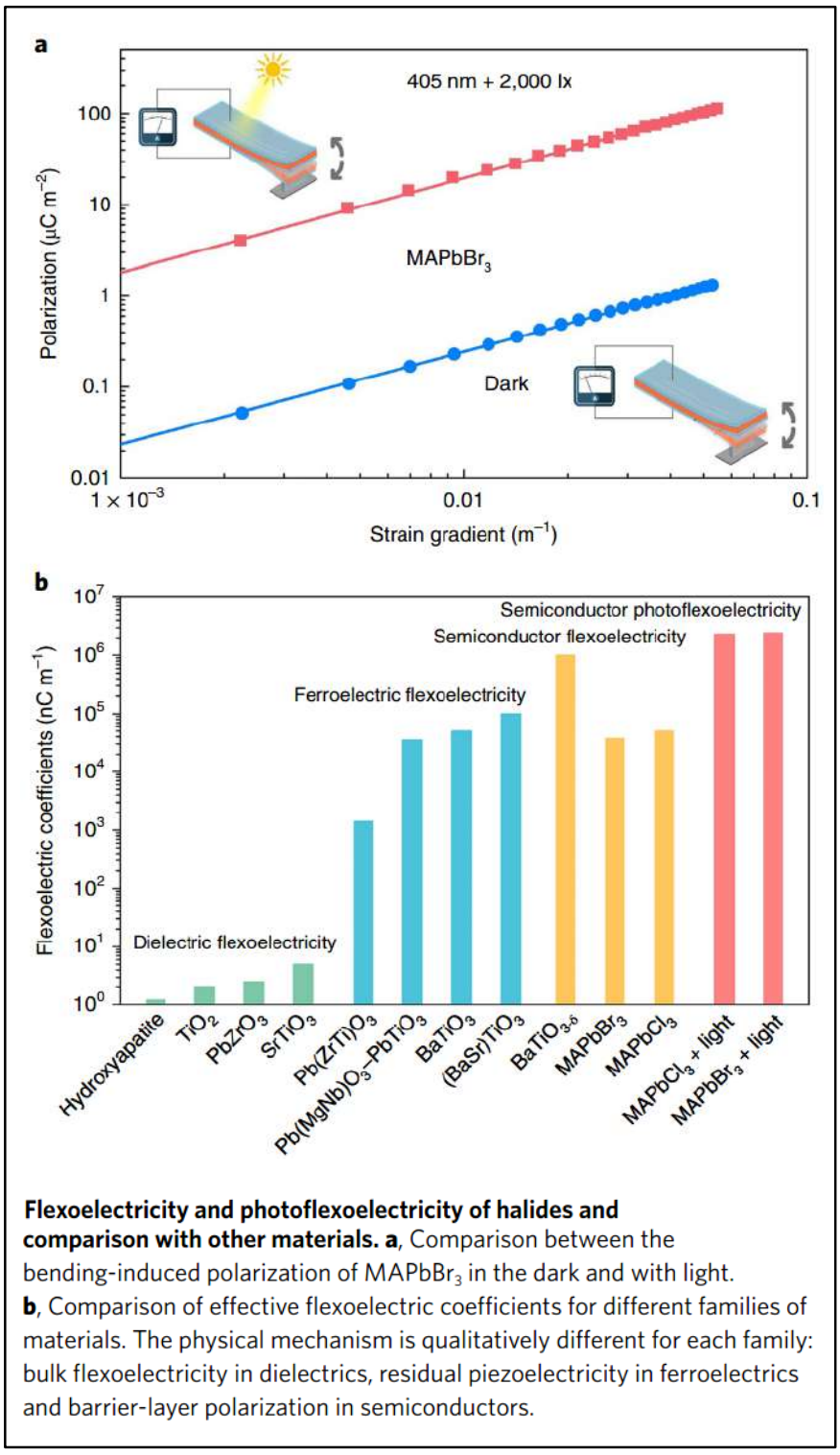

Flexoelectricity and photoflexoelectricity of halides and comparison with other materials. a, Comparison between the bending-induced polarization of $MAPbBr_3$ in the dark and with light. **b**, Comparison of effective flexoelectric coefficients for different families of materials. The physical mechanism is qualitatively different for each family: bulk flexoelectricity in dielectrics, residual piezoelectricity in ferroelectrics and barrier-layer polarization in semiconductors.

Figure 2.7: Photoflexoelectric effect. Adapted from Shu *et al.* (2020).

2.4 Concluding remarks

The continuum modeling of flexoelectricity has been reviewed. The relation between the energy and enthalpy forms of the Direct and Lifshitz-invariant flexoelectricity models has been clarified, as well as the relation between the material tensors of each. The effect of considering the gradient polarization term has been derived and discussed, leading in general to flexoelectric models that are not equivalent due to the modification of the Maxwell-Faraday's equation that states the irrotationality of the electric field.

The relation between the energy and enthalpy forms of the Direct flexoelectricity model has also been analyzed in the framework of finite deformations. We propose the first flexoelectric model at finite deformations coupling strain gradients and electric polarization by means of a fully Lagrangian flexoelectric tensor, analogous to that of infinitesimal deformations, leading to an objective energy potential by construction.

The direct and Lifshitz-invariant flexoelectricity boundary value problems have been compared in infinitesimal-deformation cantilever benchmark setups. The latter presents a higher flexoelectricity-induced stiffening of the beam, and features a boundary layer where the electric field behaves differently than in the bulk.

Based on the enthalpy forms of the direct and Lifshitz-invariant flexoelectricity models, the associated variational principles and boundary value problems have been derived accounting for strong or weak enforcement of Dirichlet boundary conditions. As a difference from other works in the literature, the contributions at the edges of the boundary arising from the 4th-order PDE have been taken into account, which is essential to maintain the self-consistency of the formulation.

The modeling presented in this Chapter is considered in Chapter 3 to solve the associated boundary value problems by means of numerical methods.

Chapter 3

Numerical solution methods

3.1 State of the art

The equations of flexoelectricity can only be solved analytically in very simple settings, such as simplified Euler-Bernoulli (Baroudi and Najar, 2019, Deng *et al.*, 2014a, Liang *et al.*, 2014) and Timoshenko beam (Zhang *et al.*, 2016a) models. Otherwise, it is necessary to resort to computational flexoelectricity. We refer to Zhuang *et al.* (2020) for a comprehensive review on computational approaches to solve flexoelectricity boundary value problems.

The major challenge is to handle the C^1 continuity of the state variables required by the fourth-order PDE system. To address this, several numerical alternatives have been proposed, such as mesh-free approximations (Abdollahi and Arias, 2015, Abdollahi *et al.*, 2015a, 2014, 2015b, Zhuang *et al.*, 2019), isogeometric analysis (Ghasemi *et al.*, 2017, 2018, Hamdia *et al.*, 2018, Nanthakumar *et al.*, 2017, Nguyen *et al.*, 2019, Thai *et al.*, 2018) and C^1 Argyris triangular element approximation (Yvonnet and Liu, 2017). Another family of numerical methods are those circumventing the C^1 continuity requirement by introducing additional variables, such as mixed formulations (Deng *et al.*, 2018, 2017, Mao *et al.*, 2016), or those based on micromorphic theories of continua (McBride *et al.*, 2020, Poya *et al.*, 2019). Recently, a few works report the application of these methods to large deformation flexoelectricity (McBride *et al.*, 2020, Nguyen *et al.*, 2019, Poya *et al.*, 2019, Thai *et al.*, 2018, Yvonnet and Liu, 2017, Zhuang *et al.*, 2019).

The aforementioned numerical approaches have some limitations or drawbacks, as listed below:

- **Difficulty to handle arbitrarily shaped geometries.** On the one hand, the isogeometric analysis is based on a conforming discretization by means of B-spline or NURBS patches, which have rectangular shape in 2D (cuboidal shape in 3D). This approach has been typically considered to model flexoelectric beams and trapezoidal shapes, but cannot handle arbitrary geometries.

On the other hand, mesh-free methods are convenient to discretize convex geometries. However, it is in general difficult to approximate more complicated geometries with internal holes or multiple features.

- **Difficulty to mesh arbitrarily shaped geometries.** The C^1 Argyris element, mixed finite elements and micromorphic approaches rely on an unstructured mesh partitioning the domain of interest. The generation of the mesh is not trivial, specially in 3D, and it can be the bottleneck of the computation for complex enough geometries.

- **Limited or suboptimal error convergence rates.** Some of the aforementioned methods present limitations regarding the error convergence rates. On the one hand, the mesh-free approximations have a limited L_2 error convergence of order $\mathcal{O}(h^2)$. Both the compactly supported radial basis function (CSRBF) shape functions presented in Zhuang *et al.* (2019), which can have C^2 or C^4 continuity, and the C^∞-continuous local maximum-entropy (LME) mesh-free approximants from Abdollahi *et al.* (2014), span functional spaces with C^1 consistency. Namely, they can exactly reproduce linear functions only. Since the flexoelectricity equations depend on the approximation of the strain gradients, a C^1-consistent approximation space is not sufficient to ensure systematic convergence upon mesh refinement.

  On the other hand, the C^1 Argyris element present in Yvonnet and Liu (2017) is C^2-consistent, yielding approximations with L_2 error convergence of $\mathcal{O}(h^3)$. However, the convergence rate cannot be systematically increased.

- **Large computational cost.** In contrast to approximations built on top of a mesh, the mesh-free methods require an intermediate step consisting on the computation of the basis functions themselves. This step yields an increase in the computational cost, specially if the aforementioned process is iterative. Moreover, richer numerical quadratures are usually required since the resulting basis functions are not polynomial.

  Another substantial increase in computational cost in mesh-based methods is due to having a large number of degrees of freedom per element. This is the case of C^1 Argyris element, mixed finite elements and micromorphic theories of continua.

- **Poor scalability.** A typical feature of mesh-free methods, specially those with non-compact basis such as the LME approximants in Abdollahi *et al.* (2014), is that the basis functions overlap with a large number of other basis functions, yielding a system matrix with a large fill-in and with an unstructured sparsity pattern. These facts deteriorate the scalability and parallelization of the method in terms of constructing and solving the algebraic system of equations.

3.2 Main contributions

In view of the limitations and drawbacks of current numerical approaches present in the computational flexoelectricity literature, an alternative approach based on immersed boundary B-Spline approximation is proposed here. This approach circumvents the limitations of other methods, at the expense of dealing with unfitted meshes and smooth, non-interpolant discretizations of the state variables. Moreover it requires enforcing essential boundary conditions weakly by adding some integral terms in the weak form.

The developed computational framework is introduced in Section 3.2.1. An overview of body-fitted B-spline approximation is given in Section 3.2.2, since it is itself a useful method for simulating flexoelectricity in rectangular or cuboidal domains. The extension to handle arbitrarily shaped geometries, i.e. the immersed boundary B-spline method, is presented in Section 3.2.3. The remaining Sections of this Chapter make use of the aforedescribed numerical methods to solve different flexoelectricity boundary value problems of practical and engineering interest.

Section 3.2.4 shows a three-dimensional simulation of a conical semicircular rod under torsion that can be used to characterize the shear flexoelectric coefficient.

Section 3.2.5 presents the sensing electrode boundary conditions and uses them towards the design of scalable flexoelectric sensors working under an applied rotation.

Section 3.2.6 shows the numerical strategy used to solve flexoelectricity boundary value problems at large deformations, which yield a nonlinear system of equations. The approach is illustrated by studying the response of soft flexoelectric rods, which constitute the simplest functional flexoelectric devices, under mechanically- or electrically-induced bending and buckling states. The rich interplay between flexoelectricity, electrostriction and geometrical instabilities is thoroughly analyzed.

Finally, Section 3.2.7 extend the previous approach for large deformations to arbitrarily-shaped soft flexoelectric devices, which requires introducing unfitted discretization and Nitsche's method to the nonlinear problem. The method is used to compute the response of a flexoelectric sensor composed by periodically-arranged collective-beams. The device works under compression, while the inner beams composing it activate the flexoelectric effect by buckling.

3.2.1 iHB-FEM computational framework

The numerical approach proposed in this Chapter presents many particularities that preclude its implementation within standard commercial finite element-based libraries. Hence, an in-house computational framework has been implemented from scratch. It is named *iHB-FEM*, which stands for I*mmersed boundary* h*ierarchical* B-*splines* f*ramework for* e*lectro*m*echanics*. Despite its name, its functionalities have been extended in various ways, and it currently allows body-fitted approximations in Cartesian domains, as well as other physical problems than electromechanics. The framework is able to handle 2D and 3D problems.

The code is written in Matlab (MATLAB, 2015), and it makes use of certain precompiled C libraries and advanced vectorization features that result in a good efficiency and reasonable scalability for an interpreted language. It belongs to the FLEXOCOMP group lead by prof. Irene Arias, and has been mainly developed and maintained by this manuscript's author with the help of Dr. Onofre Marco as a postdoctoral researcher. Its modularity, readability and documentation allow for a relatively easy hands-on for PhD students, master students and other researchers to use it and extend their features and capabilities. Remarkable contributions towards the implementation of new functionalities, testing and documentation are attributed to Jordi Barceló-Mercader, Alice Mocci and Hossein Mohammadi, current PhD students in the FLEXOCOMP group. Also, several students have used it for their master's thesis, introducing new physics and features. This is the case of Monica Dingle (Dingle Palmer, 2020) and Sergi de la Torre (De La Torre Israel, 2020).

The most essential features of the computational framework are reported in Codony *et al.* (2019).

3.2.2 Body-fitted B-spline approximation

The B-spline approximation in conforming (or body-fitted) meshes is a simple enough method to successfully resolve the flexoelectricity equations in a smooth approximation space. It can only be used to discretize rectangular (or cuboidal) geometries, and therefore is suitable for the study of flexoelectricity in cantilever beams. Moreover, in practical terms, it is also useful to test the implementation of different continuum models before implementing them within the immersed boundary framework.

3.2.2.1 Uniform B-Spline basis

B-spline functions (de Boor, 2001, Piegl and Tiller, 2012, Rogers, 2001) are smooth piece-wise polynomials with minimal (compact) support. Being p the polynomial degree, they are by construction C^{p-1}-continuous throughout the domain, and therefore can be used as basis for the smooth approximation and interpolation of functions.

Let us consider a *uniform* B-spline basis. The univariate uniform B-spline basis of degree p consisting of n basis functions is defined on the unidimensional parametric space $\xi \in \Xi = [0, n+p]$ in terms of the *uniform knot vector* $\boldsymbol{k} = [k_0, k_1, k_2, \dots, k_{n+p}] = [0, 1, 2, 3, \dots, n+p]$. The i-th function of this basis is defined recursively as (de Boor, 2001):

$$\begin{aligned} B_i^0(\xi) &= \begin{cases} 1 & k_i \leq \xi < k_{i+1} \\ 0 & \text{otherwise} \end{cases}; \\ B_i^p(\xi) &= \frac{\xi - k_i}{k_{i+p} - k_i} B_i^{p-1}(\xi) + \frac{k_{i+p+1} - \xi}{k_{i+p+1} - k_{i+1}} B_{i+1}^{p-1}(\xi); \end{aligned} \qquad i = 0, \dots, n-1. \tag{3.1}$$

B-Spline basis are smooth (C^{p-1}), positive-valued functions with compact ($p+1$) support,

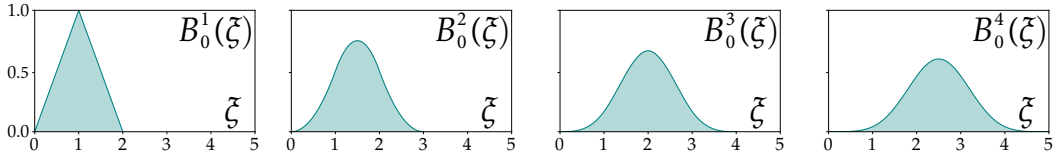

(a) Linear ($p = 1$) (b) Quadratic ($p = 2$) (c) Cubic ($p = 3$) (d) Quartic ($p = 4$)

Figure 3.1: First univariate B-spline basis function $B_0^p(\xi)$ of degree p. Figure adapted from Codony *et al.* (2019).

and they form a partition of unity. They are explicitly evaluated and exactly integrated by rich enough numerical quadratures, thanks to their piece-wise polynomial nature. However, they do not satisfy the Kronecker delta property (except for the trivial case $p = 1$).

Due to the uniformity of the knot vector, the i-th B-spline function can be expressed as a translation of the first (0th) one as $B_i^p(\xi) = B_0^p(\xi - i)$. Figure 3.1 shows the function $B_0^p(\xi)$ of the basis for degrees $p = \{1, \dots, 4\}$.

In the D-dimensional space, the $\boldsymbol{i}$-th B-spline function $B_{\boldsymbol{i}}^p(\boldsymbol{\xi})$ of a D-variate B-spline basis (where $\boldsymbol{i}$ is the D-variate index $[i_1, \dots, i_D]$) is defined as the tensor product of D univariate B-spline functions as

$$B_{\boldsymbol{i}}^p(\boldsymbol{\xi}) = B_{[i_1,\dots,i_D]}^p([\xi_1, \dots, \xi_D]) := \prod_{d=1}^{D} B_{i_d}^p(\xi_d); \qquad \text{with} \qquad i_d = 0, \dots, n_d - 1, \tag{3.2}$$

which is defined on the D-dimensional parametric space $\boldsymbol{\xi} \in \Xi = [0, n_1 + p] \otimes \cdots \otimes [0, n_D + p]$. Therefore, the parametric space is a hyperrectangle (e.g. a rectangle in 2D or a cuboid in 3D) defined globally on a D-dimensional Cartesian grid, in contrast with traditional Lagrangian basis present in standard FEM implementations, whose parametric space is defined element-wise.

3.2.2.2 Approximation of the state variables

In order to use B-Spline basis (defined in the parametric space Ξ) to approximate the state variables $\boldsymbol{u}$ and ϕ (defined in the physical space Ω), let us define the geometrical map

$$\begin{aligned} \boldsymbol{\varphi} : \Xi &\longrightarrow \Omega \\ \boldsymbol{\xi} &\longmapsto \boldsymbol{x} = \boldsymbol{\varphi}(\boldsymbol{\xi}), \end{aligned} \tag{3.3}$$

which maps a given point $\boldsymbol{\xi} \in \Xi$ in the parametric space to a given point $\boldsymbol{x} \in \Omega$ in the physical space. The basis functions $\boldsymbol{N}(\boldsymbol{x}) \in \Omega$ are defined as $\boldsymbol{N} = [\boldsymbol{B}^p \circ \boldsymbol{\varphi}^{-1}]$, in such a way that

$$[\boldsymbol{u}(\boldsymbol{x})]_d \simeq \left[\boldsymbol{u}^h(\boldsymbol{x})\right]_d = \sum_{\boldsymbol{i}} N_{\boldsymbol{i}}(\boldsymbol{x}) a^u{}_{\boldsymbol{i}d} = \sum_{\boldsymbol{i}} B^p_{\boldsymbol{i}}(\boldsymbol{\xi}) a^u{}_{\boldsymbol{i}d}, \qquad d = 1, \dots, D; \tag{3.4a}$$

$$\phi(\boldsymbol{x}) \simeq \phi^h(\boldsymbol{x}) = \sum_{\boldsymbol{i}} N_{\boldsymbol{i}}(\boldsymbol{x}) a^\phi{}_{\boldsymbol{i}} = \sum_{\boldsymbol{i}} B^p_{\boldsymbol{i}}(\boldsymbol{\xi}) a^\phi{}_{\boldsymbol{i}}; \tag{3.4b}$$

where $\{\boldsymbol{a}^{\boldsymbol{u}}, \boldsymbol{a}^{\boldsymbol{\phi}}\}$ are the degrees of freedom (known as the *control variables* in B-spline nomenclature) of the approximations $\boldsymbol{u}^h(\boldsymbol{x})$ and $\phi^h(\boldsymbol{x})$. Since B-spline bases do not satisfy in general the Kronecker delta property, the control variables do not necessarily take the value of the interpolated function at any point, and therefore one should not think of them as "nodal values" as in standard FEM.

Typically, the map $\boldsymbol{\varphi}(\boldsymbol{\xi})$ is expressed as the interpolation of a discretization of the physical space, namely:

$$[\boldsymbol{\varphi}(\boldsymbol{\xi})]_d \simeq \sum_{\boldsymbol{i}} S_{\boldsymbol{i}}(\boldsymbol{\xi}) \hat{x}_{\boldsymbol{i}d}, \qquad d = 1, \dots, D; \tag{3.5}$$

where $\boldsymbol{S}(\boldsymbol{\xi})$ are the basis functions for the interpolation of the geometry, and $\hat{\boldsymbol{x}}$ are points on the physical space defining the map (known as the *control points* in B-spline nomenclature). Different choices of $\boldsymbol{S}(\boldsymbol{\xi})$ and $\hat{\boldsymbol{x}}$ are possible. However, since $\boldsymbol{N}(\boldsymbol{x})$ must maintain the C^{p-1} continuity of B-Spline basis, $\boldsymbol{S}(\boldsymbol{\xi})$ must be C^{p-1}-continuous too, and the most natural choice is $\boldsymbol{S}(\boldsymbol{\xi}) := \boldsymbol{B}^p(\boldsymbol{\xi})$. This choice is typically known as Isogeometric (Hughes *et al.*, 2005) when $\boldsymbol{\varphi}(\boldsymbol{\xi})$ represents an exact interpolation of the geometry Ω.

Therefore, the geometrical map $\boldsymbol{x} = \boldsymbol{\varphi}(\boldsymbol{\xi})$ is globally defined, in contrast with traditional FEM implementations, where it is defined element-wise. This implies that a conforming (or body-fitted) discretization of Ω must be homeomorphic to the parametric space Ξ, i.e. Ω must be homeomorphic to a hyperrectangle. This requirement on Ω is circumvented in Section 3.2.3 by means of the Immersed boundary method, where a non-conforming (or unfitted) Cartesian discretization of Ω is considered instead, allowing Ω having any arbitrary shape.

However, in the particular case of Ω being a hyperrectangle, a conforming discretization can be directly considered, leading to a uniform Cartesian grid made of cells of size $\{h_1 \times \cdots \times h_D\}$. In such a case, the global geometry interpolation in Eq. (3.5) is equivalent to a local (cell-wise) linear mapping

$$\boldsymbol{\varphi}^c(\check{\boldsymbol{\xi}}^c) = \check{\boldsymbol{x}}^c_{\boldsymbol{0}} + \sum_{d=1}^{D} h_d \check{\xi}^c_d \boldsymbol{e}_d \tag{3.6}$$

being $\check{\boldsymbol{x}}^c_{\boldsymbol{0}}$ the first corner of the cell c, and $\check{\boldsymbol{\xi}}^c \in [0,1] \otimes \cdots \otimes [0,1]$ the cell-wise parametric space. The C^{p-1}-continuity of $\boldsymbol{N}(\boldsymbol{x})$ is not compromised thanks to the uniformity of the mesh. The

Jacobian of the geometric mapping turns out constant and diagonal, i.e.

$$\boldsymbol{J} = \nabla^{\check{\boldsymbol{\xi}}} \boldsymbol{\varphi}(\check{\boldsymbol{\xi}}^c) = \sum_{d=1}^{D} \boldsymbol{e}_d \otimes \boldsymbol{e}_d h_d = \begin{bmatrix} h_1 & 0 & 0 \\ 0 & \ddots & 0 \\ 0 & 0 & h_D \end{bmatrix}, \tag{3.7}$$

namely a scaling of the parametric space along each Cartesian direction. This simple expression is convenient for numerical computations, specially to compute the (high-order) gradients of the basis functions in Ω, since the tensor product structure of the basis is preserved, e.g.

$$\nabla^{\boldsymbol{x}}{}_j N_{\boldsymbol{i}}(\boldsymbol{x}) = \nabla^{\boldsymbol{x}}{}_j [B^p_{\boldsymbol{i}} \circ \boldsymbol{\varphi}^{-1}](\boldsymbol{x}) = \nabla^{\boldsymbol{\xi}}{}_k B^p_{\boldsymbol{i}}(\boldsymbol{\xi}) \boldsymbol{J}^{-1}_{kj} = h_j^{-1} \left(\tfrac{\partial}{\partial \xi_j} B^p_{i_j}(\xi_j) \right) \textstyle\prod_{d \neq j}^{D} B^p_{i_d}(\xi_d); \tag{3.8a}$$

$$\nabla^{\boldsymbol{x}}{}_k \left[\nabla^{\boldsymbol{x}}{}_j N_{\boldsymbol{i}} \right](\boldsymbol{x}) = \cdots = \begin{cases} h_j^{-2} \left(\tfrac{\partial^2}{\partial^2 \xi_j} B^p_{i_j}(\xi_j) \right) \prod_{d \neq j}^{D} B^p_{i_d}(\xi_d) & \text{if} \quad j = k, \\ h_j^{-1} h_k^{-1} \left(\tfrac{\partial}{\partial \xi_j} B^p_{i_j}(\xi_j) \right) \left(\tfrac{\partial}{\partial \xi_k} B^p_{i_k}(\xi_k) \right) \prod_{\substack{d \neq j \\ d \neq k}}^{D} B^p_{i_d}(\xi_d) & \text{if} \quad j \neq k; \end{cases} \tag{3.8b}$$

and so on.

3.2.2.3 Interpolant basis on the boundary: Open knot vectors

As previously mentioned, B-spline bases do not satisfy in general the Kronecker delta property, which implies they are not interpolant at the boundaries. In order to enforce boundary conditions in a strong way, the basis can be modified by knot multiplicity, as illustrated in Fig. 3.2. Let us consider a univariate basis of degree $p = 2$ with uniform knot vector $\boldsymbol{k} = [-2, -1, 0, 1, 2, 3, 4, 5, 6, 7, 8]$, cf. Fig. 3.2a. Since knots are unique, each of them have a multiplicity $m = 1$. By repeating a knot, its multiplicity is increased to $m > 1$, and in turn the continuity of the B-Spline basis at that knot is decreased to C^{p-m}. In the previous example, the knot $k_5 = 3$ is repeated (cf. Fig. 3.2b), yielding a knot vector $\boldsymbol{k} = [-2, -1, 0, 1, 2, 3, 3, 4, 5, 6, 7, 8]$. The modified basis is C^1-continuous along the whole parametric space, except at $\xi = 3$ where its continuity is decreased to C^0. Note that the new basis has one extra degree of freedom.
A special case is that of *open knot vectors*, where knots at both ends have multiplicity $m = p + 1$. In such a case, continuity at the boundaries is reduced to C^{-1} (i.e. discontinuous), yielding a boundary-interpolant (or *open*) basis suitable to enforce essential boundary conditions strongly. This is illustrated in Fig. 3.2c, which corresponds to the knot vector $\boldsymbol{k} = [0, 0, 0, 1, 2, 3, 4, 5, 6, 6, 6]$, where both ends have multiplicity $m = 3$.

In open univariate bases, the control variables corresponding to the first and last basis functions can be directly prescribed with the value of the boundary condition. In open multivariate bases, the values of the control variables on the boundary are computed by means of the L_2 projection of the boundary condition onto the space spanned by the corresponding B-spline basis functions.

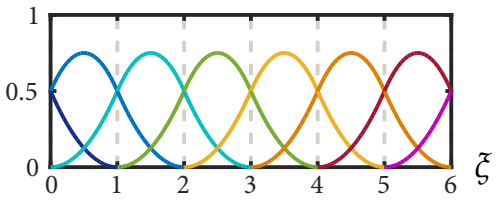

(a) Uniform B-Spline basis

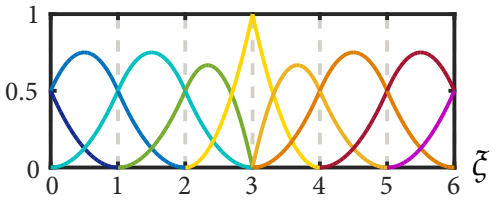

(b) Knot at $\xi = 3$ with multiplicity $m = 2$

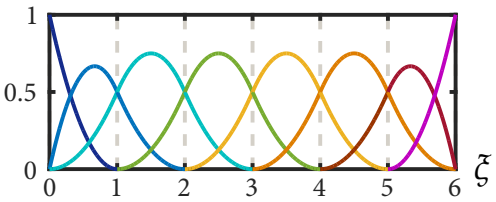

(c) Open B-Spline basis ($m = 3$ at the boundaries)

Figure 3.2: Modification of a B-Spline basis of degree $p = 2$ by means of knot multiplicity

3.2.3 Immersed boundary B-spline approximation

As discussed in Section 3.2.2.2, the geometric map $\boldsymbol{x} = \boldsymbol{\varphi}(\boldsymbol{\xi})$ is global, which implies the domain Ω must be homeomorphic to the parametric space (a hyperrectangle). Since arbitrarily-shaped geometries are not allowed, the applicability range of the method is drastically reduced. In order to circumvent this requirement on Ω, we consider the *immersed boundary* method, also known as the embedded domain method (Mittal and Iaccarino, 2005, Peskin, 2002). The main idea consists on extending the physical domain Ω to a larger *embedding domain*

$$\Omega_{\square} = \{\Omega \cup \Omega_{\text{fict}} \mid \Omega \subseteq \Omega_{\square}\} \tag{3.9}$$

with hyperrectangular shape. The geometrical map in Eq. (3.3) is redefined as

$$\begin{aligned} \boldsymbol{\varphi} : \Xi &\longrightarrow \Omega_{\square} \\ \boldsymbol{\xi} &\longmapsto \boldsymbol{x} = \boldsymbol{\varphi}(\boldsymbol{\xi}), \end{aligned} \tag{3.10}$$

which is independent on Ω, and hence arbitrary geometries are allowed. The basis functions $\boldsymbol{N}(\boldsymbol{x}) \in \Omega_{\square}$ are now defined in the embedding domain, which is discretized by means of a uniform Cartesian grid as $\Omega_{\square} = \bigcup_c \Omega_{\square}^c$, cf. Fig. 3.3a. Hence, the simplifications in Eq. (3.6)-(3.8) also hold here, i.e. the Jacobian of the geometric map remains diagonal and constant throughout $\Omega_{\square}$, preserving the tensor product structure of multivariate bases and corresponding spatial gradients.

The physical boundary $\partial\Omega$ is allowed to intersect the cells $\Omega_{\square}^c$ of the embedding mesh

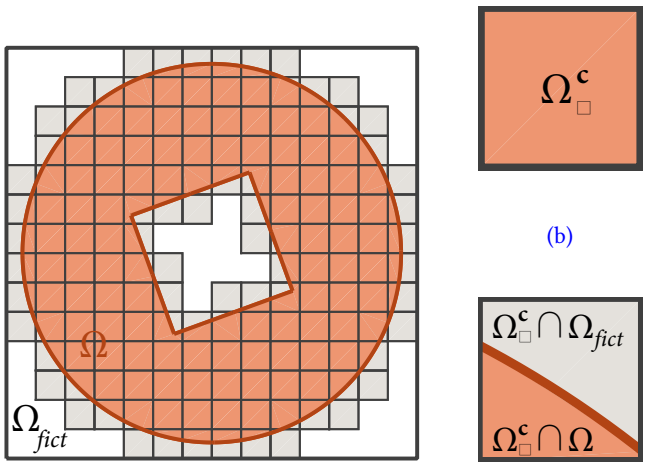

(a) (b) (c)

Figure 3.3: 2D sketch of the immersed boundary method. (a) Physical domain Ω (red) immersed in the discretization of the embedding domain $\Omega_{\square} = \Omega \cup \Omega_{\text{fict}}$ (grey); outer cells are not depicted, (b) detail of an inner cell $\Omega_{\square}^{c} \in \mathcal{I}$ and (c) detail of a cut cell $\Omega_{\square}^{c} \in \mathcal{C}$. Figure adapted from Codony *et al.* (2019).

arbitrarily, leading to a unfitted discretization of Ω. Cells in $\Omega_{\square}$ are classified into three different sets $\mathcal{I}$, $\mathcal{C}$ and $\mathcal{O}$, depending on their intersection with the physical domain Ω:

i) $\mathcal{I} := \{\Omega_{\square}^{c} : \Omega_{\square}^{c} \subseteq \Omega\}$, the set of inner cells which remain uncut within the domain (Fig. 3.3b),

ii) $\mathcal{C} := \{\Omega_{\square}^{c} : \Omega_{\square}^{c} \not\subseteq \Omega \text{ and } \Omega_{\square}^{c} \cap \Omega \neq \emptyset\}$, the set of cells cut by the boundary (Fig. 3.3c),

iii) $\mathcal{O} := \{\Omega_{\square}^{c} : \Omega_{\square}^{c} \cap \Omega = \emptyset\}$, the set of outer cells, which are neglected.

Cell classification is usually accomplished by checking whether all vertices of each cell (and possibly more points within the cell) lie within the domain Ω (inner cell), only part of them (cut cell) or none of them (outer cell). In the case of implicit boundary representation (e.g. level set approaches) it is enough to evaluate the level set function on the evaluation points (see Fries (2016), Fries and Omerović (2016), Kudela *et al.* (2016), Legrain *et al.* (2012)). For explicit boundary representation (e.g. CAD descriptions), ray-tracing procedures are required, as explained in Marco *et al.* (2017, 2015). In this work we restrict ourselves to explicit boundary representation by means of NURBS surfaces in 3D and NURBS curves in 2D.

Immersed boundary methods permit considering arbitrary geometries and involve trivial mesh generation, at the cost of having to deal with a non-conforming discretization. The main challenges are enforcing essential boundary conditions, defining a good-enough numerical integration on cut cells and alleviating ill-conditioning produced by degrees of freedom with small intersection with Ω. The former is solved by enforcing essential boundary conditions in weak form, by means of Nitsche's method, as explained in Sections 2.2.2.1.b, 2.2.2.2.b and 2.2.4.1.b. The latter are commented in next Sections.

3.2.3.1 Cut-cell integration

Bulk integrals are numerically performed in each cell, i.e. inner ones $\Omega_\square^c \in \mathcal{I}$ and also the physical part of cut ones $\Omega_\square^c \cap \Omega$, for $\Omega_\square^c \in \mathcal{C}$ (see Fig. 3.3b and 3.3c). Standard cubature rules (Witherden and Vincent, 2015) apply for the former, but not for the latter which can have arbitrary shape. To this end, the physical part $\Omega_\square^c \cap \Omega$ of every cut cell $\Omega_\square^c \in \mathcal{C}$ is divided into several non-overlapping sub-domains (e.g. cuboids or tetrahedra in 3D, triangles or trapezoids in 2D) which are easily integrated, cf. Fig. 3.4. To sub-divide cut cells we rely on the *marching cubes algorithm* (Lorensen and Cline, 1987, Marco *et al.*, 2015), which splits each cell into several conforming tetrahedra (or triangles in 2D), although other conforming (Fries, 2016, Kudela *et al.*, 2016) or non-conforming (Düster *et al.*, 2008, Schillinger and Ruess, 2015) subdivision schemes are also possible. Boundary integrals are similarly performed on each corresponding sub-domain boundary, as well as integrals on the boundary of the boundary of Ω (as sometimes required in three-dimensional fourth-order PDE).

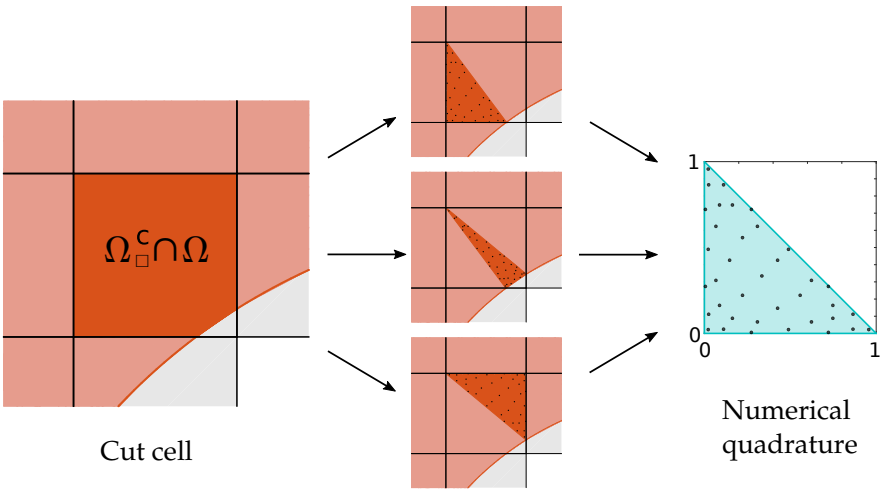

Figure 3.4: Conforming sub-division of cut cells to perform numerical integration.

Note that integration sub-domains in contact with the physical domain boundary $\partial\Omega$ might have curved faces or edges in the case $\partial\Omega$ is not flat. Hence, a linear cell-wise approximation of the geometry leads to a geometric error of order 2 which might spoil the optimal (higher-order) convergence of the method. Therefore, cell-wise polynomial approximations of the geometry of degree p are required in general. Alternatively, we exploit the explicit NURBS representation of the geometry by resorting to the NEFEM approach (Legrain, 2013, Sevilla and Fernández-Méndez, 2011, Sevilla *et al.*, 2008, 2011a,b) which captures the *exact* geometry without the need of any polynomial approximation (Marco *et al.*, 2015).

3.2.3.2 Cut-cell stabilization

The discretization of boundary value problems with immersed boundary B-spline basis leads to an algebraic system of equations for the control variables associated to the approximated fields. This system suffers from ill-conditioning (namely a large condition number) in the presence of cut cells with a small portion in the domain, i.e. when the volume fraction $\eta^c = |\Omega^c_\square \cap \Omega| \,/\, |\Omega^c_\square| \ll 1$ for some $\Omega^c_\square \in \mathcal{C}$. Ill-conditioning arises basically due to: *i)* basis functions on the trimmed cell having very small contribution to the integral terms, and *ii)* basis functions being quasi-linearly dependent on the trimmed cell (de Prenter *et al.*, 2016). According to a detailed investigation on ill-conditioning of immersed boundary methods present in de Prenter *et al.* (2016), the condition number in second order elliptic problems scales with the minimum volume fraction $\eta_{\text{min}} = \min_c(\eta_c)$ at a rate of $\eta_{\text{min}}^{-(2p+1-2/D)}$, which implies that ill-conditioning is more severe for high-order basis. A similar behavior is expected (and confirmed by numerical experiments, cf. Fig. 3.6) for the case of flexoelectricity (coupled fourth-order elliptic PDE).

Several strategies have been proposed to alleviate ill-conditioning of trimmed cells, such as the ghost penalty method (Burman, 2010), the artificial stiffness approach (Düster *et al.*, 2008, Schillinger and Ruess, 2015), the extended B-spline method (Höllig *et al.*, 2012, 2001, Rüberg and Cirak, 2012, Rüberg *et al.*, 2016) or special preconditioning techniques specifically designed for immersed boundary methods (de Prenter *et al.*, 2016), among others.

For uniform meshes, the extended B-spline approach by Höllig et al. (Höllig *et al.*, 2012, 2001, Rüberg and Cirak, 2012, Rüberg *et al.*, 2016) is considered, due to its simple form and good performance. The main idea consists on removing the critical basis functions (the ones with smaller intersection with Ω) from the approximation space and extrapolating well-behaved basis functions from neighboring cells towards the cut cell. Fig. 3.5 illustrates this process for the univariate case. The modified basis has less degrees of freedom, but the condition number and error converge rates are equivalent to those of body-fitted (untrimmed) methods (Höllig *et al.*, 2001). The extended B-spline basis stabilization can be easily implemented as a linear constraint on the approximation space of cut cells based on the uniform Cartesian structure of the discretization (Höllig *et al.*, 2012, 2001, Rüberg and Cirak, 2012, Rüberg *et al.*, 2016).

The use of the extended B-spline approach to hierarchical meshes (see Section 3.2.3.3) follows the same idea but involves a more sophisticated implementation. For the sake of simplicity, we stabilize hierarchical meshes by means of a simple diagonal scaling preconditioning.

To illustrate the effectiveness of the extended B-Spline stabilization technique, we consider the direct flexoelectricity boundary value problem in Section 2.2.2.1.b and evaluate the condition number of the resulting system matrix as a function of the minimum volume fraction η_{min} of several unfitted discretizations. Inspired by the experiment in de Prenter *et al.* (2016), we consider a background Cartesian mesh of square cells of size $h = 0.0915$. A square domain with a circular hole is considered, i.e. $\Omega = (-1,1)^2 \backslash B((0,0), 0.5)$, as depicted in Fig. 3.6a. To create different discretizations yielding different η_{min}, the domain Ω is gradually rotated θ about the origin, from 0 to $\pi/4$ in a sequence of 100 steps, while the background mesh remains

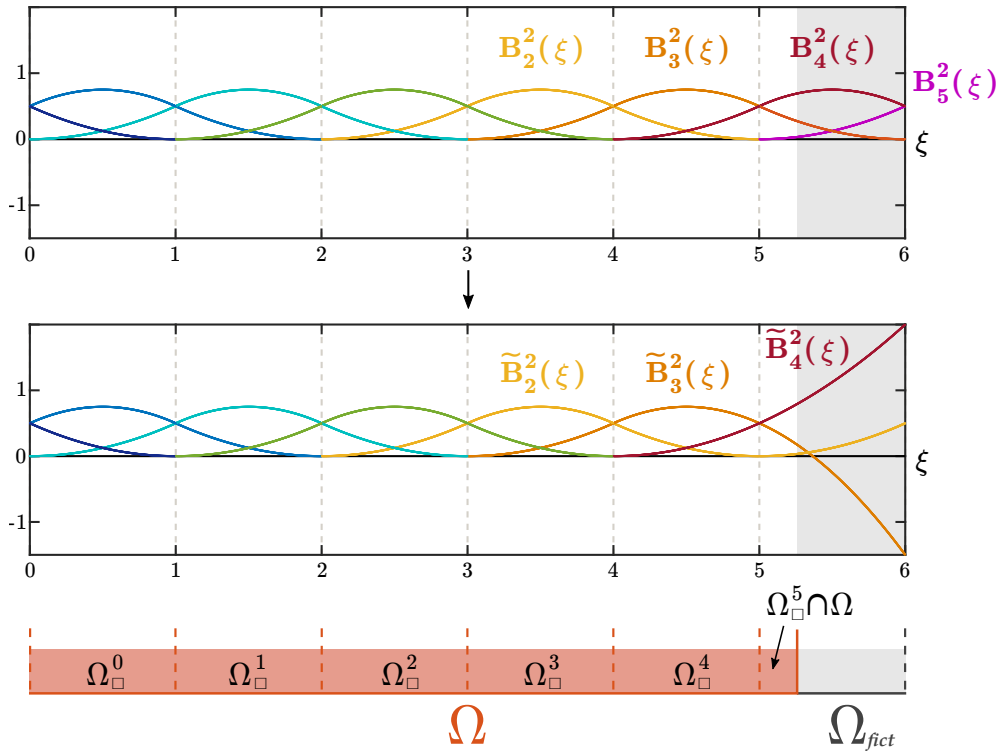

Figure 3.5: Extended B-spline approach on a univariate mesh of degree $p = 2$. Originally (top), the functional space on the trimmed cell $\Omega_\square^5 \in \mathcal{C}$ is spanned by two well-behaved B-splines $B_3^2(\xi)$, $B_4^2(\xi)$ and a critical B-spline $B_5^2(\xi)$. In order to alleviate ill-conditioning of the present functional space (bottom), the critical basis $B_5^2(\xi)$ is removed, and the basis functions $B_2^2(\xi)$, $B_3^2(\xi)$ and $B_4^2(\xi)$ spanning the functional space of the nearest inner cell, i.e. $\Omega_\square^4 \in \mathcal{I}$, are extrapolated (or extended) towards the cut cell $\Omega_\square^5$. The resulting functional space is spanned by the extended basis functions $\{\tilde{B}_2^2(\xi), \tilde{B}_3^2(\xi), \tilde{B}_4^2(\xi)\}$, instead of the original ones $\{B_2^2(\xi), B_3^2(\xi), B_4^2(\xi), B_5^2(\xi)\}$. Mathematically, the extended set is a linear combination of the original one, and the corresponding coefficients can be systematically computed for any polynomial degree p (Höllig *et al.*, 2012, 2001, Rüberg and Cirak, 2012, Rüberg *et al.*, 2016).

fixed. First order Dirichlet and second order homogeneous Neumann boundary conditions are considered at the boundaries $\partial\Omega$, with Nitsche's normalized penalty parameters $\zeta = 100$. The condition number of the system matrix that arises from the discretization is computed by means of the `condest` routine from `Matlab` (MATLAB, 2015).

Fig. 3.6b and 3.6c show condition numbers as a function of $\eta_{\min}$ for spline degrees $p = 3$ and $p = 4$ respectively. The original approximation space yields arbitrarily large condition numbers, scaling at a rate of $2p$ with respect to minimum volume fraction, revealing a similar behavior to that of second order PDE, cf. de Prenter *et al.* (2016). Therefore, the numerical results are untrustworthy and the need for an ill-conditioning alleviation strategy becomes apparent. On the one hand, the extended B-spline stabilization technique is very effective, yielding constant condition numbers regardless of the minimum volume fraction of the mesh. Therefore, it leads to robust simulations and trustworthy results in this sense. On the other

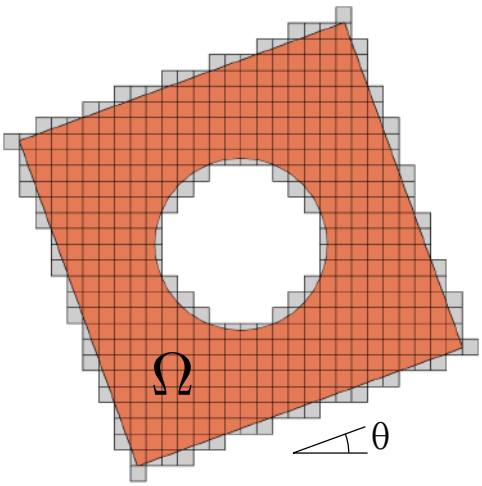

(a) Rotated domain within an unfitted background mesh.

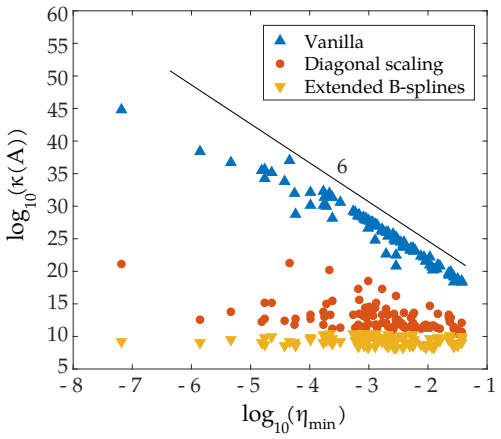

(b) Cubic spline mesh ($p = 3$).

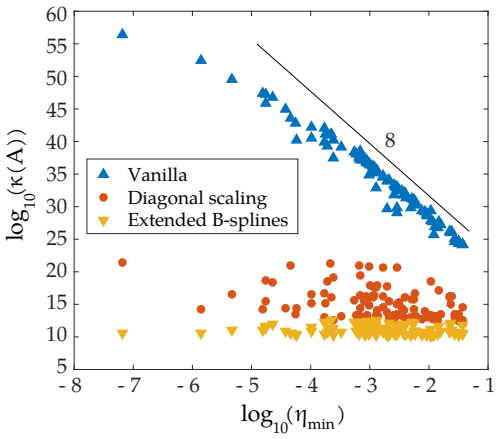

(c) Quartic spline mesh ($p = 4$).

Figure 3.6: Condition number against the minimum volume fraction using different cut-cell stabilization techniques.

hand, the simple diagonal scaling technique reduces the condition numbers but is not as effective as the extended B-spline stabilization, producing a relatively large scatter in the results.

3.2.3.3 Local mesh refinement: Hierarchical B-splines

Hierarchical B-spline refinement was first introduced by Forsey and Bartels (Forsey and Bartels, 1988). It can be understood as a technique for locally enriching the approximation space by replacing selected coarse B-splines (parents) with finer ones (children). It is based on a remarkable property of uniform B-splines: their natural refinement by subdivision. For a

uniform univariate B-spline basis of degree p, the subdivision property leads to the following *two-scale relation* (Zorin, 2000):

$$B_i^p(\xi) = \sum_{j=0}^{p+1} s_j^p B_i^p(2\xi - j) := \sum_{j=2i}^{2i+p+1} \hat{B}_j^p(\hat{\xi}), \quad \text{with} \quad s_j^p = \frac{1}{2^p}\binom{p+1}{j} = \frac{2^{-p}(p+1)!}{j!(p+1-j)!}; \tag{3.11}$$

where $\hat{\xi} := 2\xi$.

In other words, a B-spline function $B_i^p(\xi)$ can be expressed as a linear combination of contracted, translated and scaled copies $\hat{B}_j^p(\hat{\xi})$ of itself (Schillinger *et al.*, 2012), as illustrated in Fig. 3.7 for B-splines of different polynomial degree p. The extension to higher dimensions is trivial by means of the tensor product of univariate bases.

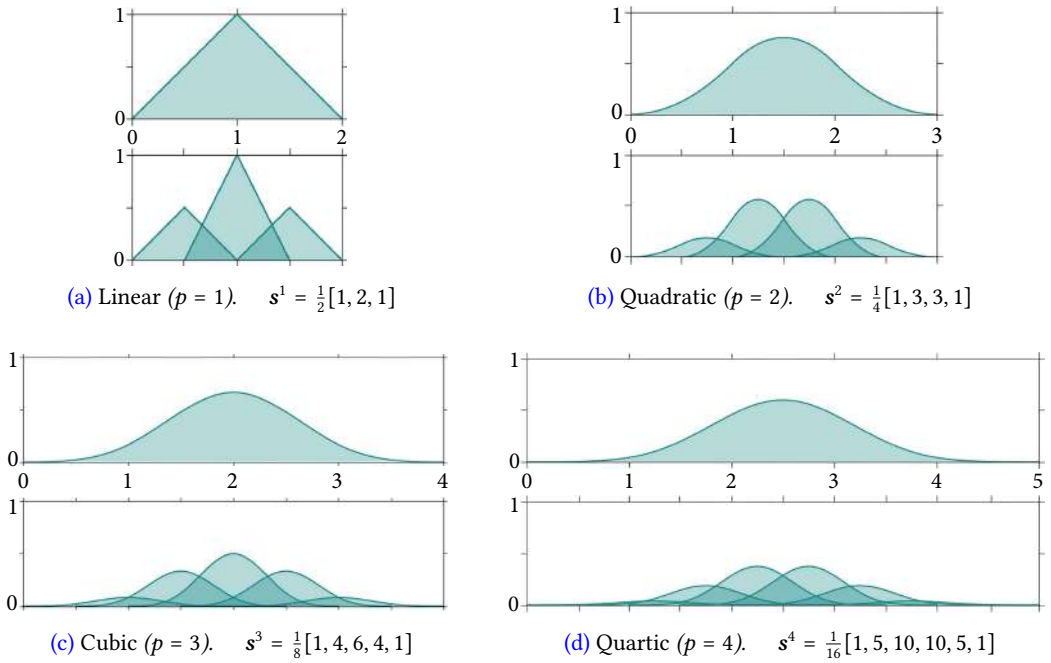

(a) Linear ($p = 1$). $\boldsymbol{s}^1 = \frac{1}{2}[1, 2, 1]$ (b) Quadratic ($p = 2$). $\boldsymbol{s}^2 = \frac{1}{4}[1, 3, 3, 1]$

(c) Cubic ($p = 3$). $\boldsymbol{s}^3 = \frac{1}{8}[1, 4, 6, 4, 1]$ (d) Quartic ($p = 4$). $\boldsymbol{s}^4 = \frac{1}{16}[1, 5, 10, 10, 5, 1]$

Figure 3.7: Two scale relation of a univariate B-spline basis function $B_0^p(\xi)$ of degree p. *Top:* Original (parent) B-spline. *Bottom:* The j-th children B-spline basis, $j = \{0, \dots, p+1\}$. Figure adapted from Codony *et al.* (2019).

A hierarchical B-spline basis is defined from a uniform B-spline basis by replacing some basis functions with their corresponding children (see Fig. 3.8). This process can be performed recursively, leading to a parent-children hierarchy spanning several levels of refinement.

In a hierarchical B-Spline framework, cell refinement translates into some basis functions to be refined. The change of focus from cell refinement (as in conventional FE) to basis refinement is the key point, which allows maintaining the smoothness of the functional space. There exist different hierarchical refinement strategies, depending on the relation between cells and basis to be refined (Bornemann and Cirak, 2013, Kraft, 1997, 1995, Schillinger *et al.*, 2012, Vuong

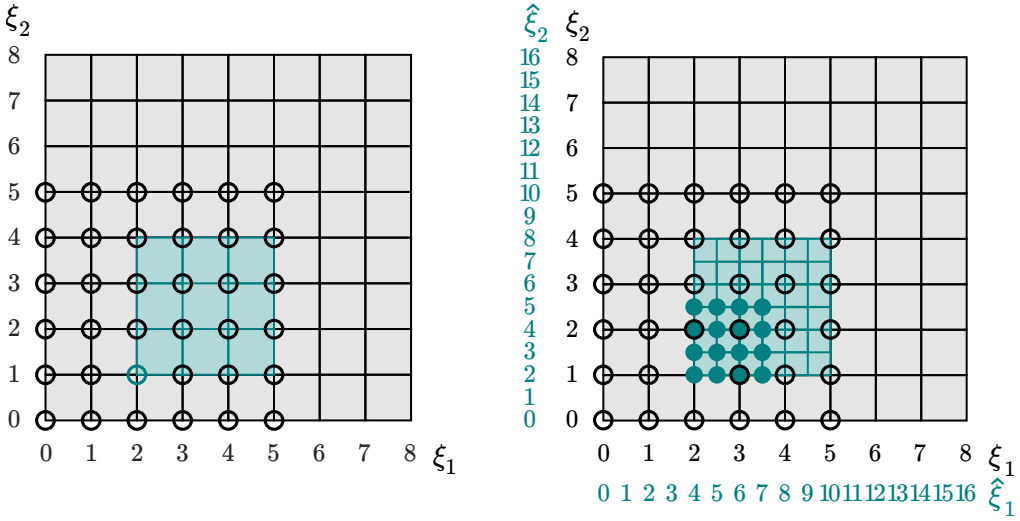

Figure 3.8: Hierarchical refinement of a quadratic ($p = 2$) bivariate B-spline basis. (a) Uniform mesh; B-spline basis function $B^2_{2,1}(\xi_1, \xi_2)$ (blue) is selected for refinement. (b) Hierarchical mesh; basis function $B^2_{2,1}(\xi_1, \xi_2)$ is replaced by their 16 children $\hat{B}^2_{i,j}(\hat{\xi}_1, \hat{\xi}_2)$ (blue), $\forall\{i, j\} = \{4, 5, 6, 7\} \otimes \{2, 3, 4, 5\}$. Figure adapted from Codony *et al.* (2019).

et al., 2011). Each of these implies a certain number N of cells in the neighborhood of the target cell that will also be refined, since the basis functions span $p + 1$ cells per dimension.

A good strategy combining efficiency and ease of implementation consists on refining the B-Spline bases whose support center lies inside the cells to be refined (Bornemann and Cirak, 2013). This strategy leads to a refinement neighborhood of $N = \lceil p/2 \rceil$ cells. Note that refining all non-vanishing B-Splines within a cell would lead to an unnecessary larger refinement neighborhood of $N = p$. Fig. 3.9 illustrates the hierarchical mesh refinement concentrated around a predefined line (black dashed) up to 5 different levels of hierarchy.

The implementation of hierarchical B-Spline basis can be made as efficient as that of uniform basis by means of the *subdivision projection technique*, cf. Bornemann and Cirak (2013). In a cell spanning several levels of refinement, the integrals arising from the discretization of boundary value problems can be computed at the finest hierarchy level only, and then projected to the corresponding coarser levels during the assembly process, thanks to the two scale relation. This procedure avoids dealing with degrees of freedom from different hierarchy levels, facilitating the implementation of hierarchical refinement on a pre-existing B-Spline-based code.

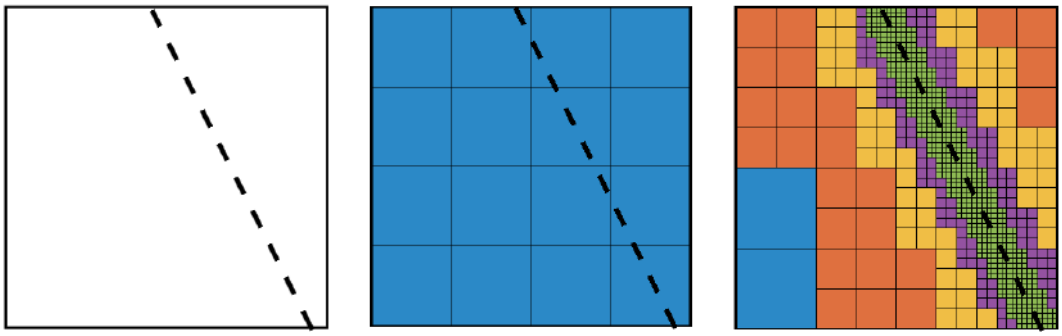

(a) Domain to be discretized (b) Starting uniform mesh (c) Final hierarchical mesh

Figure 3.9: Hierarchical discretization of a domain for a B-Spline basis of degree $p = 1$ or 2. Refinement is required along the black dashed line. Starting from a uniform mesh, the cells overlapping the refinement zone are recursively refined. The neighboring cells at a (L_1) distance $N = \lceil p/2 \rceil = 1$ are also forced to be refined. Each color represents a different level of hierarchy.

3.2.4 Application to the characterization of shear flexoelectricity

As pointed out in Section 1.2.2, the shear flexoelectricity coefficient can be measured by a conical rod with semicircular cross section under torsion (Mocci *et al.*, 2020), where a net angular polarization arises thanks to the longitudinal variation of the cone radius. In this Section we inspire in this setup to validate our formulation and implementation. This example is extracted from Codony *et al.* (2019).

Figure 3.10a shows the geometrical model of the conical semicircular rod, with a length of 100 µm, oriented along the x axis. The radii of the semicircular bases are 26.3 µm and 7.5 µm, and their centers are located at $\boldsymbol{x}_O = (0, 0, 0)$ µm and $\boldsymbol{x}_o = (100, 0, 0)$ µm.

The larger semicircular basis is clamped and grounded, and torsion is enforced at the opposite basis by prescribing the displacement field. The corresponding boundary conditions are:

$$u_x = u_y = u_z = 0 \quad \text{at} \quad x = 0 \qquad \text{(larger basis and its perimeter)}, \tag{3.12a}$$

$$u_y = -\alpha z \quad \text{at} \quad x = 100\ \mu\text{m} \qquad \text{(smaller basis and its perimeter)}, \tag{3.12b}$$

$$u_z = \alpha y \quad \text{at} \quad x = 100\ \mu\text{m} \qquad \text{(smaller basis and its perimeter)}, \tag{3.12c}$$

$$\phi = 0 \quad \text{at} \quad x = 0, \tag{3.12d}$$

where α is the tangent of the prescribed torsional angle.

The mechanical response of the rod is composed by several effects, including non-constant twisting (in-plane rotation) and warping (out-of-plane displacement). Without going into the details, one can think of the rod undergoing ε_{xy} and ε_{xz} shear strains varying along the x direction, hence triggering the shear flexoelectric effect along the $y - z$ plane.

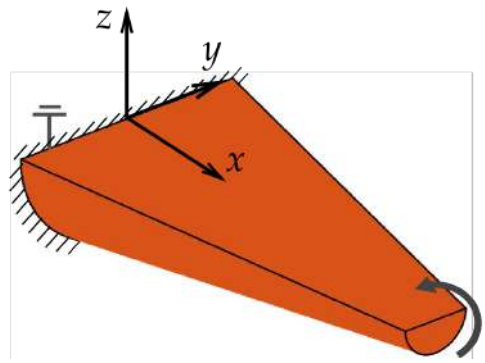

(a) Geometrical 3D model

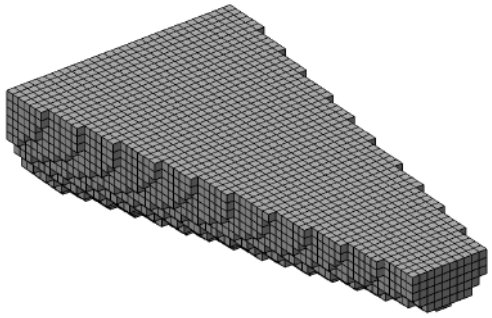

(b) Unfitted uniform B-spline mesh

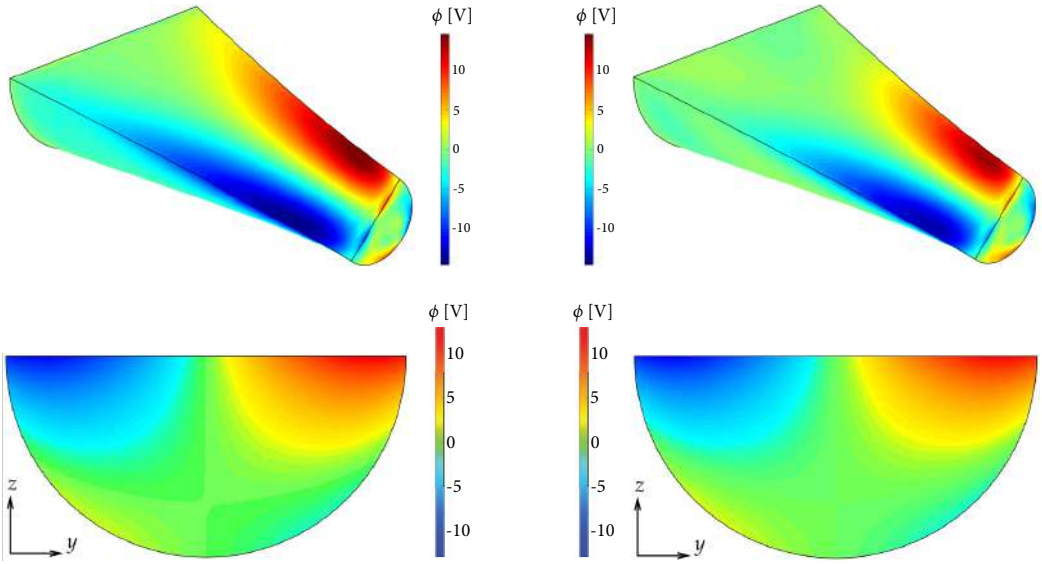

(c) Shear flexoelectric coupling

(d) Full flexoelectric coupling

Figure 3.10: Conical semicircular rod under torsion. (c) and (d) (top) show the electric potential over the deformed shape of the rod (×10 magnification) after torsion. (c) and (d) (bottom) show the electric potential distribution in the cross section at $y = 90.5\,\mu\text{m}$.

Numerical simulations are performed with a cubic ($p = 3$) trivariate B-spline basis on an unfitted uniform mesh of cell size 1.778 µm (see Fig. 3.10b). The prescribed torsion is set to $\alpha = 0.1$, which corresponds to a counterclockwise torsion of about 5.7°. The material constants are set to match those of barium strontium titanate, a strongly flexoelectric ceramic, in its paraelectric phase. That is, a Young modulus $Y = 152\,\text{GPa}$, Poisson ratio $\nu = 0.33$, $\ell_{\text{mech}} = 10\,\mu\text{m}$, $\epsilon = 11\,\text{nC/(V m)}$ and $\mu_{\text{L}} = \mu_{\text{T}} = \mu_{\text{S}} = 121\,\mu\text{C/m}$.

In order to isolate the shear flexoelectric effect, two simulations are performed. In the first one, only the shear flexoelectric coefficient is taken into account, namely $\mu_{\text{L}} = \mu_{\text{T}} = 0$, whereas in the second one the complete flexoelectricity tensor $\boldsymbol{\mu}$ is considered.

The numerical results are shown in Fig. 3.10c and 3.10d. The electric potential takes positive values for $y > 0$ and negative values otherwise, being more prominent near the free end. An effective electric field arises in the polar direction contained in the $y - z$ plane, which can be readily seen by plotting the electric potential in a cross section of the rod. This distribution allows to measuring the electric potential difference between both sides of the rod, and therefore can be used to quantify the shear flexoelectric coefficient (Mocci *et al.*, 2020).

Results do not vary much by considering or disregarding the longitudinal and transversal coefficients of the flexoelectric tensor (see Fig. 3.10c vs 3.10d). In order to quantify it, the voltage difference at the corners of the cross sections, namely at $\boldsymbol{x}_+ = (90.5, 9.265, 0)$ µm and $\boldsymbol{x}_- = (90.5, -9.265, 0)$ µm, is evaluated for the two cases, yielding

$$\begin{aligned} \phi^{\text{Shear}}(\boldsymbol{x}_+) - \phi^{\text{Shear}}(\boldsymbol{x}_-) &= 22.92\text{V}, \\ \phi^{\text{Full}}(\boldsymbol{x}_+) - \phi^{\text{Full}}(\boldsymbol{x}_-) &= 22.28\text{V}, \end{aligned}$$

which shows that considering the longitudinal and transversal coefficients of the flexoelectric tensor affects the voltage difference only by 2.87%. Therefore, it is apparent that the flexoelectric behavior of this setup is mainly controlled by the shear flexoelectric coefficient μ_S.

3.2.5 Application to electrode-based scalable flexoelectric sensors

In electromechanics, conducting electrodes are frequently attached to the surface of the devices to enable either *actuation* or *sensing*. Actuators induce a deformation due to a prescribed electric potential, whereas sensors infer the deformation state by the measured change in the electric potential. In both cases, as the electrodes are made of conducting material, the electric potential in the electrode is uniform. The electrical Dirichlet boundary condition in Eq. (2.53c) corresponds to actuating electrodes where the uniform electric potential is prescribed. In the case of sensing electrodes, however, the uniform electric potential is constant but a priori unknown, and thus requires a special treatment. Fig. 3.11 illustrates the effect of sensing electrodes in a standard benchmark for the longitudinal (direct) flexoelectric coupling: the truncated pyramid compression (Codony *et al.*, 2019).

In the following, the mathematical modeling of sensing electrodes is described in Section 3.2.5.1, and its use towards designing functional flexoelectric devices is illustrated in Section 3.2.5.2.

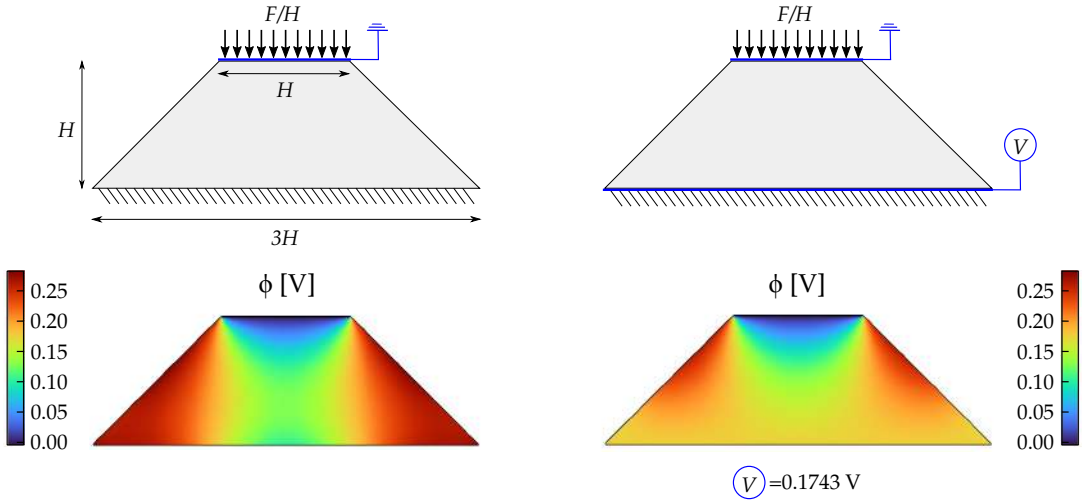

(a) No sensing electrode

(b) Sensing electrode at the base

Figure 3.11: Flexoelectric truncated pyramid of size $H = 7.5\,\mu\text{m}$ under a compressive force $F = 4500\,\mu\text{N}$, with (b) and without (a) a sensing electrode at the base. The flexoelectric material is isotropic with Young modulus $Y = 100\,\text{GPa}$, Poisson ratio $\nu = 0.37$, dielectric constant $\epsilon = 11\,\text{nC m/V}$, longitudinal and transversal flexoelectric coefficients $\mu_{\text{T}} = \mu_{\text{L}} = 1\,\mu\text{C/m}$ and other material parameters set to 0.

3.2.5.1 Sensing electrode boundary conditions

Let us consider a partition of the boundary distinguishing actuating and sensing electrodes, i.e.

$$\partial\Omega = \partial\Omega_\phi \cup \partial\Omega_\Phi \cup \partial\Omega_w, \tag{3.13}$$

where $\partial\Omega_\phi$ and $\partial\Omega_\Phi$ correspond, respectively, to actuating and sensing electrodes on the boundary, respectively, and $\partial\Omega_w$ to the electrical Neumann boundary. The sensing boundary $\partial\Omega_\Phi$ is conformed by N_Φ electrodes, namely $\partial\Omega_\Phi = \bigcup_{i=1}^{N_\Phi} \partial\Omega_\Phi^i$. The electric potential ϕ on sensing electrodes is constant, but unknown. Mathematically, the sensing electrode conditions are stated as

$$\phi - \Phi^i = 0 \quad \text{on } \partial\Omega_\Phi^i, \quad \forall i = 1, \dots, N_\Phi, \tag{3.14}$$

where at each electrode $\partial\Omega_\Phi^i$ the electric potential takes a constant (yet a priori unknown) scalar value $\Phi^i \in \mathbb{R}$.

In a body-fitted framework, the sensing electrode conditions in Eq. (3.14) are easily enforced by means of a linear constraint on the functional space so that it is constant on $\partial\Omega_\Phi^i$. In an unfitted framework, however, they must be weakly enforced. Restricting ourselves to the Direct flexoelectricity form at infinitesimal strains for simplicity, we follow Nitsche's approach

and incorporate the work $\Pi^i_\Phi[\boldsymbol{u}, \phi, \Phi^i]$ of each sensing electrode to the energy potential $\Pi^{(\mathrm{Dir})}$ in Eq. (2.64) (Codony *et al.*, 2019):

$$\Pi^i_\Phi[\boldsymbol{u}, \phi, \Phi^i] = \int_{\partial\Omega^i_\Phi} \Big(\phi - \Phi^i\Big)\, w(\boldsymbol{u}, \phi)\, \mathrm{d}\Gamma, \tag{3.15}$$

where now each Φ^i constitutes an additional state variable. The associated variational principle for the equilibrium states $(\boldsymbol{u}^*, \phi^*, \Phi^{1*}, \dots, \Phi^{N_\Phi *})$ of the body is

$$(\boldsymbol{u}^*, \phi^*, \Phi^{1*}, \dots, \Phi^{N_\Phi *}) = \arg \min_{\boldsymbol{u}\in\mathcal{U}} \max_{\phi\in\mathcal{P}} \min_{\Phi^1\in\mathbb{R}} \dots \min_{\Phi^{N_\Phi}\in\mathbb{R}} \left(\Pi^{(\mathrm{Dir})}[\boldsymbol{u}, \phi] + \sum_{i=1}^{N_\Phi} \Pi^i_\Phi[\boldsymbol{u}, \phi, \Phi^i] \right). \tag{3.16}$$

Equation (3.15) has a similar form to the Nitsche terms $\Pi^{\mathrm{Dirichlet}}[\boldsymbol{u}, \phi]$ in Eq. (2.65), but the penalty term quadratic to the boundary condition in Eq. (3.14) is omitted here, because if it was positive in sign then it could be made arbitrarily large with respect to ϕ, and, conversely, if was is negative in sign then it could be made arbitrarily large with respect to Φ^i (Codony *et al.*, 2019). Vanishing of the first variation of the energy functional in Eq. (3.16) yields

$$0 = \delta\Pi^{(\mathrm{Dir})}[\boldsymbol{u}, \phi; \delta\boldsymbol{u}, \delta\phi] + \sum_{i=1}^{N_\Phi} \delta\Pi^i_\Phi[\boldsymbol{u}, \phi, \Phi^i; \delta\boldsymbol{u}, \delta\phi, \delta\Phi^i], \quad \forall \delta\boldsymbol{u} \in \mathcal{U}, \delta\phi \in \mathcal{P}, \delta\Phi^i \in \mathbb{R}, \tag{3.17}$$

where the additional terms

$$\delta\Pi^i_\Phi[\boldsymbol{u}, \phi, \Phi^i; \delta\boldsymbol{u}, \delta\phi, \delta\Phi^i] := \int_{\partial\Omega^i_\Phi} \Big(\phi - \Phi^i\Big)\, w(\delta\boldsymbol{u}, \delta\phi)\, \mathrm{d}\Gamma + \int_{\partial\Omega^i_\Phi} w(\boldsymbol{u}, \phi) \Big(\delta\phi - \delta\Phi^i\Big)\, \mathrm{d}\Gamma. \tag{3.18}$$

The weak form of the unfitted formulation for direct flexoelectricity accounting for sensing electrodes reads:

$$\begin{aligned} &\textit{Find } (\boldsymbol{u}, \phi, \Phi^1, ..., \Phi^{N_\Phi}) \in \mathcal{U} \otimes \mathcal{P} \otimes \mathbb{R}^{N_\Phi} \textit{ such that} \\ &\textit{Eq. (3.17) holds } \forall (\delta\boldsymbol{u}, \delta\phi, \delta\Phi^1, ..., \delta\Phi^{N_\Phi}) \in \mathcal{U} \otimes \mathcal{P} \otimes \mathbb{R}^{N_\Phi}. \end{aligned} \tag{3.19}$$

3.2.5.2 Wheel-shaped (2D) flexoelectric sensor

In this Section we illustrate the usefulness of sensing electrode boundary conditions in order to design scalable flexoelectric devices. Let us consider a wheel-shaped geometry as depicted in Fig. 3.12a. It is composed by N_b radial beams of width H, ranging from the inner radius R_{in} to the outer radius R_{out}, connected by an outer circular arc of width H ranging from the first radial beam at $\alpha = 0$ until the last beam at $\alpha = 2\pi(1 - 1/N_b)$. The inner tips of the radial beams are clamped, as depicted in Fig. 3.12b.

The device can act as a flexoelectric sensor, activated by means of an applied rotation $\boldsymbol{u}_{\mathrm{R}}(\boldsymbol{x})$

of the outer circular arc as follows:

$$\boldsymbol{u}_{\mathrm{R}}(\boldsymbol{x}) = \begin{bmatrix} \cos(\alpha_{\mathrm{R}}) - 1 & -\sin(\alpha_{\mathrm{R}}) \\ \sin(\alpha_{\mathrm{R}}) & \cos(\alpha_{\mathrm{R}}) - 1 \end{bmatrix} \cdot \begin{bmatrix} x \\ y \end{bmatrix}, \tag{3.20}$$

where α_{R} is the applied rotation angle. Such deformation will induce the bending of the radial beams, generating a transversal electric field thanks to the transversal flexoelectric effect. However, the goal is not just inducing a potential difference across each beam's thickness, but also accumulating this difference from beam to beam, yielding a *scalable* device. The easiest way of doing so is attaching electrodes at the top an bottom boundaries of the radial beams, close to the inner clamped tips where the curvature is expected to be maximum, as depicted in Fig. 3.12b, with the first electrode being grounded ($\phi = 0$) and the rest being sensors. By connecting two consecutive electrodes in different beams (in other words, considering that both electrodes are actually the same electrode $\partial\Omega_{\Phi}^{i}$ at same voltage Φ^{i}) the accumulation effect will be achieved.

Fig. 3.12c depicts the electromechanical response of the wheel-shaped flexoelectric sensor with geometrical parameters $H = 0.43\,\mu\mathrm{m}$, $R_{\mathrm{in}} = 1\,\mu\mathrm{m}$, $R_{\mathrm{out}} = 5\,\mu\mathrm{m}$ and $N_b = 10$, and material parameters $Y = 100\,\mathrm{GPa}$, $\nu = 0.3$, $\epsilon = 11\,\mathrm{nC\,m/V}$, $\mu_{\mathrm{L}} = \mu_{\mathrm{T}} = 1\,\mu\mathrm{C/m}$ (other material parameters are set to 0), which correspond to a hard, isotropic flexoelectric material. The applied rotation angle is set to $\alpha_{\mathrm{R}} = \pi/12$. The unfitted Cartesian mesh has element size $h \approx 60\,\mathrm{nm}$ and spline degree $p = 3$. As expected, the rotation-induced bending of the radial beams generates electric field due to the flexoelectric effect, and it is accumulated from beam to beam thanks to the sensing electrode conditions.

Fig. 3.12d shows the value of the voltage at each sensing electrode. Since the considered material is isotropic, all radial beams present the same induced electric field, which is effectively accumulated. The total electric potential difference attained is about 59 V, which is roughly $N_b = 10$ times larger than the one present across a single bent beam. The sensitivity of this flexoelectric sensor can be measured as $V_{N_b}/\alpha_{\mathrm{R}} \approx 226\,\mathrm{V/rad} \approx (22.6N_b)\mathrm{V/rad}$. Hence, it is linearly proportional to the number of beams N_b constituting the device, allowing a systematic increase in sensitivity just by geometrical design.

By accounting for three-dimensional helical-shaped devices working under the same idea, a much larger net electric voltage is expected since the number of beams can be easily increased without the 2π angular restriction of 2D models. This idea is currently being explored (Codony *et al.*, 2021b).

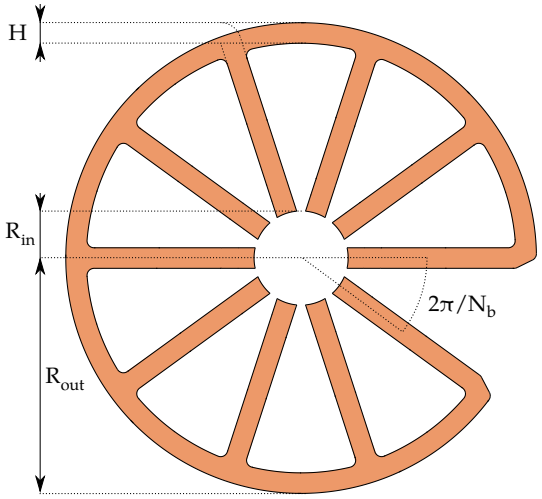

(a) Geometry

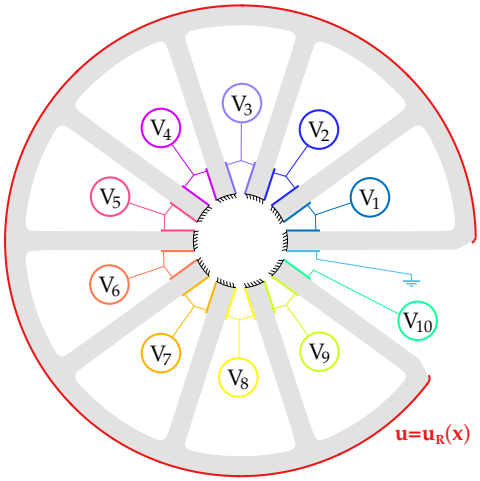

(b) Boundary conditions

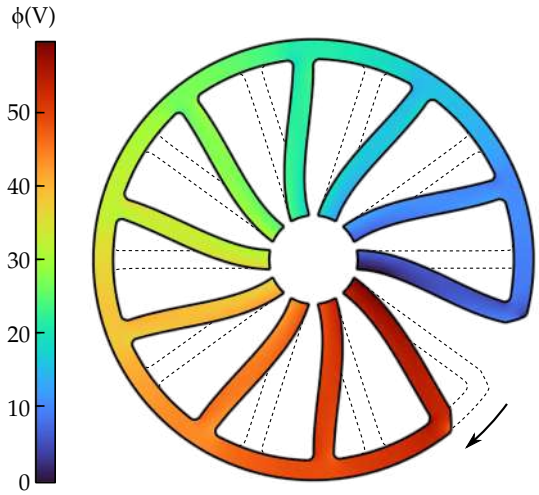

(c) Deformed shape and electric potential

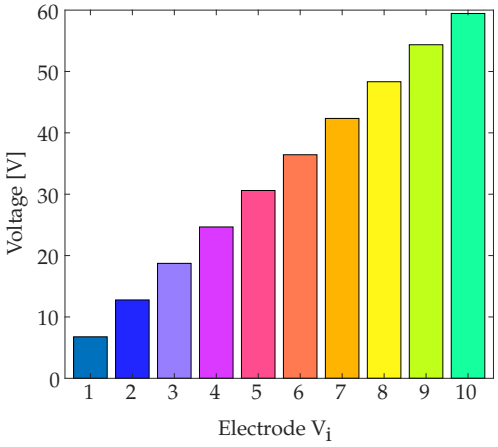

(d) Voltage at each sensing electrode

Figure 3.12: Wheel-shaped flexoelectric sensor under a rotation of $\alpha_R = \pi/12$.

3.2.6 Application to nonlinear flexoelectric rods

In this Section, the direct flexoelectricity model in the finite deformation framework in Section 2.2.4.1.a is studied on a flexoelectric rod, which constitutes the simplest functional flexoelectric device. The rod is analyzed in different settings such as axial and transversal mechanical loadings (sensing mode) and clamped-free and clamped-clamped transversal electrical loading (actuation mode), cf. Fig. 3.13. The interplay of the flexoelectric effect with other physics, such as electrostriction, and its role in several deformation states, such as mechanically or electrically-induced bending or buckling, are also analyzed. The examples are extracted and

adapted from Codony *et al.* (2020b), which is an original contribution of the author of this document.

The governing equations in Eq. (2.135) are solved numerically by means of the body-fitted B-spline approach presented in Section 3.2.2. Since we restrict ourselves to 2D rod-like geometries (i.e. rectangles), there is no need of resorting to more general approaches such as the immersed boundary (unfitted) approximation. The state variables $\{\boldsymbol{\chi}, \Phi\}$ are approximated on an open uniform cubic ($p = 3$) B-spline-based Cartesian mesh with square cells of size $h = H/10$, being H the thickness of the rod. (First order) Dirichlet boundary conditions are strongly enforced thanks to the interpolant nature of the basis at the boundaries.

The discretization of Eq. (2.135) yields a nonlinear system of equations (discretized state variables are denoted with the same notation from now on for simplicity). In order to solve it, a modified-step Newton-Raphson algorithm is considered. At the k-th iteration, an increment of the solution $\{\Delta\boldsymbol{\chi}, \Delta\Phi\}^{(k)}$ is found by vanishing the first order Taylor expansion of the residual $\mathcal{R}$ (namely the discrete version of $\delta\Pi_{\mathrm{D}}^{(\mathrm{Dir})}$ in Eq. (2.135)) around the previous solution $\{\boldsymbol{\chi}, \Phi\}^{(k-1)}$ of the $(k-1)$-th iteration:

$$\begin{aligned}\mathcal{R}\left[\boldsymbol{\chi}^{(k)}, \Phi^{(k)}; \delta\boldsymbol{\chi}, \delta\Phi\right] \approx\ & \mathcal{R}\left[\boldsymbol{\chi}^{(k-1)}, \Phi^{(k-1)}; \delta\boldsymbol{\chi}, \delta\Phi\right] \\ & + \frac{\partial \mathcal{R}}{\partial \boldsymbol{\chi}}\left[\boldsymbol{\chi}^{(k-1)}, \Phi^{(k-1)}; \delta\boldsymbol{\chi}, \delta\Phi\right] \cdot \Delta\boldsymbol{\chi}^{(k)} \\ & + \frac{\partial \mathcal{R}}{\partial \Phi}\left[\boldsymbol{\chi}^{(k-1)}, \Phi^{(k-1)}; \delta\boldsymbol{\chi}, \delta\Phi\right] \cdot \Delta\Phi^{(k)} \\ =\ & 0. \end{aligned} \tag{3.21}$$

Given $\{\boldsymbol{\chi}, \Phi\}^{(k-1)}$ at the previous iteration, Eq. (3.21) leads to an algebraic system of equations for $\{\Delta\boldsymbol{\chi}, \Delta\Phi\}^{(k)}$ of the form

$$\begin{bmatrix} \mathbf{H}_{\boldsymbol{\chi}\boldsymbol{\chi}} & \mathbf{H}_{\boldsymbol{\chi}\Phi} \\ \mathbf{H}_{\Phi\boldsymbol{\chi}} & \mathbf{H}_{\Phi\Phi} \end{bmatrix}^{(k-1)} \cdot \begin{bmatrix} \Delta\boldsymbol{\chi} \\ \Delta\Phi \end{bmatrix}^{(k)} = -\begin{bmatrix} \mathbf{R}_{\boldsymbol{\chi}} \\ \mathbf{R}_{\Phi} \end{bmatrix}^{(k-1)}, \tag{3.22}$$

where

$$\mathbf{H}_{\boldsymbol{\chi}\boldsymbol{\chi}}\left(\boldsymbol{\chi}^{(k-1)}, \Phi^{(k-1)}\right) = \frac{\partial \mathcal{R}}{\partial \boldsymbol{\chi}}\left[\boldsymbol{\chi}^{(k-1)}, \Phi^{(k-1)}; \delta\boldsymbol{\chi}, 0\right], \tag{3.23a}$$

$$\mathbf{H}_{\boldsymbol{\chi}\Phi}\left(\boldsymbol{\chi}^{(k-1)}, \Phi^{(k-1)}\right) = \frac{\partial \mathcal{R}}{\partial \Phi}\left[\boldsymbol{\chi}^{(k-1)}, \Phi^{(k-1)}; \delta\boldsymbol{\chi}, 0\right], \tag{3.23b}$$

$$\mathbf{H}_{\Phi\boldsymbol{\chi}}\left(\boldsymbol{\chi}^{(k-1)}, \Phi^{(k-1)}\right) = \frac{\partial \mathcal{R}}{\partial \boldsymbol{\chi}}\left[\boldsymbol{\chi}^{(k-1)}, \Phi^{(k-1)}; \mathbf{0}, \delta\Phi\right], \tag{3.23c}$$

$$\mathbf{H}_{\Phi\Phi}\left(\boldsymbol{\chi}^{(k-1)}, \Phi^{(k-1)}\right) = \frac{\partial \mathcal{R}}{\partial \Phi}\left[\boldsymbol{\chi}^{(k-1)}, \Phi^{(k-1)}; \mathbf{0}, \delta\Phi\right], \tag{3.23d}$$

$$\mathbf{R}_{\boldsymbol{\chi}}\left(\boldsymbol{\chi}^{(k-1)}, \Phi^{(k-1)}\right) = \mathcal{R}\left[\boldsymbol{\chi}^{(k-1)}, \Phi^{(k-1)}; \delta\boldsymbol{\chi}, 0\right], \tag{3.23e}$$

$$\mathbf{R}_{\Phi}\left(\boldsymbol{\chi}^{(k-1)}, \Phi^{(k-1)}\right) = \mathcal{R}\left[\boldsymbol{\chi}^{(k-1)}, \Phi^{(k-1)}; \mathbf{0}, \delta\Phi\right]. \tag{3.23f}$$

The explicit form of the variation of the residual $\mathcal{R}$, i.e. the second variation of the enthalpy functional $\delta\Pi_{\mathrm{D}}^{(\mathrm{Dir})}$, is found in the Appendix B of Codony *et al.* (2020b).

Once $\{\Delta\boldsymbol{\chi}, \Delta\Phi\}^{(k)}$ are found, we compute the *modified* increments $\{\overline{\Delta\boldsymbol{\chi}}, \overline{\Delta\Phi}\}^{(k)}$ by ensuring that the total increment *i)* leads to an enthalpy decrease along $\boldsymbol{\chi}$, *ii)* leads to an enthalpy increase along Φ, and *iii)* has a predefined maximum norm $\gamma_{\max} \in \mathbb{R}^+$. The first two conditions are required in accordance to the min-max variational principle in Eq. (2.132), whereas the latter is just a numerical requirement to avoid too large increments of the solution at each iteration. To formulate those conditions mathematically, let us recast the variational principle in Eq. (2.132) as

$$\widehat{\Phi}(\boldsymbol{\chi}) := \underset{\Phi\in\mathcal{P}_{\mathrm{D}}}{\operatorname{argmax}} \left(\Pi_{\mathrm{D}}^{(\mathrm{Dir})}[\boldsymbol{\chi}, \Phi]\right), \tag{3.24a}$$

$$\boldsymbol{\chi}^* = \underset{\boldsymbol{\chi}\in\mathcal{X}_{\mathrm{D}}}{\operatorname{argmin}} \left(\widehat{\Pi}_{\mathrm{D}}^{(\mathrm{Dir})}[\boldsymbol{\chi}]\right) \quad \text{with} \quad \widehat{\Pi}_{\mathrm{D}}^{(\mathrm{Dir})}[\boldsymbol{\chi}] := \Pi_{\mathrm{D}}^{(\mathrm{Dir})}[\boldsymbol{\chi}, \widehat{\Phi}(\boldsymbol{\chi})], \tag{3.24b}$$

$$\Phi^* = \widehat{\Phi}(\boldsymbol{\chi}^*). \tag{3.24c}$$

Numerically, Eq. (3.24) is equivalent to solving two linear systems consecutively, constructed from Eq. (3.22) by writing $\Delta\Phi^{(k)}$ as a function of $\Delta\boldsymbol{\chi}^{(k)}$, as follows:

$$\widehat{\mathbf{H}}_{\boldsymbol{\chi}\boldsymbol{\chi}}{}^{(k-1)} \cdot \Delta\boldsymbol{\chi}^{(k)} = -\,\widehat{\mathbf{R}}_{\boldsymbol{\chi}}{}^{(k-1)} \quad \text{with} \quad \begin{cases} \widehat{\mathbf{H}}_{\boldsymbol{\chi}\boldsymbol{\chi}}{}^{(k-1)} := \left[\mathbf{H}_{\boldsymbol{\chi}\boldsymbol{\chi}} - \mathbf{H}_{\boldsymbol{\chi}\Phi} \cdot \mathbf{H}_{\Phi\Phi}^{-1} \cdot \mathbf{H}_{\Phi\boldsymbol{\chi}}\right]^{(k-1)} \\ \widehat{\mathbf{R}}_{\boldsymbol{\chi}}{}^{(k-1)} := \left[\mathbf{R}_{\boldsymbol{\chi}} - \mathbf{H}_{\boldsymbol{\chi}\Phi} \cdot \mathbf{H}_{\Phi\Phi}^{-1} \cdot .\mathbf{R}_{\Phi}\right]^{(k-1)} \end{cases}, \tag{3.25a}$$

$$\mathbf{H}_{\Phi\Phi}{}^{(k-1)} \cdot \Delta\Phi^{(k)} = -\,\widehat{\mathbf{R}}_{\Phi}{}^{(k-1)} \quad \text{with} \quad \widehat{\mathbf{R}}_{\Phi}{}^{(k-1)} := \mathbf{R}_{\Phi}{}^{(k-1)} + \mathbf{H}_{\Phi\boldsymbol{\chi}}{}^{(k-1)} \cdot \Delta\boldsymbol{\chi}^{(k)}. \tag{3.25b}$$

From Eq. (3.25) it is clear that the descent and ascent directions are respectively identified by $\widehat{\mathbf{R}}_{\boldsymbol{\chi}}{}^{(k-1)}$ and $\widehat{\mathbf{R}}_{\Phi}{}^{(k-1)}$, i.e. the *modified* residuals which take into account the coupled nature of the enthalpy potential. Therefore, the modified increments are computed as follows:

$$\alpha_{\boldsymbol{\chi}}{}^{(k)} = \begin{cases} -1 & \text{if } \widehat{\mathbf{R}}_{\boldsymbol{\chi}}{}^{(k-1)} \cdot \Delta\boldsymbol{\chi}^{(k)} > 0, \\ +1 & \text{otherwise;} \end{cases} \tag{3.26a}$$

$$\alpha_{\Phi}{}^{(k)} = \begin{cases} -1 & \text{if } \widehat{\mathbf{R}}_{\Phi}{}^{(k-1)} \cdot \Delta\Phi^{(k)} < 0, \\ +1 & \text{otherwise;} \end{cases} \tag{3.26b}$$

$$\beta^{(k)} = \min\left\{+1, \gamma_{\max} / \sqrt{\left\|\frac{\Delta\boldsymbol{\chi}^{(k)}}{\chi_0}\right\|^2 + \left\|\frac{\Delta\Phi^{(k)}}{\Phi_0}\right\|^2}\right\}; \tag{3.26c}$$

$$\overline{\Delta\boldsymbol{\chi}}^{(k)} = \alpha_{\boldsymbol{\chi}}{}^{(k)}\beta^{(k)}\Delta\boldsymbol{\chi}^{(k)}; \tag{3.26d}$$

$$\overline{\Delta\Phi}^{(k)} = \alpha_{\Phi}{}^{(k)}\beta^{(k)}\Delta\Phi^{(k)}; \tag{3.26e}$$

with χ_0 and Φ_0 characteristic factors of the problem for displacement and potential. In practice, $\gamma_{\max}$ is treated as an adaptive heuristic parameter, tunable for proper convergence.

Finally, the solution at the k-th iteration is updated with

$$\{\boldsymbol{\chi}, \Phi\}^{(k)} = \{\boldsymbol{\chi}, \Phi\}^{(k-1)} + \{\overline{\Delta\boldsymbol{\chi}}, \overline{\Delta\Phi}\}^{(k)}. \tag{3.27}$$

The external loads are applied incrementally in a sequence of load steps, and the modified-step Newton-Raphson algorithm presented here is used to obtain converged solutions at every load step. Once convergence is reached, the stability of the solution is checked by assuring $\{\boldsymbol{\chi}, \Phi\}^{(k)}$ is a saddle point in the enthalpy functional $\Pi_{\mathrm{D}}^{(\mathrm{Dir})}[\boldsymbol{\chi}, \Phi]$ in accordance to the variational principle in Eq. (2.132). By means of Eq. (3.24), stability of $\{\boldsymbol{\chi}, \Phi\}^{(k)}$ is given by

$$\delta^2_{\boldsymbol{\chi}} \widehat{\Pi}_{\mathrm{D}}^{(\mathrm{Dir})}[\boldsymbol{\chi}^{(k)}; \Delta\boldsymbol{\chi}; \Delta\boldsymbol{\chi}] > 0 \quad \forall \Delta\boldsymbol{\chi} \in \mathcal{X}_0, \tag{3.28a}$$

$$\delta^2_{\phi} \Pi_{\mathrm{D}}^{(\mathrm{Dir})}[\boldsymbol{\chi}^{(k)}, \Phi^{(k)}; \Delta\Phi; \Delta\Phi] < 0 \quad \forall \Delta\Phi \in \mathcal{P}_0. \tag{3.28b}$$

Numerically, Eq. (3.28) is met by checking the sign of the extremal eigenvalues λ of $\widehat{\mathbf{H}}_{\boldsymbol{\chi}\boldsymbol{\chi}}{}^{(k)}$ and $\mathbf{H}_{\Phi\Phi}{}^{(k)}$ as follows:

$$\lambda_{\min}\left[\widehat{\mathbf{H}}_{\boldsymbol{\chi}\boldsymbol{\chi}}{}^{(k)}\right] > 0, \qquad \lambda_{\max}\left[\mathbf{H}_{\Phi\Phi}{}^{(k)}\right] < 0. \tag{3.29}$$

We recognize convergence to unstable solutions by the violation of Eq. (3.29). In such case, the solution $\{\boldsymbol{\chi}, \Phi\}^{(k)}$ is slightly perturbed and the iterative algorithm is run again until a stable solution is found. In practice, we found that $\lambda_{\max}\left[\mathbf{H}_{\Phi\Phi}{}^{(k)}\right]$ remains always negative, and therefore the encountered instabilities are given by $\lambda_{\min}\left[\widehat{\mathbf{H}}_{\boldsymbol{\chi}\boldsymbol{\chi}}{}^{(k)}\right]$ becoming negative only (i.e. *geometrical* instabilities). The eigenvector associated to $\lambda_{\min}\left[\widehat{\mathbf{H}}_{\boldsymbol{\chi}\boldsymbol{\chi}}{}^{(k)}\right]$ is an appropriate direction for numerical perturbations on $\boldsymbol{\chi}^{(k)}$ to reach stable solutions.

In the following examples, elasticity is modeled by isotropic hyperelastic potentials, either Saint-Venant–Kirchhoff (Eq. (A.9)) or Neo-Hookean (Eq. (A.10)) models. Both require two elastic constants, i.e. the Young's modulus Y and the Poisson's ratio ν. Strain-gradient elasticity is modeled by the analogous isotropic hyperelastic Saint-Venant–Kirchhoff law (Eq. (A.2)), which additionally depends on the characteristic length scale ℓ_{mech}. Dielectricity is isotropic, which depends on the electric permittivity ϵ, and the flexoelectric tensor $\boldsymbol{\mu}$ is assumed to have cubic symmetry with three independent constants μ_{L}, μ_{T} and μ_{S}, namely the longitudinal, transversal and shear flexoelectric coefficients (Eq. (A.8)).

An analytical 1D model for unshearable, extensible slender flexoelectric rods under large deformations was also presented in Codony *et al.* (2020b), as well as its linearized Euler-Bernoulli counterpart. Closed-form solutions for the quantities of interest (i.e. displacement, electric field, curvature and elongation) are also provided for the loading cases depicted in Fig. 3.13. Such model assumes linear strains, use a Saint-Venant–Kirchhoff hyperelastic potential for classical elasticity, neglects strain gradient elasticity (i.e. $\ell_{\mathrm{mech}} = 0$) and consider

the transversal flexoelectric effect only (i.e. $\mu_L = \mu_S = 0$). In the following examples we validate the full numerical model against the closed-form solutions present in Codony *et al.* (2020b) by considering material parameters matching the aforementioned assumptions. For some relevant examples, we also analyze general flexoelectric problems described by the more realistic Neo-Hookean hyperelastic potential and the full flexoelectric tensor.

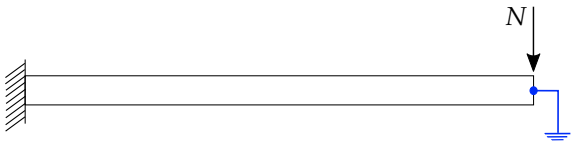

(a) Bending-based sensor

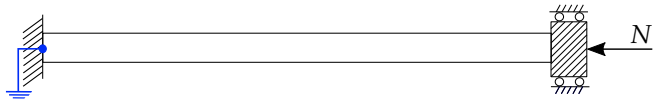

(b) Buckling-based sensor

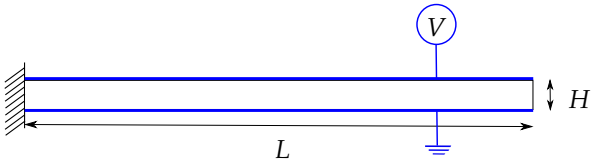

(c) Bending-based actuator

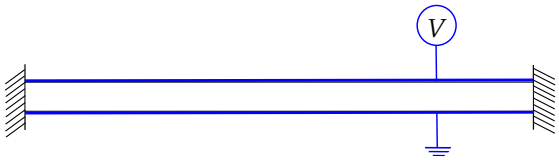

(d) Buckling-based actuator

Figure 3.13: Sketch of a flexoelectric rod of dimensions L by H under several loading and boundary conditions. (a) A cantilever rod subjected to a transversal load N at the right end tip, and electrically grounded at the mid-point in the right end cross-section. (b) A clamped-clamped rod subjected to a compressive axial load N at the right end, which is allowed to displace horizontally, and electrically grounded at the mid-point in the left end cross-section. (c) A cantilever rod sandwiched between two electrodes (depicted in blue) under applied voltage V. (d) A clamped-clamped rod sandwiched between two electrodes (blue in color) under applied voltage V. Figure adapted from Codony *et al.* (2020b).

3.2.6.1 Mechanically-induced bending

We consider here a flexoelectric cantilever rod of thickness $H = 100\text{nm}$ and slenderness of $L/H = 20$, under bending by a vertical point load in an open circuit configuration with the mechanically free end electrically grounded, cf. Fig. 3.13a. Young's modulus is chosen as $Y = 1.725\text{GPa}$ and the dielectric permittivity as $\epsilon = 0.092\text{nC/Vm}$, which correspond to polyvinylidene fluoride (PVDF) (Chu and Salem, 2012, Zhang *et al.*, 2016b, Zhou *et al.*, 2017).

Validation

Fig. 3.14 collects the validation results. Typical computational solutions are shown in Fig. 3.14a, where the electric potential ϕ is plotted on the deformed configuration. These simulations highlight the very large deformations attained. As predicted by the linear (Majdoub *et al.*, 2009, 2008) and nonlinear (Codony *et al.*, 2020b) analytical models, flexoelectricity leads to an effective stiffening of the system even though the elastic constants are kept fixed. The maximum electric field generated at the clamping cross-section exhibits a maximum for an intermediate value of the flexoelectric constant. The existence of an optimal value of μ_{T}, for which the flexoelectric response is maximized, results from the competition of the two conflicting effects of μ_{T}: *i)* the stiffening and *ii)* the flexoelectric coupling. For small values of μ_{T} the structure is very compliant and larger strain gradients are attained but the generated field is small due to the small coupling, whereas for very large values of μ_{T} the flexoelectric coupling is large but the stiffer beam attains smaller deformations and thus smaller strain gradients.

To further analyze these effects, we present in Fig. 3.14b the dependence of the cantilever rod vertical displacement at the tip on the endpoint load, and the vertical electric field on the clamped edge, for different values of transversal flexoelectric coefficient μ_{T}. The results for the tip displacement show *i)* the stiffening as μ_{T} increases, *ii)* the nonlinearity in the response of the system (particularly for the most deformable systems), *iii)* an excellent quantitative agreement with the nonlinear flexoelectric rod model, and *iv)* an agreement with the linearized E-B model for small deformations, i.e. smaller loads or stiffer cantilevers (large values of μ_{T}). Similarly, we find an excellent agreement between the numerical simulations and the nonlinear rod model in the vertical electric field on the clamped end. Its behavior is nonlinear for large loads since the electric field is directly proportional to the curvature (Codony *et al.*, 2020b). The non-monotonicity in the maximum electric field as a function of μ_{T} discussed above is also apparent from this plot.

General flexoelectric problem

We investigate now more general flexoelectric conditions beyond the restrictive assumptions of the reduced model in Codony *et al.* (2020b) by assuming an isotropic Neo-Hookean hyperelastic rod, cf. Eq. (A.10) augmented with strain gradient elasticity, with material parameters $\nu = 0.3$, $\ell_{\text{mech}} = 0.1\ \mu\text{m}$ and varying flexoelectric constants.

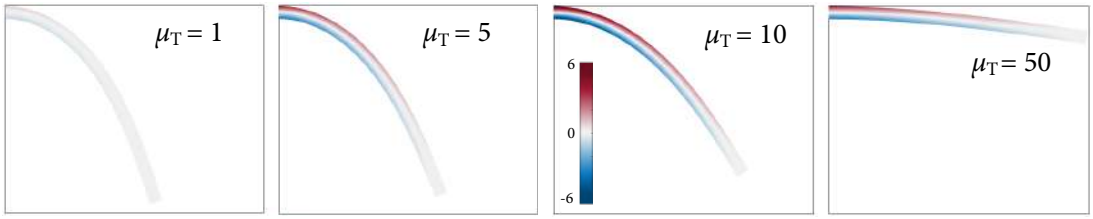

(a) Deformed shape and electric potential [V] distribution of cantilever rods of slenderness $L/H = 20$ under a point load of 20 nN, for different transversal flexoelectric coefficients μ_T.

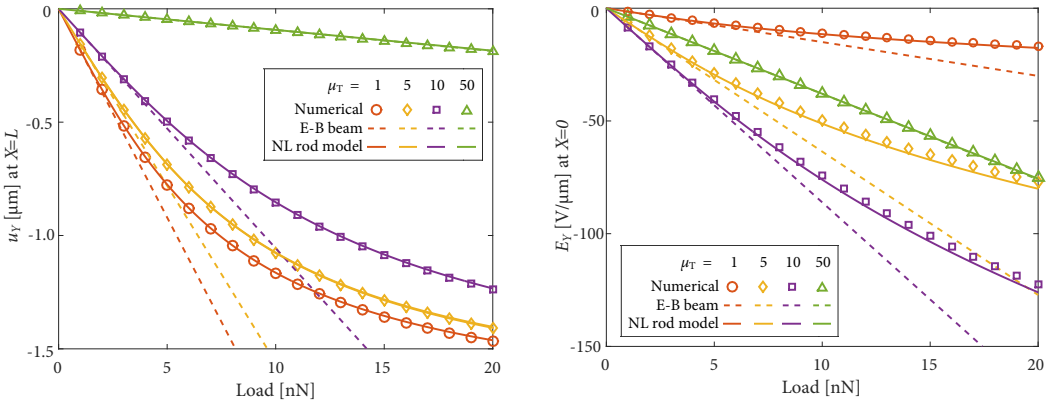

(b) Bending of a cantilever rod of slenderness $L/H = 20$ with varying transversal flexoelectric coefficient μ_T. The left plot shows the vertical displacement at the loaded end, and the right one shows the vertical electric field at the fixed end.

Figure 3.14: Electromechanical response of Saint-Venant–Kirchhoff cantilever flexoelectric sensor under bending. The transversal flexoelectric coefficient μ_T in the legends is expressed in nC/m. Figure adapted from Codony *et al.* (2020b).

Fig. 3.15 represents the electromechanical response of the open circuit cantilever rod under point load for varying flexoelectric constants $\mu_L, \mu_T, \mu_S = \{-10, 0, 10\}$nC/m. Fig. 3.15a shows the deflection u_Y of the loaded end, whereas Fig. 3.15b shows the vertical electric field E_Y at the clamped end. For the sake of brevity, some combinations of flexoelectric tensors are omitted, since we found that the responses are analogous to the ones of other combinations as follows:

$$u_Y|_{\boldsymbol{\mu}} = u_Y|_{-\boldsymbol{\mu}}; \tag{3.30a}$$

$$E_Y|_{\boldsymbol{\mu}} = -E_Y|_{-\boldsymbol{\mu}}. \tag{3.30b}$$

From Fig. 3.15a, it is clear that flexoelectricity is always increasing the bending stiffness of the rod. The largest stiffening is found with opposite μ_T and μ_L, followed by the case of vanishing μ_L. On the contrary, the simulations with $\mu_L \sim \mu_T$ and the ones with vanishing μ_T present a smaller stiffening. In all cases, the effect of the shear flexoelectric coefficient μ_S on bending stiffness is much smaller, and therefore less relevant.

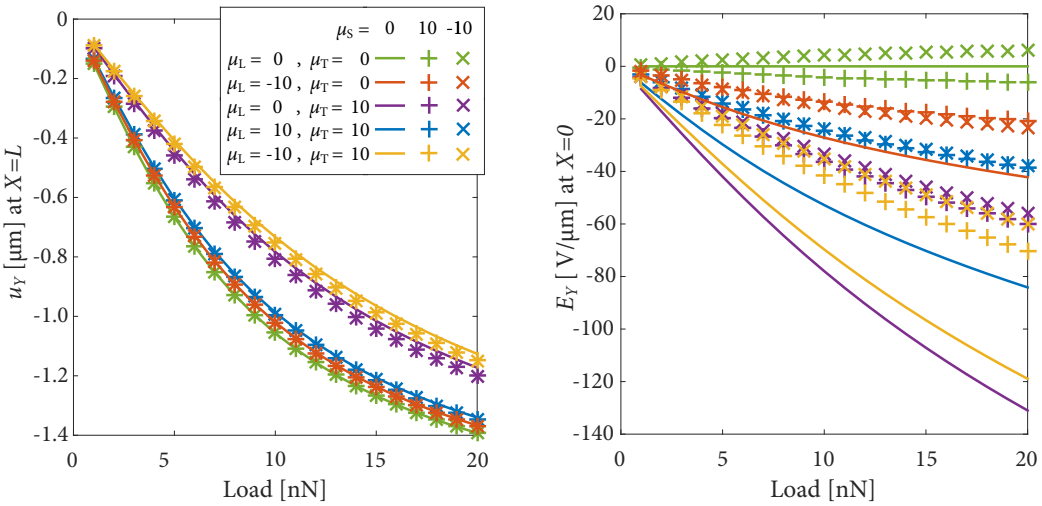

(a) Vertical displacement at the loaded end.

(b) Vertical electric field at the fixed end.

Figure 3.15: Electromechanical response of Neo-Hookean cantilever flexoelectric sensor under bending, with different flexoelectric tensors (expressed in nC/m). Figure adapted from Codony *et al.* (2020b).

Fig. 3.15b shows the electric response of the rod at the clamped tip, revealing that all three flexoelectric coefficients are relevant here. Within the studied range, a larger flexoelectricity-induced bending stiffness leads also to a larger electric field. However, in addition, the shear flexoelectric effect μ_S has a large influence on the electric field. In most cases, a non-vanishing μ_S leads to a substantial decrease in the reported electric field, which slightly depends also on the sign of μ_S. The only case in which a non-vanishing μ_S increases the electric field is the one where μ_S is the *only* non-vanishing flexoelectric coefficient.

3.2.6.2 Mechanically-induced buckling

We now compress an open-circuit flexoelectric rod of thickness $H = 100\,\text{nm}$ and slenderness $L/H = 60$ until buckling occurs, and also during the post-buckling stage. The left tip is clamped and a uniform horizontal load is applied on the right cross-section, which can only move uniformly in axial direction, i.e. vertical displacement and rotation of the right end are prevented (see Fig. 3.13b). We consider an isotropic Saint-Venant–Kirchhoff model with Young's modulus $Y = 1.725\text{GPa}$, dielectric permittivity $\epsilon = 0.092\text{nC/Vm}$ and different transversal flexoelectric coefficients: $\mu_T = \{0, 1, 5, 10\}$ nC/m. The other material parameters are set to zero ($\nu = \mu_L = \mu_S = \ell_{\text{mech}} = 0$).

As shown in Fig. 3.16, the numerical simulations and the analytical 1D model agree remarkably well. The highly nonlinear nature of the electromechanical system is clear in the responses reported in the post-buckling regime. Before buckling, the system is uniformly compressed and the flexoelectric effect is not present yet since the rod is not bent, and hence

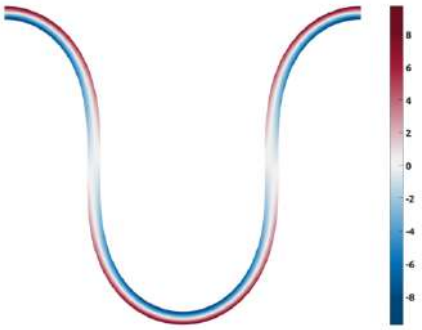

(a) Buckled rod geometry and resulting electric potential [V].

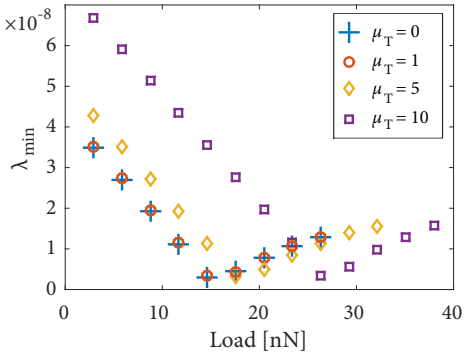

(b) Minimum eigenvalue $\lambda_{\min}\left[\widehat{\mathbf{H}}_{xx}^{(k)}\right]$.

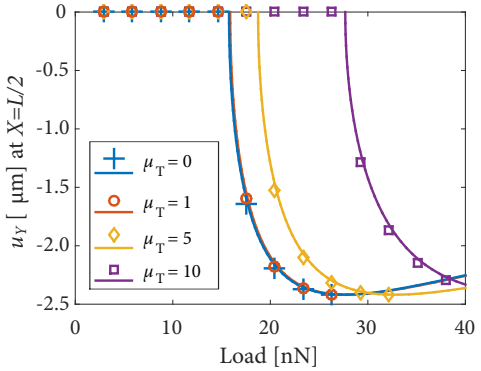

(c) Vertical displacement at the middle cross-section of the rod.

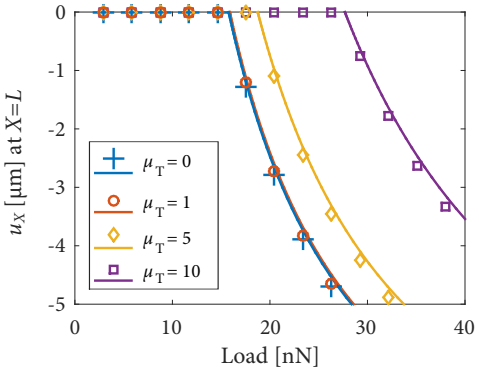

(d) Horizontal displacement at the right end of the rod.

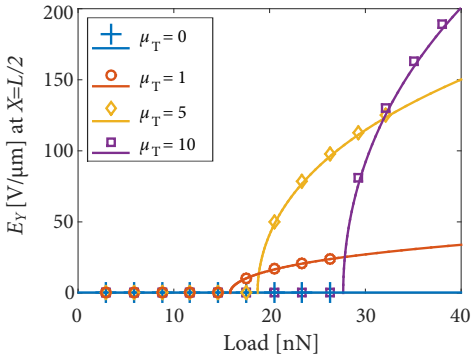

(e) Vertical electric field at the middle cross-section of the rod.

Figure 3.16: Force-controlled buckling of a flexoelectric rod. Markers refer to the numerical implementation and solid lines refer to the analytical nonlinear model for rods in Codony *et al.* (2020b). The transversal flexoelectric coefficient μ_{T} is expressed in nC/m. Figure adapted from Codony *et al.* (2020b).

the electric response is zero. Once the rod has buckled (see Fig. 3.16a), the vertical displacement at the center (Fig. 3.16c) and the horizontal displacement at the right end (Fig. 3.16d) suddenly deviate from zero and evolve nonlinearly with respect to the applied load. The flexoelectric effect arises due to the curvature induced by buckling, leading to a measurable electric field at the center of the rod, which also evolves nonlinearly with applied load (Fig. 3.16e).

The role of the magnitude of the flexoelectric coefficient μ_{T} is twofold. On the one hand, the critical buckling load becomes larger with a larger μ_{T} coefficient. This fact is in agreement with the previous example where the effective stiffness of the rod is increased due to the flexoelectric effect. Numerically, the precise value of the critical buckling load is identified by the load at which the eigenvalue $\lambda_{\min}\left[\widehat{\mathbf{H}}_{\chi\chi}{}^{(k)}\right]$ vanishes, as reported in Fig. 3.16b. On the other hand, the electric field at the post-buckling stage grows faster with a larger μ_{T} coefficient as expected. Thus, the buckling-induced flexoelectric response is delayed but stronger when μ_{T} is larger.

3.2.6.3 Electrically-induced bending

We now consider a closed-circuit flexoelectric cantilever rod of thickness $H = 1\mu\mathrm{m}$ and slenderness $L/H = 20$ which rolls up into a circle upon electrical stimulus. The geometry and boundary conditions are depicted in Fig. 3.13c. The left tip cross-section of the rod is clamped, while all other boundaries are traction-free. The electric potential at the top boundary is set to a certain non-zero value $\phi = V$, and the bottom boundary is grounded ($\phi = 0$). The voltage difference $\Delta\phi = V$ induces a transverse electric field across the rod thickness which triggers the flexoelectric and electrostrictive effects (Codony *et al.*, 2020b), thereby generating a non-uniform strain that bends the rod, as shown in Fig. 3.18d. Depending on the sign of the applied electric field the cantilever will bend upwards or downwards. This bending actuator was first used by Bursian and Zaikovskii (1968) to experimentally demonstrate for the first time the flexoelectric effect, which had been predicted theoretically by Mashkevich and Tolpygo (1957). The Young's modulus considered is $Y = 1.0\mathrm{GPa}$, and the dielectric permittivity $\epsilon = 0.11\mathrm{nC/Vm}$,

Validation

Figure 3.17 shows the electromechanical response of an elastically isotropic Saint-Venant–Kirchhoff flexoelectric rod ($\nu = \ell_{\mathrm{mech}} = 0$) with the flexoelectric constants $\mu_{\mathrm{T}} = 10\mathrm{nC/m}$, $\mu_{\mathrm{L}} = \mu_{\mathrm{S}} = 0$.

The curvature $1/R$ (Fig. 3.17a) and the axial strain ζ (Fig. 3.17b) are constant along the rod, and agree very well with the analytical derivations in Codony *et al.* (2020b) up to a relatively large value of applied voltage V. Beyond this limit, the linear strains assumption of the 1D non-linear model loose validity. According to Codony *et al.* (2020b), the rod bends thanks to the flexoelectric coupling, and elongates mainly due to electrostriction, i.e. the Maxwell stress effect.

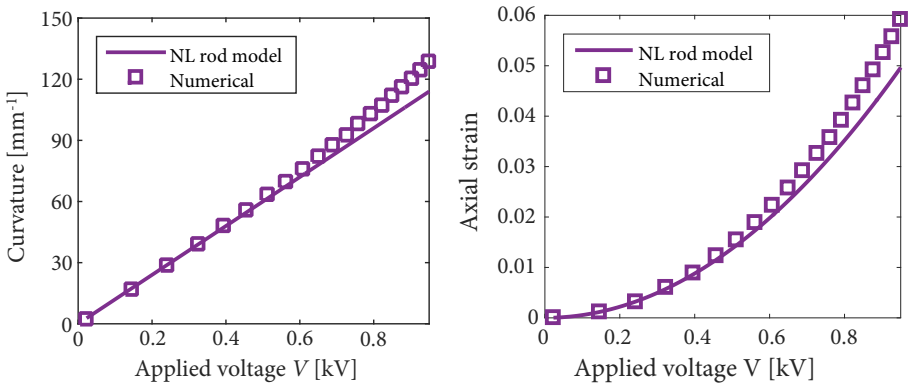

(a) Curvature $R^{-1}(V)$. (b) Axial strain $\zeta(V)$.

Figure 3.17: Actuation of Saint-Venant–Kirchhoff cantilever rod with transversal flexoelectric coefficient $\mu_T = 10\text{nC/m}$. Numerically, the axial strain corresponds to the axial component of the Green-Lagrangian strain tensor $\mathfrak{E}_{XX}$ evaluated at $Y = 0$, whereas the value from the 1D model corresponds to its Taylor approximation (Codony *et al.*, 2020b). Figure adapted from Codony *et al.* (2020b).

General flexoelectric problem

Since the curvature is uniform (Codony *et al.*, 2020b), the rod forms an arc of a circle, cf. Fig. 3.18d. Thus, a natural question that arises is which set of flexoelectric parameters achieve a fully-closed circular shape more efficiently (i.e. with a lower applied voltage). To address this question, we consider an isotropic Neo-Hookean elastic (see Eq. (A.10)) rod with $\nu = 0.37$, $\ell_{\text{mech}} = 0.03\mu\text{m}$ and varying flexoelectric constants. To quantify the curvature of the rod relative to the curvature of the closed circle, we define the normalized curvature $\overline{R^{-1}}(V) = R^{-1}(V)/R_{\circ}^{-1}(V)$, where $R_{\circ}^{-1}(V)$ is the curvature required to form a closed circular shape for a given rod length.

Figure 3.18 shows the evolution of the axial strain $\zeta(V)$, curvature R^{-1} and normalized curvature $\overline{R^{-1}}$ for flexoelectric tensors with different combinations of longitudinal (μ_L), transversal (μ_T) and shear (μ_S) flexoelectric coefficients. The cases including a non-vanishing shear coefficient are omitted, since the results do not change significantly, even when μ_S is one order of magnitude larger than μ_L or μ_T. For the sake of brevity, the simulations *(i)* with negative applied electric voltage V, and *(ii)* yielding negative curvatures, are also omitted since the results are analogous to those simulations with *(i)* positive applied voltage and *(ii)* negative flexoelectric coefficients, respectively, as

$$\zeta(V)|_{\boldsymbol{\mu}} = \zeta(-V)|_{\boldsymbol{\mu}} = \zeta(V)|_{-\boldsymbol{\mu}} = \zeta(-V)|_{-\boldsymbol{\mu}}; \tag{3.31a}$$

$$R^{-1}(V)|_{\boldsymbol{\mu}} = -R^{-1}(-V)|_{\boldsymbol{\mu}} = -R^{-1}(V)|_{-\boldsymbol{\mu}} = R^{-1}(-V)|_{-\boldsymbol{\mu}}; \tag{3.31b}$$

$$\overline{R^{-1}}(V)|_{\boldsymbol{\mu}} = -\overline{R^{-1}}(-V)|_{\boldsymbol{\mu}} = -\overline{R^{-1}}(V)|_{-\boldsymbol{\mu}} = \overline{R^{-1}}(-V)|_{-\boldsymbol{\mu}}. \tag{3.31c}$$

As expected, the axial strain of the rod (depicted in Fig. 3.18a) does not vary much with

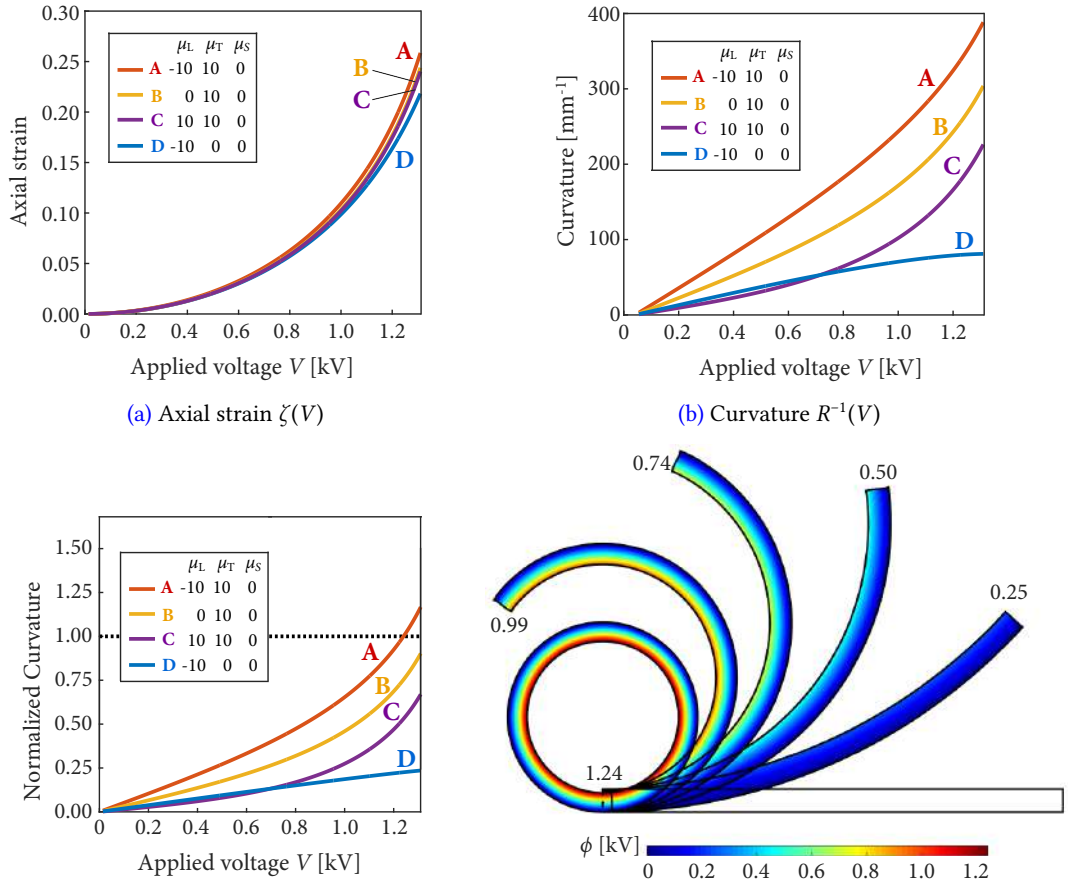

(a) Axial strain $\zeta(V)$

(b) Curvature $R^{-1}(V)$

(c) Normalized curvature $\overline{R^{-1}}(V)$

(d) Deformed configuration and electric potential distribution in case A upon increasing voltage V[kV], indicated by the number at the free end.

Figure 3.18: Actuation of Neo-Hookean cantilever rod with different flexoelectric tensors (expressed in nC/m). Figure adapted from Codony *et al.* (2020b).

the different flexoelectric parameters, since it is mainly a consequence of electrostriction. The curvature (Fig. 3.18b), instead, varies significantly for the different combinations of flexoelectric parameters. The dominant parameter is the transversal flexoelectric coefficient μ_T which leads to positive curvature, as shown in case B. The longitudinal flexoelectric coefficient μ_L is also relevant and leads to negative curvature, as shown in case D. The largest response is found with positive μ_T and negative μ_L, as shown in case A. Finally, case C corresponds to positive μ_L and μ_T, and yields curvatures in between cases B (purely transversal $\boldsymbol{\mu}$) and D (purely longitudinal $\boldsymbol{\mu}$).

The normalized curvature is shown in Fig. 3.18c. For sufficiently large actuation, case A reaches $\overline{R^{-1}} > 1$, which indicates that the actuator rolls up forming a closed circle. This process is shown in Fig. 3.18d, where the deformed configuration and electric potential distribution

within the rod is depicted at different applied voltages.

3.2.6.4 Electrically-induced buckling

In the previous example, the rod undergoes elongation upon electrical actuation mainly due to electrostriction. In this Section, we present a similar setup where the right tip is also clamped, as shown in Fig. 3.13d. In this case, an axial compressive force is expected at the clamped ends since the elongation of the rod is prevented. According to the analytical derivations in Codony *et al.* (2020b), electrostriction induces an axial force which grows quadratically with the applied voltage and, for a large enough applied (critical) voltage V_{cr}, a mechanical instability is reached, inducing buckling of the rod.

Figure 3.19 shows numerical simulations of a flexoelectric Saint-Venant–Kirchhoff rod ($\nu = \ell_{\text{mech}} = 0$) of dimensions $L = 20\mu\text{m}$, $H = 1\mu\text{m}$, with Young's modulus $Y = 1.0\text{GPa}$, dielectric permittivity $\epsilon = 0.11\text{nC/Vm}$ and transversal flexoelectric coefficient $\mu_{\text{T}} = 10\text{nC/m}$ ($\mu_{\text{L}} = \mu_{\text{S}} = 0$). The postbuckling configuration and the evolution of the maximum deflection and axial strain with respect to applied voltage are depicted in Fig. 3.19a-3.19c, showing an excellent match between the numerical results and the analytical expressions in Codony *et al.* (2020b). The critical voltage at which the rod buckles (see Fig. 3.19d) matches also with the one predicted by the analytical 1D nonlinear model, and the critical electric field (cf. Fig. 3.19e) is inversely proportional to the slenderness of the rod.

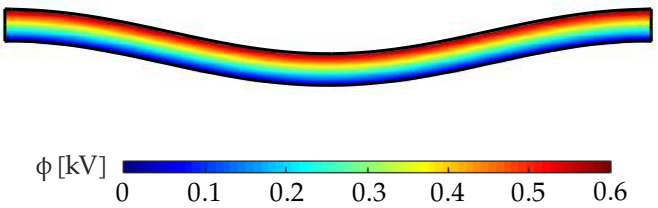

(a) Buckled shape and electric potential distribution of the $L/H = 20$-slender rod upon electrical loading of 0.6kV.

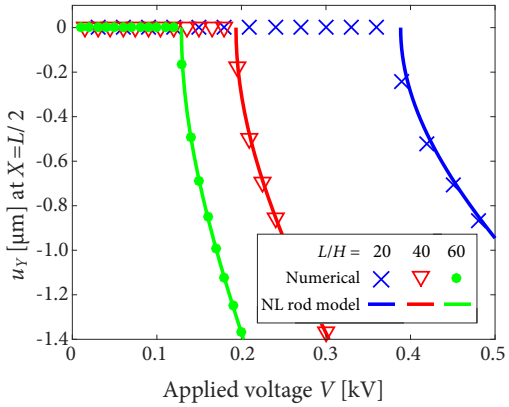

(b) Vertical deflection at the center of the rod.

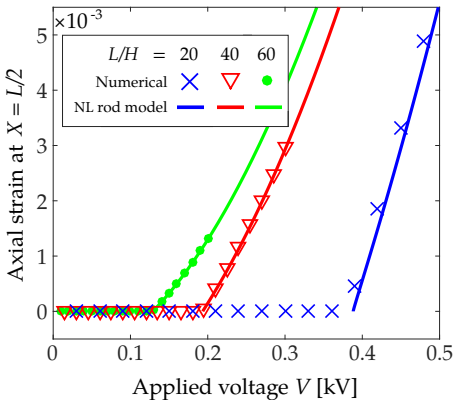

(c) Axial strain at the center of the rod.

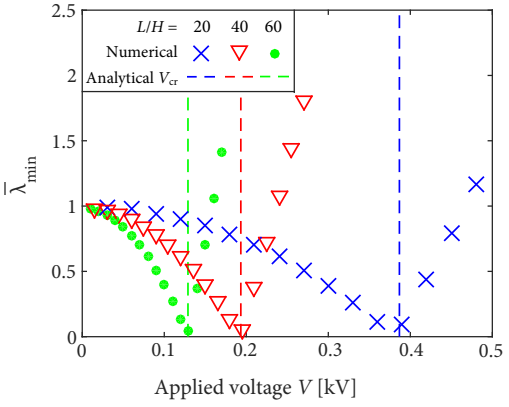

(d) Normalized minimum eigenvalue $\lambda_{\min}\left[\widehat{\mathbf{H}}_{xx}^{(k)}\right]$ and critical voltage of analytical 1D model.

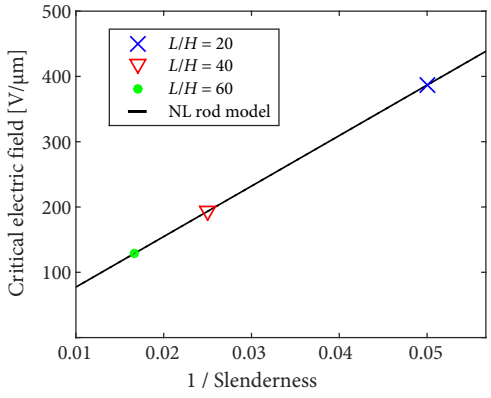

(e) Critical electric field as a function of slenderness.

Figure 3.19: Actuation of Saint-Venant–Kirchhoff clamped-clamped rod with transversal flexoelectric coefficient $\mu_T = 10$nC/m and varying slenderness. In (d), $\bar{\lambda}_{\min} = \lambda_{\min}\,(n_{\text{DOF}}/n_0)^4$, where n_{DOF} is the number of degrees of freedom of each simulation, and $n_0 = 312$ is an arbitrary normalization constant, chosen such that $\bar{\lambda}_{\min}(0) \approx 1$. Figure adapted from Codony *et al.* (2020b).

3.2.7 Application to arbitrarily-shaped soft flexoelectric devices

The direct flexoelectricity model at finite deformations has been illustrated in Section 3.2.6 by studying flexoelectric rods discretized with body-fitted (i.e. rectangular) meshes. In this Section we go beyond simple body-fitted meshes and consider unfitted meshes, which can handle arbitrarily-shaped geometries. We employ Nitsche's formulation presented in Section 2.2.4.1.b in order to enforce essential boundary conditions weakly.

In the same way as in Section 3.2.6, the nonlinear system of equations arising from the weak form in Eq. (2.147) is solved by the modified-step Newton-Raphson algorithm. In this case, the residual $\mathcal{R}$ in Eq. (3.21) has extra terms $\mathcal{R}^{\text{Nitsche}}$ coming from the Nitsche integrals at the Dirichlet boundaries:

$$\begin{aligned}\mathcal{R}^{\text{Nitsche}}[\boldsymbol{\chi},\Phi;\delta\boldsymbol{\chi},\delta\Phi] = &\int_{\partial\Omega_0^{\chi}}\Big(\left(\chi_i-\overline{\chi}_i\right)\left(\beta_{\chi}\delta\chi_i-\delta T_i\right)-T_i\delta\chi_i\Big)\,\mathrm{d}\Gamma_0\\ &+\int_{\partial\Omega_V}\Big(\left(\partial_0^N\chi_i-\overline{V}_i\right)\left(\beta_V\partial_0^N\delta\chi_i-\delta R_i\right)-R_i\partial_0^N\delta\chi_i\Big)\,\mathrm{d}\Gamma_0\\ &+\int_{\partial\Omega_0^{\Phi}}\Big(-\left(\Phi-\overline{\Phi}\right)\left(\beta_{\Phi}\delta\Phi-\delta W\right)+W\delta\Phi\Big)\,\mathrm{d}\Gamma_0\\ &+\int_{C_0^{\chi}}\Big(\left(\chi_i-\overline{\chi}_i\right)\left(\beta_{C_{\chi}}\delta\chi_i-\delta J_i\right)-J_i\delta\chi_i\Big)\,\mathrm{d}s_0,\end{aligned}\tag{3.32}$$

with the variations $\delta\boldsymbol{T}(\boldsymbol{\chi},\phi;\delta\boldsymbol{\chi},\delta\Phi)$, $\delta\boldsymbol{R}(\boldsymbol{\chi},\phi;\delta\boldsymbol{\chi},\delta\Phi)$, $\delta W(\boldsymbol{\chi},\phi;\delta\boldsymbol{\chi},\delta\Phi)$ and $\delta\boldsymbol{J}(\boldsymbol{\chi},\phi;\delta\boldsymbol{\chi},\delta\Phi)$ defined in Eq. (2.148). At the k-th iteration, the solution increment $\{\Delta\boldsymbol{\chi},\Delta\Phi\}^{(k)}$ is found by vanishing the first order Taylor expansion of the residual $\mathcal{R}+\mathcal{R}^{\text{Nitsche}}$ around the previous solution $\{\boldsymbol{\chi},\Phi\}^{(k-1)}$, yielding the following algebraic system of equations:

$$\left(\begin{bmatrix}\mathbf{H}_{\chi\chi} & \mathbf{H}_{\chi\Phi}\\ \mathbf{H}_{\Phi\chi} & \mathbf{H}_{\Phi\Phi}\end{bmatrix}+\begin{bmatrix}\mathbf{H}_{\chi\chi}^{\text{Nitsche}} & \mathbf{H}_{\chi\Phi}^{\text{Nitsche}}\\ \mathbf{H}_{\Phi\chi}^{\text{Nitsche}} & \mathbf{H}_{\Phi\Phi}^{\text{Nitsche}}\end{bmatrix}\right)^{(k-1)}\cdot\begin{bmatrix}\Delta\boldsymbol{\chi}\\ \Delta\Phi\end{bmatrix}^{(k)}=-\left(\begin{bmatrix}\mathbf{R}_{\chi}\\ \mathbf{R}_{\Phi}\end{bmatrix}+\begin{bmatrix}\mathbf{R}_{\chi}^{\text{Nitsche}}\\ \mathbf{R}_{\Phi}^{\text{Nitsche}}\end{bmatrix}\right)^{(k-1)},\tag{3.33}$$

where

$$\mathbf{H}_{\chi\chi}^{\text{Nitsche}}\left(\boldsymbol{\chi}^{(k-1)},\Phi^{(k-1)}\right)=\frac{\partial\mathcal{R}^{\text{Nitsche}}}{\partial\boldsymbol{\chi}}\left[\boldsymbol{\chi}^{(k-1)},\Phi^{(k-1)};\delta\boldsymbol{\chi},0\right],\tag{3.34a}$$

$$\mathbf{H}_{\chi\Phi}^{\text{Nitsche}}\left(\boldsymbol{\chi}^{(k-1)},\Phi^{(k-1)}\right)=\frac{\partial\mathcal{R}^{\text{Nitsche}}}{\partial\Phi}\left[\boldsymbol{\chi}^{(k-1)},\Phi^{(k-1)};\delta\boldsymbol{\chi},0\right],\tag{3.34b}$$

$$\mathbf{H}_{\Phi\chi}^{\text{Nitsche}}\left(\boldsymbol{\chi}^{(k-1)},\Phi^{(k-1)}\right)=\frac{\partial\mathcal{R}^{\text{Nitsche}}}{\partial\boldsymbol{\chi}}\left[\boldsymbol{\chi}^{(k-1)},\Phi^{(k-1)};\mathbf{0},\delta\Phi\right],\tag{3.34c}$$

$$\mathbf{H}_{\Phi\Phi}^{\text{Nitsche}}\left(\boldsymbol{\chi}^{(k-1)},\Phi^{(k-1)}\right)=\frac{\partial\mathcal{R}^{\text{Nitsche}}}{\partial\Phi}\left[\boldsymbol{\chi}^{(k-1)},\Phi^{(k-1)};\mathbf{0},\delta\Phi\right],\tag{3.34d}$$

$$\mathbf{R}_{\chi}^{\text{Nitsche}}\left(\boldsymbol{\chi}^{(k-1)},\Phi^{(k-1)}\right)=\mathcal{R}^{\text{Nitsche}}\left[\boldsymbol{\chi}^{(k-1)},\Phi^{(k-1)};\delta\boldsymbol{\chi},0\right],\tag{3.34e}$$

$$\mathbf{R}_{\Phi}^{\text{Nitsche}}\left(\boldsymbol{\chi}^{(k-1)},\Phi^{(k-1)}\right)=\mathcal{R}^{\text{Nitsche}}\left[\boldsymbol{\phi}^{(k-1)},\Phi^{(k-1)};\mathbf{0},\delta\Phi\right].\tag{3.34f}$$

The variation $\delta\mathcal{R}^{\text{Nitsche}}[\boldsymbol{\chi}, \Phi; \delta\boldsymbol{\chi}, \delta\Phi; \Delta\boldsymbol{\chi}, \Delta\Phi]$ required to compute Eq. (3.34) is approximated as

$$\begin{aligned}\delta\mathcal{R}^{\text{Nitsche}}[\boldsymbol{\chi}, \Phi; \delta\boldsymbol{\chi}, \delta\Phi; \Delta\boldsymbol{\chi}, \Delta\Phi] \approx & \int_{\partial\Omega_0^\chi} \left(\Delta\chi_i \left(\beta_\chi \delta\chi_i - \delta T_i\right) - \Delta T_i \delta\chi_i\right) \mathrm{d}\Gamma_0 \\ & + \int_{\partial\Omega_V} \left(\partial_0^N \Delta\chi_i \left(\beta_V \partial_0^N \delta\chi_i - \delta R_i\right) - R_i \partial_0^N \delta\chi_i\right) \mathrm{d}\Gamma_0 \\ & + \int_{\partial\Omega_0^\Phi} \left(- \Delta\Phi \left(\beta_\Phi \delta\Phi - \delta W\right) + \Delta W \delta\Phi\right) \mathrm{d}\Gamma_0 \\ & + \int_{C_0^\chi} \left(\Delta\chi_i \left(\beta_{C_\chi} \delta\chi_i - \delta J_i\right) - \Delta J_i \delta\chi_i\right) \mathrm{d}s_0, \end{aligned} \tag{3.35}$$

where $\Delta\boldsymbol{T} = \delta\boldsymbol{T}(\boldsymbol{\chi}, \phi; \Delta\boldsymbol{\chi}, \Delta\Phi)$, $\Delta\boldsymbol{R} = \delta\boldsymbol{R}(\boldsymbol{\chi}, \phi; \Delta\boldsymbol{\chi}, \Delta\Phi)$, $\Delta W = \delta W(\boldsymbol{\chi}, \phi; \Delta\boldsymbol{\chi}, \Delta\Phi)$ and $\Delta\boldsymbol{J} = \delta\boldsymbol{J}(\boldsymbol{\chi}, \phi; \Delta\boldsymbol{\chi}, \Delta\Phi)$. Eq. (3.35) is not exact because the following terms have been neglected:

$$\begin{aligned} 0 \approx & - \int_{\partial\Omega_0^\chi} \left(\chi_i - \overline{\chi}_i\right) \Delta\delta T_i \, \mathrm{d}\Gamma_0 - \int_{\partial\Omega_V} \left(\partial_0^N \chi_i - \overline{V}_i\right) \Delta\delta R_i \, \mathrm{d}\Gamma_0 \\ & + \int_{\partial\Omega_0^\Phi} \left(\Phi - \overline{\Phi}\right) \Delta\delta W \, \mathrm{d}\Gamma_0 - \int_{C_0^\chi} \left(\chi_i - \overline{\chi}_i\right) \Delta\delta J_i \, \mathrm{d}s_0. \end{aligned} \tag{3.36}$$

Note that the $\Delta\delta$ operator in Eq. (3.36) refers to the second variations of $\boldsymbol{T}$, $\boldsymbol{R}$, W and $\boldsymbol{J}$, which are extremely difficult to compute, specially since they involve third derivatives of the enthalpy functionals. Luckily, the terms in Eq. (3.36) can be neglected since they rapidly tend to zero as Dirichlet boundary conditions are met, i.e. after one or two iterations in the modified-step Newton-Raphson algorithm.

Once $\{\Delta\boldsymbol{\chi}, \Delta\Phi\}^{(k)}$ are found by solving Eq. (3.33), the *modified* increments $\{\overline{\Delta\boldsymbol{\chi}}, \overline{\Delta\Phi}\}^{(k)}$ are computed as described in Section 3.2.6, and the solution is updated with Eq. (3.27) until convergence.

The proposed numerical scheme is illustrated in the following example in Section 3.2.7.1.

3.2.7.1 Collective-beam sensor triggered by compression

We consider here a soft flexoelectric device which yields a scalable potential difference when subjected to uniform compression, hence mimicking the response of a piezoelectric sensor. The device (see Fig. 3.20a) is composed by an horizontal arrangement of n_b vertical cantilevers of width H_b and length L_Y, separated at a distance s, and connected at the center with a transversal rod of width H_a. The cantilevers are clamped at both ends and the central point of the device is grounded (i.e. $\Phi = 0$). The main idea is to axially compress the device by applying a vertical displacement $u_Y = -\delta$ on the top boundary until the vertically-arranged cantilevers undergo buckling. As previously seen in Section 3.2.6.2, a mechanically-induced buckling on flexoelectric rods yields an electric field across the rod thickness due to the buckling-induced curvature and the flexoelectric effect. Since the buckled rods are connected at the

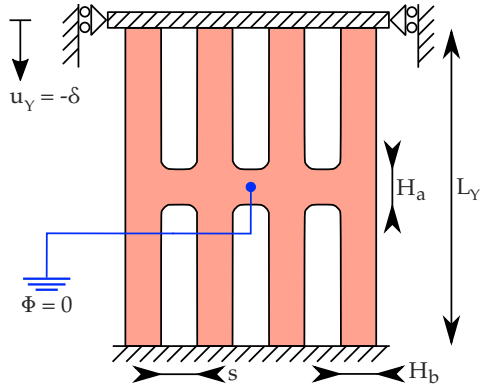

(a) Geometry and boundary conditions

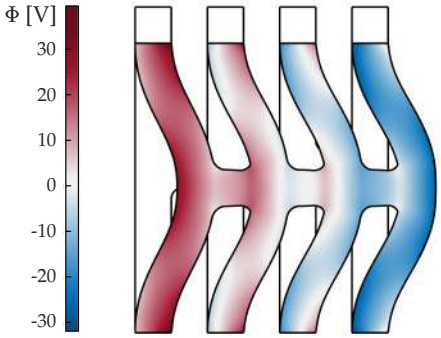

(b) Deformed shape and electric potential at $\delta = \delta_{max}$

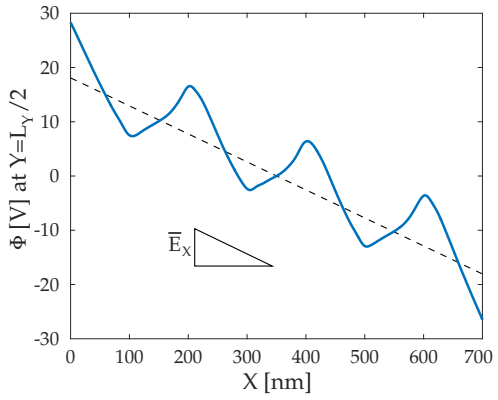

(c) Electric potential along $Y = L/2$ at $\delta = \delta_{max}$.

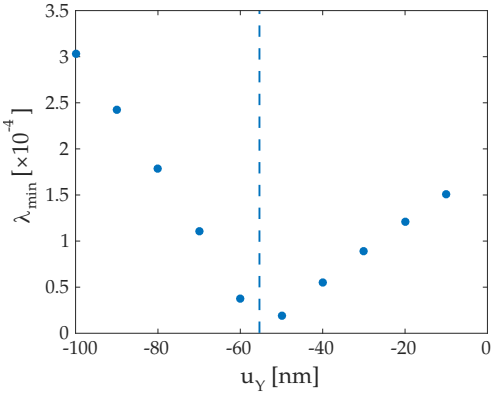

(d) Minimum eigenvalue

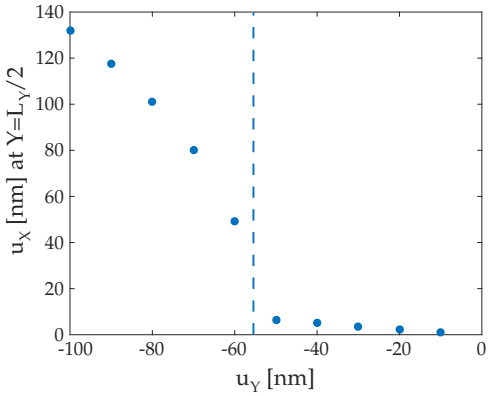

(e) Horizontal deflection

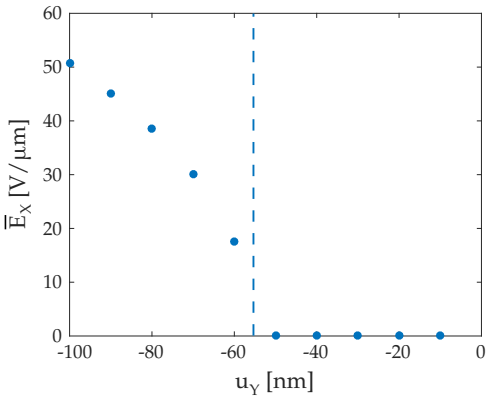

(f) Macroscopic horizontal electric field

Figure 3.20: Flexoelectric collective-beam sensor triggered by compression. (b)-(c) refer to the solution at last load step ($\delta = \delta_{max} = 100$nm), whereas (d)-(f) show different quantities of interest at each load step. The vertical blue dashed lines in (d)-(f) denote the critical δ at which the buckling instability is triggered.

location at which curvature, and hence electric field, is maximum, an effective accumulation of the potential difference across the many rods composing the device is expected. The device is scalable since the expected response (voltage difference between left and right ends) will increase linearly with the width of the device, hence making it possible to harness the flexoelectric effect, occurring at sub-micron scales, at larger (meso-) scales.

Fig. 3.20 shows the results of the aforedescribed flexoelectric sensor with design parameters $n_b = 4$, $H_a = H_b = s = 100\text{nm}$ and $L_Y = 700\text{nm}$, under an increasing compression δ ranging from 0 to $\delta_{\max} = 100\text{nm}$. The material parameters correspond to polyvinylidene fluoride (PVDF) (Chu and Salem, 2012, Zhang *et al.*, 2016b, Zhou *et al.*, 2017), that is, Young's modulus $Y = 1.725\text{GPa}$, Poisson ratio $\nu = 0.38$, dielectric permittivity $\epsilon = 0.092\text{nC/Vm}$, and $\mu_{\text{T}} = -10\text{nC/m}$. Other material parameters are set to 0. The unfitted Cartesian mesh has element size $h \approx 12\text{nm}$ and spline degree $p = 3$.

Fig. 3.20b shows the electromechanical state of the device at the maximum compression $\delta_{\max}$. The buckled shape of the constituent cantilever rods is apparent, as well as the electric potential distribution within the device induced due to the flexoelectric coupling. The electric potential along the horizontal rod connecting the cantilevers (i.e. along $Y = L_Y/2$) is shown in Fig. 3.20c. As expected, the difference in electric potential across the rods is accumulated from rod to rod, yielding a scalable device: if the number of constituent cantilevers is doubled ($2n_b = 8$), the potential difference along the X coordinate will double as well. Remarkably, the electric potential is not monotonic along the horizontal rod: the junctions between vertical cantilevers undergo an opposite trend to the one across the cantilevers. This is due to the opposite strain gradients at the junctions compared to the cantilever centers. Indeed, since the concave side of cantilevers undergoes transversal compression while the convex one undergoes traction, the junctions between them undergo the opposite behavior. Overall, a measurable (non-vanishing) macroscopic electric field $\overline{E}_X = -(\Phi_R - \Phi_L)/(X_R - X_L)$ is obtained, independently of n_b.

Figures 3.20d-3.20f show the evolution of the minimum eigenvalue $\lambda_{\min}$ of the algebraic system of equations, the horizontal deflection u_X and the macroscopic electric field $\overline{E}_X$ as a function of the increasing compression δ. The critical compression δ^{cr} at which the buckling, and hence the electromechanical transduction, is triggered corresponds to the point at which $\lambda_{\min} = 0$ in Fig. 3.20d, and is about $\delta^{\text{cr}} = 55\text{nm}$. The horizontal deflection (Fig. 3.20e) and the macroscopic electric field (Fig. 3.20f) are 0 until the critical compression is reached. Then, both quantities undergo a highly nonlinear increase with respect to the applied compression δ.

The optimal design parameters maximizing $\overline{E}_X$ and yielding a desired δ^{cr} can be obtained by means of a shape optimization analysis, which is left to future work.

In view of the results in Fig. 3.20, devices built by a periodic material arrangement (also called *architected materials*) yield *generalized periodic* solution fields, that is, solutions that are periodic up to a constant value, just like the electric potential profile in Fig. 3.20c. In other words, the first derivatives of the solutions (in this case, the electric fields) are periodic. In those situations, is it possible to reduce the computation to a single unit cell by means of

generalized periodic conditions in order to characterize the behavior of architected materials in a very efficient way. This idea has been already developed in our research group but is out of the scope of this thesis. We refer to Barceló-Mercader *et al.* (2021a) and Mocci *et al.* (2021) for further details.

3.3 On-going and future work

3.3.1 Residual-based weak form stabilization

As discussed in Remark 2.5 in Section 2.2.2.3, depending on the geometry of Ω, the boundary conditions, the material parameters and the mesh size, the numerical solution to the flexoelectricity problem features spurious oscillations which completely spoil the quality of the results. Fig. 3.21 shows an example of spurious oscillations arising in a Lifshitz-form flexoelectric cantilever beam under open circuit boundary conditions.

In view of the results in Section 2.2.2.3, and further confirmed by the experience of this manuscript's author, the numerical instabilities are associated with the presence of boundary layers in the electric field, which may appear when considering the Lifshitz-invariant flexoelectricity form (cf. Section 2.2.2.2). Such spurious oscillations are not encountered in the literature of computational flexoelectricity since only the direct flexoelectricity form (cf. Section 2.2.2.1) has been considered so far.

In the following, we resort to the Galerkin least-squares (GLS) method (Baiocchi *et al.*, 1993, Franca and Stenberg, 1991, Thompson and Pinsky, 1995) to stabilize the problem, due to its simple form and implementation. The idea is to increase the effective mechanical and electrical length scales in a self-consistent manner, providing control on the second derivatives of the state variables.

To this end, it is useful to think of a simplified 1D-version of the Euler-Lagrange equations associated to the Lifshitz-invariant flexoelectricity form (cf. Eq. (2.81)) as follows:

$$\begin{cases} \partial\left(\widehat{\sigma} - \partial\tilde{\sigma}\right) + \overline{b} = 0, \\ \partial\left(\widehat{D} - \partial\widetilde{D}\right) - \overline{q} = 0, \end{cases} \quad \Longrightarrow \quad \begin{cases} \mathcal{L}_{uu}u + \mathcal{L}_{u\phi}\phi \equiv Yu^{II} - Y\ell_{\text{mech}}^2 u^{IV} - \mu\phi^{III} = -\overline{b}, \\ \mathcal{L}_{\phi u}u + \mathcal{L}_{\phi\phi}\phi \equiv -\epsilon\phi^{II} + \epsilon\ell_{\text{elec}}^2\phi^{IV} + \mu u^{III} = \overline{q}, \end{cases} \tag{3.37}$$

depending on just five material parameters, namely the Young modulus Y and mechanical length scale ℓ_{mech}, the dielectric constant ϵ and the dielectric length scale ℓ_{elec}, and the flexoelectric coefficient μ. The corresponding weak form is

$$\begin{cases} a_{uu}(\delta u, u) + a_{u\phi}(\delta u, \phi) = l_u(\delta u), \\ a_{\phi\phi}(\delta\phi, \phi) + a_{u\phi}(u, \delta\phi) = l_\phi(\delta\phi), \end{cases} \tag{3.38}$$

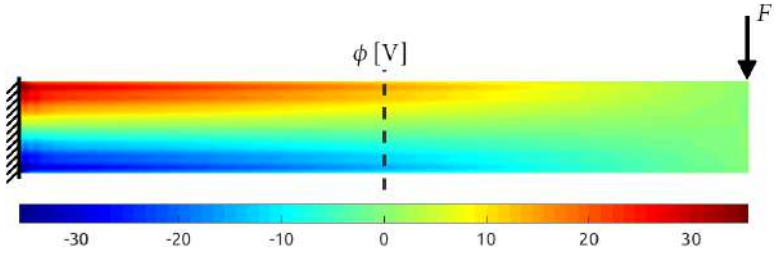

(a) Electric potential distribution within the cantilever.

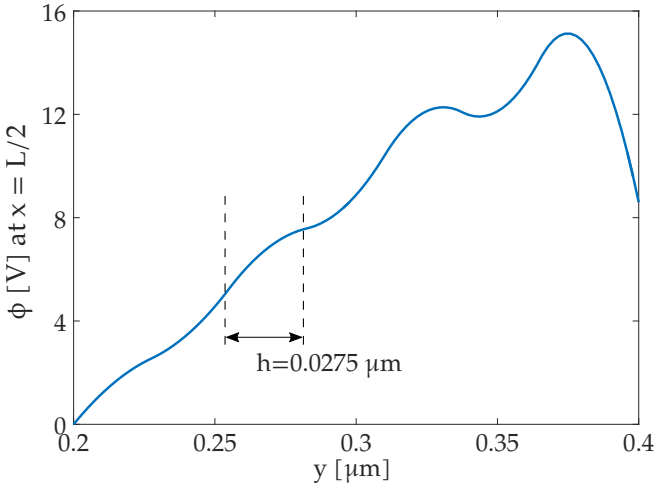

(b) Detail of the electric potential along the cross section at $x = L/2$.

Figure 3.21: Spurious, mesh-dependent oscillatory behavior of the electric potential ϕ in a Lifshitz-invariant flexoelectric cantilever beam of dimensions $L = 3.2\mu m$ by $H = 0.4\mu m$ under bending with open circuit boundary conditions. The mesh size is $h = 0.0275\mu m$. The Young modulus is $Y = 100GPa$, the Poisson ratio $\nu = 0.37$, the dielectric permittivity $\epsilon = 11nJ/V^2m$ and the longitudinal and transversal flexoelectric coefficients $\mu_L = \mu_T = 1\mu J/Vm$. Other material coefficients are 0. The applied force is $F = 100\mu N$.

with appropriate boundary conditions, where

$$a_{uu}(\delta u, u) = (\delta u^I, Y u^I)_\Omega + (\delta u^{II}, Y \ell^2_{\text{mech}} u^{II})_\Omega, \tag{3.39a}$$

$$a_{\phi\phi}(\delta\phi, \phi) = (\delta\phi^I, -\epsilon\phi^I)_\Omega + (\delta\phi^{II}, -\epsilon\ell^2_{\text{elec}}\phi^{II})_\Omega, \tag{3.39b}$$

$$a_{u\phi}(\delta u, \phi) = -\frac{1}{2}\mu\left((\delta u^I, \phi^{II})_\Omega - (\delta u^{II}, \phi^I)_\Omega\right), \tag{3.39c}$$

$$l_u(\delta u) = (\delta u, \overline{b})_\Omega, \tag{3.39d}$$

$$l_\phi(\delta\phi) = (\delta\phi, -\overline{q})_\Omega. \tag{3.39e}$$

Following the GLS method, we make use of Eq. (3.37) to define the following bilinear forms:

$$\mathcal{A}_{\text{mech}}(\{u,\phi\},\{\delta u,\delta\phi\}) := \left(\mathcal{L}_{uu}\delta u + \mathcal{L}_{u\phi}\delta\phi,\, \tau_{\text{mech}} r_{\text{mech}}(u,\phi)\right)_\Omega, \tag{3.40a}$$

$$\mathcal{A}_{\text{elec}}(\{u,\phi\},\{\delta u,\delta\phi\}) := \left(\mathcal{L}_{\phi u}\delta u + \mathcal{L}_{\phi\phi}\delta\phi,\, -\tau_{\text{elec}} r_{\text{elec}}(u,\phi)\right)_\Omega, \tag{3.40b}$$

with the residuals

$$r_{\text{mech}}(u,\phi) := \mathcal{L}_{uu}u + \mathcal{L}_{u\phi}\phi + \overline{b}, \tag{3.41a}$$

$$r_{\text{elec}}(u,\phi) := \mathcal{L}_{\phi u}u + \mathcal{L}_{\phi\phi}\phi - \overline{q}. \tag{3.41b}$$

Note that a solution fulfilling Eq. (3.37) yields vanishing residuals in Eq. (3.41), and therefore the bilinear forms in Eq. (3.40) vanish too. Hence, they can be added to the original weak form in Eq. (3.38) while maintaining self-consistency:

$$\begin{cases} a_{uu}(\delta u,u) + a_{u\phi}(\delta u,\phi) + \mathcal{A}_{\text{mech}}(\{u,\phi\},\{\delta u,0\}) + \mathcal{A}_{\text{elec}}(\{u,\phi\},\{\delta u,0\}) = l_u(\delta u), \\ a_{\phi\phi}(\delta\phi,\phi) + a_{u\phi}(u,\delta\phi) + \mathcal{A}_{\text{mech}}(\{u,\phi\},\{0,\delta\phi\}) + \mathcal{A}_{\text{elec}}(\{u,\phi\},\{0,\delta\phi\}) = l_\phi(\delta\phi). \end{cases} \tag{3.42}$$

The stabilization parameters $\tau_{\text{mech}}, \tau_{\text{elec}}$ provide control on the second derivatives of the state variables and can be tuned as a function of mesh size and material parameters.

Remark 3.1 (*Relation to the variational multiscale method).* The stabilizing forms in Eq. (3.40) are constructed following the GLS approach, considering the same differential operator as in the strong form in Eq. (3.37). If the *adjoint* operator was considered instead, the algebraic subgrid scale (ASGS) stabilization method (Codina, 1998, 2000, Guasch and Codina, 2007) would be obtained, in the context of variational multiscale methods (VMS) (Codina *et al.*, 2018, Hughes *et al.*, 1998). Remarkably, since the considered problem is a (high-order, coupled) *elliptic* PDE, the associated differential operator is self-adjoint, and both ASGS and GLS stabilization methods yield the same result. This can be easily seen by noticing that $\mathcal{L}_{uu} = \mathcal{L}^*_{uu}$, $\mathcal{L}_{u\phi} = \mathcal{L}^*_{\phi u}$, $\mathcal{L}_{\phi u} = \mathcal{L}^*_{u\phi}$ and $\mathcal{L}_{\phi\phi} = \mathcal{L}^*_{\phi\phi}$.

The optimal choice of $\tau_{\text{mech}}, \tau_{\text{elec}}$ remains unclear and is a matter of author's current research. However, a reasonable choice can be made based on the following analysis. The stabilizing bilinear forms in Eq. (3.40) are simplified for the case of a B-spline discretization of degree $p = 2$, since the coupling operators $\mathcal{L}_{u\phi}$ and $\mathcal{L}_{\phi u}$ vanish as well as the fourth-order terms in $\mathcal{L}_{uu}$ and $\mathcal{L}_{\phi\phi}$, yielding the simplified uncoupled forms

$$\mathcal{A}_{\text{mech}}(u,\delta u) = \left(Y\delta u^{II}, \tau_{\text{mech}} Y u^{II}\right)_\Omega + \left(Y\delta u^{II}, \tau_{\text{mech}}\overline{b}\right)_\Omega, \tag{3.43a}$$

$$\mathcal{A}_{\text{elec}}(\phi,\delta\phi) = -\left(\epsilon\delta\phi^{II}, \tau_{\text{elec}}\epsilon\phi^{II}\right)_\Omega - \left(\epsilon\delta\phi^{II}, \tau_{\text{elec}}\overline{q}\right)_\Omega. \tag{3.43b}$$

Hence, the weak form Eq. (3.42) is simplified to

$$\begin{cases} \hat{a}_{uu}(\delta u, u) + a_{u\phi}(\delta u, \phi) = \hat{l}_u(\delta u), \\ \hat{a}_{\phi\phi}(\delta\phi, \phi) + a_{u\phi}(u, \delta\phi) = \hat{l}_\phi(\delta\phi), \end{cases} \tag{3.44}$$

where

$$\hat{a}_{uu}(\delta u, u) = (\delta u^I, Y u^I)_\Omega + (\delta u^{II}, Y(\ell^2_{\text{mech}} + Y\tau_{\text{mech}})u^{II})_\Omega, \tag{3.45a}$$

$$\hat{a}_{\phi\phi}(\delta\phi, \phi) = (\delta\phi^I, -\epsilon\phi^I)_\Omega + (\delta\phi^{II}, -\epsilon(\ell^2_{\text{elec}} + \epsilon\tau_{\text{elec}})\phi^{II})_\Omega, \tag{3.45b}$$

$$\hat{l}_u(\delta u) = (\delta u - \delta u^{II} Y\tau_{\text{mech}}, \overline{b})_\Omega = (\delta u, (1 - Y\tau_{\text{mech}}\nabla^2)\overline{b})_\Omega, \tag{3.45c}$$

$$\hat{l}_\phi(\delta\phi) = (\delta\phi - \delta\phi^{II}\epsilon\tau_{\text{elec}}, -\overline{q})_\Omega = (\delta\phi, -(1 - \epsilon\tau_{\text{elec}}\nabla^2)\overline{q})_\Omega. \tag{3.45d}$$

From Eq. (3.45) it is apparent that $Y\tau_{\text{mech}} \sim \ell^2_{\text{mech}}$ and $\epsilon\tau_{\text{elec}} \sim \ell^2_{\text{elec}}$. Therefore, an appealing choice for $\tau_{\text{mech}}, \tau_{\text{elec}}$ is

$$\tau_{\text{mech}} = \alpha_{\text{mech}}\frac{h^2}{Y}, \qquad \tau_{\text{elec}} = \alpha_{\text{elec}}\frac{h^2}{\epsilon}, \tag{3.46a}$$

where h represents the mesh size and $\alpha_{\text{mech}}, \alpha_{\text{elec}}$ are dimensionless scalars that can either be chosen as constant or dependent on the relation between material parameters and mesh size. With this choice, the ($p = 2$) stabilized flexoelectric weak form in Eq. (3.44) corresponds to the original one in Eq. (3.38) with modified (effective) mechanical and electrical length scales and

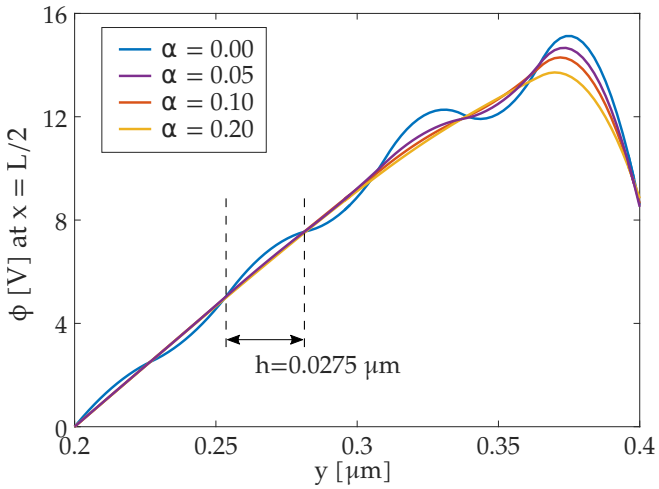

Figure 3.22: Simplified residual-based weak form stabilization in Eq. (3.44) with spline degree $p = 2$ on the 2D Lifshitz-invariant flexoelectric cantilever beam. The stabilization parameters are chosen as $\alpha_{\text{mech}} = \alpha_{\text{elec}} = \alpha$.

modified (non-local) source terms as

$$\ell^2_{\text{mech}} \longrightarrow \hat{\ell}^2_{\text{mech}} = \ell^2_{\text{mech}} + \alpha_{\text{mech}} h^2, \qquad \overline{b} \longrightarrow \hat{b} = \overline{b}\left(1 - \alpha_{\text{mech}} h^2 \nabla^2\right), \tag{3.47a}$$

$$\ell^2_{\text{elec}} \longrightarrow \hat{\ell}^2_{\text{mech}} = \ell^2_{\text{elec}} + \alpha_{\text{elec}} h^2, \qquad \overline{q} \longrightarrow \hat{q} = \overline{q}\left(1 - \alpha_{\text{elec}} h^2 \nabla^2\right). \tag{3.47b}$$

By choosing large enough α_{mech} and α_{elec}, spurious oscillations in the numerical solution can be prevented. A 2D implementation of the simplified stabilization forms in Eq. (3.43) for spline degree $p = 2$ is illustrated in Fig. 3.22, showing the control on the subscales as the stabilization parameters are tuned, and a robust approximation of $\{u, \phi\}$ for large enough stabilization parameters.

The convergence properties of the method depend on the choice of stabilization parameters. A rigorous analytical study could determine the optimal values yielding the best convergence rates, which is being pursued by the author of this manuscript, as well as rigorous generalization of the stabilization strategy to higher spatial dimensions.

3.4 Concluding remarks

A novel computational flexoelectricity framework based on the immersed boundary hierarchical B-Spline method has been proposed, circumventing the limitations of other state-of-the-art approaches. In particular, arbitrarily shaped geometries are allowed by the consideration of unfitted meshes, which imply a negligible meshing cost. The state variables are approximated in a smooth enough functional space defined in terms of B-Spline basis functions, which allows spatial adaptivity thanks to the hierarchical B-spline mesh refinement. The unfitted nature of the approximation space requires specific numerical integration schemes for trimmed cells, stabilization of the trimmed basis functions and a weak enforcement of essential boundary conditions. However, the associated error convergence rates are optimal even for high-order approximations, outperforming other methods in the literature. The method is computationally efficient since the number of degrees of freedom for a given continuity and spatial resolution is minimum as compared to other approaches, and the purely polynomial nature of the basis functions and all their real-space derivatives facilitates their evaluation and numerical integration. The stencils generated by the discretization are completely structured and very sparse, facilitating the solution of the associated algebraic systems of equations.

The method has been used to solve many boundary value problems with particular engineering interest, both at infinitesimal and finite deformations. The examples in this manuscript include the characterization of the shear flexoelectric effect by a conical semicircular rod under torsion, the design of complex-shaped functional flexoelectric devices such as sensors and actuators in the regimes of infinitesimal and finite deformations, and the study of soft flexoelectric nano-rods under bending and buckling deformations.

In short, a robust and efficient infrastructure for computational flexoelectricity has been developed, outperforming other state-of-the-art methodologies.

Chapter 4

Quantum electromechanics of flexoelectricity

4.1 State of the art

In this Section we briefly review the basics of quantum mechanics, and more specifically density functional theory, and present the state of the art of computational flexoelectricity within this field. The review does not intend to be comprehensive, but rather to give a quick glimpse on the foundations of quantum mechanics and DFT to any reader unfamiliar with it.

4.1.1 Density functional theory

4.1.1.1 Foundations

In quantum mechanics, a system composed by N particles is identified with a wave function $\Psi(\mathbf{r}_1, \dots, \mathbf{r}_N; t)$ which is, mathematically, a complex-valued function defined in the so-called configuration space of the system, depending on the coordinates $\mathbf{r}_n = (x_n, y_n, z_n, s_n)\,, \quad n = 1, \dots, N$ (including spin) of each particle in the system. Therefore, the configuration space is $4N$-dimensional in general (or $3N$-dimensional if spin can be ignored), and the wave function of the system maps at time t each point in the configuration space to a complex number. According to the Pauli exclusion principle, two or more identical fermions (matter particles such as electrons, neutrons and protons) cannot occupy the same quantum state within a quantum system simultaneously. This implies the wave function being antisymmetric with respect to the exchange of two particles, namely

$$\Psi(\mathbf{r}_1, \dots, \mathbf{r}_i, \dots, \mathbf{r}_j \dots, \mathbf{r}_N; t) = -\Psi(\mathbf{r}_1, \dots, \mathbf{r}_j, \dots, \mathbf{r}_i \dots, \mathbf{r}_N; t), \qquad \forall i \neq j. \tag{4.1}$$

The quantum state of a system is completely determined by the wave function. For instance, under a probabilistic interpretation, the squared norm of a single-particle normalized wave

function yields the probability density of finding that particle at position $\mathbf{r}$ and time t:

$$f(\mathbf{r};t) = |\Psi(\mathbf{r};t)|^2 = \Psi^*(\mathbf{r};t)\Psi(\mathbf{r};t) \in (0,1) \tag{4.2}$$

where the asterisk indicates the complex conjugate.

The wave function of a system can be found by solving the Schrödinger's equation, which is the fundamental equation in quantum mechanics, playing an analogous role of Newton's laws and conservation of energy in classical mechanics. Its time-independent, non relativistic form is

$$\widehat{H}\Psi = E\Psi, \tag{4.3}$$

where $\Psi(\mathbf{r}_1,\dots,\mathbf{r}_N)$ is time-independent now and E is a scalar denoting the total energy of the system. The symbol $\widehat{H}$ denotes the Hamiltonian operator, which corresponds to the sum of the kinetic energies $\widehat{T}$ of all the particles, plus the potential energy $\widehat{V}$ in the system:

$$\widehat{H}(\mathbf{r}_1,\dots,\mathbf{r}_N) = \sum_{n=1}^{N} \widehat{T}_n + \widehat{V}(\mathbf{r}_1,\dots,\mathbf{r}_N), \tag{4.4a}$$

$$\widehat{T}_n = \frac{|\boldsymbol{p}_n|^2}{2m_n} = \frac{-\hbar^2}{2m_n}\nabla_n^2, \tag{4.4b}$$

where $\boldsymbol{p} = -i\hbar\nabla$ is the momentum operator, $\hbar$ is the reduced Planck constant, ∇^2 is the Laplacian operator, and m_n is the mass of the n-th particle.

Typically, the goal of computational quantum mechanics is to solve the Schrödinger's equation for a system consisting of many electrons and nuclei (a many-body problem). This approach is exact, but unfortunately intractable due to the computational complexity of the problem: given that the dimension of configuration space grows linearly with the number N of particles constituting the system, the computational effort to solve the Schrödinger's equation scales exponentially with N.

Therefore, simplifying assumptions are generally required. A frequent assumption is the Born–Oppenheimer approximation (Born and Oppenheimer, 1927). Because of the large difference in mass between the electrons and nuclei and the fact that the forces on the particles must be same, the electrons respond almost instantaneously to the motion of the nuclei. Thus, it is a reasonable assumption separating the many-body wave function in terms of electronic and nuclear coordinates. This reduces the many-body problem to the solution of the quantum state of the electrons in some frozen-ion configuration of the nuclei. However, even with this simplification, the many-body problem remains unaffordable.

A further simplification, which gives rise to *density functional theory* (DFT) (Hohenberg and Kohn, 1964, Kohn and Sham, 1965) allows mapping exactly the electron many-body problem (in the presence of nuclei) onto that of a *single* electron moving in an effective nonlocal potential. This simplification is crucial, since the configuration space is reduced to the

real space, regardless of the number of particles in the system, and hence the computational complexity is drastically reduced. The key variable in DFT is the *electron density*, represented by $\rho(\mathbf{x})$, which is defined as

$$\rho(\mathbf{x}) = \int_{\mathbf{r}_2} \cdots \int_{\mathbf{r}_N} \Psi(\mathbf{x}, \mathbf{r}_2, \dots, \mathbf{r}_N)\, \mathrm{d}\mathbf{r}_2 \cdots \mathrm{d}\mathbf{r}_n. \tag{4.5}$$

Hohenberg and Kohn (1964) rigorously proved the existence of an electron density, and stated the two Hohenberg–Kohn theorems:

- "The ground state Ψ of any interacting many particle system with a given fixed inter-particle interaction is a unique *functional* of the electron density $\rho(\mathbf{x})$", namely $\Psi = \Psi[\rho(\mathbf{x})]$. This directly implies that the energy is also a functional of the electron density, i.e. $E = E[\rho(\mathbf{x})]$.
- "The electron density that minimizes the energy functional is the true electron density corresponding to the full solutions of the Schrödinger equation".

Therefore, the goal now is finding the electron density of the system. Once it is found, all the quantities of interest deriving from the wave function can also be written in terms of the electron density.

4.1.1.2 Nonlinear Kohn-Sham eigenvalue problem

In order to find the electron density of a system with N_e electrons of mass m_e and N_n (frozen-ion) nuclei, one must solve the Kohn-Sham equations in Ω (Kohn and Sham, 1965). By neglecting spin, they can be stated as (Ghosh and Suryanarayana, 2017, Suryanarayana and Phanish, 2014)

$$K[\rho(\mathbf{x})]\phi_i(\mathbf{x}) = \lambda_i \phi_i(\mathbf{x}), \qquad \forall i = 1, \dots, N_\mathrm{s}, \quad \text{s.t.} \quad \int_\Omega \phi_i^*(\mathbf{x})\phi_j(\mathbf{x})\, \mathrm{d}\Omega = \delta_{ij}, \tag{4.6a}$$

$$\text{where} \qquad K[\rho(\mathbf{x})] = -\frac{\hbar^2}{2m_\mathrm{e}}\nabla^2 + V_\mathrm{eff}[\rho(\mathbf{x})], \tag{4.6b}$$

$$\text{and} \qquad \rho(\mathbf{x}) = 2\sum_{i=1}^{N_\mathrm{s}} f_i |\phi_i(\mathbf{x})|^2, \tag{4.6c}$$

complemented with appropriate boundary conditions. In the above equations, $K[\rho]$ is the Kohn-Sham operator with eigenvalues λ_i and (orthonormal) eigenfunctions (or Kohn-Sham orbitals) ϕ_i, $V_\mathrm{eff}[\rho]$ is the effective potential and $N_\mathrm{s} > N_\mathrm{e}/2$ is the total number of states. The thermalized orbital occupations $0 \leq f_i \leq 1$ arise from the Fermi-Dirac smearing equation (Mermin, 1965)

$$f_i = \left(1 + \exp\left(\frac{\lambda_i - \lambda_\mathrm{f}}{\sigma}\right)\right)^{-1} \quad \text{with} \quad \lambda_\mathrm{f} \quad \text{s.t.} \quad 2\sum_{i=1}^{N_\mathrm{e}} f_i = N_\mathrm{e} \tag{4.7}$$

with the smearing parameter σ, where λ_f is the Fermi level. As a result of the above equations, note that the electron density satisfies

$$\int_\Omega \rho(\mathbf{x})\,\mathrm{d}\Omega = N_\mathrm{e} \tag{4.8}$$

as expected.

The Kohn-Sham equations must be solved self-consistently, typically by a fixed-point iteration with respect to the electron density ρ (or the effective potential V_eff), commonly referred to as the self consistent field (SCF) method (Slater, 1974). In each iteration, the (linearized) Kohn-Sham operator is constructed by evaluating Eq. (4.6b) using the electron density ρ^{k-1} of the previous iteration (or an initial guess for the first iteration), and the lowest N_s orbitals resulting from solving the (linearized) eigenvalue problem in Eq. (4.6a) are used to calculate ρ^k from Eq. (4.6c) and (4.7). Once convergence on ρ is achieved, the resulting force on each frozen nuclei can be computed. If these forces are non-vanishing, the atomic structure is not in equilibrium. Hence an outer iterative loop known as *structural relaxation* is performed, where the nuclei positions and the domain Ω are optimized with respect to the atomic forces resulting from the SCF iteration on ρ. At the end of the process, a relaxed configuration $\{\mathbf{r}_1, \dots, \mathbf{r}_{N\mathrm{n}}\}$ is obtained, along with the corresponding electron density $\rho(\mathbf{x})$.

The effective potential $V_\mathrm{eff}[\rho(\mathbf{x})]$ in Eq. (4.6b) includes the interactions between the "particles" present in the system, including the frozen-ion nuclei. It can be expressed as

$$V_\mathrm{eff}[\rho(\mathbf{x})] = V_\mathrm{ext}(\mathbf{x}) + V_\mathrm{Hartree}[\rho(\mathbf{x})] + V_\mathrm{xc}[\rho(\mathbf{x})], \tag{4.9}$$

where $V_\mathrm{ext}(\mathbf{x})$ is the *external potential* accounting for the interaction between the nuclei and the electron density, and

$$V_\mathrm{Hartree}[\rho(\mathbf{x})] = \frac{e^2}{4\pi\epsilon_0}\int_\Omega \frac{\rho(\mathbf{x})}{|\mathbf{r}-\mathbf{x}|}\,\mathrm{d}\mathbf{r} \tag{4.10}$$

is the Hartree potential, accounting for the interaction of the electron density with itself, i.e. the analogous of the electron-electron interactions in a (discrete) many-body system. $V_\mathrm{xc}[\rho]$ is a correction term known as the *exchange-correlation* potential, that accounts for the fact that particles in the many-body problem are actually correlated and obey the Pauli exclusion principle. The exact expression of $V_\mathrm{xc}[\rho]$ is unknown and must be approximated. Several methods are available in literature, such as the local density (LDA) (Kohn and Sham, 1965) and generalized gradient (GGA) (Perdew *et al.*, 1996, Perdew and Yue, 1986) approaches. The exchange-correlation term is the key approximation in DFT computations, which makes it a non-exact method, i.e. not equivalent to Schrödinger's equation.

The external potential $V_\mathrm{ext}(\mathbf{x})$ accounting for the interaction of the electron density with

the nuclei is a collection of Coulomb point-charge interactions of the form

$$V_{\text{ext}}(\mathbf{x}) = -\frac{e^2}{4\pi\epsilon_0}\sum_{i=1}^{N_\text{n}}\frac{Z_n}{|\mathbf{x}-\mathbf{r}_n|}, \tag{4.11}$$

where Z_n is the atomic number of the n-th nucleus (i.e. the number of protons in the nucleus). As $|\mathbf{x}-\mathbf{r}_n| \longrightarrow 0$, i.e. in the vicinity of the nuclei, the external potential is very strong, and the tightly bound core orbitals physically oscillate very rapidly. In order to capture a decent numerical approximation of these orbitals, e.g. by finite elements (FE), finite differences (FD) or spectral methods such as plane wave (PW) expansions, an extremely rich approximation space is required (i.e. very fine FE mesh, very small FD grid size or very high PW cut-off energy, respectively). Therefore, in practical (computational) terms, the actual external potential makes the problem intractable and one further approximation is typically required, known as the *pseudopotential theory* (Heine *et al.*, 1970, Phillips, 1958). Since most physical properties of solids depend on the *valence* electrons to a much greater extent than on the *core* electrons (Payne *et al.*, 1992), the pseudopotential theory allows replacing the strong external potential V_{ext} with a much weaker potential (a pseudopotential) that describes all the salient features of valence electrons in the system. Thus the original solid is now replaced by pseudo-(valence)-electrons and pseudo-ion cores composed by the actual nuclei and core electrons. These pseudo-electrons experience exactly the same potential outside the core region as the original electrons but have a much weaker potential inside the core region, cf. Fig. 4.1, which eliminates the need of extremely rich approximation spaces for $\phi_i(\mathbf{x})$. The Kohn-Sham problem is posed then on the orbitals corresponding to *valence* electrons only, which is also computationally favourable since N_e, and thus N_s, is decreased. There exist a wide range of pseudopotentials, and in fact the development of accurate pseudopotentials is actually a focus of active research within the DFT community. The most recent and accepted pseudopotentials are the optimized norm-conserving Vanderbilt pseudopotentials (ONCV) (Hamann, 2013).

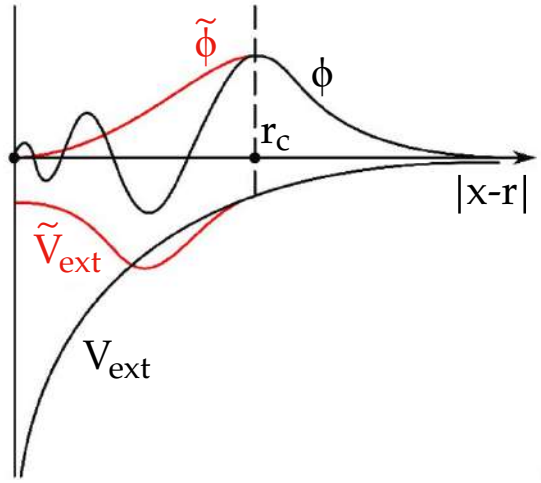

Figure 4.1: A schematic illustration of the pseudopotential $\widetilde{V}_{\text{ext}}(\mathbf{x})$ and Kohn-Sham pseudo-orbitals $\tilde{\phi}(\mathbf{x})$ (depicted in red color) inside ($|\mathbf{x}-\mathbf{r}| < r_c$) and outside ($|\mathbf{x}-\mathbf{r}| > r_c$) the core region of an atom, with respect to the actual potential $V_{\text{ext}}(\mathbf{x})$ and Kohn-Sham orbitals $\phi(\mathbf{x})$ (depicted in black color). Figure adapted from Liu (2017).

4.1.1.3 Periodicity in Ω: Bloch's theorem

Usually in condensed matter physics, crystalline solids are considered to extend infinitely over the real space, i.e. $\Omega = \mathbb{R}^3$. Obviously, this is computationally impossible to handle, and periodic (or extended) systems are considered instead by means of *Bloch's theorem*.

Let us consider a periodic lattice in Ω with lattice vectors $\mathbf{a}_1, \mathbf{a}_2, \mathbf{a}_3$, and a generic lattice translational vector $\mathbf{R} = n_1\mathbf{a}_1 + n_2\mathbf{a}_2 + n_3\mathbf{a}_3$, with $n_1, n_2, n_3 \in \mathbb{N}$. The Bloch's theorem states that each electronic orbital in the periodic lattice takes the form of a periodic function modulated by a plane wave:

$$\phi_i(\mathbf{x}) = \exp(i\mathbf{k}\cdot\mathbf{x})\, u_i(\mathbf{x}), \tag{4.12}$$

where $u_i(\mathbf{x}) = u_i(\mathbf{x}+\mathbf{R})$ has the same periodicity in real space as the crystal lattice, and $\mathbf{k}$ are simply referred to as ***k** points*, defined in the first Brillouin zone (Brillouin, 1953), i.e. the specific region of reciprocal-space of the lattice which is closest to the origin. The electronic orbitals $\phi_i(\mathbf{x})$ are in general *not* periodic in real space, and fulfill the following Bloch boundary conditions instead:

$$\phi_i(\mathbf{x}+\mathbf{R}) = \exp(i\mathbf{k}\cdot(\mathbf{x}+\mathbf{R}))\, u_i(\mathbf{x}+\mathbf{R}) = \exp(i\mathbf{k}\cdot\mathbf{R})\, \phi_i(\mathbf{x}). \tag{4.13}$$

By Eq. (4.6c) it is easy to see that, if electronic orbitals are Bloch periodic (i.e. fulfill the Bloch boundary condition in Eq. (4.13)), the electron density *is* actually periodic in real space. In other words, what Bloch's theorem states is that only the magnitude of the orbitals must be periodic, whereas the phase is not necessarily so.

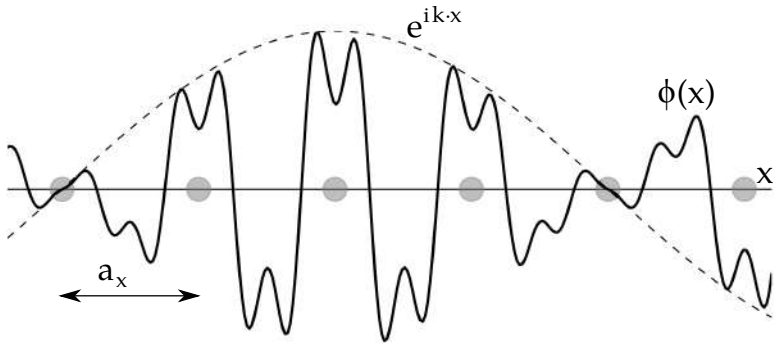

Figure 4.2: A schematic of a typical Bloch wave in one dimension. The real part is depicted in solid line. The dashed line represents the plane wave modulation factor. The light circles represent atoms. Figure adapted from Wikimedia Commons (2016).

The Bloch's theorem changes the problem of calculating an infinite number of electronic orbitals to one of calculating a finite number of electronic orbitals at all the possible (infinite) **k** points in reciprocal space (or Brillouin zone). However, the electronic orbitals at **k** points that are very close together will be almost identical (Payne *et al.*, 1992). Hence it is possible to represent all their contributions as an integral in **k** space which, in practical terms, is performed via numerical integration. Therefore, only a few computations at different **k** points are actually required. The choice of **k** points in a crystalline lattice reciprocal space is known as ***k** point sampling* (Monkhorst and Pack, 1976). The output of numerical solutions to the Kohn-Sham equations will converge as the density of **k** points is increased.

4.1.2 Cyclic density functional theory

After the recent discovery of graphene, 1D nanostructures possessing a cylindrical-type geometry (e.g. nanotubes, nanowires, and nanorods), as well as their 2D counterparts, have received a lot of attention due to their unusual and fascinating material properties (Ghosh *et al.*, 2019). Though these 2D structures are originally planar, they take up cylindrical-type geometries when subject to bending deformations. These kind of structures are typically computed with traditional DFT implementations by means of periodic supercells, that is, considering a cyclic structure surrounded by vacuum in a large enough periodic domain Ω so that the interactions between the periodic images are negligible. This approach is very challenging, even with state-of-the-art DFT codes, since DFT calculations are highly expensive, scaling cubically with system size (Martin, 2004). Since traditional DFT approaches are restricted to affine coordinate systems, they are unable to fully exploit the cyclic symmetry to reduce the computational cost (Ghosh *et al.*, 2019).

Cyclic density functional theory (cyclic DFT) (Banerjee and Suryanarayana, 2016, Ghosh *et al.*, 2019) is a particularization of DFT for cyclic structures which exploits the cyclic symmetry of electronic structures. The key idea behind it is to consider unit cells of structures with cyclic symmetry, as depicted in Fig. 4.3, and enforce cyclic boundary conditions to the electronic

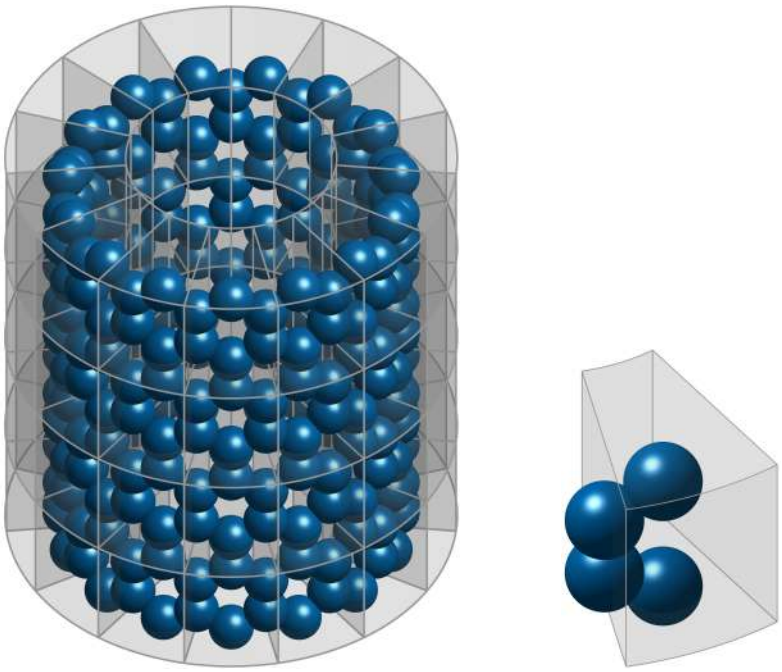

(a) Cyclic structure (b) Unit cell

Figure 4.3: Cyclic structure corresponding to a graphene nanotube in zigzag configuration. The (infinite) system corresponds to replicating a unit cell in angular and axial directions.

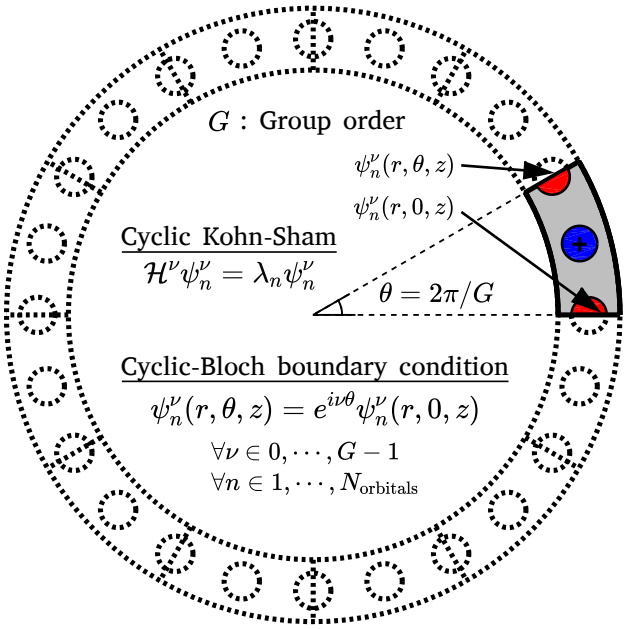

Figure 4.4: Overview of the cyclic symmetry-adapted formulation for the Kohn-Sham eigenproblem arising from cyclic DFT. Figure adapted from Codony *et al.* (2020a).

density. In so doing, the computational cost is drastically reduced, scaling only linearly with respect to radius of curvature (Codony *et al.*, 2020a). Since cyclic boundary conditions locally simulate the behavior of a system subjected to uniform bending, cyclic DFT makes it possible to carry out systematic ab-initio simulations of nanostructures subjected to bending deformations (Banerjee and Suryanarayana, 2016), even in the case of extremely large curvature radii (Ghosh *et al.*, 2019).

In cyclic DFT, the cyclic unit cell Ω (see Fig. 4.3b) is defined in cylindrical coordinates as

$$\Omega = \left\{ \mathbf{x} = [r\cos(\vartheta), r\sin(\vartheta), z]^T \text{ s.t. } (\vartheta, r, z) \in [0, \theta) \times [R_{\text{in}}, R_{\text{out}}) \times [0, L_z) \right\}, \tag{4.14}$$

with $0 < R_{\text{in}} < R_{\text{out}}$, $L_z > 0$ and $\theta = 2\pi/G$, with $G \in \mathbb{N}^+$ denoting the group order of the cyclic symmetry.

The cyclic DFT formulation consists on reformulating the Kohn-Sham equations defined in a cyclic extended system to the reduced Kohn-Sham equations in a single cyclic unit cell as

$$\begin{aligned} \mathcal{H}^\nu[\rho(\mathbf{x})]\psi_i^\nu(\mathbf{x}) = \lambda_i^\nu \psi_i^\nu(\mathbf{x}), \quad \text{s.t.} \quad & \int_\Omega \psi_i^{\nu *}(\mathbf{x})\psi_j^\nu(\mathbf{x})\,\mathrm{d}\Omega = \frac{1}{G}\delta_{ij}, \\ & \forall \nu \in 0, \dots, G-1, \quad \forall i = 1, \dots, N_{\text{s}}, \end{aligned} \tag{4.15}$$

where $\mathcal{H}^\nu[\rho]$ is the *cyclic* Kohn-Sham operator and ψ_i^ν are the orbitals in a cyclic DFT framework (Banerjee and Suryanarayana, 2016). The ν-points in cyclic structures are, in short, the analogous to $\mathbf{k}$ points in periodic structures, with the particularity that the ν space is discrete while $\mathbf{k}$ space is continuous. The electronic charge density ρ satisfies cyclic symmetry, which implies cyclic-Bloch boundary conditions for the atomic orbitals, cf. Fig. 4.4. Standard Bloch boundary conditions are enforced in axial direction, whereas zero-Dirichlet boundary conditions are applied in the radial one.

4.1.3 Transversal flexoelectricity in electronic systems

In a DFT framework, the polarization is defined as electric dipole moment (accounting for both electron density and nuclei) per unit volume:

$$\boldsymbol{p}(\mathbf{x}) = \boldsymbol{p}[\rho(\mathbf{x})] = \frac{e}{\|\Omega\|}\left(\int_\Omega \mathbf{x}\rho(\mathbf{x})\,\mathrm{d}\Omega - \sum_{n=1}^{N_{\text{n}}} \mathbf{r}_n Z_n \right). \tag{4.16}$$

The calculation of the transversal flexoelectric coefficient μ_{T} requires the derivative of the polarization $\boldsymbol{p}$ with respect to curvature κ. There exist mainly two approaches to compute this derivative: *(i)* a direct evaluation of it at $\kappa = 0$ by means of density functional *perturbation* theory (DFPT) (Baroni *et al.*, 2001, Gonze and Lee, 1997), or *(ii)* a numerical approximation of it by means of DFT, which requires computing $\boldsymbol{p}$ on bent systems at multiple curvatures in the vicinity of the curvature κ at which μ_{T} is desired.

The first approach, based on perturbative (DFPT) methods, has been explored by many

authors, e.g. Dreyer *et al.* (2018), Hong and Vanderbilt (2013), Resta (2010), Stengel (2013, 2014). However, the coefficients so computed correspond to the asymptotic zero curvature limit. Therefore, they are restricted to linear response, likely not representative at the relatively large curvatures commonly encountered in experimental investigations involving bending deformations (Chen *et al.*, 2015, Han *et al.*, 2020, Lindahl *et al.*, 2012, Qu *et al.*, 2019).

Given the complexities and challenges associated with DFPT-based methods, a convenient alternative is the second aforementioned approach, where the derivative is approximated by direct evaluations of $\boldsymbol{p}$ at multiple κ, as done in Dumitrică *et al.* (2002), Kalinin and Meunier (2008), Shi *et al.* (2018). However, as illustrated in Fig. 4.5 , a fundamental issue in this context is that μ_{T} becomes an ill-defined quantity on employing the standard definition of polarization (Codony *et al.*, 2020a), since it depends on the choice of the unit cell. In fact, in the limiting case of the unit cell of the bent structure encompassing a complete circle, $\mu_{\mathrm{T}} = 0$ for any charge distribution, a result that is clearly incorrect. Even for structures that are finite along the angular direction, μ_{T} has an artificial dependence—not attributable to edge-related effects—on the corresponding dimension of the structure, i.e., on the angle subtended by the bent structure (Codony *et al.*, 2020a).

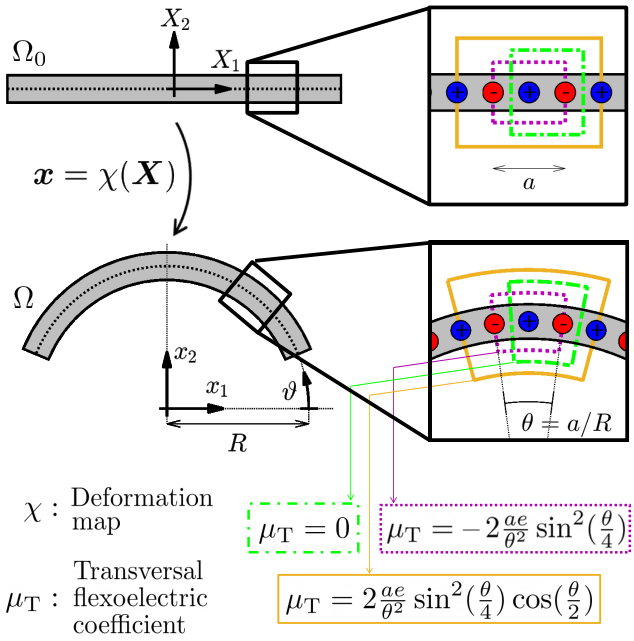

Figure 4.5: Illustration depicting the ill-defined nature of the transversal flexoelectric coefficient for a (bent) structure composed by discrete charges. Figure adapted from Codony *et al.* (2020a).

4.2 Main contributions

In view of the ill-defined nature of the transversal flexoelectric coefficient μ_T in uniformly bent structures, we introduce the concept of *radial polarization* in Section 4.2.1, and reformulate the definition of μ_T in terms of it. The definition and properties of the radial polarization within a electronic structure framework are discussed in Section 4.2.2. We then use this approach in Section 4.2.3 to calculate μ_T for group IV atomic monolayers by means of cyclic DFT. The aforementioned contributions have been published in (Codony *et al.*, 2020a).

4.2.1 Radial polarization: Reformulating the transversal flexoelectricity coefficient

Recalling the framework of continuum modeling at finite deformations, Eq. (2.121) describes a way to characterize the flexoelectricity tensor from measurements of the spatial polarization $\boldsymbol{p}$ and the Green-Lagrangian strain gradients $\widetilde{\mathfrak{E}}$ in a finite deformation framework:

$$\mu_{LIJK} = \left.\frac{\partial\left(p_l F_{lL}\right)}{\partial \widetilde{\mathfrak{E}}_{IJK}}\right|_E , \tag{4.17}$$

where $\mathbf{F}$ denotes the deformation gradient. Let us then consider the case of a uniformly bent slab with some thickness (see Fig. 4.5). On identifying Ω_0 (undeformed state) with the flat slab in the X_1-X_3 plane, pure bending around the X_3 axis can be represented using the deformation map

$$\begin{bmatrix} x_1 & x_2 & x_3 \end{bmatrix}^T = \boldsymbol{\chi}\left(\begin{bmatrix} X_1 & X_2 & X_3 \end{bmatrix}^T\right) = \begin{bmatrix} (R+X_2)\cos\vartheta \\ (R+X_2)\sin\vartheta \\ \lambda_3 X_3 \end{bmatrix}, \tag{4.18}$$

where R is the radius of curvature, $\vartheta = \pi/2 - X_1/R$, and λ_3 is the axial stretch. The deformation gradient and strain gradient tensors then take the form:

$$\mathbf{F} = \begin{bmatrix} +(J/\lambda_3)\sin\vartheta & \cos\vartheta & 0 \\ -(J/\lambda_3)\cos\vartheta & \sin\vartheta & 0 \\ 0 & 0 & \lambda_3 \end{bmatrix}, \tag{4.19}$$

$$\widetilde{\mathfrak{E}} = \frac{J}{\lambda_3}\left[\begin{bmatrix} 0 & 0 & 0 \\ 0 & 0 & 0 \\ 0 & 0 & 0 \end{bmatrix}\begin{bmatrix} 1/R & 0 & 0 \\ 0 & 0 & 0 \\ 0 & 0 & 0 \end{bmatrix}\begin{bmatrix} 0 & 0 & 0 \\ 0 & 0 & 0 \\ 0 & 0 & 0 \end{bmatrix}\right], \tag{4.20}$$

where $J/\lambda_3 = (1 + X_2/R) \approx 1$, assuming that R is large relative to the thickness of the system, which generally holds true for nanostructures. The only component of $\widetilde{\mathfrak{E}}$ that does not vanish is $\widetilde{\mathfrak{E}}_{112} \approx 1/R = \kappa$, where κ is the curvature. It therefore follows from Eq. (4.17) that the

transverse flexoelectric coefficient $\mu_{\mathrm{T}} := \mu_{2112} = \partial\left(p_l F_{l2}\right)/\partial\kappa$, which can be rewritten using Eq. (4.19) as:

$$\mu_{\mathrm{T}} = \frac{\partial\left(\boldsymbol{p}\cdot\boldsymbol{n}\right)}{\partial\kappa} = \frac{\partial p_{\mathrm{r}}}{\partial\kappa}, \tag{4.21}$$

where $p_{\mathrm{r}} := \boldsymbol{p}\cdot\boldsymbol{n}$ is defined to be the *radial polarization* (Codony *et al.*, 2020a), with $\boldsymbol{n} = [\cos(\vartheta), \sin(\vartheta), 0]^{\mathrm{T}}$ representing the unit vector normal to the uniformly bent structure.

The above formulation reveals the fundamental difference between the standard and proposed definitions for the transverse flexoelectric coefficient μ_{T}. Specifically, Eq. (4.21) suggests that μ_{T} is the rate at which the radial polarization p_{r} changes with curvature, instead of the x_2-component of the polarization, as assumed previously (Kalinin and Meunier, 2008, Shi *et al.*, 2018). The proposed definition is also in agreement with reduced models for flexoelectric membranes (Ahmadpoor and Sharma, 2015), which assume that flexoelectricity-induced polarization is normal to the membrane.

The definition presented here can be viewed as a generalization of the standard one to finite bending deformations, agreeing in the limit $\kappa \longrightarrow 0$. Indeed, the proposed formulation is applicable even to the nonlinear regime, overcoming a key limitation of the standard definition.

4.2.2 Radial polarization in electronic structure computations

In electronic structure calculations (e.g. standard or cyclic DFT), the radial polarization p_{r} is a functional of the electronic density $\rho(\mathbf{x})$ as follows:

$$p_{\mathrm{r}} = p_{\mathrm{r}}[\rho(\mathbf{x})] = \frac{1}{\|\Omega\|}\int_{\Omega}(r - R^{\mathrm{eff}})\rho(\mathbf{x})\ \mathrm{d}\Omega, \tag{4.22}$$

analogously to the standard polarization in Eq. (4.16), and the integral can be interpreted as the *radial dipole moment*. Specifically, $r := \mathbf{x}\cdot\boldsymbol{n} = R + X_2$ signifies the radial component of $\mathbf{x}$ and R^{eff} is the *radial centroid* of the ions. Note that p_{r} and therefore μ_{T} are independent of the choice of unit cell for structures extended in the X_1-direction, and do not display an artificial dependence on the corresponding width for finite structures, thereby overcoming a fundamental limitation of the standard definition. With the proposed approach, both p_{r} and μ_{T} are invariant against *(i)* angular shift, *(ii)* axial shift, *(iii)* angular replication and *(iv)* axial replication of the unit cell Ω, thanks to the cyclic-periodic nature of the electron charge density ρ:

$$\rho(\vartheta, r, z) = \rho(\vartheta + n_\Omega\theta, r, z + m\lambda_3 L_z), \quad \forall(n_\Omega \times m) \in [0, \dots, G-1] \times \mathbb{Z}. \tag{4.23}$$

Mathematically, the following statements hold:

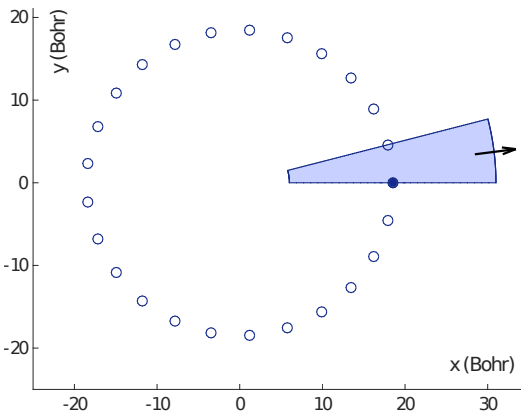

(a) Top view of the cyclic Silicon chain. Simulation is carried out considering only one atom in the unit cell.

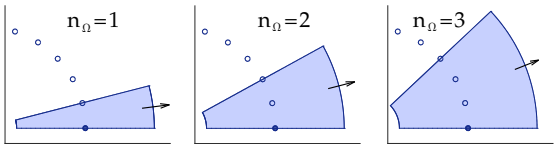

(b) Replication n_Ω of the unit cell along the angular direction, with no angular shift, i.e. $\vartheta_s = 0$.

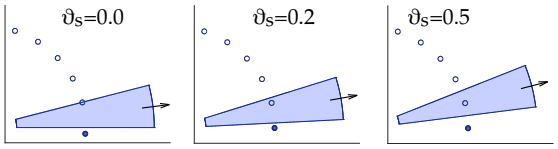

(c) Shift ϑ_s of the unit cell along the angular direction, with no angular replication, i.e. $n_\Omega = 1$.

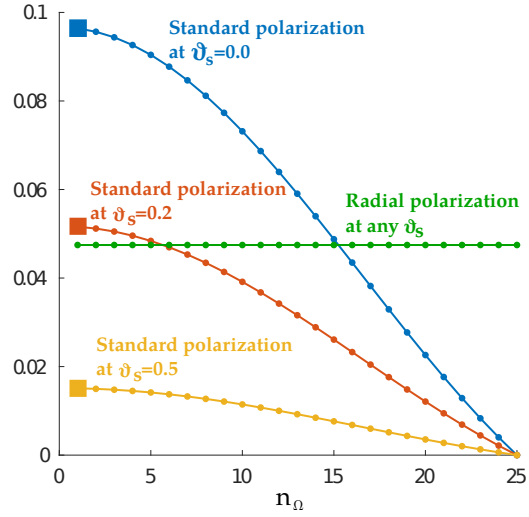

(d) Polarization as a function of the angular replication.

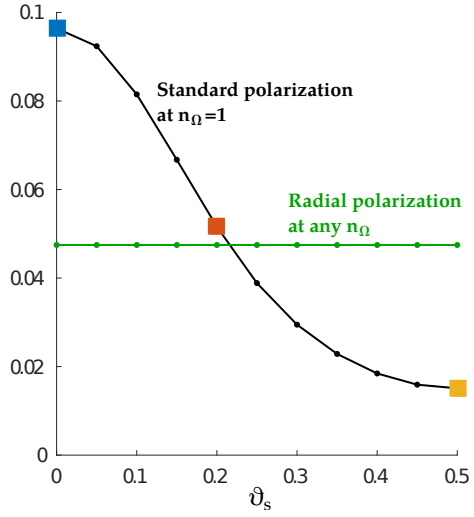

(e) Polarization as a function of the angular shift.

Figure 4.6: Cyclic DFT benchmark simulation showing the polarization of a silicon chain of 25 atoms under pure bending. The unit cell Ω (depicted in (a) in blue color) is of group order $G = 25$ and length $L_z = 40$ bohr, and contains one Si atom at $(\vartheta, r, z) = (0, 18.5 \text{ bohr}, 20 \text{ bohr})$ (1 bohr=5.2918e-11m). The standard polarization $\boldsymbol{p}$ is computed along the direction of the bisector of the shifted and replicated unit cell (denoted by a black arrow in (a),(b),(c)) with the standard approach in Eq. (4.16). Different number of replicated domains n_Ω and relative angular shifts lead to different values of polarization. However, radial polarization computed with Eq. (4.22) remains invariant.

(i) Angular shift invariance: $\forall \vartheta_0 \in \mathbb{R}$:

$$p_{\mathrm{r}} = \frac{1}{\|\Omega\|} \int_0^{L_z} \int_{R_{\mathrm{in}}}^{R_{\mathrm{out}}} \int_{\vartheta_0}^{\vartheta_0+\vartheta} (r - R^{\mathrm{eff}}) \rho r \, \mathrm{d}\vartheta \, \mathrm{d}r \, \mathrm{d}z. \tag{4.24}$$

(ii) Axial shift invariance: $\forall z_0 \in \mathbb{R}$:

$$p_{\mathrm{r}} = \frac{1}{\|\Omega\|} \int_{z_0}^{z_0+L_z} \int_{R_{\mathrm{in}}}^{R_{\mathrm{out}}} \int_0^{\vartheta} (r - R^{\mathrm{eff}}) \rho r \, \mathrm{d}\vartheta \, \mathrm{d}r \, \mathrm{d}z. \tag{4.25}$$

(iii) Angular replication invariance: $\forall n_\Omega \in 1, \dots, G$:

$$p_{\mathrm{r}} = \frac{1}{n_\Omega \|\Omega\|} \int_0^{L_z} \int_{R_{\mathrm{in}}}^{R_{\mathrm{out}}} \int_0^{n_\Omega \vartheta} (r - R^{\mathrm{eff}}) \rho r \, \mathrm{d}\vartheta \, \mathrm{d}r \, \mathrm{d}z. \tag{4.26}$$

(iv) Axial replication invariance: $\forall m \in \mathbb{Z}^+$:

$$p_{\mathrm{r}} = \frac{1}{m \|\Omega\|} \int_0^{mL_z} \int_{R_{\mathrm{in}}}^{R_{\mathrm{out}}} \int_0^{\vartheta} (r - R^{\mathrm{eff}}) \rho r \, \mathrm{d}\vartheta \, \mathrm{d}r \, \mathrm{d}z. \tag{4.27}$$

Fig. 4.6 illustrates the invariance cases *(i)* and *(iii)* in a benchmark simulation of a uniformly bent 1D Silicon chain. Whereas the (ill-defined) standard definition of polarization yields results depending on the angular shift and replication of the unit cell, the proposed radial polarization approach yields invariant results.

In order to further investigate the invariant nature of the proposed radial polarization, we write its expression in the undeformed configuration as

$$p_{\mathrm{r}} = \frac{1}{\|\Omega_0\|} \int_{\Omega_0} (X_2 - X_2^{\mathrm{eff}}) \rho_0(\mathbf{X}) \, \mathrm{d}\Omega_0, \tag{4.28}$$

where $X_2^{\mathrm{eff}} = R^{\mathrm{eff}} - R$, and $\rho_0 = J\rho$ is the nominal electron density. Interestingly, the radial dipole moment in the deformed configuration Ω corresponds to the standard dipole moment along the X_2-direction in the undeformed configuration Ω_0. This confirms the purely Lagrangian nature of the flexoelectric tensor as discussed in Remark 2.6.

4.2.3 Transversal flexoelectricity coefficient using cyclic DFT

Using the aforedescribed methodology, we compute the transversal flexoelectric coefficient μ_{T} for the following group IV atomic monolayers: graphene (C), silicene (Si), germanene (Ge), and stanene (Sn), which possess a honeycomb lattice structure. The materials are bent around the X_3 axis at curvatures of $\kappa \sim 0.19 - 0.75$ nm^{-1}, which are representative curvatures of those encountered in realistic experiments (Chen *et al.*, 2015, Han *et al.*, 2020, Lindahl *et al.*, 2012,

Qu *et al.*, 2019). To assess the anisotropy of μ_T, we consider bending along the two principal directions of the materials; that is, armchair and zigzag directions (cf. Fig. 4.7). The analysis is done with both LDA and GGA exchange-correlation functionals and ONCV pseudopotentials.

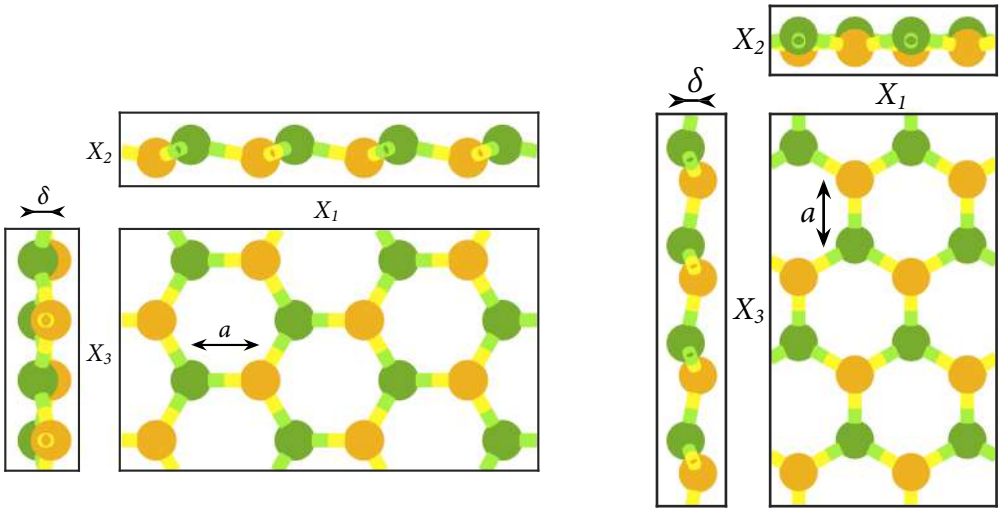

(a) Armchair configuration

(b) Zigzag configuration

Figure 4.7: Generic flat group-IV monolayer in armchair and zigzag directions, prior to bending. The lattice constants for each material are reported in Tab. 4.1.

		LDA	GGA
Graphene	a	2.6603	2.6870
	δ	0.0000	0.0000
Silicene	a	4.1732	4.2207
	δ	0.7872	0.8742
Germanene	a	4.3237	4.4198
	δ	1.2134	1.2813
Stanene	a	4.9715	5.1044
	δ	1.5183	1.6015

Table 4.1: Lattice constants [bohr] of group IV atomic monolayers.

	Zigzag		Armchair	
	LDA	**GGA**	**LDA**	**GGA**
Graphene	0.22	0.22	0.22	0.22
Silicene	0.19	0.19	0.19	0.18
Germanene	0.28	0.27	0.28	0.27
Stanene	0.27	0.27	0.26	0.27

Table 4.2: Transversal flexoelectric coefficient μ_T [e] of group IV atomic monolayers.

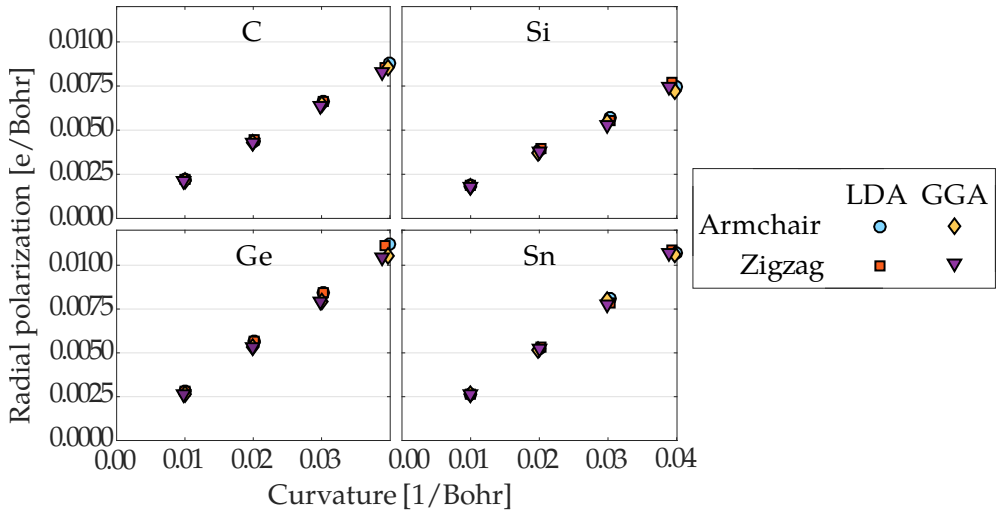

Figure 4.8: Radial polarization p_r (normalized by area) as a function of the bending curvature κ. Figure adapted from Codony *et al.* (2020a).

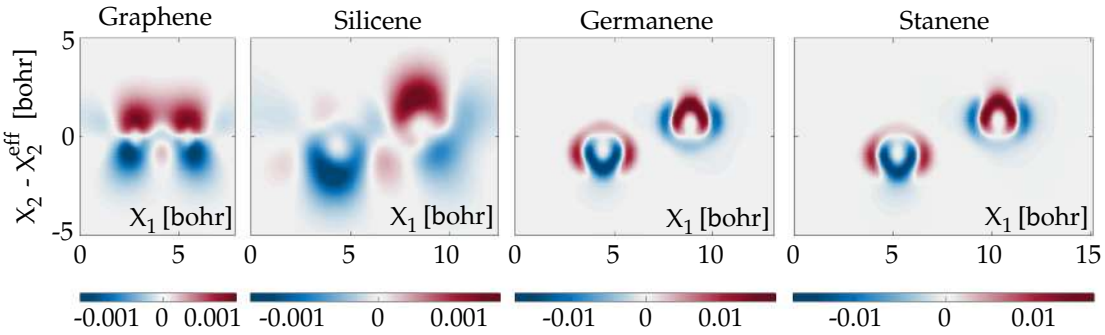

Figure 4.9: Contours of nominal electron density difference [e/bohr^3] between the armchair bent (κ = 0.19 nm^{-1}) and flat atomic monolayers. The contours are in the $X_1 - X_2$ plane passing through the two fundamental atoms. Figure adapted from Codony *et al.* (2020a).

The numerical implementation of cyclic DFT (Xu *et al.*, 2020a,b) relies on the real space approximation of the electronic density onto a symmetry-adapted high-order finite differences (FD) grid in (ϑ, r, z) directions. Once $\rho(\mathbf{x})$ is found, the radial polarization can be evaluated accurately and naturally by means of numerical integration in cylindrical coordinates, without the need of auxiliary symmetry-adapted projections as it would be required by other traditional approaches such as plane wave (PW) DFT.

The values of μ_T obtained for the group IV monolayers are presented in Tab. 4.2. Due to the disagreement in literature over the thickness of atomic monolayers (Huang *et al.*, 2006), the radial dipole moments are normalized with respect to the area instead of volume while computing the radial polarization using Eq. 4.22, i.e. the units of μ_T here are [e] (1e=1.6022e-10μC), rather than the conventionally used [e/ bohr]. Note that a single curvature-independent

value is listed for each entry in the table since the flexoelectric coefficients have been found to be essentially constant for the bending deformations considered here (see Fig. 4.8), signaling linear response for the chosen curvatures. Therefore, the values of μ_T reported here can also be interpreted as those corresponding to the asymptotic limit of $\kappa \longrightarrow 0$.

Notably, the results are independent of the exchange-correlation functional, the key approximation within DFT. In addition, the nearly identical values in the zigzag and armchair directions indicate that group IV monolayers are transversely isotropic with regards to flexoelectricity. The flexoelectric coefficients between the different materials are comparable, with germanene/stanene having the largest value ($\mu_T \sim 0.27e$), silicene having the smallest ($\mu_T \sim 0.19e$), and graphene towards the lower end ($\mu_T = 0.22e$). Notably, the value for graphene is twice as large as that reported by Dumitrică *et al.* (2002), Kalinin and Meunier (2008). The significantly smaller coefficient obtained previously can be attributed to the artificial dependence on the width, a consequence of using the standard definition of the polarization.

To get insights into the underlying nature of the flexoelectric effect for the chosen monolayers, we plot in Fig. 4.9 the nominal electronic charge redistribution on the $X_1 - X_2$ plane passing through the two fundamental atoms. For all materials, there is a net radial charge transfer that occurs from below the neutral axis to above it. However, the plots indicate that there is a fundamental difference between graphene and the other members in its group. For graphene, bending introduces an asymmetry in the p-orbital overlap. However, the charge transfer in the other monolayers occurs between the two atoms instead.

4.3 On-going and future work

As an outcome of this work, the transversal flexoelectricity constant of just four Group-IV monolayers has been characterized. However, the methodology can be directly applied to other 2D monolayers. The work in Kumar *et al.* (2020) computes the flexoelectric coefficient of other relevant 2D monolayers that have been successfully synthesized, such as those with honeycomb lattice structure (i.e. Groups III-V, V monolayers, transition metal dichalcogenides (TMDs) and Group III monochalcogenides) as well as materials with rectangular lattice structure (i.e. Group V monolayers, Group IV monochalcogenides, transition metal trichalcogenides (TMTs) and Group V chalcogenides).

Since the framework developed here is general and not restricted to the linear response of atomic monolayers, an appealing research line is the computation of the transversal flexoelectric coefficients for interesting and more complex systems, including multilayered materials such as graphite and their corresponding analogs, as well as ferroelectric perovskites, which are widely considered in flexoelectricity-based technologies due to its large bulk flexoelectric constants according to experimental measurements. Surface effects might be apparent also from this study.

Another line of research consists on deriving an analogous concept to radial polarization for structures featuring not only cyclic but *helical* symmetry, which essentially corresponds to

bending+twisting deformation modes. It is likely that other flexoelectric constants rather than the transversal one will be characterized following this approach.

4.4 Concluding remarks

We have presented a novel formulation for calculating the transversal flexoelectric coefficient of nanostructures at finite deformations from first principles. Specifically, we have introduced the concept of *radial polarization* to redefine the flexoelectric coefficient, making it a well-defined quantity for uniform bending deformations. The proposed framework has been used to calculate the coefficients for group IV atomic monolayers using cyclic DFT simulations. In the case of graphene, which is perhaps the most widely studied 2D material, the flexoelectric coefficient is significantly larger than that reported previously, with a charge transfer mechanism that fundamentally differs from the other members of its group. Furthermore, the reported transversal flexoelectric coefficients are constant within a large range of bending curvatures, confirming the linearity of the flexoelectric coupling in continuum models.

Chapter 5

Conclusions

This PhD thesis has addressed multiple open questions in the current state of the art of the flexoelectric effect in solids, focusing on theoretical and computational modeling at the continuum level, but also exploring its connection to first principles. The main contributions are listed below:

- The relation between the energy and enthalpy forms of the Direct and Lifshitz-invariant flexoelectricity continuum models at infinitesimal deformations has been clarified. The bulk energy and enthalpy densities of a dielectric, with consideration of a gradient polarization term, are not equivalent due to the modification of the Maxwell-Faraday's equation about the irrotationality of the electric field. Otherwise, they are indeed equivalent.

- The first objective model for flexoelectricity at finite deformations has been proposed, coupling strain gradients and electric polarization by means of a fully Lagrangian flexoelectric tensor. Previous attempts in the literature were not objective, or were not considering the polarization field for the flexoelectric coupling. The model is illustrated by means of a robust numerical implementation able to handle very large nonlinearities such as large deformation bending, electrostriction or buckling.

- The connection between direct and Lifshitz-invariant flexoelectricity boundary value problems at infinitesimal deformations has been established. As both formulations differ in null Lagrangians, their Euler-Lagrange equations coincide, but the expressions of the Neumann terms (e.g. tractions and surface charges) and thus the meaning of natural boundary conditions are different. According to the cantilever beam benchmarks, the Lifshitz-invariant formulation is apparently stiffer than the direct one.

- The need for stabilization methods in order to properly capture boundary layers that can arise in the electric field has been suggested. So far, such boundary layers have been reported in the Lifshitz-invariant formulation only.

- A numerical stabilization technique to alleviate spurious oscillations whenever boundary layers arise has been implemented for the first time. A simple Galerkin least squares method has been proposed, and it has been shown to be effective for the cantilever beam benchmarks.

- The first flexoelectricity formulation for unfitted meshes has been developed, including boundary conditions arising at the edges of the boundary. First order, second order and edge essential boundary conditions are enforced weakly via Nitsche's method. Considering unfitted meshes facilitates the meshing and computation of complex geometries, and the construction of smooth-enough approximation spaces, required due to the fourth-order nature of the equations. The proposed implementation considers functional spaces spanned by hierarchical B-spline basis, which have convenient numerical and computational properties. The method yields optimal high-order convergence rates, outperforming other methods in the literature.

- The proposed computational infrastructure has been used to solve many boundary value problems with particular engineering interest, both at infinitesimal and finite deformations. The numerical examples in this manuscript correspond to functional devices for electromechanical transduction based on the flexoelectric effect, with potential applications in nanotechnology. The examples include the design of complex-shaped sensors and actuators made of hard ceramics, rod-shaped compliant polymeric sensors and actuators under bending and buckling conditions, and arbitrarily-shaped soft electromechanical sensors.

- The continuum modeling of flexoelectricity at finite deformations has been linked with atomistic simulations in order to develop a novel formulation for calculating the transversal flexoelectric coefficient of nanostructures at finite deformations from first principles. The concept of radial polarization has been introduced in a density functional theory (DFT) framework to redefine the transversal flexoelectric coefficient in systems under bending, overcoming a well-established intrinsic ill-definition of the flexoelectric coefficient in previous works.

- The transversal flexoelectric coefficients for group-IV 2D materials (graphene, silicene, germanene and stanene) have been quantified using the novel proposed formulation in a cyclic DFT implementation. In the case of graphene, the transversal flexoelectric coefficient is significantly larger than that reported previously, with a charge transfer mechanism that fundamentally differs from the other members of its group. Germanene and stanene present the largest flexoelectric constants among the studied materials.

- The linearity of the flexoelectric coupling in continuum models has been confirmed for the studied materials from ab-initio simulations, since the computed transversal flexoelectric coefficients are constant within a large range of bending curvatures.

The are still many open questions left to future work. Regarding the continuum modeling, the Legendre transform between bulk energy and enthalpy densities in a large deformation framework remains unexplored. Also, the effect of considering homogeneous Neumann boundary conditions instead of continuity conditions with the dielectric surrounding media has not been assessed. The relation between the different flexoelectricity models and surface effects such as surface piezoelectricity remains unaddressed, as well as the investigation of the reason for the appearance of unexpected boundary layers in the electric field. Moreover, the modeling can be extended to other related physics such as photoflexoelectricity, with promising technological applications.

As for the numerical modeling, the most critical issue requiring further research is the robust alleviation of numerical oscillations in any formulation, geometry or loading conditions. Besides that, it would be extremely interesting to combine the present infrastructure with geometry/topology optimization toolboxes, in order to maximize the performance of the proposed electromechanical devices. Also, for practical reasons, it would be convenient to rewrite the in-house implementation within a high performance computation (HPC) scalable environment, allowing the efficient and accurate computation and design of large flexoelectric devices, including three-dimensional geometries at large deformations.

Considering the ab-initio computations, the proposed methodology can be systematically applied to multiple materials such as other atomic monolayers, multilayered materials such as graphite or even bulk materials such as ferroelectric perovskites. The appearance and relevance of surface effects and other relevant physics can be also studied from there, allowing the development of more complete and accurate continuum models. Finally, apart from bending, other interesting setups can be studied such as wrinkling or twisting, potentially allowing for the characterization of other coefficients of the flexoelectric tensor.

Appendices

A Material characterization

A.1 Infinitesimal deformation framework: Material tensors

In the infinitesimal deformation framework, the material is characterized by specfiying the material tensors of elasticity $\mathbf{c}$, strain gradient elasticity $\mathbf{h}$, dielectricity $\boldsymbol{\kappa}$, piezoelectricity $\boldsymbol{e}$, flexoelectricity $\boldsymbol{\mu}$ and eventually gradient dielectricity $\mathbf{M}$. We recall that the Lamé parameters λ and μ are related with the Young modulus Y and the Poisson's ratio ν as $\lambda = Y\nu/(1+\nu)(1-2\nu)$ and $\mu = Y/2(1+\nu)$.

Elasticity tensor c

Isotropic elasticity is represented by the fourth-order tensor $\mathbf{c}$, which depends on λ and μ in the following form:

$$c_{IJKL} = \lambda\delta_{IJ}\delta_{KL} + 2\mu\delta_{IK}\delta_{JL}. \tag{A.1}$$

Strain gradient elasticity tensor h

We consider an isotropic simplified strain gradient elasticity tensor (Altan and Aifantis, 1997), which depends on λ, μ and the mechanical length scale ℓ_{mech} in the following form:

$$h_{IJKLMN} = \left(\lambda\delta_{IJ}\delta_{LM} + 2\mu\delta_{IL}\delta_{JM}\right)\ell^2_{\text{mech}}\delta_{KN}. \tag{A.2}$$

Dielectricity tensor $\boldsymbol{\kappa}$

Isotropic dielectricity is represented by the second-order tensor $\boldsymbol{\kappa}$, which depends on the electric permittivity ϵ as

$$\kappa_{ij} = \epsilon\delta_{ij}. \tag{A.3}$$

Gradient dielectricity tensor M

Isotropic gradient dielectricity is represented by the fourth-order tensor $\mathbf{M}$, which depends on the electric permittivity ϵ and the dielectric length scale ℓ_{elec} as

$$M_{ijkl} = \epsilon\ell^2_{\text{elec}}\delta_{ik}\delta_{jl}. \tag{A.4}$$

Piezoelectricity tensor $\boldsymbol{e}$

Piezoelectricity is represented by the third-order tensor $\boldsymbol{e}$.

Tetragonal symmetry is considered, which has a principal direction and involves longitudinal, transversal and shear couplings represented by the parameters e_L, e_T and e_S, respectively.

For a material with principal direction $\boldsymbol{x}_1$, the piezoelectric tensor $\boldsymbol{e}^{<\boldsymbol{x}_1>}$ reads

$$e^{<\boldsymbol{x}_1>}{}_{LIJ} = \begin{cases} e_{\mathrm{L}}, & \text{for } L = I = J = 1, \\ e_{\mathrm{T}}, & \text{for } L = 1,\ I = J, \\ e_{\mathrm{S}}, & \text{for } J = 1,\ L = I \text{ or } I = 1,\ L = J, \\ 0 & \text{otherwise.} \end{cases} \tag{A.5}$$

The piezoelectric tensor $\boldsymbol{e}$ oriented in an arbitrary direction $\boldsymbol{d}$ is obtained by rotating $\boldsymbol{e}^{<\boldsymbol{x}_1>}$ as

$$e_{lij} = R_{lL} R_{iI} R_{jJ} e^{<\boldsymbol{x}_1>}{}_{LIJ}, \tag{A.6}$$

where $\mathbf{R}$ is a rotation matrix that rotates $\boldsymbol{x}_1$ onto $\boldsymbol{d}$.

Flexoelectricity tensor $\boldsymbol{\mu}$.

The cubic flexoelectric tensor depends on the longitudinal μ_{L}, transversal μ_{T} and shear μ_{S} parameters (Codony *et al.*, 2019, Le Quang and He, 2011). In the Cartesian axes, it takes the following form:

$$\mu^{<\boldsymbol{x}_1>}{}_{LIJK} = \begin{cases} \mu_{\mathrm{L}}, & \text{for } L = I = J = K, \\ \mu_{\mathrm{T}}, & \text{for } I = J \neq K = L, \\ \mu_{\mathrm{S}}, & \text{for } L = I \neq J = K \text{ or } L = J \neq I = K, \\ 0 & \text{otherwise.} \end{cases} \tag{A.7}$$

The flexoelectric tensor $\boldsymbol{\mu}$ oriented in an arbitrarily rotated Cartesian basis is obtained by rotating $\boldsymbol{\mu}^{<\boldsymbol{x}_1>}$ as

$$\mu_{lijk} = R_{lL} R_{iI} R_{jJ} R_{kK} \mu^{<\boldsymbol{x}_1>}{}_{LIJK}, \tag{A.8}$$

where $\mathbf{R}$ is the rotation matrix associated to the unit vectors of the rotated basis.

A.2 Finite deformation framework: Hyperelastic potentials

In the finite deformation framework, the material is characterized by specfiying the material tensors of flexoelectricity $\boldsymbol{\mu}$ and strain gradient elasticity $\mathbf{h}$, the electric permittivity ϵ and, additionally, the elastic energy density $\Psi^{\mathrm{Elast}}(\mathbf{C})$. We present here two isotropic models for $\Psi^{\mathrm{Elast}}(\mathbf{C})$, namely the Saint-Venant–Kirchhoff and Neo-Hookean models.

Isotropic Saint-Venant–Kirchhoff model.

It corresponds to the extension of the linear isotropic elastic material model to the non-linear regime, and depends on λ and μ as follows:

$$\Psi^{\text{Elast}}(\mathbf{C}) = \frac{\lambda}{2}[\text{Tr}(\mathfrak{E})]^2 + \mu\,\text{Tr}(\mathfrak{E}^2), \tag{A.9a}$$

$$\frac{\partial \Psi^{\text{Elast}}(\mathbf{C})}{\partial C_{IJ}} = \frac{\lambda}{2}[\text{Tr}(\mathfrak{E})]\,\delta_{IJ} + \mu \mathfrak{E}_{IJ}, \tag{A.9b}$$

$$\frac{\partial^2 \Psi^{\text{Elast}}(\mathbf{C})}{\partial C_{IJ} C_{KL}} = \frac{\lambda}{4}\delta_{IJ}\delta_{KL} + \frac{\mu}{2}\delta_{IK}\delta_{JL}. \tag{A.9c}$$

Isotropic Neo-Hookean model

The Neo-Hookean model is adequate for describing nonlinear stress-strain behavior of cross-linked polymers at moderate strains. It is mathematically defined as

$$\Psi^{\text{Elast}}(\mathbf{C}) = \frac{\lambda}{2}[\log(J)]^2 + \frac{\mu}{2}[\text{Tr}(\mathbf{C}) - n_{\text{sd}}], \tag{A.10a}$$

$$\frac{\partial \Psi^{\text{Elast}}(\mathbf{C})}{\partial C_{IJ}} = \frac{\lambda}{2}\log(J) C^{-1}_{IJ} + \frac{\mu}{2}\left(\delta_{IJ} - C^{-1}_{IJ}\right), \tag{A.10b}$$

$$\frac{\partial^2 \Psi^{\text{Elast}}(\mathbf{C})}{\partial C_{IJ} C_{KL}} = \frac{\lambda}{4} C^{-1}_{IJ} C^{-1}_{KL} + \frac{1}{4}[\mu - \lambda \log(J)]\left(C^{-1}_{IK} C^{-1}_{JL} + C^{-1}_{IL} C^{-1}_{JK}\right). \tag{A.10c}$$

B Variations of stresses and electric displacement in a finite deformation framework

In this Appendix the expressions for the variations $\delta \mathrm{S}(\boldsymbol{\chi}, \phi; \delta\boldsymbol{\chi}, \delta\Phi)$, $\delta\tilde{\mathrm{S}}(\boldsymbol{\chi}, \phi; \delta\boldsymbol{\chi}, \delta\Phi)$, $\delta\nabla\tilde{\mathrm{S}}(\boldsymbol{\chi}, \phi; \delta\boldsymbol{\chi}, \delta\Phi)$ and $\delta\boldsymbol{D}(\boldsymbol{\chi}, \phi; \delta\boldsymbol{\chi}, \delta\Phi)$ are derived, which are present in the Nitsche's weak form for the direct flexoelectricity model at finite deformations in Section 2.2.4.1.b. To this end, let us define the second gradient of the deformation gradient $\check{\mathbf{F}}$, the second gradient of the Green-Lagrangian strains $\nabla\tilde{\mathfrak{E}}$, and the electric field gradient as

$$\check{F}_{iJKL} := \frac{\partial^2 F_{iJ}}{\partial X_K \partial X_L} = \frac{\partial^3 x_i}{\partial X_J \partial X_K \partial X_L}, \tag{B.1a}$$

$$\widetilde{\mathfrak{E}}_{IJK,L} := \frac{\partial^2 \mathfrak{E}_{IJ}}{\partial X_K \partial X_L} = \underset{IJ}{\operatorname{symm}} \underset{KL}{\operatorname{symm}} \left(\check{F}_{kIKL} F_{kJ} + \tilde{F}_{kIK} \tilde{F}_{kJL} \right), \tag{B.1b}$$

$$E_{I,J} := -\frac{\partial^2 \Phi}{\partial X_I \partial X_J}; \tag{B.1c}$$

and their corresponding variations

$$\delta\check{F}_{iJKL} = \frac{\partial^3 \delta\chi_i}{\partial X_J \partial X_K \partial X_L}, \tag{B.2a}$$

$$\delta\widetilde{\mathfrak{E}}_{IJK,L} = \underset{IJ}{\operatorname{symm}} \underset{KL}{\operatorname{symm}} \left(\delta\check{F}_{kIKL} F_{kJ} + \check{F}_{kIKL} \delta F_{kJ} + 2\delta\tilde{F}_{kIK} \tilde{F}_{kJL} \right), \tag{B.2b}$$

$$\delta E_{I,J} = -\frac{\partial^2 \delta\Phi}{\partial X_I \partial X_J}. \tag{B.2c}$$

Then, from the expressions of $\mathrm{S}(\boldsymbol{\chi}, \phi)$, $\tilde{\mathrm{S}}(\boldsymbol{\chi}, \phi)$, $\boldsymbol{D}(\boldsymbol{\chi}, \phi)$ in Eq. (2.141a), (2.138), (2.141b) and

$$\tilde{S}_{IJK,Q} = h_{IJKLMN} \widetilde{\mathfrak{E}}_{LMN,Q} - J C^{-1}_{LM} E_{M,Q} \mu_{LIJK} + J \mathscr{C}_{LMAB} \widetilde{\mathfrak{E}}_{ABQ} E_M \mu_{LIJK}, \tag{B.3}$$

their corresponding variations are derived as follows:

$$\begin{aligned}
\delta S_{IJ}(\boldsymbol{\chi}, \phi; \delta\boldsymbol{\chi}, \delta\Phi) = &\left(4\frac{\partial^2 \Psi^{\text{Elast}}(\mathbf{C})}{\partial C_{IJ}\partial C_{AB}} - J\mathscr{C}_{MLAB}E_{M,K}\mu_{LIJK} + \frac{J}{2}\mathcal{C}_{MLIJAB}E_M\epsilon E_L\right)\delta\mathfrak{E}_{AB} \\
&- \left(h_{IJKLMN}\right)\delta\widetilde{\mathfrak{E}}_{LMN,K} \\
&+ \left(J\mathscr{C}_{MLIJ}E_M\epsilon\right)\delta E_L \\
&+ \left(JC^{-1}_{LM}\mu_{LIJK}\right)\delta E_{M,K}, \qquad \text{(B.4a)} \\
\delta\tilde{S}_{IJK}(\boldsymbol{\chi}, \phi; \delta\boldsymbol{\chi}, \delta\Phi) = &\left(J\mathscr{C}_{LMAB}\mu_{LIJK}E_M\right)\delta\mathfrak{E}_{AB} \\
&+ \left(h_{IJKLMN}\right)\delta\widetilde{\mathfrak{E}}_{LMN} \\
&- \left(JC^{-1}_{LM}\mu_{LIJK}\right)\delta E_M, \qquad \text{(B.4b)} \\
\delta\tilde{S}_{IJK,Q}(\boldsymbol{\chi}, \phi; \delta\boldsymbol{\chi}, \delta\Phi) = &\left(J\mu_{LIJK}\left(\mathscr{C}_{LMAB}E_{M,Q} + \mathcal{C}_{LMCDAB}\widetilde{\mathfrak{E}}_{CDQ}E_M\right)\right)\delta\mathfrak{E}_{AB} \\
&+ \left(J\mathscr{C}_{LMAB}E_M\mu_{LIJK}\right)\delta\widetilde{\mathfrak{E}}_{ABQ} \\
&+ \left(h_{IJKLMN}\right)\delta\widetilde{\mathfrak{E}}_{LMN,Q} \\
&+ \left(J\mathscr{C}_{LMAB}\widetilde{\mathfrak{E}}_{ABQ}\mu_{LIJK}\right)\delta E_M \\
&- \left(JC^{-1}_{LM}\mu_{LIJK}\right)\delta E_{M,Q}, \qquad \text{(B.4c)} \\
\delta D_L(\boldsymbol{\chi}, \phi; \delta\boldsymbol{\chi}, \delta\Phi) = &- \left(J\mathscr{C}_{KLAB}\left(\epsilon E_K + \mu_{KIJM}\widetilde{\mathfrak{E}}_{IJM}\right)\right)\delta\mathfrak{E}_{AB} \\
&+ \left(JC^{-1}_{KL}\mu_{KIJM}\right)\delta\widetilde{\mathfrak{E}}_{IJM} \\
&+ \left(JC^{-1}_{KL}\epsilon\right)\delta E_K, \qquad \text{(B.4d)}
\end{aligned}$$

where

$$\begin{aligned}
\mathcal{C}_{ABCDEF} &:= \frac{2}{J}\frac{\partial\left(J\mathscr{C}_{ABCD}\right)}{\partial C_{EF}} \\
&= \mathbb{D}_{CADBEF} + \mathbb{D}_{DBCAEF} + \mathbb{D}_{CBDAEF} + \mathbb{D}_{ADCBEF} - \mathbb{D}_{CDABEF} - \mathbb{D}_{ABCDEF} \qquad \text{(B.5)}
\end{aligned}$$

and

$$\mathbb{D}_{ABCDEF} := C^{-1}_{AB}\left(\frac{1}{2}C^{-1}_{CD}C^{-1}_{EF} - C^{-1}_{CE}C^{-1}_{DF} - C^{-1}_{CF}C^{-1}_{DE}\right). \qquad \text{(B.6)}$$

Bibliography

A. Abdollahi and I. Arias. Constructive and destructive interplay between piezoelectricity and flexoelectricity in flexural sensors and actuators. *J. Appl. Mech.* **82**, 121003 (2015).

A. Abdollahi, D. Millán, C. Peco, M. Arroyo, and I. Arias. Revisiting pyramid compression to quantify flexoelectricity: A three-dimensional simulation study. *Phys. Rev. B* **91**, 104103 (2015a).

A. Abdollahi, C. Peco, D. Millán, M. Arroyo, and I. Arias. Computational evaluation of the flexoelectric effect in dielectric solids. *J. Appl. Phys.* **116**, 093502 (2014).

A. Abdollahi, C. Peco, D. Millán, M. Arroyo, G. Catalan, and I. Arias. Fracture toughening and toughness asymmetry induced by flexoelectricity. *Phys. Rev. B* **92**, 094101 (2015b).

F. Ahmadpoor and P. Sharma. Flexoelectricity in two-dimensional crystalline and biological membranes. *Nanoscale* **7**, 16555 (2015).

B. Altan and E. Aifantis. On some aspects in the special theory of gradient elasticity. *J. Mech. Behav. Mater.* **8**, 231 (1997).

L. Anqing, Z. Shenjie, Q. Lu, and C. Xi. A flexoelectric theory with rotation gradient effects for elastic dielectrics. *Modell. Simul. Mater. Sci. Eng.* **24**, 015009 (2015).

N. Aravas. Plane-strain problems for a class of gradient elasticity models - A stress function approach. *J. Elast.* **104**, 45 (2011).

H. Askes and E. C. Aifantis. Gradient elasticity in statics and dynamics: an overview of formulations, length scale identification procedures, finite element implementations and new results. *Int. J. Solids Struct.* **48**, 1962 (2011).

C. Baiocchi, F. Brezzi, and L. P. Franca. Virtual bubbles and Galerkin-least-squares type methods (Ga. LS). *Comput. Meth. Appl. Mech. Eng.* **105**, 125 (1993).

A. S. Banerjee and P. Suryanarayana. Cyclic density functional theory: A route to the first principles simulation of bending in nanostructures. *J. Mech. Phys. Solids* **96**, 605 (2016).

J. Barceló-Mercader, D. Codony, and I. Arias. Generalized periodicity conditions for the computational modeling of flexoelectric metamaterials. (2021a). To be submitted.

J. Barceló-Mercader, D. Codony, O. Marco, S. Fernández-Méndez, and I. Arias. Nitsche's method for interfaces in flexoelectricity and application to periodic structures. (2021b). To be submitted.

S. Baroni, S. de Gironcoli, A. Dal Corso, and P. Giannozzi. Phonons and related crystal properties from density-functional perturbation theory. *Rev. Mod. Phys.* **73**, 515 (2001).

S. Baroudi and F. Najar. Dynamic analysis of a nonlinear nanobeam with flexoelectric actuation. *J. Appl. Phys.* **125**, 044503 (2019).

S. Baroudi, F. Najar, and A. Jemai. Static and dynamic analytical coupled field analysis of piezoelectric flexoelectric nanobeams: A strain gradient theory approach. *Int. J. Sol. Struct.* **135**, 110 (2018).

S. Baskaran, X. He, Q. Chen, and J. Fu. Experimental studies on the direct flexoelectric effect in α-phase polyvinylidene fluoride films. *Appl. Phys. Lett.* **98**, 242901 (2011a).

S. Baskaran, X. He, Y. Wang, and J. Fu. Strain gradient induced electric polarization in α-phase polyvinylidene fluoride films under bending conditions. *J. Appl. Phys.* **111**, 014109 (2012).

S. Baskaran, N. Ramachandran, X. He, S. Thiruvannamalai, H. Lee, H. Heo, Q. Chen, and J. Fu. Giant flexoelectricity in polyvinylidene fluoride films. *Phys. Lett. A* **375**, 2082 (2011b).

I. B. Bersuker. Pseudo-Jahn–Teller Effect. A Two-State Paradigm in Formation, Deformation, and Transformation of Molecular Systems and Solids. *Chem. Rev.* **113**, 1351 (2013).

U. K. Bhaskar, N. Banerjee, A. Abdollahi, Z. Wang, D. G. Schlom, G. Rijnders, and G. Catalan. A flexoelectric microelectromechanical system on silicon. *Nat. Nanotechnol.* **11**, 263 (2016).

M. Born and R. Oppenheimer. Zur quantentheorie der molekeln. *Ann. Phys.* **389**, 457 (1927).

P. Bornemann and F. Cirak. A subdivision-based implementation of the hierarchical b-spline finite element method. *Comput. Meth. Appl. Mech. Eng.* **253**, 584 (2013).

L. Breger, T. Furukawa, and E. Fukada. Bending piezoelectricity in polyvinylidene fluoride. *Japanese Journal of Applied Physics* **15**, 2239 (1976).

L. Brillouin. Wave propagation in periodic structures: electric filters and crystal lattices. (1953).

E. Burman. Ghost penalty. *CR Math.* **348**, 1217 (2010).

J. Bursian and O. Zaikovskii. Changes in curvature of a ferroelectric film due to polarization. *Sov. Phys. Solid State* **10**, 1121 (1968).

G. Catalan, L. Sinnamon, and J. Gregg. The effect of flexoelectricity on the dielectric properties of inhomogeneously strained ferroelectric thin films. *J. Condens. Matter Phys.* **16**, 2253 (2004).

P. Chen, H. Zhang, and B. Chu. Strain gradient induced thermal-electrical response in paraelectric $Na_{0.5}Bi_{0.5}TiO_3$3-based ceramics. *Phys. Rev. Mater.* **2**, 034401 (2018).

X. Chen, S. Xu, N. Yao, and Y. Shi. 1.6 V nanogenerator for mechanical energy harvesting using PZT nanofibers. *Nano Lett.* **10**, 2133 (2010).

X. Chen, C. Yi, and C. Ke. Bending stiffness and interlayer shear modulus of few-layer graphene. *Appl. Phys. Lett.* **106**, 101907 (2015).

B. Chu and D. Salem. Flexoelectricity in several thermoplastic and thermosetting polymers. *Appl. Phys. Lett.* **101**, 103905 (2012).

B. Chu, W. Zhu, N. Li, and L. E. Cross. Flexure mode flexoelectric piezoelectric composites. *J. Appl. Phys.* **106**, 104109 (2009).

R. Codina. Comparison of some finite element methods for solving the diffusion-convection-reaction equation. *Comput. Meth. Appl. Mech. Eng.* **156**, 185 (1998).

R. Codina. On stabilized finite element methods for linear systems of convection-diffusion-reaction equations. *Comput. Meth. Appl. Mech. Eng.* **188**, 61 (2000).

R. Codina, S. Badia, J. Baiges, and J. Principe. Variational multiscale methods in computational fluid dynamics. *Encyclopedia of Computational Mechanics Second Edition* , 1 (2018).

D. Codony and I. Arias. Lifshitz-invariant flexoelectricity. (2021a). To be submitted.

D. Codony and I. Arias. Residual-based weak form stabilization for flexoelectricity. (2021b). To be submitted.

D. Codony and I. Arias. Switchable flexoelectric device by buckling. (2021c). To be submitted.

D. Codony, S. Fernández-Méndez, and I. Arias. Nitsche's method for finite deformation flexoelectricity. (2021a). To be submitted.

D. Codony, A. Mocci, O. Marco, and I. Arias. Wheel-shaped and helical torsional flexoelectric devices. (2021b). To be submitted.

D. Codony, I. Arias, and P. Suryanarayana. Transversal flexoelectric coefficient for nanostructures at finite deformations from first principles. *arXiv preprint arXiv:2010.01747* (2020a).

D. Codony, P. Gupta, O. Marco, and I. Arias. Modeling flexoelectricity in soft dielectrics at finite deformation. *J. Mech. Phys. Solids* **146**, 104182 (2020b).

D. Codony, O. Marco, S. Fernández-Méndez, and I. Arias. An Immersed Boundary Hierarchical B-spline method for flexoelectricity. *Comput. Meth. Appl. Mech. Eng.* **354**, 750 (2019).

L. Cross. Flexoelectric effects: Charge separation in insulating solids subjected to elastic strain gradients. *J. Mater. Sci.* **41**, 53 (2006).

C. Dagdeviren, P. Joe, O. L. Tuzman, K.-I. Park, K. J. Lee, Y. Shi, Y. Huang, and J. A. Rogers. Recent progress in flexible and stretchable piezoelectric devices for mechanical energy harvesting, sensing and actuation. *Extreme Mech. Lett.* **9**, 269 (2016).

C. de Boor. *A Practical Guide to Splines*. Applied Mathematical Sciences (Springer New York, 2001).

S. De La Torre Israel. *Theoretical and computational modeling of charge transport in flexo-photovoltaics*. Master's thesis. UPC, Facultat de Matemàtiques i Estadística, Departament d'Enginyeria Civil i Ambiental (2020).

F. de Prenter, C. Verhoosel, G. van Zwieten, and E. van Brummelen. Condition number analysis and preconditioning of the finite cell method. *Comput. Meth. Appl. Mech. Eng.* (2016).

F. Deng, Q. Deng, and S. Shen. A three-dimensional mixed finite element for flexoelectricity. *J. Appl. Mech.* **85** (2018).

F. Deng, Q. Deng, W. Yu, and S. Shen. Mixed finite elements for flexoelectric solids. *J. Appl. Mech.* **84** (2017).

Q. Deng, M. Kammoun, A. Erturk, and P. Sharma. Nanoscale flexoelectric energy harvesting. *Int. J. Solid. Struct.* **51**, 3218 (2014a).

Q. Deng, L. Liu, and P. Sharma. Electrets in soft materials: Nonlinearity, size effects, and giant electromechanical coupling. *Phys. Rev. E* **90**, 012603 (2014b).

Q. Deng, L. Liu, and P. Sharma. Flexoelectricity in soft materials and biological membranes. *J. Mech. Phys. Solids* **62**, 209 (2014c).

M. Dingle Palmer. *Multiscale modelling of surface effects in small-scale electromechanics*. Master's thesis. UPC, Escola Tècnica Superior d'Enginyeria de Camins, Canals i Ports de Barcelona, Departament d'Enginyeria Civil i Ambiental (2020).

G. Dong, S. Li, T. Li, H. Wu, T. Nan, X. Wang, H. Liu, Y. Cheng, Y. Zhou, W. Qu, *et al.*. Periodic Wrinkle-Patterned Single-Crystalline Ferroelectric Oxide Membranes with Enhanced Piezoelectricity. *Adv. Mater.* , 2004477 (2020).

A. Dorfmann and R. Ogden. Nonlinear electroelasticity. *Acta Mech.* **174**, 167 (2005).

L. Dorfmann and R. W. Ogden. *Nonlinear theory of electroelastic and magnetoelastic interactions*. Vol. 1 (Springer, 2014).

L. Dorfmann and R. W. Ogden. Nonlinear electroelasticity: material properties, continuum theory and applications. *Proc. Math. Phys. Eng. Sci.* **473**, 20170311 (2017).

C. E. Dreyer, M. Stengel, and D. Vanderbilt. Current-density implementation for calculating flexoelectric coefficients. *Phys. Rev. B* **98**, 075153 (2018).

T. Dumitrică, C. M. Landis, and B. I. Yakobson. Curvature-induced polarization in carbon nanoshells. *Chem. Phys. Lett.* **360**, 182 (2002).

A. Düster, J. Parvizian, Z. Yang, and E. Rank. The finite cell method for three-dimensional problems of solid mechanics. *Comput. Meth. Appl. Mech. Eng.* **197**, 3768 (2008).

E. A. Eliseev, M. D. Glinchuk, V. Khist, V. V. Skorokhod, R. Blinc, and A. N. Morozovska. Linear magnetoelectric coupling and ferroelectricity induced by the flexomagnetic effect in ferroics. *Phys. Rev. B* **84**, 174112 (2011).

E. Eliseev, A. Morozovska, M. Glinchuk, and R. Blinc. Spontaneous flexoelectric/flexomagnetic effect in nanoferroics. *Phys. Rev. B* **79**, 165433 (2009).

L. Evans. *Partial Differential Equations*. Graduate studies in mathematics (American Mathematical Society, 2010).

X. Feng, B. D. Yang, Y. Liu, Y. Wang, C. Dagdeviren, Z. Liu, A. Carlson, J. Li, Y. Huang, and J. A. Rogers. Stretchable ferroelectric nanoribbons with wavy configurations on elastomeric substrates. *Acs Nano* **5**, 3326 (2011).

S. Fernández-Méndez and A. Huerta. Imposing essential boundary conditions in mesh-free methods. *Comput. Meth. Appl. Mech. Eng.* **193**, 1257 (2004).

D. Forsey and R. Bartels. Hierarchical B-spline refinement. *ACM Siggraph Comp. Graph.* **22**, 205 (1988).

J. Fousek, L. Cross, and D. Litvin. Possible piezoelectric composites based on the flexoelectric effect. *Mat. Lett.* **39**, 287 (1999).

L. P. Franca and R. Stenberg. Error analysis of Galerkin least squares methods for the elasticity equations. *SIAM J. Numer. Anal.* **28**, 1680 (1991).

T. Fries. Higher-Order Accurate Integration for Cut Elements with Chen-Babuška Nodes. in *Advances in Discretization Methods: Discontinuities, Virtual Elements, Fictitious Domain Methods* (Springer International Publishing, 2016) pp. 245–269.

T. Fries and S. Omerović. Higher-order accurate integration of implicit geometries. *Int. J. Num. Meth. Eng.* **106**, 323 (2016). nme.5121.

J. Y. Fu, W. Zhu, N. Li, and L. E. Cross. Experimental studies of the converse flexoelectric effect induced by inhomogeneous electric field in a barium strontium titanate composition. *J. Appl. Phys.* **100**, 024112 (2006).

J. Y. Fu, W. Zhu, N. Li, N. B. Smith, and L. Eric Cross. Gradient scaling phenomenon in microsize flexoelectric piezoelectric composites. *Appl. Phys. Lett.* **91**, 182910 (2007).

H. Ghasemi, H. Park, and T. Rabczuk. A level-set based IGA formulation for topology optimization of flexoelectric materials. *Comput. Meth. Appl. Mech. Eng.* **313**, 239 (2017).

H. Ghasemi, H. S. Park, and T. Rabczuk. A multi-material level set-based topology optimization of flexoelectric composites. *Comput. Meth. Appl. Mech. Eng.* **332**, 47 (2018).

I.-D. Ghiba, P. Neff, A. Madeo, and I. Münch. A variant of the linear isotropic indeterminate couple-stress model with symmetric local force-stress, symmetric nonlocal force-stress, symmetric couple-stresses and orthogonal boundary conditions. *Mathematics and Mechanics of Solids* **22**, 1221 (2017).

S. Ghosh, A. S. Banerjee, and P. Suryanarayana. Symmetry-adapted real-space density functional theory for cylindrical geometries: Application to large group-IV nanotubes. *Phys. Rev. B* **100**, 125143 (2019).

S. Ghosh and P. Suryanarayana. SPARC: Accurate and efficient finite-difference formulation and parallel implementation of Density Functional Theory: Isolated clusters. *Comput. Phys. Commun.* **212**, 189 (2017).

X. Gonze and C. Lee. Dynamical matrices, Born effective charges, dielectric permittivity tensors, and interatomic force constants from density-functional perturbation theory. *Phys. Rev. B* **55**, 10355 (1997).

O. Guasch and R. Codina. An algebraic subgrid scale finite element method for the convected Helmholtz equation in two dimensions with applications in aeroacoustics. *Comput. Meth. Appl. Mech. Eng.* **196**, 4672 (2007).

A. R. Hadjesfandiari. Size-dependent piezoelectricity. *Int. J. Solids Struct.* **50**, 2781 (2013).

D. R. Hamann. Optimized norm-conserving Vanderbilt pseudopotentials. *Phys. Rev. B* **88**, 085117 (2013).

K. M. Hamdia, H. Ghasemi, X. Zhuang, N. Alajlan, and T. Rabczuk. Sensitivity and uncertainty analysis for flexoelectric nanostructures. *Comput. Meth. Appl. Mech. Eng.* **337**, 95 (2018).

E. Han, J. Yu, E. Annevelink, J. Son, D. A. Kang, K. Watanabe, T. Taniguchi, E. Ertekin, P. Y. Huang, and A. M. van der Zande. Ultrasoft slip-mediated bending in few-layer graphene. *Nat. Mater.* **19**, 305 (2020).

J. K. Han, D. H. Jeon, S. Y. Cho, S. W. Kang, S. A. Yang, S. D. Bu, S. Myung, J. Lim, M. Choi, M. Lee, *et al.*. Nanogenerators consisting of direct-grown piezoelectrics on multi-walled carbon nanotubes using flexoelectric effects. *Sci. Rep.* **6**, 1 (2016).

P. Hana. Study of flexoelectric phenomenon from direct and from inverse flexoelectric behavior of PMNT ceramic. *Ferroelectrics* **351**, 196 (2007).

P. Hana, M. Marvan, L. Burianova, S. Zhang, E. Furman, and T. R. Shrout. Study of the inverse flexoelectric phenomena in ceramic lead magnesium niobate-lead titanate. *Ferroelectrics* **336**, 137 (2006).

J. Harden, B. Mbanga, N. Éber, K. Fodor-Csorba, S. Sprunt, J. T. Gleeson, and A. Jakli. Giant flexoelectricity of bent-core nematic liquid crystals. *Phys. Rev. Lett.* **97**, 157802 (2006).

V. Heine, M. Cohen, and D. Weaire. Solid State Phys. vol. 24. The Pseudopotential Concept. (1970).

P. Hohenberg and W. Kohn. Density functional theory (DFT). *Phys. Rev.* **136**, B864 (1964).

K. Höllig, J. Hörner, and A. Hoffacker. Finite element analysis with B-splines: weighted and isogeometric methods. in *International Conference on Curves and Surfaces* (Springer, 2012) pp. 330–350.

K. Höllig, U. Reif, and J. Wipper. Weighted extended B-spline approximation of Dirichlet problems. *SIAM J. Numer. Anal.* **39**, 442 (2001).

C.-H. Hong, H.-P. Kim, B.-Y. Choi, H.-S. Han, J. S. Son, C. W. Ahn, and W. Jo. Lead-free piezoceramics–Where to move on? *J. Materiomics* **2**, 1 (2016).

J. Hong and D. Vanderbilt. First-principles theory and calculation of flexoelectricity. *Phys. Rev. B* **88**, 174107 (2013).

S. Hu and S. Shen. Variational principles and governing equations in nano-dielectrics with the flexoelectric effect. *Sci. China Phys. Mech. Astron.* **53**, 1497 (2010).

S. Huang, T. Kim, D. Hou, D. Cann, J. L. Jones, and X. Jiang. Flexoelectric characterization of $BaTiO_3$-0.08 $Bi(Zn_{1/2}Ti_{1/2})O_3$. *Appl. Phys. Lett.* **110**, 222904 (2017).

S. Huang, L. Qi, W. Huang, L. Shu, S. Zhou, and X. Jiang. Flexoelectricity in dielectrics: Materials, structures and characterizations. *J. Adv. Dielectr.* **8**, 1830002 (2018).

W. Huang, K. Kim, S. Zhang, F.-G. Yuan, and X. Jiang. Scaling effect of flexoelectric (Ba,Sr)TiO_3 microcantilevers. *Phys. Stat. Solid. RRL* **5**, 350 (2011).

Y. Huang, J. Wu, and K. C. Hwang. Thickness of graphene and single-wall carbon nanotubes. *Phys. Rev. B* **74**, 245413 (2006).

T. J. R. Hughes, J. A. Cottrell, and Y. Bazilevs. Isogeometric analysis: CAD, finite elements, NURBS, exact geometry and mesh refinement. *Comput. Meth. Appl. Mech. Eng.* **194**, 4135 (2005).

T. J. Hughes, G. R. Feijóo, L. Mazzei, and J.-B. Quincy. The variational multiscale method-a paradigm for computational mechanics. *Comput. Meth. Appl. Mech. Eng.* **166**, 3 (1998).

X. Jiang, W. Huang, and S. Zhang. Flexoelectric nano-generator: Materials, structures and devices. *Nano Energy* **2**, 1079 (2013).

S. V. Kalinin, S. Jesse, W. Liu, and A. A. Balandin. Evidence for possible flexoelectricity in tobacco mosaic viruses used as nanotemplates. *Appl. Phys. Lett.* **88**, 153902 (2006).

S. V. Kalinin and V. Meunier. Electronic flexoelectricity in low-dimensional systems. *Phys. Rev. B* **77**, 033403 (2008).

S. M. Kogan. Piezoelectric effect during inhomogeneous deformation and acoustic scattering of carriers in crystals. *Sov. Phys. Solid State* **5**, 2069 (1964).

W. Kohn and L. J. Sham. Self-consistent equations including exchange and correlation effects. *Phys. Rev.* **140**, A1133 (1965).

R. Kraft. *Adaptive and Linearly Independent Multilevel B-splines*. Bericht (SFB 404, Geschäftsstelle, 1997).

R. Kraft. Hierarchical B-splines. (1995). unpublished.

S. Krichen and P. Sharma. Flexoelectricity: A perspective on an unusual electromechanical coupling. *J. Appl. Mech.* **83**, 030801 (2016).

L. Kudela, N. Zander, S. Kollmannsberger, and E. Rank. Smart octrees: Accurately integrating discontinuous functions in 3D. *Comput. Meth. Appl. Mech. Eng.* **306**, 406 (2016).

S. Kumar, D. Codony, I. Arias, and P. Suryanarayana. Flexoelectricity in atomic monolayers from first principles. *Nanoscale* , (2020).

S. R. Kwon, W. Huang, L. Shu, F.-G. Yuan, J.-P. Maria, and X. Jiang. Flexoelectricity in barium strontium titanate thin film. *Appl. Phys. Lett.* **105**, 142904 (2014).

L. D. Landau and E. M. Lifshitz. *Course of theoretical physics* (Elsevier, 2013).

M. Lax and D. Nelson. Maxwell equations in material form. *Phys. Rev. B* **13**, 1777 (1976).

H. Le Quang and Q.-C. He. The number and types of all possible rotational symmetries for flexoelectric tensors. *Proc. Math. Phys. Eng. Sci.* **467**, 2369 (2011).

G. Legrain, N. Chevaugeon, and K. Dréau. High order X-FEM and levelsets for complex microstructures: Uncoupling geometry and approximation. *Comput. Meth. Appl. Mech. Eng.* **241**, 172 (2012).

G. Legrain. A NURBS enhanced extended finite element approach for unfitted CAD analysis. *Comput. Mech.* **52**, 913 (2013).

A. Li, S. Zhou, L. Qi, and X. Chen. A reformulated flexoelectric theory for isotropic dielectrics. *J. Phys. D: Appl. Phys.* **48**, 465502 (2015).

Y. Li, L. Shu, W. Huang, X. Jiang, and H. Wang. Giant flexoelectricity in $Ba_{0.6}Sr_{0.4}TiO_3/Ni_{0.8}Zn_{0.2}Fe_2O_4$ composite. *Appl. Phys. Lett.* **105**, 162906 (2014).

Y. Li, L. Shu, Y. Zhou, J. Guo, F. Xiang, L. He, and H. Wang. Enhanced flexoelectric effect in a non-ferroelectric composite. *Appl. Phys. Lett.* **103**, 142909 (2013).

X. Liang, S. Hu, and S. Shen. Effects of surface and flexoelectricity on a piezoelectric nanobeam. *Smart Mater. Struct.* **23**, 035020 (2014).

X. Liang, S. Hu, and S. Shen. Nanoscale mechanical energy harvesting using piezoelectricity and flexoelectricity. *Smart Mater. Struct.* **26**, 035050 (2017).

E. Lifshitz and L. Landau. Statistical Physics (Course of Theoretical Physics, Volume 5). (1984).

N. Lindahl, D. Midtvedt, J. Svensson, O. A. Nerushev, N. Lindvall, A. Isacsson, and E. E. B. Campbell. Determination of the Bending Rigidity of Graphene via Electrostatic Actuation of Buckled Membranes. *Nano Lett.* **12**, 3526 (2012).

C. Liu, H. Wu, and J. Wang. Giant piezoelectric response in piezoelectric/dielectric superlattices due to flexoelectric effect. *Appl. Phys. Lett.* **109**, 192901 (2016a).

L. Liu. An energy formulation of continuum magneto-electro-elasticity with applications. *J. Mech. Phys. Solids* **63**, 451 (2014).

P. Liu. Low scaling GW method: implementation and applications. (2017).

Y. Liu, J. Chen, H. Deng, G. Hu, D. Zhu, and N. Dai. Anomalous thermoelectricity in strained Bi_2Te_3 films. *Sci. Rep.* **6**, 32661 (2016b).

W. E. Lorensen and H. E. Cline. Marching cubes: A high resolution 3D surface construction algorithm. *Comput. Graph.* **21**, 163 (1987).

H. Lu, C.-W. Bark, D. E. De Los Ojos, J. Alcala, C.-B. Eom, G. Catalan, and A. Gruverman. Mechanical writing of ferroelectric polarization. *Science* **336**, 59 (2012).

W. Ma and L. Cross. Flexoelectric polarization of barium strontium titanate in the paraelectric state. *Appl. Phys. Lett.* **81**, 3440 (2002).

W. Ma and L. Cross. Flexoelectric effect in ceramic lead zirconate titanate. *Appl. Phys. Lett.* **86**, 072905 (2005).

W. Ma and L. Cross. Flexoelectricity of barium titanate. *Appl. Phys. Lett.* **88**, 232902 (2006).

W. Ma and L. E. Cross. Large flexoelectric polarization in ceramic lead magnesium niobate. *Appl. Phys. Lett.* **79**, 4420 (2001a).

W. Ma and L. E. Cross. Observation of the flexoelectric effect in relaxor Pb ($Mg_{1/3}$ $Nb_{2/3}$) O_3 ceramics. *Appl. Phys. Lett.* **78**, 2920 (2001b).

W. Ma and L. E. Cross. Strain-gradient-induced electric polarization in lead zirconate titanate ceramics. *Appl. Phys. Lett.* **82**, 3293 (2003).

M. S. Majdoub, P. Sharma, and T. Çağin. Erratum: Enhanced size-dependent piezoelectricity and elasticity in nanostructures due to the flexoelectric effect [Phys. Rev. B 77, 125424 (2008)]. *Phys. Rev. B* **79**, 119904 (2009).

M. Majdoub, P. Sharma, and T. Çağin. Enhanced size-dependent piezoelectricity and elasticity in nanostructures due to the flexoelectric effect. *Phys. Rev. B* **77**, 125424 (2008).

S. Mao and P. K. Purohit. Insights Into Flexoelectric Solids From Strain-Gradient Elasticity. *J. Appl. Mech.* **81**, 1 (2014).

S. Mao, P. K. Purohit, and N. Aravas. Mixed finite-element formulations in piezoelectricity and flexoelectricity. *Proc. Math. Phys. Eng. Sci.* **472** (2016).

R. Maranganti, N. Sharma, and P. Sharma. Electromechanical coupling in nonpiezoelectric materials due to nanoscale nonlocal size effects: Green's function solutions and embedded inclusions. *Phys. Rev. B* **74**, 014110 (2006).

O. Marco, J. J. Ródenas, J. M. Navarro-Jiménez, and M. Tur. Robust h-adaptive meshing strategy considering exact arbitrary CAD geometries in a Cartesian grid framework. *Comput. Struct.* **193**, 87 (2017).

O. Marco, R. Sevilla, Y. Zhang, J. J. Ródenas, and M. Tur. Exact 3D boundary representation in finite element analysis based on Cartesian grids independent of the geometry. *Int. J. Num. Meth. Eng.* **103**, 445 (2015).

R. M. Martin. *Electronic Structure: Basic Theory and Practical Methods* (Cambridge University Press, 2004).

M. Marvan and A. Havránek. Flexoelectric effect in elastomers. in *Relationships of Polymeric Structure and Properties* (Springer, 1998) pp. 33–36.

V. S. Mashkevich and K. B. Tolpygo. Electrical, optical and elastic properties of diamond type cristals. 1. *Sov. Phys. Solid State* **5**, 435 (1957).

MATLAB. *8.6 (R2015b)* (The MathWorks Inc., Natick, Massachusetts, 2015).

A. McBride, D. Davydov, and P. Steinmann. Modelling the flexoelectric effect in solids: a micromorphic approach. *Comput. Meth. Appl. Mech. Eng.* **371**, 113320 (2020).

N. D. Mermin. Thermal properties of the inhomogeneous electron gas. *Phys. Rev.* **137**, A1441 (1965).

R. B. Meyer. Piezoelectric effects in liquid crystals. *Phys. Rev. Lett.* **22**, 918 (1969).

R. D. Mindlin and N. N. Eshel. On first strain-gradient theories in linear elasticity. *Int. J. Solids Struct.* **4**, 109 (1968).

R. D. Mindlin and H. F. Tiersten. Effects of couple-stresses in linear elasticity. *Arch. Ration. Mech. Anal.* **11**, 415 (1962).

R. D. Mindlin. Polarization gradient in elastic dielectrics. *Int. J. Solids Struct.* **4**, 637 (1968).

R. Mittal and G. Iaccarino. Immersed boundary methods. *Annu. Rev. Fluid Mech.* **37**, 239 (2005).

A. Mocci, J. Barceló-Mercader, D. Codony, and I. Arias. Geometrically polarized architected dielectrics with effective piezoelectricity. (2021). To be submitted.

A. Mocci, A. Abdollahi, and I. Arias. Quantification of shear flexoelectricity in ferroelectrics. (2020). To be submitted.

H. J. Monkhorst and J. D. Pack. Special points for Brillouin-zone integrations. *Phys. Rev. B* **13**, 5188 (1976).

S. Nanthakumar, X. Zhuang, H. S. Park, and T. Rabczuk. Topology optimization of flexoelectric structures. *J. Mech. Phys. Solids* **105**, 217 (2017).

J. Narvaez and G. Catalan. Origin of the enhanced flexoelectricity of relaxor ferroelectrics. *Appl. Phys. Lett.* **104**, 162903 (2014).

J. Narvaez, S. Saremi, J. Hong, M. Stengel, and G. Catalan. Large flexoelectric anisotropy in paraelectric barium titanate. *Phys. Rev. Lett.* **115**, 037601 (2015).

B. Nguyen, X. Zhuang, and T. Rabczuk. NURBS-based formulation for nonlinear electro-gradient elasticity in semiconductors. *Comput. Meth. Appl. Mech. Eng.* **346**, 1074 (2019).

T. D. Nguyen, S. Mao, Y.-W. Yeh, P. K. Purohit, and M. C. McAlpine. Nanoscale flexoelectricity. *Adv. Mater.* **25**, 946 (2013).

J. Nitsche. Über ein Variationsprinzip zur Lösung von Dirichlet-Problemen bei Verwendung von Teilräumen, die keinen Randbedingungen unterworfen sind. *Abhandlungen aus dem Mathematischen Seminar der Universität Hamburg* **36**, 9 (1971).

J. S. Oghalai, H.-B. Zhao, J. W. Kutz, and W. E. Brownell. Voltage-and tension-dependent lipid mobility in the outer hair cell plasma membrane. *Science* **287**, 658 (2000).

A. O'Halloran, F. O'malley, and P. McHugh. A review on dielectric elastomer actuators, technology, applications, and challenges. *J. Appl. Phys.* **104**, 9 (2008).

K.-I. Park, S. Xu, Y. Liu, G.-T. Hwang, S.-J. L. Kang, Z. L. Wang, and K. J. Lee. Piezoelectric $BaTiO_3$ thin film nanogenerator on plastic substrates. *Nano Lett.* **10**, 4939 (2010).

S. M. Park, B. Wang, S. Das, S. C. Chae, J.-S. Chung, J.-G. Yoon, L.-Q. Chen, S. M. Yang, and T. W. Noh. Selective control of multiple ferroelectric switching pathways using a trailing flexoelectric field. *Nat. Nanotechnol.* **13**, 366 (2018).

S. Patel, A. Chauhan, N. A. Madhar, B. Ilahi, and R. Vaish. Flexoelectric induced caloric effect in truncated Pyramid shaped $Ba_{0.67}Sr_{0.33}TiO_3$ ferroelectric material. *J. Elec. Mater.* **46**, 4166 (2017).

M. C. Payne, M. P. Teter, D. C. Allan, T. Arias, and a. J. Joannopoulos. Iterative minimization techniques for ab initio total-energy calculations: molecular dynamics and conjugate gradients. *Rev. Mod. Phys.* **64**, 1045 (1992).

R. E. Pelrine, R. D. Kornbluh, and J. P. Joseph. Electrostriction of polymer dielectrics with compliant electrodes as a means of actuation. *Sens. Actuator A Phys.* **64**, 77 (1998).

A. W. Peng, F. T. Salles, B. Pan, and A. J. Ricci. Integrating the biophysical and molecular mechanisms of auditory hair cell mechanotransduction. *Nat. Commun.* **2**, 1 (2011).

J. P. Perdew, K. Burke, and M. Ernzerhof. Generalized gradient approximation made simple. *Phys. Rev. Lett.* **77**, 3865 (1996).

J. P. Perdew and W. Yue. Accurate and simple density functional for the electronic exchange energy: Generalized gradient approximation. *Phys. Rev. B* **33**, 8800 (1986).

C. S. Peskin. The immersed boundary method. *Acta Num.* **11**, 479 (2002).

A. G. Petrov. Flexoelectric model for active transport. in *Physical and Chemical Bases of Biological Information Transfer* (Springer, 1975) pp. 111–125.

A. G. Petrov. Flexoelectricity of model and living membranes. *Biochim. Biophys. Acta (BBA)* **1561**, 1 (2002).

J. C. Phillips. Energy-band interpolation scheme based on a pseudopotential. *Phys. Rev.* **112**, 685 (1958).

L. Piegl and W. Tiller. *The NURBS Book*. Monographs in Visual Communication (Springer Berlin Heidelberg, 2012).

R. Poya, A. J. Gil, R. Ortigosa, and R. Palma. On a family of numerical models for couple stress based flexoelectricity for continua and beams. *J. Mech. Phys. Solids* **125**, 613 (2019).

J. Prost and J. Marcerou. On the microscopic interpretation of flexoelectricity. *J. Phys.* **38**, 315 (1977).

Y. Qi, J. Kim, T. D. Nguyen, B. Lisko, P. K. Purohit, and M. C. McAlpine. Enhanced Piezoelectricity and Stretchability in Energy Harvesting Devices Fabricated from Buckled PZT Ribbons. *Nano Lett.* **11**, 1331 (2011).

W. Qu, S. Bagchi, X. Chen, H. B. Chew, and C. Ke. Bending and interlayer shear moduli of ultrathin boron nitride nanosheet. *J. Phys. D: Appl. Phys.* **52**, 465301 (2019).

R. Resta. Towards a bulk theory of flexoelectricity. *Phys. Rev. Lett.* **105**, 127601 (2010).

J. Rödel, W. Jo, K. T. Seifert, E.-M. Anton, T. Granzow, and D. Damjanovic. Perspective on the development of lead-free piezoceramics. *J. Am. Ceram. Soc.* **92**, 1153 (2009).

D. Rogers. *An Introduction to NURBS: With Historical Perspective*. Morgan Kaufmann Series in Computer Graphics and Geometric Modeling (Morgan Kaufmann Publishers, 2001).

S. Rosset and H. R. Shea. Small, fast, and tough: Shrinking down integrated elastomer transducers. *Appl. Phys. Rev.* **3**, 031105 (2016).

T. Rüberg and F. Cirak. Subdivision-stabilised immersed b-spline finite elements for moving boundary flows. *Comput. Meth. Appl. Mech. Eng.* **209**, 266 (2012).

T. Rüberg, F. Cirak, and J. M. García Aznar. An unstructured immersed finite element method for nonlinear solid mechanics. *Adv. Model. Simul. Eng. Sci.* **3**, 22 (2016).

E. Sahin and S. Dost. A strain-gradients theory of elastic dielectrics with spatial dispersion. *Int. J. Eng. Sci.* **26**, 1231 (1988).

A. Schiaffino, C. E. Dreyer, D. Vanderbilt, and M. Stengel. Metric wave approach to flexoelectricity within density functional perturbation theory. *Phys. Rev. B* **99**, 085107 (2019).

D. Schillinger, L. Dedè, M. A. Scott, J. A. Evans, M. J. Borden, E. Rank, and T. J. Hughes. An isogeometric design-through-analysis methodology based on adaptive hierarchical refinement of NURBS, immersed boundary methods, and T-spline CAD surfaces. *Comput. Meth. Appl. Mech. Eng.* **249–252**, 116 (2012).

D. Schillinger, I. Harari, M.-C. Hsu, D. Kamensky, S. K. Stoter, Y. Yu, and Y. Zhao. The non-symmetric Nitsche method for the parameter-free imposition of weak boundary and coupling conditions in immersed finite elements. *Comput. Meth. Appl. Mech. Eng.* **309**, 625 (2016).

D. Schillinger and M. Ruess. The Finite Cell Method: A Review in the Context of Higher-Order Structural Analysis of CAD and Image-Based Geometric Models. *Arch. Comp. Meth. Eng.* **22**, 391 (2015).

R. Sevilla and S. Fernández-Méndez. Numerical integration over 2D NURBS-shaped domains with applications to NURBS-enhanced FEM. *Finite Elem. Anal. Des.* **47**, 1209 (2011).

R. Sevilla, S. Fernández-Méndez, and A. Huerta. NURBS-enhanced finite element method (NEFEM). *Int. J. Num. Meth. Eng.* **76**, 56 (2008).

R. Sevilla, S. Fernández-Méndez, and A. Huerta. 3D NURBS-enhanced finite element method (NEFEM). *Int. J. Num. Meth. Eng.* **88**, 103 (2011a).

R. Sevilla, S. Fernández-Méndez, and A. Huerta. NURBS-enhanced finite element method (NEFEM). *Arch. Comp. Meth. Eng.* **18**, 441 (2011b).

N. Sharma, C. Landis, and P. Sharma. Piezoelectric thin-film superlattices without using piezoelectric materials. *J. Appl. Phys.* **108**, 1 (2010).

N. Sharma, R. Maranganti, and P. Sharma. On the possibility of piezoelectric nanocomposites without using piezoelectric materials. *J. Mech. Phys. Solids* **55**, 2328 (2007).

S. Shen and S. Hu. A theory of flexoelectricity with surface effect for elastic dielectrics. *J. Mech. Phys. Solids* **58**, 665 (2010).

W. Shi, Y. Guo, Z. Zhang, and W. Guo. Flexoelectricity in Monolayer Transition Metal Dichalcogenides. *J. Phys. Chem. Lett.* **9**, 6841 (2018).

L. Shu, W. Huang, S. Ryung Kwon, Z. Wang, F. Li, X. Wei, S. Zhang, M. Lanagan, X. Yao, and X. Jiang. Converse flexoelectric coefficient f_{1212} in bulk $Ba_{0.67}Sr_{0.33}TiO_3$. *Appl. Phys. Lett.* **104**, 232902 (2014).

L. Shu, S. Ke, L. Fei, W. Huang, Z. Wang, J. Gong, X. Jiang, L. Wang, F. Li, S. Lei, *et al.*. Photoflexoelectric effect in halide perovskites. *Nat. Mater.* , 1 (2020).

L. Shu, T. Li, Z. Wang, F. Li, L. Fei, Z. Rao, M. Ye, S. Ke, W. Huang, Y. Wang, *et al.*. Flexoelectric behavior in PIN-PMN-PT single crystals over a wide temperature range. *Appl. Phys. Lett.* **111**, 162901 (2017).

L. Shu, R. Liang, Z. Rao, L. Fei, S. Ke, and Y. Wang. Flexoelectric materials and their related applications: A focused review. *J. Adv. Ceram.* , 1 (2019).

L. Shu, T. Wang, X. Jiang, and W. Huang. Verification of the flexoelectricity in barium strontium titanate through d_{33} meter. *AIP Adv.* **6**, 125003 (2016).

L. Shu, X. Wei, L. Jin, Y. Li, H. Wang, and X. Yao. Enhanced direct flexoelectricity in paraelectric phase of $Ba(Ti_{0.87}Sn_{0.13})O_3$ ceramics. *Appl. Phys. Lett.* **102**, 152904 (2013).

L. Shu, X. Wei, T. Pang, X. Yao, and C. Wang. Symmetry of flexoelectric coefficients in crystalline medium. *J. Appl. Phys.* **110**, 104106 (2011).

J. C. Slater. *The self-consistent field for molecules and solids.* Vol. 4 (McGraw-Hill, 1974).

P. Steinmann and D. K. Vu. Computational challenges in the simulation of nonlinear electroelasticity. *Comput. Assist. Meth. Eng. Sci.* **19**, 199 (2017).

M. Stengel. Flexoelectricity from density-functional perturbation theory. *Phys. Rev. B* **88**, 174106 (2013).

M. Stengel. Surface control of flexoelectricity. *Phys. Rev. B* **90**, 201112 (2014).

S. Su, H. Huang, Y. Liu, and Z. H. Zhu. Wrinkling of flexoelectric nano-film/substrate systems. *J. Phys. D* **51**, 075309 (2018).

P. Suryanarayana and D. Phanish. Augmented Lagrangian formulation of orbital-free density functional theory. *J. Comput. Phys.* **275**, 524 (2014).

A. K. Tagantsev. Piezoelectricity and flexoelectricity in crystalline dielectrics. *Phys. Rev. B* **34**, 5883 (1986).

A. K. Tagantsev. Electric polarization in crystals and its response to thermal and elastic perturbations. *Phase Transit. A* **35**, 119 (1991).

T. Q. Thai, T. Rabczuk, and X. Zhuang. A large deformation isogeometric approach for flexoelectricity and soft materials. *Comput. Meth. Appl. Mech. Eng.* **341**, 718 (2018).

L. L. Thompson and P. M. Pinsky. A Galerkin least-squares finite element method for the two-dimensional Helmholtz equation. *Int. J. Num. Meth. Eng.* **38**, 371 (1995).

A. Todorov, A. Petrov, M. O. Brandt, and J. H. Fendler. Electrical and real-time stroboscopic interferometric measurements of bilayer lipid membrane flexoelectricity. *Langmuir* **7**, 3127 (1991).

K. Tolpygo. Long wavelength oscillations of diamond-type crystals including long range forces. *Sov. Phys. Solid State* **4**, 1297 (1963).

C. Trabi, C. Brown, A. Smith, and N. Mottram. Interferometric method for determining the sum of the flexoelectric coefficients (e_1+ e_3) in an ionic nematic material. *Appl. Phys. Lett.* **92**, 223509 (2008).

F. Vásquez Sancho. *Flexoelectricity in biomaterials*. Ph.D. thesis. Universitat Autònoma de Barcelona (2018).

F. Vasquez-Sancho, A. Abdollahi, D. Damjanovic, and G. Catalan. Flexoelectricity in bones. *Adv. Mater.* **30**, 1705316 (2018).

J. Ventura, D. Codony, and S. Fernández-Méndez. A C0 interior penalty finite element method for flexoelectricity. *arXiv preprint arXiv:2008.12391* (2020).

J. Ventura Siches. *Computational modelling of flexoelectric materials based on C0-FEM for 4th order PDEs*. Master's thesis. UPC, Facultat de Matemàtiques i Estadística, Departament d'Enginyeria Civil i Ambiental (2020).

D. Vu, P. Steinmann, and G. Possart. Numerical modelling of non-linear electroelasticity. *Int. J. Num. Meth. Eng.* **70**, 685 (2007).

A.-V. Vuong, C. Giannelli, B. Jüttler, and B. Simeon. A hierarchical approach to adaptive local refinement in isogeometric analysis. *Comput. Meth. Appl. Mech. Eng.* **200**, 3554 (2011).

M. Wan, Z. Yong, W. Huang, S. Zhang, N. Zhou, and L. Shu. Design of a flexure composite with large flexoelectricity. *J. Mat. Sci.* **28**, 6505 (2017).

B. Wang, Y. Gu, S. Zhang, and L.-Q. Chen. Flexoelectricity in solids: Progress, challenges, and perspectives. *Prog. Mater Sci.* (2019).

J. C. Weaver, G. W. Milliron, A. Miserez, K. Evans-Lutterodt, S. Herrera, I. Gallana, W. J. Mershon, B. Swanson, P. Zavattieri, E. DiMasi, *et al.*. The stomatopod dactyl club: a formidable damage-tolerant biological hammer. *Science* **336**, 1275 (2012).

Wikimedia Commons. File:OdontodactylusScyllarus2.jpg. (2010). Accessed: 2020-12-08.

Wikimedia Commons. File:Bloch function.svg. (2016). Accessed: 2020-10-18.

Wikimedia Commons. File:Odontodactylus_scyllarus_2.png. (2020). Accessed: 2020-12-08.

F. Witherden and P. Vincent. On the identification of symmetric quadrature rules for finite element methods. *Comput. Math. Appl.* **69**, 1232 (2015).

Q. Xu, A. Sharma, B. Comer, H. Huang, E. Chow, A. J. Medford, J. E. Pask, and P. Suryanarayana. SPARC: Simulation Package for Ab-initio Real-space Calculations. *arXiv preprint arXiv:2005.10431* (2020a).

Q. Xu, A. Sharma, and P. Suryanarayana. M-SPARC: Matlab-Simulation Package for Ab-initio Real-space Calculations. *SoftwareX* **11**, 100423 (2020b).

Z. Yan and L. Jiang. Flexoelectric effect on the electroelastic responses of bending piezoelectric nanobeams. *J. Appl. Phys.* **113**, 194102 (2013).

Z. Yan. Modeling of a nanoscale flexoelectric energy harvester with surface effects. *Phys. E* **88**, 125 (2017).

M.-M. Yang, D. J. Kim, and M. Alexe. Flexo-photovoltaic effect. *Science* **360**, 904 (2018).

N. A. Yaraghi, N. Guarín-Zapata, L. K. Grunenfelder, E. Hintsala, S. Bhowmick, J. M. Hiller, M. Betts, E. L. Principe, J.-Y. Jung, L. Sheppard, *et al.*. A sinusoidally architected helicoidal biocomposite. *Adv. Mater.* **28**, 6835 (2016).

P. Yudin and A. Tagantsev. Fundamentals of flexoelectricity in solids. *Nanotechnol.* **24**, 1 (2013).

A. Yurkov and A. Tagantsev. Strong surface effect on direct bulk flexoelectric response in solids. *Appl. Phys. Lett.* **108**, 022904 (2016).

J. Yvonnet and L. Liu. A numerical framework for modeling flexoelectricity and Maxwell stress in soft dielectrics at finite strains. *Comput. Meth. Appl. Mech. Eng.* **313**, 450 (2017).

R. Zhang, X. Liang, and S. Shen. A Timoshenko dielectric beam model with flexoelectric effect. *Meccanica* **51**, 1181 (2016a).

S. Zhang, K. Liu, M. Xu, H. Shen, K. Chen, B. Feng, and S. Shen. Investigation of the 2312 flexoelectric coefficient component of polyvinylidene fluoride: Deduction, simulation, and mensuration. *Sci. Rep.* **7**, 1 (2017).

S. Zhang, M. Xu, G. Ma, X. Liang, and S. Shen. Experimental method research on transverse flexoelectric response of poly (vinylidene fluoride). *Jpn. J. Appl. Phys.* **55**, 071601 (2016b).

X. Zhang, J. Liu, M. Chu, and B. Chu. Flexoelectric piezoelectric metamaterials based on the bending of ferroelectric ceramic wafers. *Appl. Phys. Lett.* **109**, 072903 (2016c).

W. Zhou, P. Chen, Q. Pan, X. Zhang, and B. Chu. Lead-free metamaterials with enormous apparent piezoelectric response. *Adv. Mater.* **27**, 6349 (2015).

Y. Zhou, J. Liu, X. Hu, B. Chu, S. Chen, and D. Salem. Flexoelectric effect in PVDF-based polymers. *IEEE Trans. Dielectr. Electr. Insul.* **24**, 727 (2017).

W. Zhu, J. Y. Fu, N. Li, and L. Cross. Piezoelectric composite based on the enhanced flexoelectric effects. *Appl. Phys. Lett.* **89**, 192904 (2006).

X. Zhuang, S. S. Nanthakumar, and T. Rabczuk. A meshfree formulation for large deformation analysis of flexoelectric structures accounting for the surface effects. *arXiv preprint arXiv:1911.06553* (2019).

X. Zhuang, B. H. Nguyen, S. S. Nanthakumar, T. Q. Tran, N. Alajlan, and T. Rabczuk. Computational Modeling of Flexoelectricity: A Review. *Energies* **13**, 1326 (2020).

D. Zorin. Subdivision for Modeling and Animation. *SIGGRAPH 2000 Course Notes* , 65 (2000).

P. Zubko, G. Catalan, A. Buckley, P. Welche, and J. Scott. Strain-gradient-induced polarization in $SrTiO_3$ single crystals. *Phys. Rev. Lett.* **99**, 167601 (2007).

P. Zubko, G. Catalan, and A. K. Tagantsev. Flexoelectric effect in solids. *Annu. Rev. Mat. Res.* **24**, 387 (2013).